

**COMPUTER MODELLING OF TEMPERATURE, FLOW
STRESS AND MICROSTRUCTURE DURING THE HOT
ROLLING OF STEELS**

By

Abdellatif Laasraoui

**A Thesis Submitted to the Faculty of Graduate Studies
and Research in Partial Fulfillment of the Requirements
for the Degree of Doctor of Philosophy**

**Department of Mining and Metallurgical Engineering
McGill University
Montreal, Canada**

January 1990

©Abdellatif Laasraoui 1990

ABSTRACT

With the aim of simulating the hot rolling process, single and double hit compression tests were performed in the temperature range 800 to 1200 °C at strain rates of 0.2 to 50 s⁻¹ on selected low carbon steels containing niobium, boron and copper. The stress/strain curves determined at high strain rates were corrected for adiabatic heating and constitutive equations were formulated. When dynamic recovery is the only softening mechanism, these involve a rate equation, consisting of a hyperbolic sine law, and an evolution equation with one internal variable. When dynamic recrystallization takes place, the incorporation of the dynamically recrystallized fraction in the above evolution equation makes it possible to predict the flow stress after the peak.

The kinetics of static recrystallization were characterized in terms of the mean flow stresses, which lead to more accurate results than alternative methods. Appropriate expressions were formulated for the recrystallization kinetics and the mean austenite grain size as a function of predeformation, temperature and particularly strain rate.

Particular attention was paid to prediction of the temperature distribution through the thickness of the rolled plate or strip. The effects taken into account are radiation and convection from the surface when the material is between stands, and conduction to the rolls and the temperature increase due to mechanical work when the material is in the roll gap. An explicit finite difference method was used to calculate the temperature distribution through the thickness of the workpiece during processing.

On the basis of the temperature model and the constitutive and recrystallization kinetics equations, a computer model for the prediction of multi-stage rolling force and microstructural evolution was developed. The predictions of these models are in good agreement with measurements on both experimental and commercial steels. Also, by appropriate control of the thermomechanical parameters, high strength steels with transition temperatures below -100 °C were developed. These results constitute a step towards the on-line control of plate and hot strip mills, and the development of new tough high strength steels.

RÉSUMÉ

Dans le but de simuler le procédé de laminage à chaud, quatre aciers choisis ont été soumis aux tests de compression continue et interrompue dans le domaine de température 800 et 1200°C, à des taux de déformation entre 0.2 et 50 s⁻¹. Les courbes contrainte/déformation produites aux hautes vitesses de déformation ont été corrigées de l'effet d'échauffement adiabatique et des équations constitutives ont été formulées. Dans le cas où la restauration dynamique est le seul mécanisme d'adoucissement, ces relations incluent une équation de vitesse qui consiste en une loi sinus hyperbolique et une équation d'évolution avec une variable interne. Quand la recristallisation dynamique se produit, l'utilisation simultanée de l'équation d'évolution ci-dessus et de la fraction recristallisée dynamiquement permet la prédiction de la contrainte d'écoulement après le pic.

Les cinétiques de recristallisation statique ont été caractérisées en terme de la contrainte d'écoulement moyenne, ce qui a mené à des résultats plus précis qu'en utilisant d'autres méthodes. Des expressions appropriées ont été formulées pour les cinétiques de recristallisation et pour la taille moyenne du grain austénitique en fonction de la prédéformation, de la température et plus particulièrement du taux de déformation.

Une attention particulière a été portée à la prédiction de la distribution de température à travers l'épaisseur de la tôle. Les effets pris en considération sont la radiation et la convection de la surface quand le matériau se trouve entre les cages; la conduction aux cylindres et l'augmentation de la température due au travail mécanique quand le matériau est déformé. Une méthode explicite de différences finies a été utilisée pour calculer cette distribution de température durant le procédé de laminage.

En se basant sur le modèle de température, sur les équations constitutives ainsi que sur les cinétiques de recristallisation statique, un modèle sur ordinateur pour la prédiction des forces séparatrices et l'évolution microstructurale durant le laminage a été développé. Les prédictions de ces modèles sont en accord avec les mesures effectuées tant sur des aciers

expérimentaux que commerciaux. Aussi, avec un contrôle approprié des traitements thermomécaniques, des aciers à haute résistance ayant une température de transition inférieure à -100°C ont été développés. Ces résultats constituent un pas vers le contrôle automatique des laminoirs, ainsi que le développement de nouveaux aciers tenaces à haute résistance.

ACKNOWLEDGMENTS

I am very grateful to the individuals listed below; it is not possible for me to thank them adequately in these acknowledgements.

First, I would like to express my greatest appreciation to my supervisor Professor John Jonas who provided support and guidance during my stay at McGill University. His broad experience and encouragement throughout the course of this project made this research possible.

I also would like to thank Dr. Don Baragar of MTL in CANMET for his involvement in a part of the experimental study through cam plastometer testing and pilot mill rolling. His comments and discussions helped me in developing and extending the area of research during this work.

I am indebted to Professor Frank Mucciardi for his guidance regarding the temperature model and to Professor Steve Yue of McGill University for helping me in various ways. Special thanks go to Rémy Stachowiak of Steltech for providing the mill data and to Stuart Brown of M.I.T. for his interesting discussions concerning the fundamental basis of the flow behavior of metals.

I am eternally grateful to my parents, brothers and sisters for their invaluable moral support and encouragement, and to my friend Nancy Gignac for her patience and understanding.

The friendly international environment created by my fellow graduate students of the Steel Processing Group, especially during the meetings in Thomson House, along with their comments and suggestions are greatly appreciated.

Finally, I wish to thank Martin Knoepfel for his assistance in the preparation of test specimens, Lorraine Mello for help of various kinds, and Susan Arseneau and Joanne Guimond for carrying out the metallographic work.

*To my parents,
brothers, sisters and friends.*

To my country.

TABLE OF CONTENTS

	<u>Page</u>
ABSTRACT	<i>i</i>
RÉSUMÉ	<i>ii</i>
ACKNOWLEDGMENTS	<i>iv</i>
TABLE OF CONTENTS	<i>vi</i>
LIST OF FIGURES	<i>xiii</i>
LIST OF TABLES	<i>xxvi</i>
 Chapter ONE INTRODUCTION	
1.1. OBJECTIVES	1
1.2. FORM OF THE STUDY	3
 Chapter TWO PHYSICAL METALLURGY OF HOT WORKING OF STEELS	
2.1. INTRODUCTION	4
2.2. DYNAMIC RESTORATION DURING HOT DEFORMATION OF STEELS	
2.2.1. Dynamic Recovery	6
2.2.2. Dynamic Recrystallization	8
2.3. STATIC CHANGES FOLLOWING HOT DEFORMATION	
2.3.1. Static Recovery	11
2.3.2. Static Recrystallization	12
2.3.3. Metadynamic Recrystallization	14
2.3.4. Grain Growth	16
2.3.5. Solute and Strain-Induced Precipitation Effects	17
2.4. EFFECT OF ALLOYING ELEMENTS	18
2.4.1. Manganese	18
2.4.2. Carbon	19

2.4.3. Niobium	19
2.4.4. Titanium	21
2.4.5. Boron	21
2.4.6. Copper	22
2.5. STRUCTURAL CHANGES DURING THE THERMOMECHANICAL PROCESSING OF STEELS	22
2.6. TYPES OF MICROSTRUCTURES IN HSLA STEELS	27
2.7. SUMMARY	29

Chapter THREE TEMPERATURE EVOLUTION AND ROLLING LOAD CALCULATIONS DURING HOT ROLLING -AN OVERVIEW-

3.1. INTRODUCTION	30
3.2. MODELLING OF TEMPERATURE CHANGES DURING HOT ROLLING	
3.2.1. Heat Conduction in the Rolled Material	31
3.2.2. Heat Losses Outside the Stands	
3.2.2.1. Radiation and Convection During Air Cooling	31
3.2.2.2. Water Cooling	34
3.2.3. Heat Losses in the Roll Gap	36
3.2.3.1. Conduction to the Rolls	37
3.2.3.2. Heat Generated by Deformation	38
3.3. ROLLING THEORIES	
3.3.1. Introduction	39
3.3.2. Orowan Formulation	39
3.3.3. Sims Approach	43
3.3.4. Effect of Friction	45
3.4. SIMPLIFIED EMPIRICAL-ANALYTICAL EQUATIONS FOR CALCULATION OF THE DEFORMATION RESISTANCE	45
3.5. SUMMARY	48

Chapter FOUR EXPERIMENTAL MATERIALS AND METHODS

4.1.	INTRODUCTION	50
4.2.	EXPERIMENTAL MATERIALS	50
4.3.	SPECIMEN PREPARATION AND DIMENSIONS	52
4.4.	SOLUTION TREATMENT	55
4.4.1.	Solubility Product for Nb(C,N)	55
4.4.2.	Reheated Austenite Grain Size	56
4.5.	HOT COMPRESSION TESTING	
4.5.1.	Experimental Equipment	60
4.5.1.1.	MTS Automated Testing System	60
4.5.1.2.	Cam Plastometer	63
4.5.2.	Continuous Tests	
4.5.2.1.	Stress/Strain Experiments	63
4.5.2.2.	Strain Rate Control	69
4.5.2.3.	Data Treatment	69
4.5.2.4.	Correction for Elastic Distortion	70
4.5.2.5.	Correction for Temperature	72
4.5.3.	Interrupted Tests	74
4.6.	ROLLING	
4.6.1.	Rolling Mill	74
4.6.2.	Temperature, Rolling Load and Roll Gap Measurements	77
4.6.3.	Rolling Schedules	77
4.7.	MICROSTRUCTURAL STUDIES	
4.7.1.	Optical Microscopy	78
4.7.2.	Electron Microscopy	79
4.8.	MECHANICAL TESTING	79
4.9.	SUMMARY	79

Chapter FIVE DATA ANALYSIS AND NUMERICAL TECHNIQUES

5.1.	INTRODUCTION	83
5.2.	STRESS/STRAIN CURVE ANALYSIS	
5.2.1.	Smoothing Stress/Strain Curves	83

5.2.2.	Non-linear Fitting of the Bergström Model	85
5.2.3.	Work Hardening Rate Calculation	87
5.3.	SOFTENING PARAMETER DETERMINATION	
5.3.1.	Introduction	87
5.3.2.	Offset, Back Extrapolation and Recovered Strain Fraction Methods	87
5.3.3.	Mean Stress Method	90
5.4.	CORRECTION FOR ADIABATIC HEATING DURING HIGH STRAIN RATE COMPRESSION TESTING	92
5.5.	TEMPERATURE PREDICTION DURING HOT ROLLING	
5.5.1.	Introduction	95
5.5.2.	Description of the Model	96
5.5.2.1.	Radiation and Convection	99
5.5.2.2.	Cooling Due to Water	101
5.5.2.3.	Contact with the Rolls	102
5.5.2.4.	Heat Due to Deformation	105
5.5.3.	Temperature Calculation Algorithm	105
5.6.	SUMMARY	105

Chapter SIX MODELLING THE EFFECT OF HIGH TEMPERATURES AND STRAIN RATES ON THE FLOW BEHAVIOR OF STEEL

6.1.	INTRODUCTION	108
6.2.	TRUE STRESS/TRUE STRAIN CURVES	
6.2.1.	General Characteristics	109
6.2.2.	Temperature Rise Due to Adiabatic Heating	115
6.3.	RATE EQUATION	
6.3.1.	Effect of Temperature and Strain Rate on the Saturation Stress	121
6.3.2.	Activation Analysis	
6.3.2.1.	Apparent Activation Enthalpy	134
6.3.2.2.	Apparent Activation Volume	138
6.3.2.3.	Activation Free Enthalpy	140

6.4.	EVOLUTION EQUATION	
6.4.1.	Work Hardening Rate	
6.4.1.1.	Stress, Strain Rate and Temperature	
	Dependence of the Work Hardening Rate	144
6.4.1.2.	Phenomenological Formalism of the Θ - σ Law	145
6.4.2.	Model of the Stress/Strain Curve	
6.4.2.1.	Mechanistic Interpretation	151
6.4.2.2.	Effect of Temperature and Strain Rate on Ω	156
6.4.2.3.	Effect of Temperature and Strain Rate on U	158
6.4.2.4.	Relationship Between Ω , U, and the Hollomon	
	Coefficients	160
6.5.	HART ANALYSIS	162
6.6.	EFFECT OF DYNAMIC RECRYSTALLIZATION ON FLOW	
	SOFTENING	169
6.7.	SUMMARY	177

Chapter SEVEN EFFECT OF THERMOMECHANICAL AND METALLURGICAL PARAMETERS ON THE MICROSTRUCTURAL EVOLUTION OF AUSTENITE AFTER DEFORMATION

7.1.	INTRODUCTION	178
7.2.	STATIC SOFTENING MEASUREMENT METHODS	
7.2.1.	Comparison of the Mean Stress, Offset, Back Extrapolation and Recovered Strain Fraction Methods	179
7.2.2.	Relationship Between Static Softening and Recrystallization	181
7.2.3.	Correction of the Softening Rate for Adiabatic Heating	184
7.3.	INFLUENCE OF DEFORMATION CONDITIONS ON RECRYSTALLIZATION KINETICS	
7.3.1.	Effect of Reheating Temperature	190
7.3.2.	Effect of Deformation Temperature and Prestrain	192
7.3.3.	Effect of Strain Rate	194
7.3.4.	Modelling the Effect of Deformation Conditions on Recrystallization Kinetics	

7.3.4.1.	Static Recrystallization Rate	199
7.3.4.2.	Dependence of $t_{0.5}$ on Initial Grain Size and Prestrain	203
7.3.4.3.	Apparent Activation Energies for Recrystallization	205
7.3.4.4.	Modelling the Effect of Strain Rate	208
7.3.4.5.	Mathematical Expressions for Recrystallization Kinetics	208
7.4.	INFLUENCE OF DEFORMATION CONDITIONS ON AUSTENITE GRAIN SIZE	213
7.5.	EFFECT OF ALLOYING ELEMENTS ON RECRYSTALLIZATION KINETICS	220
7.6.	SUMMARY	224

Chapter EIGHT FOCUS OF THE STUDY - INDUSTRIAL APPLICATIONS

8.1.	INTRODUCTION	225
8.2.	TEMPERATURE CHANGES DURING HOT ROLLING	
8.2.1.	Prediction of the Temperature Distribution	227
8.2.2.	Heat Transfer Coefficients during Cooling Between the Stands	236
8.2.3.	Temperature Drop during Contact with the Rolls	
8.2.3.1.	Heat Transfer Coefficient at the Interface	237
8.2.3.2.	Comparison of the Heat Balance Method with Hollander's Approach	239
8.2.4.	Stability Validation	243
8.3.	FLOW STRESS AND MICROSTRUCTURAL EVOLUTION CALCULATIONS	
8.3.1.	Flow Chart	243
8.3.2.	Flow Stress Prediction during Hot Rolling	247
8.3.3.	Evolution of the Mean Austenite Grain Size	252
8.4.	EXTENSION OF THE TEMPERATURE, FLOW STRESS AND MICROSTRUCTURE EVOLUTION MODELS TO INDUSTRIAL PROCESSING	256

8.5. ROLLING TRIALS OF THE Cu-Nb-B STEEL	
8.5.1. Introduction	258
8.5.2. Microstructures	258
8.5.3. Mechanical Properties	263
8.6. SUMMARY	266

Chapter NINE CONCLUSIONS AND RECOMMENDATIONS

9.1. CONCLUSIONS	269
9.2. RECOMMENDATIONS FOR FUTURE WORK	272

STATEMENT OF ORIGINALITY AND CONTRIBUTION TO KNOWLEDGE	274
---	------------

REFERENCES

APPENDIX A	Derivation of the Expression for the Activation Free Energy
APPENDIX B	Derivation of the Expression for the Dislocation Density During Deformation
APPENDIX C	Listings of the Programs Used for the Analysis of the Stress/Strain Curves and for Correction for Adiabatic Heating

LIST OF FIGURES

Figure		Page
2.1	Restoration processes in hot working operations of metals ^[1] .	5
2.2	a) Shape of stress/strain curves in high stacking fault energy Armco iron b) Subgrain development during straining ^[1] .	7
2.3	Shape of flow curves pertaining to dynamic recrystallization: a) low strain rate b) high strain rate ^[4] .	9
2.4	Strain dependence of time for 50% recrystallization in C-Mn and low alloy steels ^[17] .	13
2.5	Schematic relationship between the three static processes ^[15] .	15
2.6	Temperature dependence of austenite grain size ^[36] .	20
2.7	Iron-copper phase diagram ^[41] .	23
2.8	Austenite grain size changes during controlled rolling ^[22] .	25
2.9	Microstructural evolution of bainitic steels ^[40] .	28
3.1	Distribution of heat transfer coefficient during water cooling ^[53] .	35
3.2	Stress distribution in the roll gap for homogeneous and inhomogeneous deformation ^[55] .	40
3.3	Roll gap geometry and force equilibrium.	42

3.4	Illustration of softening by recovery ^[74].	49
4.1	MTS compression test sample geometry and groove design ^[81].	53
4.2	Cam plastometer compression test sample geometry.	54
4.3.	Dissolved niobium as a function of temperature for the Nb steels.	57
4.4	Microstructures of the reheated samples prior to testing. Magnification 400X.	58
4.5.	Dependence of austenite grain size on reheating temperature in the boron-containing steels.	59
4.6	View of the high temperature computerized MTS compression testing equipment.	61
4.7	View of the CENTORR high temperature furnace.	62
4.8	View of the cam plastometer machine used for high strain rate testing.	64
4.9	Schematic of: a) the cam follower insertion mechanism b) the plastometer drive train ^[97].	65
4.10	Schematic representation of the method used during: a) single hit tests b) double hit tests.	67
4.11	Dependence of the maximum cooling rate on testing temperature when the CENTORR furnace is turned off ^[93].	68
4.12	Determination of the actual height of a deformed specimen in the MTS machine ^[96].	71

4.13	Elastic distortion of the MTS testing system. (Data are from ref. [96]).	73
4.14	Typical outputs after interrupted MTS compression testing: <ul style="list-style-type: none"> a) load-time plot b) true stress/true strain curve c) true strain versus time. 	75
4.15	MTL pilot-scale rolling mill with its design specifications ^[106] .	76
4.16	Method for thin foil preparation.	80
4.17	Summary of the experimental methods used.	82
5.1	Determination of the flow stresses used in the evaluation of the softening rate by the offset and back extrapolation methods.	89
5.2	Determination of the mean stresses used in the evaluation of the softening rate by the mean stress method.	91
5.3	Procedure used for determination of the temperature increase and the corresponding flow softening during adiabatic compression.	94
5.4	Heat transfer mechanisms during hot rolling.	97
5.5	Representative section for the temperature distribution calculations.	98
5.6	Discretization of slab half thickness into nodes for finite difference analysis.	100
5.7	Temperature profile with: <ul style="list-style-type: none"> a) perfect contact b) imperfect contact. 	103

5.8	Flow chart of computer program for calculating workpiece temperature distribution.	106
6.1	Effect of temperature on flow stress in the base steel deformed at a) 0.2 s^{-1} b) 2 s^{-1} .	110
6.2	Effect of temperature on flow stress in the Nb steel deformed at a) 0.2 s^{-1} b) 2 s^{-1} .	111
6.3	Effect of temperature on flow stress in the Nb-B steel deformed at a) 10 s^{-1} b) 50 s^{-1} .	112
6.4	Effect of temperature on flow stress in the Cu-Nb-B steel reheated at a) 1100°C , b) 1200°C .	113
6.4	Effect of temperature on flow stress in the Cu-Nb-B steel reheated at 1200°C and deformed at c) 10 s^{-1} , d) 50 s^{-1} .	114
6.5	Effect of testing temperature and strain rate on the temperature increase per unit strain during deformation.	117
6.6	a) Effect of adiabatic heating on flow stress during deformation of the Nb-B steel. b) Strain dependence of the coefficient $\partial\sigma/\partial(1/T) _{t,\epsilon}$.	119
6.7	a) Schematic representation of the change in Θ with stress. b) Definition of the hypothetical saturation stress σ_{ss}^* .	122

6.8	Strain rate and temperature dependencies of the saturation stress σ_{ss}^* using Eq. 6.6:	
	a) base steel	
	b) Nb steel.	124
6.8	Strain rate and temperature dependencies of the saturation stress σ_{ss}^* using Eq. 6.6:	
	c) Nb-B steel	
	d) Cu-Nb-B steel.	125
6.9	Dependencies of the saturation stress σ_{ss}^* on temperature in the	
	a) base steel	
	b) Nb steel	
	c) Nb-B steel	
	d) Cu-Nb-B steel.	127
6.10	Dependencies of the saturation stress σ_{ss}^* on strain rate in the	
	a) base steel	
	b) Nb steel	
	c) Nb-B steel	
	d) Cu-Nb-B steel.	128
6.11	Relation between the normalized strain rate sensitivity and saturation stress at 0 K for different materials. Data for Al, Cu and S.S. are taken from reference [131].	130
6.12	Dependence of the coefficient $\partial \ln(\sigma_{ss}^*) / \partial \ln \dot{\epsilon} _T$ on temperature for the HSLA and 316 stainless steels.	133
6.13	Temperature dependence of the strain rate at constant saturation stress in the	
	a) base steel	
	b) Nb-B steel.	135

6.14	Stress dependence of the apparent activation volume in the a) base steel b) Nb-B steel.	139
6.15	Dependence of the apparent activation volume on the modulus-reduced stress in the base steel.	141
6.16	a) Stress dependence of the activation free energy in the Nb-B steel. b) Dependence of the modulus-reduced activation free energy on σ_{SS}/μ in the Nb-B steel.	142
6.17	Stress dependence of the work hardening rate at different temperatures in the base steel: a) $\dot{\epsilon} = 0.2 \text{ s}^{-1}$ b) $\dot{\epsilon} = 2 \text{ s}^{-1}$ c) $\dot{\epsilon} = 10 \text{ s}^{-1}$.	146
6.18	Stress dependence of the work hardening rate at different temperatures in the Nb steel. a) $\dot{\epsilon} = 0.2 \text{ s}^{-1}$ b) $\dot{\epsilon} = 2 \text{ s}^{-1}$.	147
6.19	Stress dependence of the work hardening rate at different temperatures in the Nb-B steel. a) $\dot{\epsilon} = 10 \text{ s}^{-1}$ b) $\dot{\epsilon} = 50 \text{ s}^{-1}$.	148
6.20	Stress dependence of the work hardening rate at different temperatures in the Cu-Nb-B steel. a) $\dot{\epsilon} = 2 \text{ s}^{-1}$ b) $\dot{\epsilon} = 50 \text{ s}^{-1}$.	149
6.21	Dependence of the work hardening rate Θ on the inverse stress for the base and Nb-B steels.	152

6.22	Comparison between Θ evaluated according to Eq. 6.19 and measured from the stress/strain curves.	153
6.23	Dependence of Ω on temperature and strain rate in the a) base steel b) Nb-B steel.	157
6.24	a) Dependence of $(\alpha\mu b)^2 U$ on temperature and strain rate. b) Dependence of $\alpha^2 U$ on temperature and strain rate.	159
6.25	a) Log stress versus log strain for the Nb steel deformed at 900°C at a rate of 2 s ⁻¹ . b) Strain dependence of the coefficient n_H in the Hollomon equation. c) Comparison of calculated $\sigma(\epsilon)$ relations using the Hollomon (Eq. 6.29) and Bergström (Eq. 6.24) equations with measured data.	161
6.26	Schematic representation of constant hardness curves "y" and constant work hardening rate curves "H".	164
6.27	Dependence of the work hardening coefficient H on stress and strain rate in the base steel deformed at a) 900°C b) 1000°C.	166
6.27	Dependence of the work hardening coefficient H on stress and strain rate in the Nb-B steel deformed at c) 800°C d) 1100°C.	167
6.28	Dependence of the apparent strain rate sensitivity on temperature and strain.	170
6.29	Effect of temperature and strain rate on the steady state stress σ_{ss}^{drxn} associated with dynamic recrystallization.	172

6.30	Effect of temperature and strain rate on the peak strain for dynamic recrystallization.	174
6.31	Determination of the constants n_D and K_D in Eq. 6.42b for the base steel at different temperatures and strain rates.	175
6.32	Comparison between predicted (Eq. 6.42a and b) and experimental stress/strain curves in the base steel deformed at a) 0.2 s^{-1} b) 2 s^{-1} .	176
7.1	Comparison of different softening parameters.	180
7.2	a) Relationship between the restoration index based on offset flow stress and recrystallized fraction at prestrains of 0.25 and 0.5. b) Relationship between the restoration indices based on offset and mean flow stress at a prestrain of 0.25 ^[105] .	182
7.3	Relationship between the softening parameters determined by the mean stress, offset and back extrapolation methods.	183
7.4	Schematic representation of interrupted compression flow curves showing continuous deformation (1), softening by static recovery (2), softening by static recrystallization (3) and full softening (4) ^[100] .	185
7.5	Description of the method used to correct the softening parameter for adiabatic heating.	187
7.6	Temperature dependence of the mean flow stress determined at a strain of 0.25.	189

7.7	Effect of reheating temperature on the softening rate in the a) Nb-B steel b) Cu-Nb-B steel.	191
7.8	a) Effect of temperature on softening in the base steel prestrained to 0.25. b) Effect of temperature on softening in the Nb steel prestrained to 0.25 at 2 s^{-1} . c) Effect of temperature on softening in the Nb-B steel.	193
7.9	a) Effect of prestrain on softening in the base steel prestrained to 0.125 and 0.25. b) Effect of prestrain on softening in the Nb-B steel. c) Effect of prestrain on softening in the Cu-Nb-B steel deformed at different temperatures.	195
7.10	a) Effect of strain rate on softening in the base steel prestrained to 0.125. b) Effect of strain rate on softening in the Nb steel prestrained to 0.25. c) Effect of strain rate on softening in the Nb-B steel. d) Effect of strain rate on softening in the Cu-Nb-B steel.	196
7.11	a) Dependence of $\ln \ln[1/(1-X_0)]$ on $\ln(t)$ under different conditions of prestrain, strain rate and temperature in the base steel. b) Dependence of $\ln \ln[1/(1-X_0)]$ on $\ln(t)$ under different conditions of prestrain, strain rate and temperature in the Nb steel. c) Dependence of $\ln \ln[1/(1-X_0)]$ on $\ln(t)$ under different conditions of prestrain, strain rate and temperature in the Nb-B steel. d) Dependence of $\ln \ln[1/(1-X_0)]$ on $\ln(t)$ under different conditions of prestrain, strain rate and temperature in the Cu-Nb-B steel.	201

7.12	Dependence of $t_{0.5}$ on prestrain for the base and Cu-Nb-B steels.	204
7.13	Temperature dependence of the time for 50% softening in the base and Nb steels.	206
7.14	Dependence of the time for 50% softening on strain rate in the a) base and Nb steels b) Nb-B and Cu-Nb-B steels.	209
7.15	a) Comparison of the time for 50% softening and the deformation variables in the base steel. b) Comparison of the time for 50% softening and the deformation variables in the Nb steel. The single point which is encircled is representative of strain-induced precipitation. c) Comparison of the time for 50% softening and the deformation variables in the Nb-B steel. The encircled points correspond to conditions of strain-induced precipitation. d) Comparison of the time for 50% softening and the deformation variables in the Cu-Nb-B steel.	211
7.16	Optical microstructures of the Nb-B samples showing the prior austenite grains after a deformation of 0.4 at $10s^{-1}$. The grains are deformed at the two lower temperatures and equiaxed at $1100^{\circ}C$. Magnification 400X.	214
7.17	Evolution of the mean austenite grain size \bar{d}_{γ} of the partially recrystallized structure with the softening rate X_{ϕ} .	215
7.18a	Optical microstructures of the Nb-B steel showing the prior austenite grain structure after a double compression with a total deformation of 0.6 at $10s^{-1}$. Magnification 250X.	216

7.18b	Optical microstructures of the Nb-B steel showing the prior austenite grain structure and grain size distribution after a double compression with a total deformation of 0.6 at 10 s^{-1} . Magnification 400X.	217
7.19	Influence of fractional softening on the residual strain ^[161] . ($\bar{\epsilon}^*$ is the residual strain, ϵ_1 strain in the first pass and $X_a^{(1)}$ is the fractional softening between the first and second passes.)	219
7.20	Effect of Nb and B addition on softening at a) 1000°C b) 900°C .	222
7.21	Effect of Cu addition on softening at 1000 and 900°C .	223
8.1	Schematic diagram illustrating the computer sub-models used in simulating hot rolling.	226
8.2	Schematic diagram of hot strip mill at Stelco, Lake Erie Works.	228
8.3	Evolution of temperature distribution during hot rolling of strip at Stelco.	230
8.4	Comparison of measured and predicted surface temperatures for a strip ^[61] .	231
8.5	Evolution of temperature distribution during the hot rolling of thick strip.	232
8.6a	Evolution of temperature distribution during hot rolling of the experimental Cu-Nb-B steel on the pilot mill (Schedule D1).	233
8.6b	Evolution of temperature distribution during hot rolling of the experimental Cu-Nb-B steel on the pilot mill (Schedule D2).	234

8.6c	Evolution of temperature distribution during hot rolling of the experimental Cu-Nb-B steel on the pilot mill (Schedule C1).	235
8.7	Temperature distribution in a surface element.	240
8.8	Effect of contact time on the roll gap heat transfer coefficient ^[196] . a) after 35 and 50% reductions b) after rerolling.	242
8.9	Simplified flow chart for rolling load and mean austenite grain size predictions during hot rolling.	244
8.10	Stress/strain curves predicted by the present program for the hot rolling of the Cu-Nb-B steel.	248
8.11	Comparison of calculated and measured mean stresses for rolling of the experimental Cu-Nb-B steel.	253
8.12	Comparison of calculated and measured mean stresses for rolling of the experimental Cu-Nb-B steel.	254
8.13	Predicted mean austenite grain sizes during the experimental rolling of the Cu-Nb-B steel.	255
8.14	Predicted mean austenite grain sizes during the hypothetical rolling of a C-Mn steel with a large initial grain size.	257
8.15	Optical microstructures obtained after rolling and quenching the Cu-Nb-B steel.	259
8.16	Transmission electron micrograph showing the high dislocation density lath structure (56,000X) ^[80] .	260

- 8.17 Optical micrographs of the microstructures produced using two different finish rolling temperatures in the Cu-Nb-B steel. 261
- 8.18 Optical photograph showing the prior austenite grain boundaries after pancaking ($RT = 1250^{\circ}\text{C}$, $FRT = 830^{\circ}\text{C}$). Magnification 500X. 262
- 8.19 Charpy transition curves for the Cu-Nb-B steel. 265
- 8.20 Load and energy-time curves obtained in the Charpy impact tests carried out at -40°C :
a) $RT = 1250^{\circ}\text{C}$, $FRT = 830^{\circ}\text{C}$
b) $RT = 1100^{\circ}\text{C}$, $FRT = 750^{\circ}\text{C}$. 267

LIST OF TABLES

Table		Page
3.1	Heat transfer coefficients at roll/slab interface ($\text{kW m}^{-2} \text{K}^{-1}$) ^[65] .	38
4.1	Chemical compositions of the experimental steels.	51
4.2	Range of experimental conditions.	74
4.3	Rolling schedules used for the Cu-Nb-B steel.	78
6.1a	Calculated temperature increases and the corresponding stress decreases in the Nb-B steel deformed at 10 s^{-1} .	120
6.1b	Calculated temperature increases and the corresponding stress decreases in the Cu-Nb-B steel.	120
6.1c	Calculated temperature increases and the corresponding stress decreases in the HSLA steels ^[116] .	121
6.2a	Normalized variables shown in Fig. 6.9a for the base steel.	126
6.2b	Normalized variables shown in Fig. 6.9b for the Nb steel.	129
6.2c	Normalized variables shown in Fig. 6.9c for the Nb-B steel.	129
6.2d	Normalized variables shown in Fig. 6.9d for the Cu-Nb-B steel.	131
6.3	Numerical values of the parameters in Eq. 6.7 pertaining to the four steels investigated. Data for Al, Cu and stainless steel (S.S.) are included for comparison.	131
6.4	Normalized apparent strain rate sensitivities for the four steels studied.	132

6.5	Comparison of numerical values of the modulus-reduced initial work hardening rate θ_0/μ .	150
7.1	Corrected and uncorrected values of fractional softening during the interrupted compression testing of Nb-B steel deformed at 900°C and 10s ⁻¹ with a prestrain of 0.25.	188
7.2	Summary of the strain, strain rate and temperature dependencies of the time for 50% recrystallization for the four steels investigated.	210
7.3	Empirical equations for the prediction of recrystallized austenite grain size.	220
8.1	Comparison of calculated values for H_{CTC} (kWm ⁻² K ⁻¹).	238
8.2	Comparison of calculated surface temperatures.	241
8.3a	Evolution of the residual strain, recrystallized fraction and mean flow stress during hot rolling of the Cu-Nb-B steel (RT = 1100°C, FRT = 750°C)	249
8.3b	Evolution of the residual strain, recrystallized fraction and mean flow stress during hot rolling of the Cu-Nb-B steel (RT = 1100°C, FRT = 830°C)	249
8.3c	Evolution of the residual strain, recrystallized fraction and mean flow stress during hot rolling of the Cu-Nb-B steel (RT = 1250°C, FRT = 830°C)	250
8.4	Comparison of the effective (accumulated) strain and peak strain for dynamic recrystallization during hot rolling of the base steel.	251
8.5	Mechanical properties of the Cu-Nb-B steel.	264

Chapter ONE

INTRODUCTION

1.1. OBJECTIVES

In its general meaning, deformation processing refers to the deformation mechanisms involved in a specific working operation such as rolling, forging or extrusion. These processes had initially been developed because they decrease significantly the energy required to deform the metal and increase the ability of the latter to flow without cracking. In many of these forming operations, recent studies have focused on producing beneficial deformation-induced microstructures in order to improve the subsequent deformation and fracture properties of the final product.

In these processes, the metal is heated to one-half to nine-tenths of its melting point and is deformed at strain rates ranging from 10^{-2} s^{-1} for forging to 10^2 s^{-1} or more in finish rolling and extrusion. Also, large deformations with equivalent strains easily exceeding 1 or 2 are applied and the corresponding stresses (and therefore the loads) can be extremely high. This usually requires interruptions during the hot working operation, encompassing multiple passes with intervening holding times. At the same time, the temperatures are changing as a function of both time and position in the workpiece, during both deformation as well as holding. Moreover, the deformation mode can be inhomogeneous, with large gradients in strain and strain rate. The final state of the hot worked material is therefore strongly dependent on its deformation history.

From a metallurgical point of view, the microstructural state during deformation at high temperatures involves physical events such as work hardening, dynamic recovery and dynamic recrystallization. A very important phenomenon occurs during holding between deformation passes which strongly alters the current microstructure. This phenomenon is *static recrystallization*. In its simplest picture, static recrystallization is the transformation of the deformed microstructure into newly formed, strain-free grains.

During the last three years, a research project was undertaken at McGill University with the objective of clarifying some of the problems associated with mill automation in the Canadian steel industry. The present study was designed primarily to develop a computer model for on-line gauge control during hot forming operations, with specific application to the hot rolling of steels. The goals of the investigation were:

- i) To develop a heat flow model to predict the temperature distribution through the thickness of the rolled plate or strip. This model is necessary because the temperature gradients generated during processing strongly affect most of the mechanical and microstructural parameters.
- ii) To formulate constitutive equations which can describe accurately the high temperature-high strain rate flow behavior of steels. To this end, data from laboratory experiments are necessary to characterize the constitutive response of the steels of interest under hot working conditions.
- iii) To characterize and model the evolution of microstructure during hot rolling, i.e. the recrystallization kinetics and the austenite grain size. Extensive laboratory testing is required in this part of the investigation to provide the data necessary for modelling.

When *i*, *ii* and *iii* are coupled together, they constitute the basis of the computer model designed for the process control of hot rolling.

1.2. FORM OF THE STUDY

Since the present investigation deals with both the metallurgical and thermomechanical aspects of hot rolling, the two chapters that follow, i.e. 2 and 3, survey the theoretical framework associated with these two topics. Chapter 4 describes the experimental materials and equipment employed in this work. Several data analysis methods and numerical techniques were developed and used throughout this study; these are presented in Chapter 5.

The results that emerged from the present study are divided for simplicity and discussed in three parts. Chapter 6 concerns the effect of high temperatures and strain rates on the flow behavior of steels. These effects are quantified and modelled. The influence of both thermomechanical and metallurgical factors on the evolution of the microstructure during interpass rolling are described and also modelled in Chapter 7. Chapter 8 is the focus of the present study and applies the basic concepts developed in the previous chapters. The accuracy of the model predictions, and the feasibility of rolling a candidate Cu-Nb-B steel are discussed here in terms of the microstructure and mechanical properties.

Finally, in Chapter 9, general conclusions are drawn from the study, and future topics of investigation are suggested.

Chapter TWO

PHYSICAL METALLURGY OF HOT WORKING OF STEELS

2.1. INTRODUCTION

When a metal is deformed plastically in a hot working operation, the material can undergo restoration processes both during and after deformation (Fig. 2.1). Restoration during deformation is referred to as dynamic and affects the shape and level of the stress/strain curve, while restoration after deformation, which is driven by the stored energy and referred to as static, determines the microstructure submitted to a subsequent deformation. Recovery and recrystallization can occur both dynamically and statically. It is the objective of this chapter to summarize the information related to these processes, although a complete review can be found in the paper published by McQueen and Jonas [1].

The first section deals with dynamic recovery and recrystallization, and is followed by a description of static changes such as static recovery and recrystallization, metadynamic recrystallization and strain-induced precipitation. These two sections are supplemented by a brief outline of the effect of important alloying elements on metallurgical phenomena in steels. Finally, the different types of microstructures developed after the transformation of austenite are distinguished tentatively.

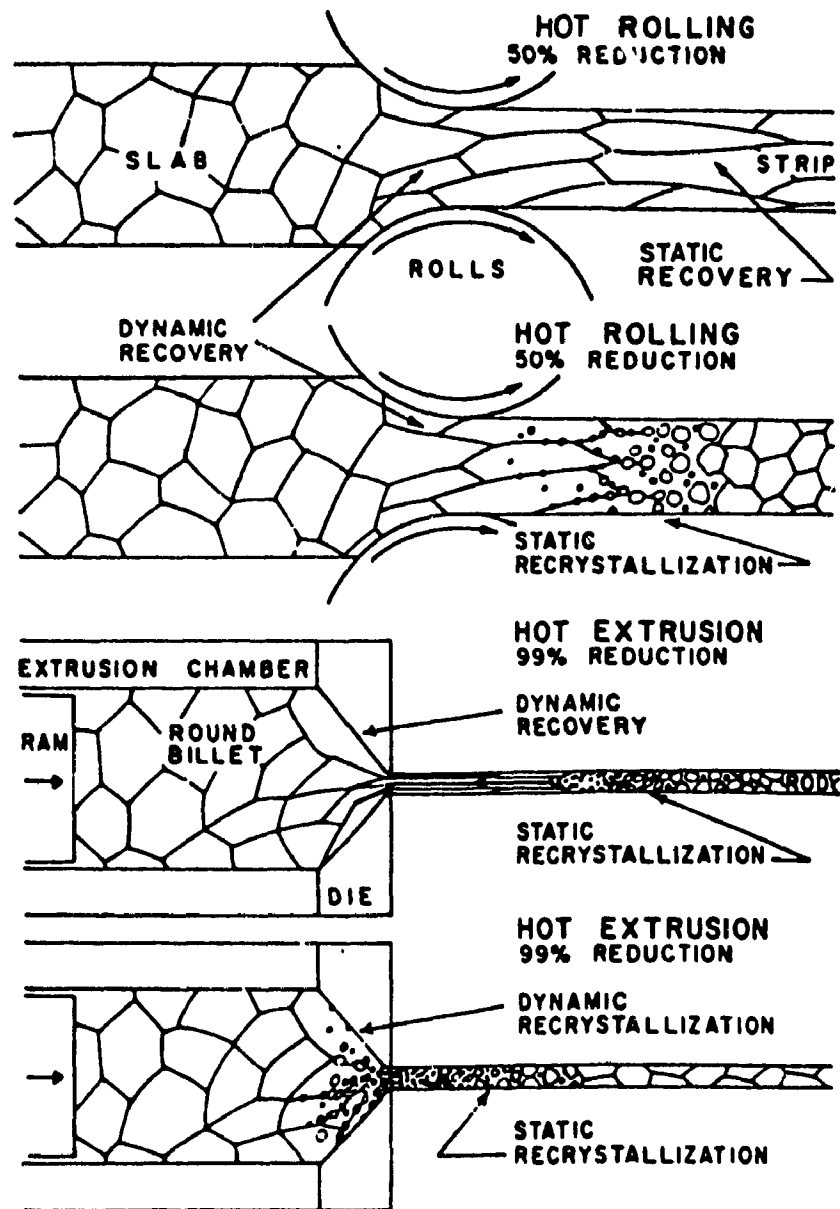


Figure 2.1 Restoration processes in hot working operations of metals⁽¹⁾.

2.2. DYNAMIC RESTORATION DURING HOT DEFORMATION OF STEELS

2.2.1. Dynamic Recovery

During hot working of a metal at high temperatures, dynamic recovery occurs as a result of thermal activation. In the case of low stacking fault energy materials, recovery may be followed by dynamic recrystallization, a phenomenon that will be described in the next subsection. For high stacking fault energy metals such as aluminum and bcc iron, dynamic recovery is the only restoration process, even at large strains. The shape of the flow curves pertaining to the case when the flow rate is limited by dynamic recovery alone is illustrated in Fig. 2.2a. During the initial work hardening region of the stress/strain curve, the dislocation density increases. The dislocations become entangled and form sub-boundaries (Fig. 2.2b), a process which results in subgrain development [1]. As deformation proceeds, the work hardening rate gradually decreases due to an increase in the annihilation rate of dislocations, which is dependent on the dislocation density itself. When the rate of annihilation of dislocations is equal to the rate of generation of dislocations, the steady state regime is reached. The steady state in hot working is characterized by the constancy of stress and an equilibrium subgrain size which is maintained during flow. The mean subgrain size d in the steady state regime is dependent on temperature and strain rate through the following relation [1]:

$$d^{-1} = a + b \ln Z \quad (2.1)$$

where a and b are empirical constants, and the Zener-Hollomon parameter Z is given by:

$$Z = \dot{\epsilon} \exp\left(\frac{Q}{RT}\right) \quad (2.2)$$

Q in Eq. 2.2 is the experimental activation energy associated with the temperature dependence of the flow stress and R is the gas constant.

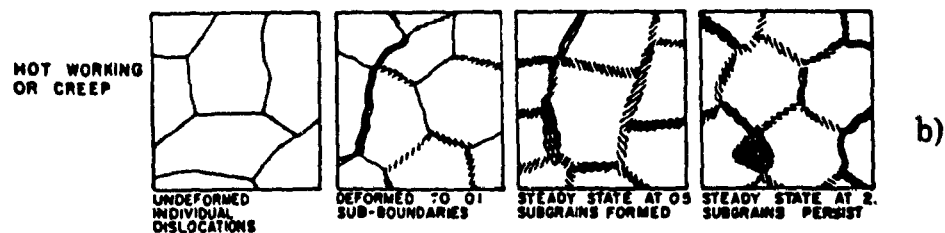
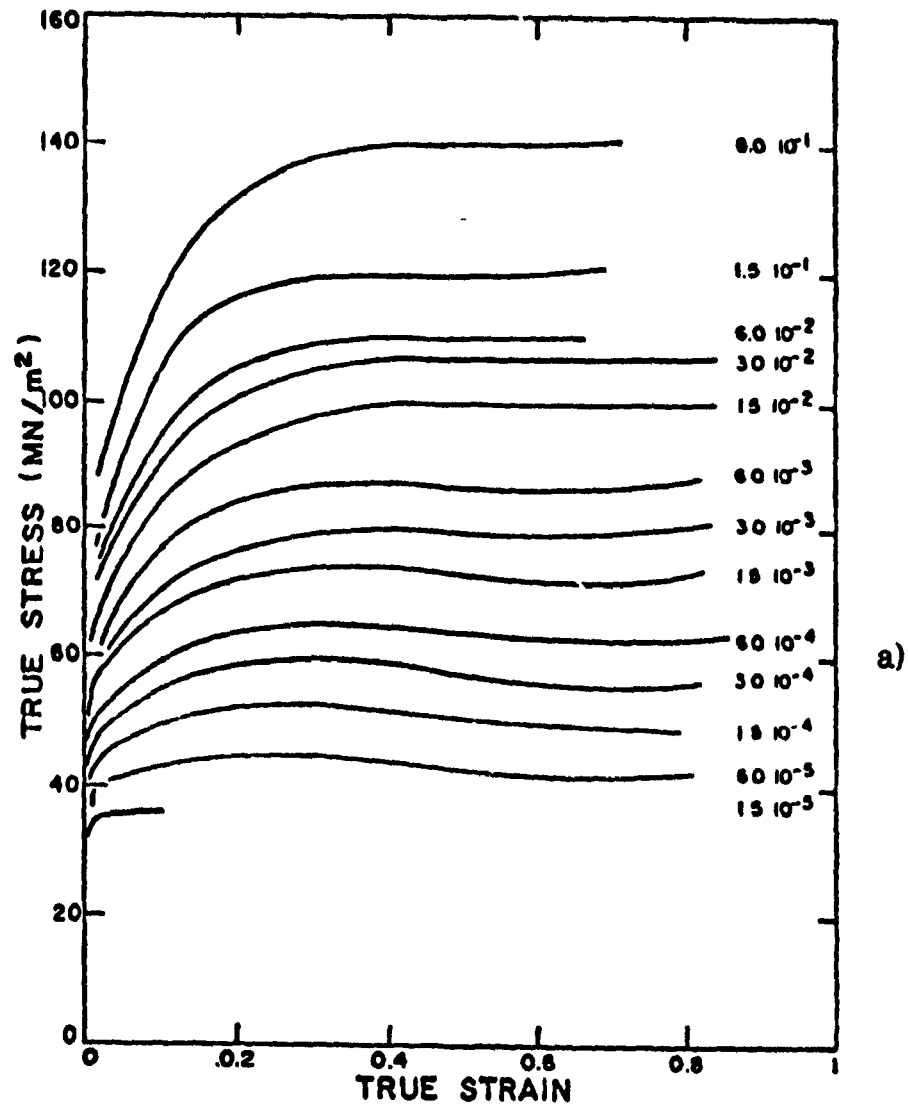


Figure 2.2 a) Shape of stress/strain curves in high stacking fault energy Armco iron

b) Subgrain development during straining^[1].

The steady state stress is also related to the Zener-Hollomon parameter and can take the following general form [1, 2]:

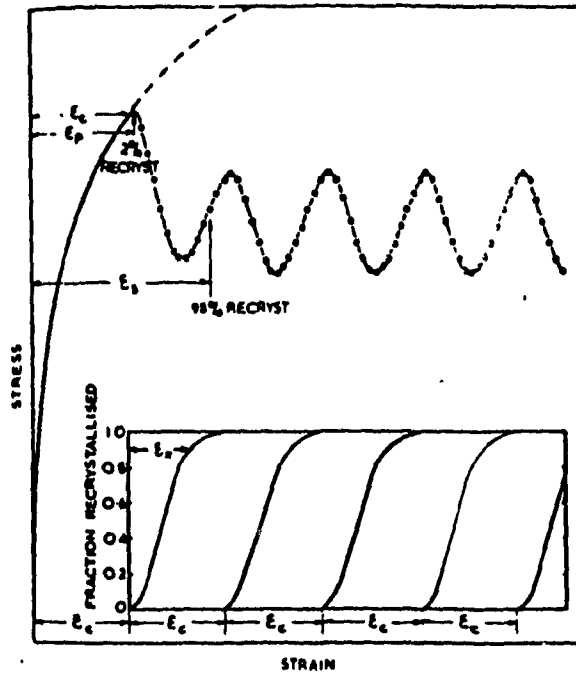
$$Z = f(\sigma_{\text{steady state}}) \quad (2.3)$$

where f can be a power, exponential or hyperbolic sine function.

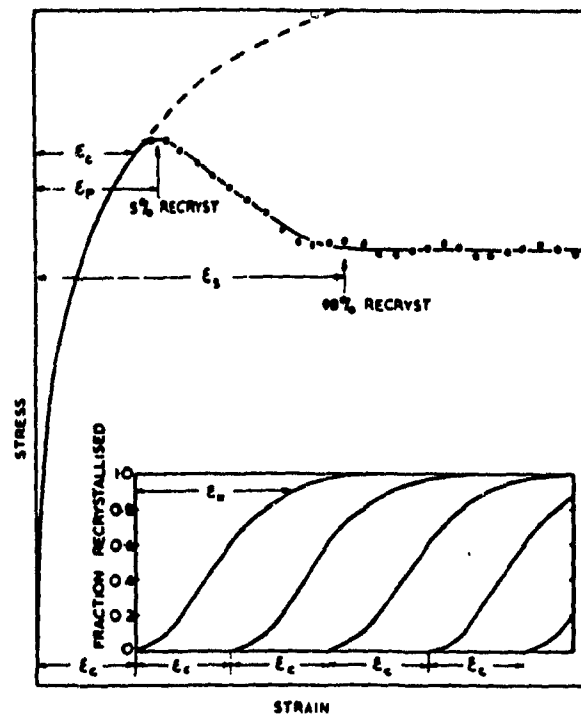
2.2.2. Dynamic Recrystallization

In metals of low stacking fault energy, mainly fcc metals, the dislocation substructure developed in the initial stages of deformation recovers poorly and a critical dislocation density depending on the deformation conditions can be attained. In such a case, the nucleation of recrystallization takes place by grain boundary bulging [3]. Dislocations are annihilated in large numbers through the migration of a high angle boundary [1] and the structure is replaced by a new strain-free one. The resultant flow curves differ from those shown in Fig. 2.2a, and are portrayed in Fig. 2.3.

At low strain rates, the drop in flow stress due to dynamic recrystallization after the first peak (Fig. 2.3a) is followed by periodic cycles, each containing a work hardening followed by a softening region. The cycles seem to have a constant period with the amplitude declining as the deformation is continued [5]. Under such conditions, Luton and Sellars [4] found that nucleation occurs by the bulging of an existing grain boundary. Because deformation proceeds continuously during nucleation and growth, the new growing grains are concurrently deformed and the gradient of strain energy from the center of the recrystallized grains to the advancing boundaries is low. Since the region behind a boundary is free of dislocations and the unrecrystallized one in front of it is highly dislocated, the driving force due to the difference in dislocation density on both sides of the boundary is decreased by continuous deformation [1]. The result is a complete cycle of recrystallization but with grains that are deformed at their centers. The latter differ from strain-free statically recrystallized grains of the same size. If deformation continues, the dislocation density and therefore the flow stress increase, and the same phenomenon is repeated leading to another cycle of recrystallization, and so on.



a)



b)

Figure 2.3 Shape of flow curves pertaining to dynamic recrystallization:

a) low strain rate

b) high strain rate ^[4].

When the strain rate is high, (Fig. 2.3b), the flow stress rises to a maximum corresponding to the peak strain ϵ_p , and drops to a value between the yield and maximum stress as a result of dynamic recrystallization. Since the strain is higher near the grain boundaries, the strain energy gradient from center to boundary of a recrystallized grain is high and the region just behind the moving boundary is also highly dislocated. This leads to a decrease in the driving force and hence to a reduction of the rate of migration relative to that in static recrystallization [1]. When deformation proceeds, and before the completion of a local cycle of recrystallization, the dislocation densities at the centers of the recrystallizing grains have already reached the critical value required to start another cycle. So, at any level of "average deformation", different grains are at different stages of recrystallization, a situation which results in an average flow stress somewhere between the yield and peak stress.

The critical strain for the nucleation of dynamic recrystallization is slightly less than the peak strain ϵ_p on the flow curve. This was explained by McQueen and Jonas [1] in terms of concurrent softening and hardening. In fact, while the first nuclei are softening the material in some local regions, the remaining material continues to become stronger, with the difference between ϵ_c and ϵ_p being greater at higher strain rates. Rossard [6] found that ϵ_c is approximately $5/6\epsilon_p$ and Sakui and coworkers [7] reported that this critical strain is around $0.7\epsilon_p$.

The progress of dynamic recrystallization can be followed by means of metallographic techniques. The kinetics of dynamic recrystallization can be described in terms of normal S-curves of volume recrystallized expressed as a function of log time. These are similar to those observed in classical recrystallization. In constant strain rate tests, time can be replaced by strain and the recrystallized fraction can be described by the following Avrami equation [8]:

$$X_D = 1 - \exp[-K(\epsilon - \epsilon_c)^{n_D}] \quad (2.4)$$

where K and n_D are constants.

Finally, it is important to note that the grain size developed during dynamic recrystallization is closely correlated to the high temperature flow stress [1]. This empirical relation takes the following form:

$$\sigma_{steady\ state} = A d_{dyn}^{-q} \quad (2.5)$$

and has been observed by many authors for several materials [4, 9, 10]. In Eq. 2.5, A and q are constants and depend on the material.

2.3. STATIC CHANGES FOLLOWING HOT DEFORMATION

2.3.1. Static Recovery

After plastic deformation, some portion of the deformation energy is stored within the metal, which makes the latter thermodynamically unstable. Immediately after unloading, the metal softens by recovery, which involves the annihilation and rearrangement of dislocations in individual events. No motion of grain boundaries occurs during recovery, so that no observable change can be detected in the microstructure. The decrease in internal stress due to the reduction in the average dislocation density and the rearrangement of the dislocations can decrease the yield stress by up to 40% [11].

If the critical strain for static recrystallization (around 10%) is not reached, the recovery process does not lead to full softening but to a plateau well below 100% [1].

An increase in temperature results in an increase in the rate of recovery because of enhanced thermal activation. Increasing the strain or strain rate also increases the rate of recovery due to the higher dislocation density, which constitutes a driving force increase. An increase in the solute content results in a reduction in the stacking fault energy which can decrease the rate of static recovery in a similar way to dynamic recovery.

2.3.2. Static Recrystallization

Recrystallization is the process by which new grains form and grow at the expense of the deformed and recovered structure. These new grains are strain free and grow by the migration of high angle boundaries. The occurrence of static recrystallization is possible only when a critical value of prestrain is exceeded, and after an incubation time during which static recovery creates the recrystallization nuclei. Some qualitative informations regarding the "laws of recrystallization" can be summarized as follows [12]:

- i) A minimum strain is necessary to start recrystallization,
- ii) The smaller the amount of deformation, the higher the temperature required to cause recrystallization,
- iii) An increase in the holding time decreases the temperature necessary for recrystallization,
- iv) The recrystallized grain size depends in the first place on the amount of deformation and slightly on the holding temperature. The greater the degree of deformation and the lower the holding temperature, the smaller the recrystallized grain size,
- v) When recrystallization is complete, subsequent holding causes an increase in grain size.

According to Sellars [13], three parameters determine the rate of recrystallization. These are the stored energy, the density of favorable nucleation sites and the temperature.

The stored energy increases with decreasing deformation temperature and increasing strain rate and strain. The effect of strain is the most important, with the time for 50% recrystallization depending on the amount of deformation to the minus fourth power [14-16]. This effect is illustrated in Fig. 2.4 for different temperatures, and it can be seen that the time for 50% softening by recrystallization decreases by as much as two orders of magnitude with

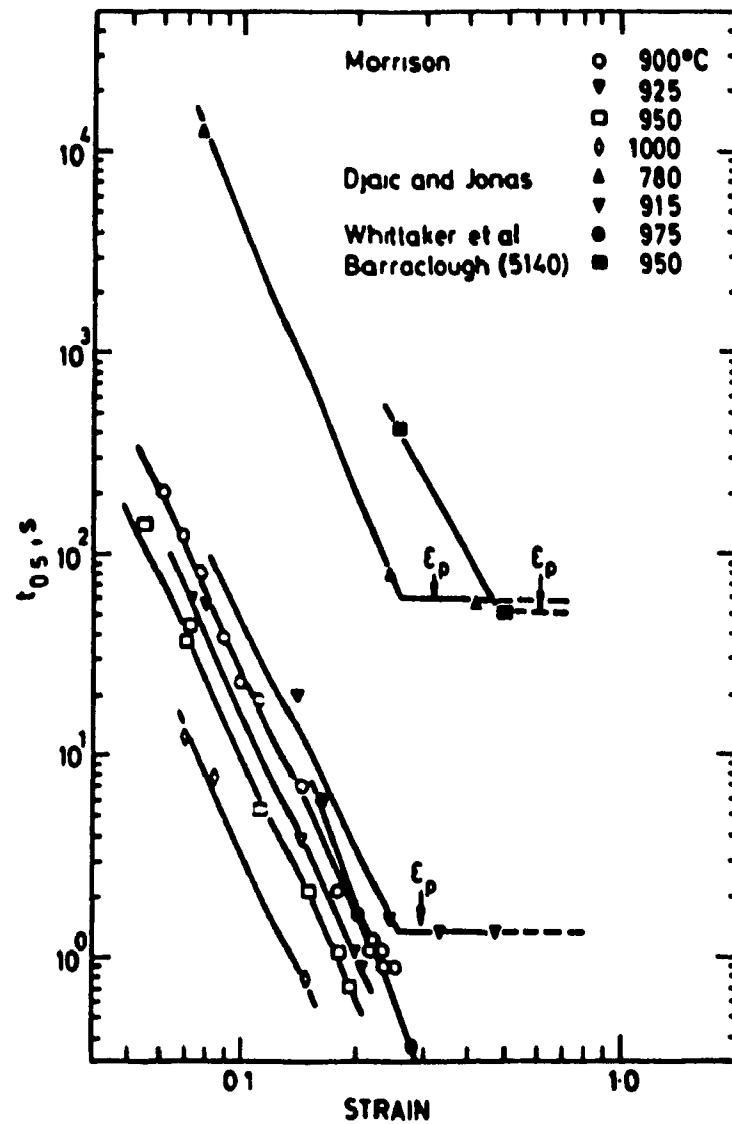


Figure 2.4 Strain dependence of time for 50% recrystallization in C-Mn and low alloy steels ^[17].

increasing strain.

The effect of strain rate on recrystallization rate is expected because the flow stress, and therefore the stored energy, depend on the Zener-Hollomon parameter. However, there is some controversy regarding this subject; the effect of strain rate is not clear and thus needs more extensive work.

The second parameter that determines the recrystallization rate is the density of nucleation sites. Since nucleation takes place mainly by the migration of grain boundary bulges, as suggested by McQueen and Jonas [1] and Jonas et al. [18], the density of favorable sites for nucleation increases with a decrease in grain size, which results in faster recrystallization kinetics.

Finally, the effect of holding temperature on recrystallization kinetics is also strong. An increase in temperature of 50°C leads to an increase in recrystallization rate of about one order of magnitude [1]. Djaic and Jonas [19] have shown that the dependence of recrystallization rate on temperature follows an Arrhenius law.

2.3.3. Metadynamic Recrystallization

When the critical strain for dynamic recrystallization, ϵ_c , is exceeded during deformation, and if high temperature deformation is stopped, softening occurs by a type of static recrystallization which does not have an analogous process in the annealing of cold worked materials. This high temperature process is called metadynamic or postdynamic recrystallization and does not involve an incubation time for nucleation since the nuclei are already present within the metal upon the termination of deformation. Some of the grain boundaries formed by dynamic recrystallization are already migrating and sweeping out regions which become strain free. These become static nuclei without a nucleation interval. In the regions which do not contain dynamic nuclei, conventional nucleation for static recrystallization can still take place.

Figure 2.5 shows schematically the relationship between the three static softening processes which depends on the prior or interruption strain. Below some critical strain for static recrystallization (point B), limited softening takes

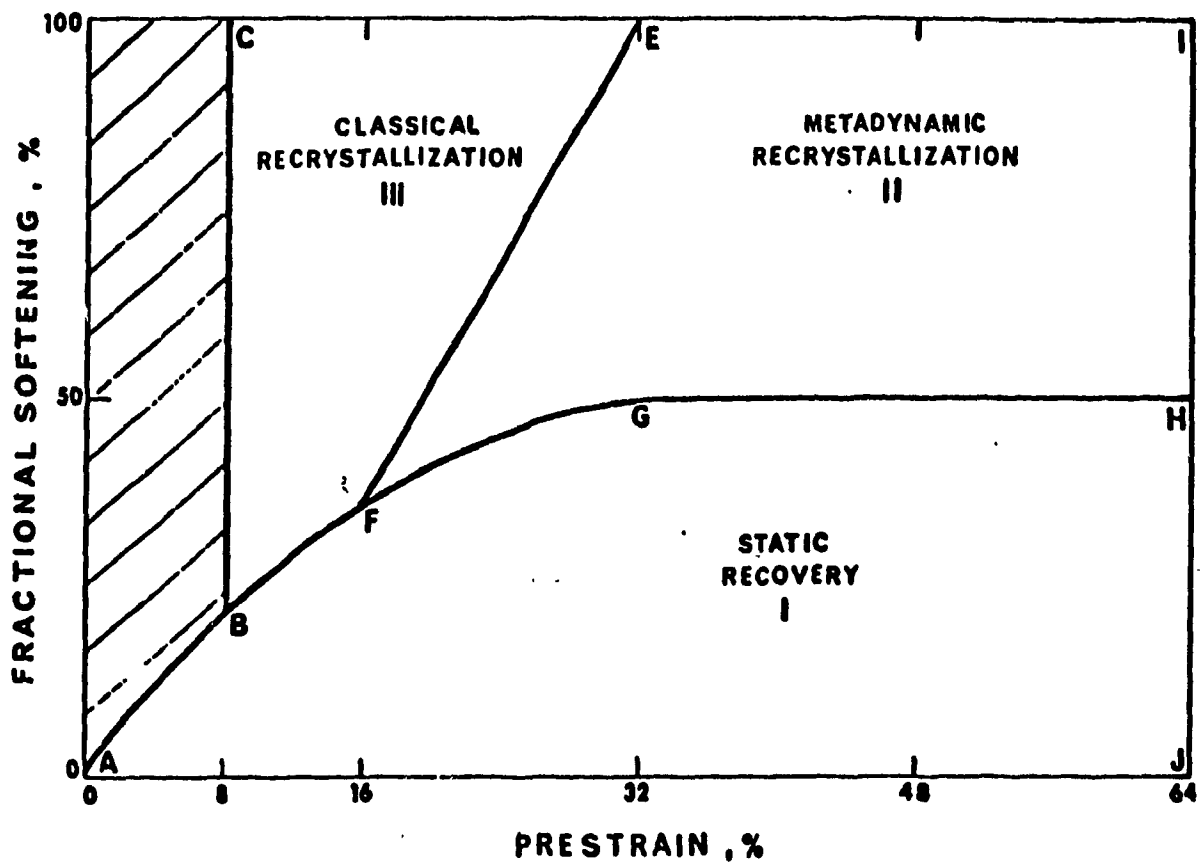


Figure 2.5 Schematic relationship between the three static processes [15].

place solely by static recovery. When the prestrain is larger than the critical strain for static recrystallization but smaller than that for dynamic recrystallization (point F), classical recrystallization follows static recovery. If the prestrain exceeds the critical value for dynamic recrystallization but is less than the steady state strain (point G), metadynamic recrystallization occurs from the nuclei already formed during deformation. Finally, when the steady state strain is exceeded, metadynamic recrystallization completely replaces classical recrystallization†.

The overall rate of metadynamic recrystallization is influenced by the same factors as static recrystallization following dynamic recovery. However, after steady state, the stored energy is no longer dependent on strain and the original grains have already disappeared. In such a case, the relevant variables are the strain rate and temperature of deformation and holding [14, 19]. The practical importance of metadynamic recrystallization remains in the absence of any prior incubation period so that it is about an order of magnitude faster than classical recrystallization [1].

2.3.4. Grain Growth

Grain growth during reheating or after recrystallization should follow the same pattern. Theoretical derivations based on the assumption that the growth rate is proportional to the excess free energy per unit volume associated with the grain boundaries has led to the following equation which describes isothermal grain growth:

$$D^2 = D_0^2 + Kt \exp\left(-\frac{Q}{RT}\right) \quad (2.6)$$

† According to more recent investigations, this simple picture is no longer valid. The main difference is that metadynamic recrystallization is not able to lead to full softening (see section 7.3.2.).

where D and D_0 are the grain sizes at time t and just after the completion of recrystallization, respectively. K is a constant which includes the grain boundary specific energy and Q_{gg} is the activation energy for grain growth.

In metals, the agreement between Eq. 2.6 and practice is not particularly successful; the experimentally observed values of the grain size exponent are usually larger than the theoretical value of 2.

When titanium is present, because of the high stability of the fine dispersion of TiN, grain growth is suppressed. During reheating, grain coarsening temperatures higher than 1200°C can be obtained if Ti/N ratios around the stoichiometric value of 3.42 are employed [20]. Only a small volume fraction of precipitates is required for the control of grain size. Grain growth after the completion of recrystallization in such steels has been found by Ouchi et al. [20] to be negligible even after times longer than 1000 seconds and with the recrystallized grain size smaller than the reheated one.

2.3.5. Solute and Strain-Induced Precipitation Effects

The addition of carbide/nitride forming elements, such as niobium or titanium, to austenite leads to the formation of stable alloy carbonitrides. Static precipitation can occur in undeformed austenite or following deformation, whereas dynamic precipitation only occurs during the hot deformation process. In the case of deformed austenite, precipitation is called strain-induced. Strain-induced precipitates are usually very fine (around 5 nm) and influence the work hardening rate [21].

The retardation of recrystallization by microalloy additions in HSLA steels is due to two mechanisms. These are the pinning effect of strain-induced precipitates and the solute drag caused by the microalloying elements in solution. While the role of the precipitate forming process has been discounted by some researchers who have favored an explanation based on solutes or on the formation of a type of pre-precipitate [22], others have concluded that solute effects are of incidental importance and that strain-induced precipitation is responsible for the retardation of recrystallization [23-26]. Subsequently, several authors have pointed out that both effects may be involved [27-29].

Despite this controversy, there are masses of data which show that solute atoms can be effective in delaying both recovery and recrystallization [30] and that precipitation contributes to a still greater extent to this retardation [30-35].

The retardation of recrystallization by solute effects is considered to be due to the creation of a substantial drag force that opposes moving dislocations or boundaries. Fine precipitates on grain boundaries can also produce a drag force which leads to the suppression of recrystallization. If precipitates become coarse, they are no longer effective as barriers [27, 28].

Using high temperature isothermal compression testing, Jonas and Weiss [27, 28] determined the kinetics of precipitation after deformation. They showed that when precipitation starts before recrystallization, the latter was delayed by more than an order of magnitude in time. Their observations have proved that the retardation of recrystallization is due to the presence of solute atoms at high temperatures and to precipitates at the relatively low temperatures corresponding to the finishing stage of hot rolling.

2.4. EFFECT OF ALLOYING ELEMENTS

The properties of HSLA steels are determined by composition because austenite is greatly affected by the presence of alloying elements during processing. Second phase particles also play an important role in delaying the recrystallization of austenite, by affecting the $\gamma \rightarrow \alpha$ transformation, or by causing precipitation hardening in austenite or ferrite.

2.4.1. Manganese

The addition of Mn results in ferrite grain size refinement by depressing the $\gamma \rightarrow \alpha$ transformation. The amount of Mn should, however, be limited to about 1.5% to 1.7%, otherwise undesirable transformed microstructures can be formed, impairing the strength and toughness.

2.4.2. Carbon

Due to its low cost, carbon has been widely used as a strengthener. Its potential for strengthening by solid solution effects is about 100 MPa with a maximum solubility of 0.02% in ferrite. Above this limit of solubility, the segregation of carbon occurs at slow cooling rates, leading to the formation of pearlite [24]. For better impact properties and weldability, it is important to keep the carbon content low.

2.4.3. Niobium

Small additions of Nb can provide grain size control by precipitating carbonitride particles at austenite grain boundaries; it thus improves strength and toughness through grain refinement. By subsequent thermomechanical treatment, high strength with moderate toughness or moderate strength with high toughness can be obtained, depending on whether the carbonitride phase is precipitated in the austenite for grain size control or in the ferrite for precipitation hardening.

The optimum amount of Nb addition that can be made without any detrimental effect on the toughness has not been well studied, nor has the influence of austenitizing temperature on austenite grain coarsening behavior. However, it was found in a recent study [36] that the austenite grain size in a steel containing 0.06% Nb increased linearly with increasing temperature up to 1000°C, above which grain growth become slow. In steels containing Nb, the presence of carbonitrides pins the grain boundaries and the grain size remains unchanged during heating (Fig. 2.6). At higher temperatures, when the grain growth inhibitors become ineffective as a result of solution or coalescence, the rate of grain coarsening suddenly increases. This is because the restricted grains tend to attain equilibrium size as quickly as possible when the precipitates are no longer effective.

Another effect of Nb is that the dissolved carbonitrides can retard both recovery and recrystallization; this increases the refinement of the austenite microstructure during controlled rolling [37]. The retardation of recrystallization is due to the great solute drag effect of Nb, which is greater

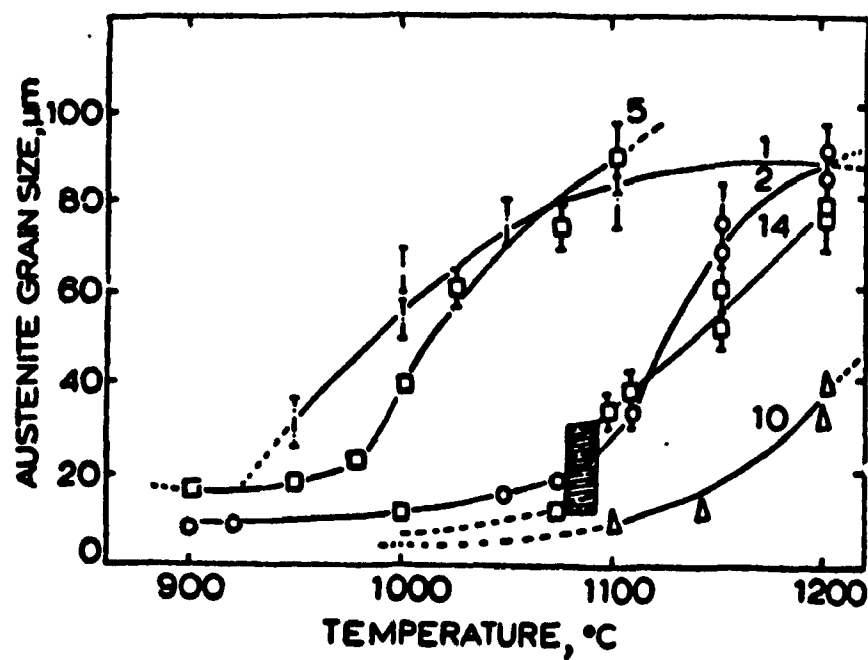


Figure 2.6 Temperature dependence of austenite grain size ^[36].
(The numbers 1, 2, 5, 10 and 14 refer to C-Mn, 0.06% Nb, 0.07% Al,
0.21% Nb and 0.03% Nb steels, respectively)

than that due to other alloying additions. However, some controversy remains about whether such solutes are not simply precipitates that cannot be detected by present metallographic techniques.

2.4.4. Titanium

Titanium forms nitrides, carbides, sulfides and oxides in low carbon steels. The formation of carbides in low carbon steels can be used for precipitation strengthening, while the formation of sulfides elevates the transverse shelf energy. The high reactivity of titanium causes control problems that have delayed the commercial development of these steels [38]. The formation of titanium oxide is undesirable because *i*) it limits the amount of titanium available for grain refinement, precipitation strengthening and sulphide inclusion shape control, and *ii*) it produces dirty steels. To counter the high affinity of titanium for oxygen, it is necessary to deoxidize the molten steel with aluminum prior to the addition of titanium. Ti also has a high affinity for nitrogen (but lower than that for oxygen). The great stability of TiN and its slow growth rate [37] enables it to act as a grain growth inhibitor at high preheating temperatures. However, high levels of Ti can be detrimental because the TiN particles that form under these conditions are large and do not restrict austenite grain growth. In general, the effect of Ti is similar to that of Nb, but Nb is a less effective grain refiner than Ti and this is associated with its higher degree of solubility.

2.4.5. Boron

Boron has been shown to enlarge the α -solid solution domain [39]. Its maximum solubility in ferrite is about 0.002%. The potential for B to increase the hardenability is due to its segregation at austenite grain boundaries [40]. This reduces the ferrite nucleation rate during transformation, which suppresses the formation of polygonal ferrite. The transformation temperature is lowered in particular when other microalloying elements such as Nb or Cu are present because of the synergistic effect of these elements [41]. However, the mechanism by which boron increases the hardenability is not completely clear.

While the effect of boron on tensile strength is known through its influence on the hardenability, its influence on toughness is still controversial. It was reported that the detrimental effect of boron on toughness is related to the formation of embrittling intergranular borocarbides ($\text{Fe}_{23}(\text{BC})_6$) when the content exceeds 0.0025%. However, Sojka [41] found that a higher boron content was responsible for higher initiation and propagation energies by decreasing the effective grain size.

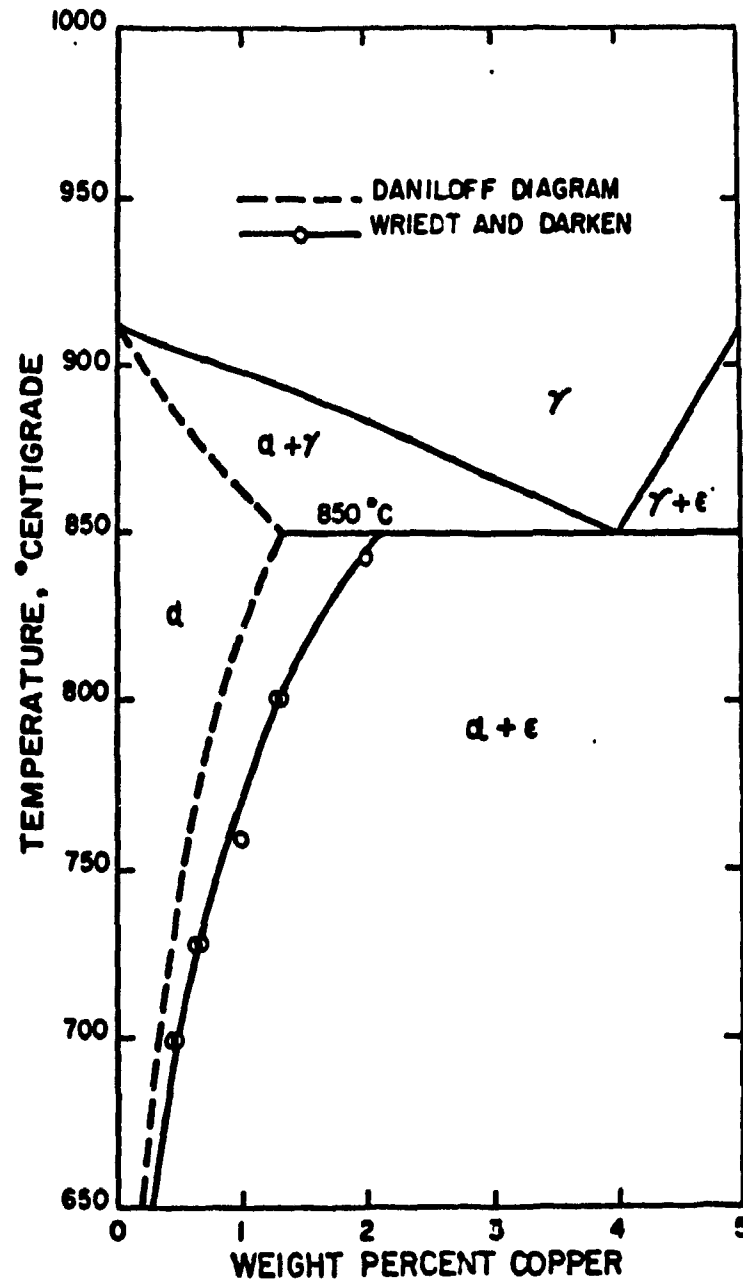
2.4.6. Copper

Copper is a potential precipitation hardening element, although it has not been used extensively due to production problems such as hot shortness or contamination of other alloys. Its solubility is high at 850°C and above (Fig. 2.7); however, after the transformation to ferrite, this solubility is greatly reduced. In addition to the potential for precipitation strengthening, copper has other beneficial effects, which are [42] : i) improved atmospheric corrosion resistance, ii) marked strengthening by solid solution with an increase of about 40 MPa per 1% copper being reported, iii) depression of the $\gamma \rightarrow \alpha$ transformation, which refines the ferrite [43] , and iv) the low carbon equivalent of copper in steel.

2.5. STRUCTURAL CHANGES DURING THE THERMOMECHANICAL PROCESSING OF STEELS

The need for higher strength steels has prompted a major upsurge in the study of microstructural changes during processing. Methods such as conventional hot rolling, quenching and tempering, and normalizing have been used to produce steel plates, but the most efficient method is modern controlled rolling. It has been realized that only by careful control of the thermal and mechanical processing history can fine ferrite grain sizes and hence stronger and tougher steels be produced.

The grain size developed after the $\gamma \rightarrow \alpha$ transformation during cooling depends strongly on the austenite grain size because of the strong tendency for the nucleation of ferrite on austenite grain boundaries. Therefore, the finer the austenite grain size brought about by controlled rolling, the finer the

Figure 2.7 Iron-copper phase diagram ^[41].

transformed final structure.

Controlled rolling consists of the following steps [44]:

- i) a suitable slab reheating temperature (soaking) to produce large and uniform austenite grains,
- ii) austenite grain refinement through repeated recrystallization cycles after deformation (roughing),
- iii) deformation in the no-recrystallization range (pancaking), and
- iv) controlled cooling.

Soaking consists of reheating the steel to a temperature conventionally between 1200 and 1300°C. The aim of soaking is to bring all the microalloy carbonitrides such as Nb(C,N) into solution. Low reheating temperatures produce relatively small initial grains but can lead to the presence of undissolved precipitates. The latter is responsible for a loss in efficiency in the retardation of recrystallization in the subsequent stages of rolling, as well as less effectiveness in precipitation strengthening.

During roughing passes ($\sim 1100^\circ\text{C}$), recrystallization is very rapid and the resulting grain size remains quite large (part I in Fig. 2.8). In the intermediate temperature range, complete static recrystallization cycles can be achieved if the temperature, deformation and interpass holding times are carefully chosen (case c in part II). If these thermomechanical conditions are not properly controlled, slow and incomplete recrystallization may occur and mixed austenite structures result. Conversely, rapid static recrystallization may be followed by localized undesirable grain growth (case b).

In the low temperature range above the A_{r3} temperature where recrystallization does not take place (corresponding to finishing in hot rolling and to part III in Fig. 2.8), the fine homogeneous recrystallized structure obtained in the roughing stage is further modified by deformation and results in elongated grains. In this range, the average grain volume is not affected but the

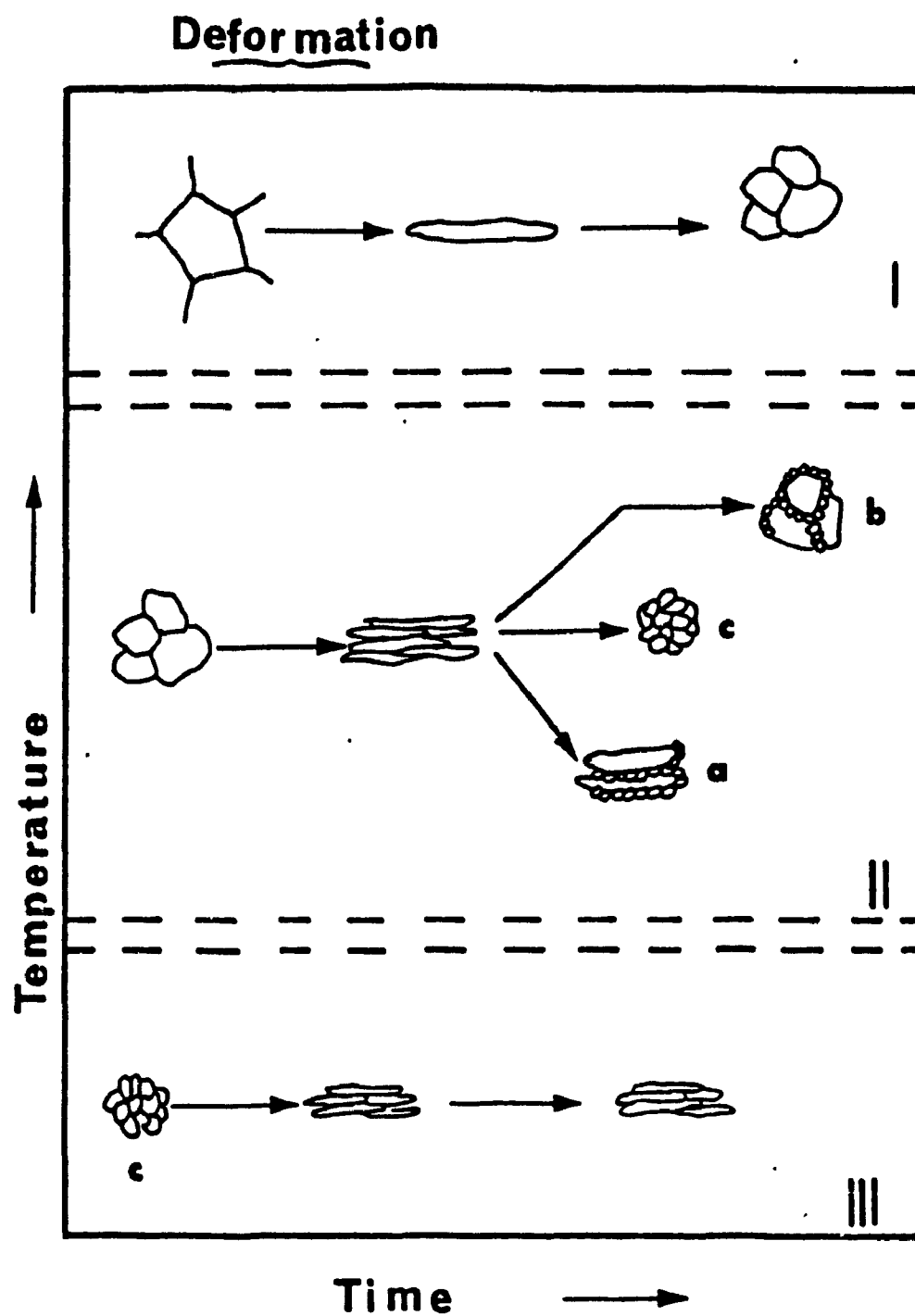


Figure 2.8 Austenite grain size changes during controlled rolling ^[22].

grain surface to grain volume ratio S_v is increased. As a result, the number of potential nucleation sites for the austenite-to-ferrite transformation is increased, which leads to finer final microstructures [45]. In addition to the austenite grain boundaries, deformation bands within the grains can act as nucleation sites for ferrite formation, as has been observed by Sellars and co-workers [46] in deformed nickel.

In addition to the rolling stages shown in Fig. 2.8, finish rolling is sometimes extended into the austenite-ferrite two phase region [44, 47]. The major purpose of rolling below the A_{r3} temperature is to increase the tensile strength. In this region, the material behaves like a dual phase steel, with the duplex structure consisting of soft and hard grains. Under these conditions, the strength can be expressed in terms of the volume fractions of the two types of structures. Gladman et al. [48] have estimated both the contribution of this substructural strengthening together with the textural strengthening. While Tanaka and his coworkers [49] have found that excessive straining in the $\alpha + \gamma$ range degraded the toughness, the same author [47] pointed out, however, that the impact properties can be improved by the presence of a fine grained, recrystallized structure.

Finally, controlled cooling from the finish rolling temperature can be practised to yield benefits in terms of productivity and material properties. With regard to mechanical properties, rapid cooling is used to restrict coarsening of the refined austenite grains, to depress the transformation temperature, to limit growth of the transformed ferrite grains and to reduce the extent of carbonitride precipitation [37, 50]. A low transformation temperature enlarges the no-recrystallization region and also refines the ferrite structure because ferrite grain growth is limited at lower temperatures. The limited precipitation in austenite prior to transformation leaves a larger amount of the alloying elements available to form fine precipitates in the ferrite, which leads to desirable strengthening.

2.6. TYPES OF MICROSTRUCTURES IN HSLA STEELS

The different microstructures usually present after controlled rolling HSLA steels can be classified into two main types: ferrite-based and bainite-based. The ferrite structures are further divided into two groups: polygonal and apolygonal. The former forms at relatively high transformation temperatures, nucleates and grows from the austenite grain boundaries or the deformation bands in the austenite [51]. Polygonal ferrite is characterized by an equiaxed shape and a low dislocation density. It usually contains pearlite, the volume fraction of which depends on the carbon content.

Apolygonal ferrite is characterized by a general irregular microstructure and includes free bainite, massive ferrite and acicular ferrite. Acicular ferrite forms on continuous cooling by a mixed diffusion and shear mode of transformation that begins at a temperature slightly higher than the upper bainitic transformation range. Due to shearing, acicular ferrite consists of a highly substructured, nonequiaxed ferrite with or without a lath structure. Due to diffusion, acicular ferrite contains a martensite-austenite (MA) microconstituent which consists of a mixture of martensite (and/or bainite) and retained austenite.

Massive ferrite can be identified as rather large grains of ferrite with little evidence of a fine substructure. Being non-polygonal, it belongs to the acicular ferrite sub-group.

Bainite forms on continuous cooling by a mixed mode of transformation, including shearing and diffusion. Due to shearing, bainite exhibits ferrite laths; due to diffusion, it contains cementite precipitates. Two types of bainite can be distinguished, depending upon the transformation range : upper and lower bainite.

These bainitic structures are the basis of an important group of HSLA steels widely used for structural applications and the same microstructures are also often found in low carbon weld metals and heat affected zones, as shown in Fig. 2.9.





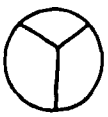



Steel	Chemical composition	Plate rolling			Microstructure and properties
		Slab-heating	Rough rolling	Finish rolling	
Newly-developed ULCB steel	<ol style="list-style-type: none"> 1. Very low carbon content, approximately up to 0.03%. 2. Utilization of maximum benefit of grain refinement by fine dispersed TiN particles. 3. Optimal combinations of alloying elements, such as Mn, Nb, B etc. 4. Low-carbon equivalent. 	<p>Inhibition of austenite-grain growth by fine dispersed TiN particles and low-temperature heating. Fine and homogeneous austenite-grain.</p>  <p>ASTM No.5 to 6</p>	<p>Refinement of austenite-grain through repeating recrystallization. Fine and homogeneous recrystallized austenite-grain.</p> 	<p>Elongation of austenite-grain and formation of deformation bands with large amounts of reduction in non-recrystallization region of austenite.</p> 	<p>Highly-substructured, fine and homogeneous bainitic structure. Good toughness in both base metal and HAZ. Excellent combination of strength, toughness and weldability.</p> 
Conventional bainitic steel	<ol style="list-style-type: none"> 1. High-carbon content approximately 0.10%. 2. Large amounts of alloying elements, such as Mn, Cr, Mo etc. 3. High-carbon equivalent, more than 0.55%. 	<p>Coarse and heterogeneous austenite-grain.</p>  <p>ASTM No.-3 to 0</p>	<p>Coarse and heterogeneous recrystallized austenite-grain.</p> 	<p>Insufficient reduction in non-recrystallization region of austenite.</p> 	<p>Coarse bainite. Poor toughness in both base metal and HAZ. Poor weldability.</p> 

Figure 2.9 Microstructural evolution of bainitic steels [40].

2.7. SUMMARY

In this chapter, the basic concepts of physical metallurgy pertaining to hot working operations were reviewed. Both dynamic and static changes were described, with emphasis on modern controlled rolling as an application. An appropriate link between these metallurgical concepts and the thermomechanical history of a hot rolled steel can constitute an efficient tool in the computer modelling of deformation processing. The next chapter will therefore be consecrated to a literature review concerning the thermomechanical changes that take place during hot rolling.

Chapter THREE

TEMPERATURE EVOLUTION AND ROLLING LOAD CALCULATIONS DURING HOT ROLLING -AN OVERVIEW-

3.1. INTRODUCTION

In the previous chapter, the metallurgical aspects of hot deformation processing were presented. Most the variables describing this process are strongly temperature dependent. The first part of the present chapter is dedicated to a description of the different heat transfer mechanisms involved in hot rolling; these are:

- i)* radiation and convection during air cooling,
- ii)* convection by water cooling,
- iii)* heat conduction between the metal being worked and the rolls, and
- iv)* heat generation by plastic deformation.

A brief summary is given here regarding the different methods of heat transfer calculation during hot rolling. In the second part of the present chapter, the existing rolling theories used to compute rolling loads and torques during hot rolling are described. Finally, because the most important parameter in the above theories is the flow stress, a brief summary of the empirical-analytical equations for the deformation resistance is given.

3.2. MODELLING OF TEMPERATURE CHANGES DURING HOT ROLLING

3.2.1. Heat Conduction in the Rolled Material

Heat conduction within a metal depends mainly on the initial temperature distribution. The temperature gradient is a function of time and can be solved by considering the heat conduction equation:

$$\rho c \frac{\partial T}{\partial t} = k \left(\frac{\partial^2 T}{\partial x^2} + \frac{\partial^2 T}{\partial y^2} + \frac{\partial^2 T}{\partial z^2} \right) + A_w \quad (3.1)$$

where:

α = thermal diffusivity ($\alpha = k/\rho c$), $\text{m}^2 \text{s}^{-1}$

k = thermal conductivity, $\text{W m}^{-1} \text{K}^{-1}$

ρ = material density, Kg m^{-3}

c = specific heat, $\text{J Kg}^{-1} \text{K}^{-1}$

A_w = energy input due to mechanical work, Wm^{-3} ($A_w = 0$ outside the stands).

k , ρ and c are assumed to be temperature independent; however, this is not always the case.

To simulate temperature evolution during hot rolling, an analytical solution of the above differential equation is not possible because the boundary conditions are constantly changing with time. Numerical analysis has been used by some authors and their formulations concerning the numerical solutions are similar [52-54]. However, their assumptions about the boundary conditions are different.

3.2.2. Heat Losses Outside the Stands

3.2.2.1. Radiation and Convection During Air Cooling

Heat loss by radiation is the most significant factor affecting the temperature drop during hot rolling. Two methods have been employed to calculate the temperature change due to radiation [55]. The first method assumes that the temperature gradient within the material is not significant

and the heat radiated to the air is calculated using the following Stefan-Boltzmann law:

$$\frac{dq}{dt} = A \sigma_{SB} \epsilon_m (T^4 - T_A^4) \quad (3.2)$$

where:

q = heat radiated by a body, J

A = surface area of body subjected to radiation, m^2

σ_{SB} = Stefan-Boltzmann constant ($5.6699 \times 10^{-8} \text{ W m}^{-2} \text{ K}^{-4}$)

T = temperature at time t , K

T_A = temperature of environment, K

ϵ_m = emissivity (ϵ_m varies with temperature from 0.75 to 0.85).

Since we also have:

$$dq = \rho c V dT \quad (3.3)$$

where V is the volume of body subjected to radiation, the rate of temperature loss α_R can be calculated:

$$\alpha_R = \frac{dT}{dt} = \frac{A \sigma_{SB} \epsilon_m}{\rho C V} (T^4 - T_A^4) \quad (3.4)$$

and the temperature loss ΔT_R during the radiation time t_R is simply given by:

$$\Delta T_R = \int_0^{t=t_R} \alpha_R dt \quad (3.5)$$

Simple expressions for α_R were derived as functions of the surface temperature and thickness of the rolled material. A summary of these expressions can be found in reference [55].

The second method takes into account heat transfer within the material. In other words, Eq. 3.1 is solved numerically together with Eq. 3.2. In such a case, T in the last equation is taken as the surface temperature, T_s .

The convection losses during air cooling are given by Newton's law:

$$\frac{dq}{dt} = AH_C(T_s - T_A) \quad (3.6)$$

where H_C is the heat convection coefficient in $W m^{-2} K^{-1}$. The ideal situation is to determine H_C , which depends on the material temperature, the ambient temperature, the material specific heat and density and the dynamic viscosity of air flow and its characteristics (free, forced, laminar, turbulent, etc.). However, mathematical expressions for H_C can be controversial and are beyond the scope of this chapter. Some investigators find that a simple way to account for convection is to express the temperature loss as a percentage of the temperature loss due to radiation, with a coefficient of proportionality varying from 0.01 to 0.22 [55]. Others disregard convection and include its effect in the value of the emissivity, as it can account for up to 8% of heat losses [56]. Partington and Talbot [54], however, considered convection as an independent component. Harding [57] combined Eqs. 3.2 and 3.6 and by dropping the term T_A^4 , arrived at:

$$H_q = b_1(T_s - T_A) + b_2(T_s + 273)^4 \quad (3.7)$$

where H_q is the heat loss per unit area per unit time ($kW m^{-2}$) and b_1 and b_2 are constants ($b_2 = \epsilon_m \sigma_{SB}$). Setting $\epsilon_m = 0.84$, Harding fitted computed cooling curves to experimental cooling curves on stainless steel and obtained the following expression:

$$H_q = -0.6875 + 0.01224T_s + 4.762810^{-11}(T_s + 273)^4 \quad (3.8)$$

where T_s is in degrees Celsius.

3.2.2.2. Water Cooling

During hot rolling, water is used at different stages:

- i) to cool the work rolls in order to control their thermal history
- ii) to remove scale from the workpiece surface, and
- iii) to control the final mechanical properties of the rolled material on the run out table.

Newton's law of convection (Eq. 3.6) applies to all three of these situations. However, the value of H_C differs from one case to the other.

The cooling of roll surfaces has been studied by many investigators [58, 59], but this effect remains unclear. Sekimoto [60], for example, used a value of $H_C = 0.332$ to $3.6 \text{ cal cm}^{-2} \text{ sec}^{-1} \text{ K}^{-1}$ to simulate this process.

To remove surface scale before roughing and finishing, high pressure water jets are used. While some researchers have attempted to estimate the temperature drop of the slab surface from the temperature rise of the water and the physical properties of the rolled material, Hollander [53] found that H_C was not constant along the contact area between the jet and the strip surface (Fig. 3.1). For these reasons, he formulated the heat loss as follows:

$$\Phi_w = \frac{LA_1}{bv} \quad (3.9)$$

where

Φ_w = quantity of heat removed from 1 cm^2 of surface

L = total quantity of water applied in the cooling bank, l

A_1 = the amount of heat taken up by 1 liter of water (cal/l) (A_1 depends on the geometry and pressure)

b = width of the cooling bank, cm

v = speed of the steel, cm s^{-1}

On the run out table, laminar jets are used to control the coiling temperature which, in turn, controls the final mechanical properties of the rolled strip.

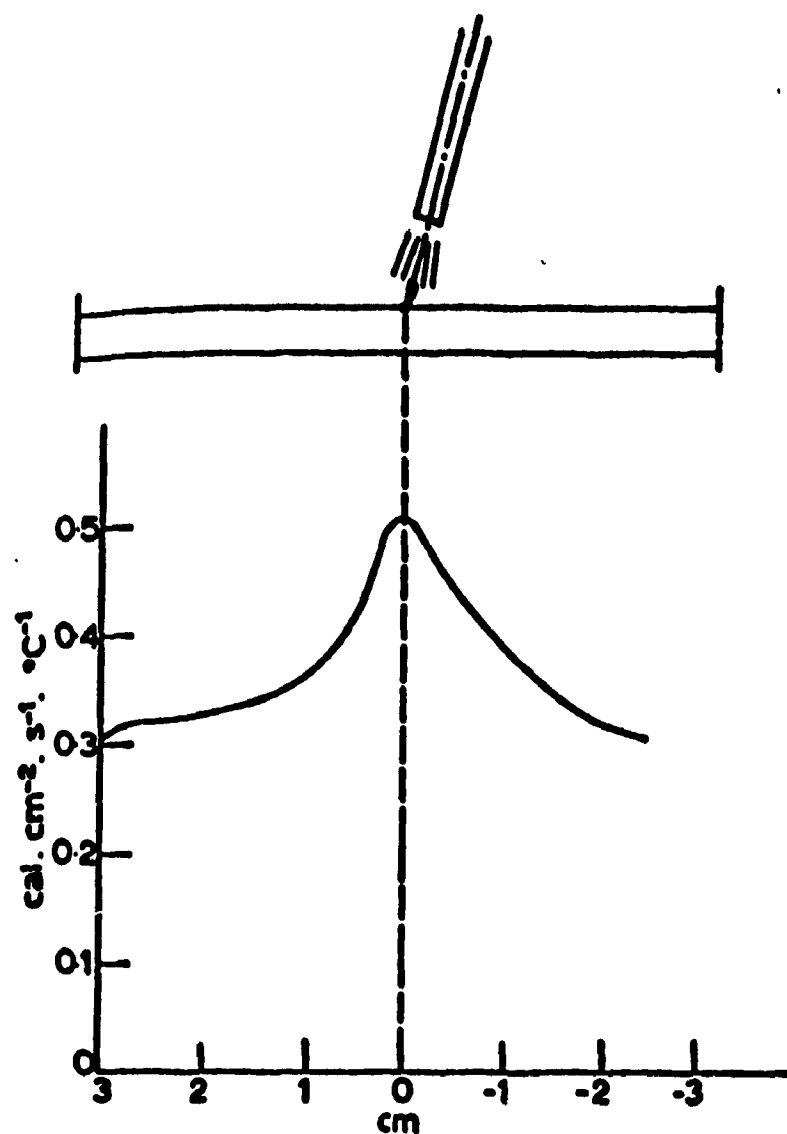


Figure 3.1 Distribution of heat transfer coefficient during water cooling ^[53].

Sigalla [59] has estimated the quantity of heat removed from the rolled material by a laminar jet using the following expression:

$$Q_{wat} = \frac{\pi D^2}{2b} k(T_s - T_{wat}) \sqrt{\frac{D}{\pi a v}} \quad (3.10)$$

where:

D = diameter of the laminar jet at the point of impact, cm

v = strip velocity, cm s⁻¹

b = distance between two adjacent jets across the width of the rolled material, cm.

For moving strip in a mill where the contact times range from 10⁻² to 10⁻³ seconds, Hollander [53] used Eq. 3.10, which gave good agreement between measured and calculated temperatures. Based on several experiments, Devadas and Samarasekera [61] have shown that forced convection occurred between the laminar water curtain and the hot steel. The heat transfer coefficient in such a case was estimated as a function of the Reynolds and Prandtl numbers by the following relation :

$$H_c = 0.063 \left(\frac{k_{wat}}{r} \right) Re^{0.8} Pr^{0.33} \quad (3.11)$$

where r is the radius of the forced cooling zone.

3.2.3. Heat Losses in the Roll Gap

In the roll gap, the top and bottom surfaces are chilled by contact with the rolls and, at the same time, the strip or plate changes its dimensions and gains heat due to the deformation. In the literature, there are few models that deal with the calculation of temperature changes during deformation. These models vary mainly in the assumptions made about the homogeneity of deformation and whether the contact is perfect or not.

3.2.3.1. Conduction to the Rolls

To simulate heat transfer during contact with the rolls, different approaches have been formulated in order to estimate the temperature drop at the surface of the rolled material. David et al. [62] introduced a thermal contact resistance, characteristic of heat propagation through the interface, which results in a discontinuity of the temperature profile across the boundary (see Fig. 5.7 below). The temperatures T_1^{surf} and T_2^{surf} were expressed in terms of the boundary temperature T_p and the interface conductance.

Conversely, Hollander [53] assumed perfect thermal contact between the roll and the deformed strip. He formulated the temperature drop at the surface using the source solution of the differential equation describing the temperature distribution for non-stationary problems (see Chapter Five for more details).

Harding [57] computed the temperature change during the contact time, both in the slab and in the roll. He assumed that the rate of heat transfer per unit area between the slab and the roll was proportional to the difference in the respective surface temperatures. He then defined a mean heat transfer coefficient during the time interval in terms of the heat transfer coefficient at the start and at the end of this time interval. The temperature drop at the slab surface and the temperature rise in the roll were calculated in terms of the mean heat transfer coefficient, the interval time, and the physical properties.

While some researchers have considered the heat conducted to the rolls to be balanced by the heat gained from the deformation [63], many attempts have been made by other investigators to determine the heat transfer coefficient between the material and roll during hot deformation. Stevens et al. [64] found that the heat transfer coefficient at the roll gap interface during roughing varies with the contact time from 18 to 37 kW m⁻² K⁻¹. Murata et al. [65] used uniaxial compression to see the effect of lubricant and scale at the interface on heat transfer between the metals in contact. They found that, in the absence of scale, with water as a lubricant, the heat transfer coefficient at the interface varied from 23 to 81 kW m⁻² K⁻¹ (Table 3.1).

Table 3.1. Heat transfer coefficients at roll/slab interface ($\text{kW m}^{-2} \text{K}^{-1}$)^[65].

Condition	No scale	Scale (10 μm)
No lubricant	29.1 - 34.9	7 - 10.5
Water	23.3 - 81.4	10.5
Hot rolling oil	20.0 - 46.0	5.8
Hot rolling oil + 20%CaCO ₃	69.8 - 175	12.8 - 23.3
Hot rolling oil + 40%CaCO ₃	12.79 - 17.4	-
KPO ₃	5.8	-

Contact times are between 1 and 3 sec.

3.2.3.2. Heat Generated by Deformation

During deformation of the slab between the rolls, heat is generated due to plastic deformation of the steel and the frictional work at the interface. The heat generated by friction was estimated by Sekimoto [60] as a function of the mean rolling pressure and coefficient of friction. However, the contribution of friction to the temperature rise is generally neglected.

The temperature rise due to deformation has been estimated from the developed rolling power or the measured specific torque [53, 54]. Devadas and Samarasekera [61] and Höfgen and coworkers [52] have used the mean deformation resistance $\bar{\sigma}$ to estimate this temperature rise as follows:

$$\Delta T = \frac{\bar{\sigma}}{\rho C} \ln\left(\frac{h_1}{h_2}\right) \quad (3.12)$$

where h_1 and h_2 are the initial and final thicknesses, respectively. The ΔT calculated is then added uniformly or concentrated only near the surface, depending on the author's formulation.

3.3. ROLLING THEORIES

3.3.1. Introduction

The most comprehensive theory of rolling is the one developed by Orowan [66], who accounted for friction at the interface between the material and the rolls, and also for the inhomogeneity of deformation in the roll gap. In the previous rolling theories, these factors were omitted. Orowan showed that the frictional conditions can vary even in a single pass from the coulomb situation, where the interfacial shear stress τ is equal to μs (μ is the friction coefficient and s the local pressure), to a completely different situation in which τ is equal to the shear yield stress of the material. With regard to the inhomogeneity of deformation, which means a departure from the simple assumption of "plane sections remaining plane" (Fig. 3.2), he introduced an inhomogeneity factor to account for this complicated situation. In addition to the nonuniform deformation factor, he also considered the temperature and strain rate dependence of the yield stress in the roll gap and pointed out how this change of yield stress can be incorporated in his theory. This approach relies on numerical integration, which led later researchers, especially Bland and Ford [67] and Sims [68], to make additional assumptions that allowed analytical solutions to be achieved, thereby avoiding the numerical integration required in the Orowan theory.

3.3.2. Orowan Formulation

In his rolling theory, Orowan used the slab method [66]. In such a technique, a geometrically well-defined part of the plastically deforming material is isolated and the horizontal equilibrium of forces is applied to it through the following equation:

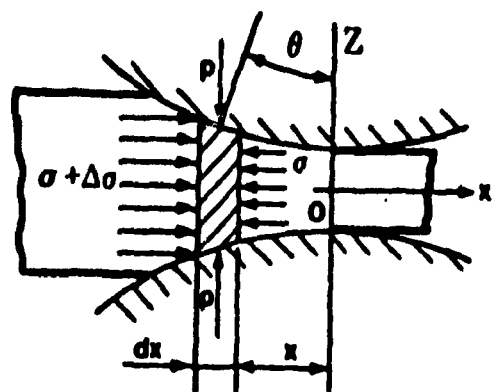
$$\frac{df}{d\phi} = 2 R s (\sin\phi \pm \mu \cos\phi) \quad (3.13)$$

where:

f = horizontal force per unit width of the rolled material,

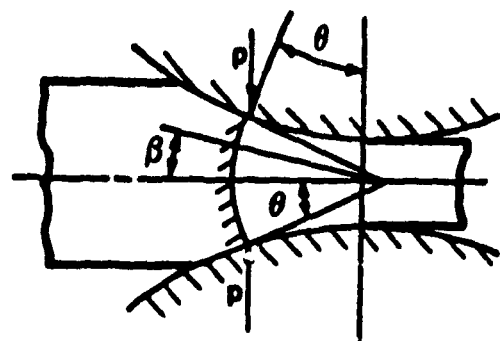
ϕ = angular coordinate of the arc of contact

R = roll radius



Plane vertical sections of sheet before rolling remain plane during rolling.

Stress distribution in vertical plane is homogeneous.
 $\sigma(Z) = \text{constant}$



Plane vertical sections of sheet before rolling are deformed during rolling.

Stress distribution in vertical plane is not homogeneous.

Figure 3.2 Stress distribution in the roll gap for homogeneous and inhomogeneous deformation ^[55].

s = the normal roll pressure

μ = coefficient of friction

The positive sign refers to the exit side and the negative one to the entry side.

If the deformation is assumed to be homogeneous (Fig. 3.3), i.e. plane sections remain plane, the horizontal pressure σ and the vertical pressure are constant within a vertical section. In such a case, we have:

$$f = \sigma h \quad (3.14)$$

where h is the current height of the rolled stock.

Differential equation 3.13 contains two unknowns, f and s , which are both functions of ϕ . To solve this equation with only one unknown, for instance $f(\phi)$, Orowan employed the following solution proposed by Nadai [69] for the stress distribution in a plastic wedge compressed between non-parallel plates:

$$f(\phi) = h \left[s \left(1 \pm \mu \left(\frac{1}{\phi} - \frac{1}{\tan \phi} \right) \right) - \sigma_Y' w \right] \quad (3.15a)$$

where:

$$w = \frac{1}{\sin \phi} \int_0^\phi \left[\sqrt{1 - a^2 \left(\frac{\theta}{\phi} \right)^2} \right] \cos \theta \, d\theta \quad (3.15b)$$

$$a = \frac{\mu s}{(\sigma_Y'/2)} \quad (3.15c)$$

θ is any intermediate angle less than ϕ and σ_Y' is the yield stress of the material in plane strain compression.

In the case where the material sticks to the rolls, the frictional drag μs tends to $\sigma_Y'/2$; a is then equal to 1 and w tends to $\pi/4$. In such a case, Eq. 3.15a becomes:

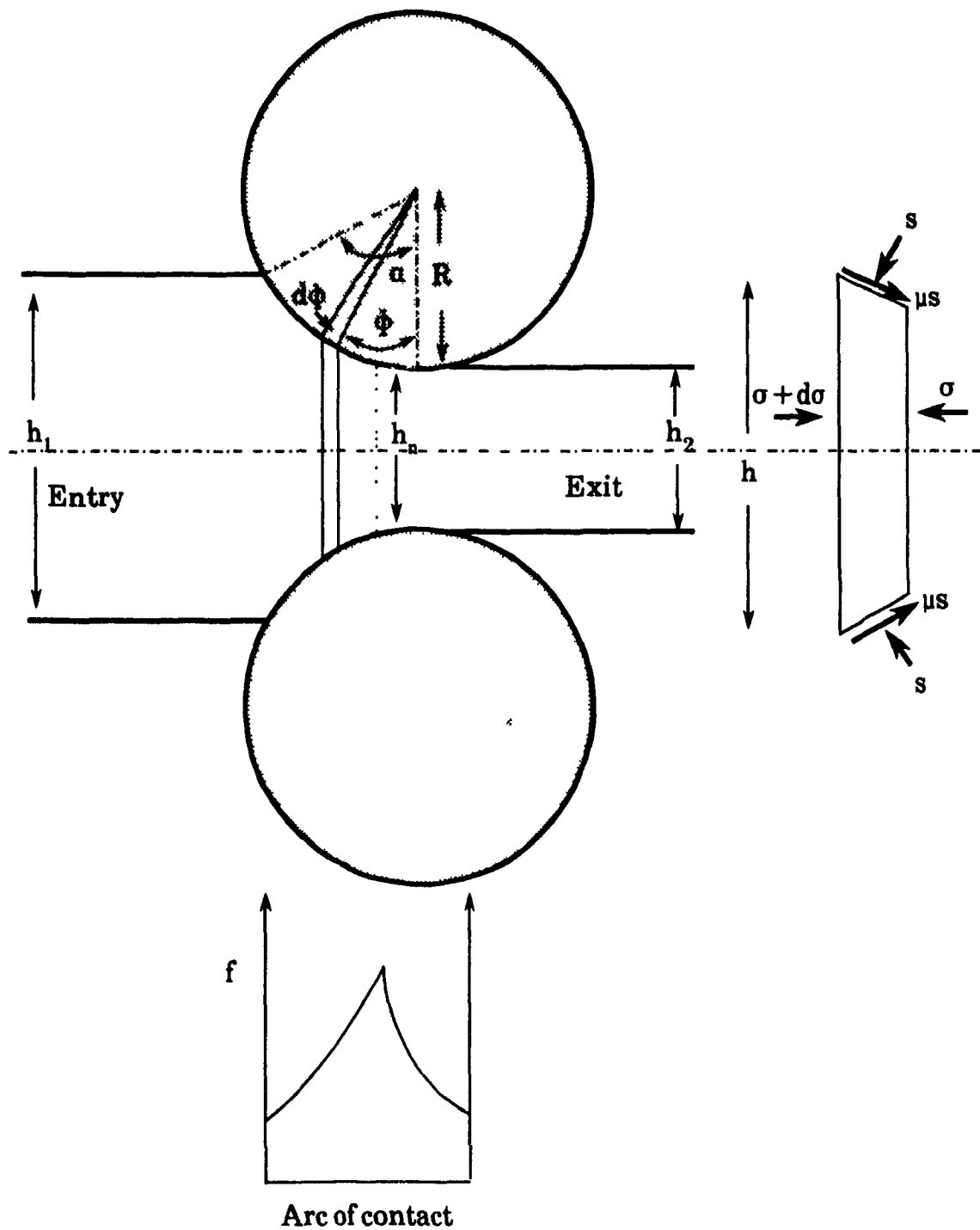


Figure 3.3 Roll gap geometry and force equilibrium.

$$f(\phi) = h \left[s - \sigma_Y' \left[\frac{\pi}{4} \mp \frac{1}{2} \left(\frac{1}{\phi} - \frac{1}{\tan \phi} \right) \right] \right] \quad (3.16a)$$

If slipping occurs, i.e., when μ is assumed to be small, Eq. 3.15a is reduced to the following expression:

$$f(\phi) = h(s - \sigma_Y' w) \quad (3.16b)$$

s can be taken from Eq. 3.16 a or b and substituted into Eq. 3.13. One can then solve this differential equation for f , determine the normal pressure distribution and then the roll force. The transition from conditions of sticking to slipping friction is dictated by $\mu s = \sigma_Y'/2$.

Alexander [70] left out the inhomogeneity factor w (Eq. 3.15b) and used a fourth order Runge-Kutta technique to determine the normal pressure distribution and then the roll force. Sims [68] made still more simplifying assumptions to Orowan's theory to obtain an analytical solution of Eq. 3.13. His approach is described in the subsection that follows.

3.3.3. Sims Approach

Sims [68] modified Orowan's method [66] by assuming that sticking friction occurs over the entire arc of contact and that :

$$\sin \phi = \tan \phi = \phi \quad (3.17a)$$

$$\cos \phi = 1 \quad (3.17b)$$

$$1 - \cos \phi = \phi^2/2 \quad (3.17c)$$

Eq. 3.13 then becomes:

$$\frac{df}{d\phi} = 2 R s (\phi \pm \mu) \quad (3.18)$$

To derive f , he used the same assumption as Orowan that the rolling process is equivalent to deformation between rough, inclined plates (Eq. 3.16a). When the last equation is coupled with Eq. 3.17a, it is easy to show that:

$$f = h \left(s - \frac{\pi}{4} \bar{\sigma}_Y' \right) \quad (3.19)$$

By substituting Eq. 3.19 into Eq. 3.18 and solving the resulting differential equation analytically, Sims obtained:

$$\frac{s^+}{\bar{\sigma}_Y'} = \frac{\pi}{4} \ln\left(\frac{h}{h_2}\right) + \frac{\pi}{4} + \sqrt{\frac{R}{h_2}} \tan^{-1} \sqrt{\frac{R}{h_2}} \phi \quad (3.20a)$$

at the plane of exit, and

$$\frac{s^-}{\bar{\sigma}_Y'} = \frac{\pi}{4} \ln\left(\frac{h}{h_1}\right) + \frac{\pi}{4} + \sqrt{\frac{R}{h_2}} \tan^{-1} \sqrt{\frac{R}{h_2}} \alpha - \sqrt{\frac{R}{h_2}} \tan^{-1} \sqrt{\frac{R}{h_2}} \phi \quad (3.20b)$$

from the plane of entry towards the plane of exit.

On the assumption that the angular coordinate ϕ is small so that the difference between the normal roll pressure and the vertical pressure can be neglected, the specific rolling load is given by:

$$P = R \int_0^\alpha s d\phi \quad (3.21)$$

After substitution of Eqs. 3.20a and b in Eq. 3.21, Sims showed that:

$$P = \bar{\sigma}_Y [\sqrt{R(h_1 - h_2)}] Q_p \quad (3.22)$$

where $\bar{\sigma}_Y$ is the mean deformation resistance of the rolled material and h_n is the thickness at the plane of intersection. Q_p is a geometrical factor given by:

$$Q_p = \left[\frac{\pi}{2} \sqrt{\frac{1-r}{r}} \tan^{-1} \sqrt{\frac{r}{1-r}} - \frac{\pi}{4} - \sqrt{\frac{1-r}{r}} \sqrt{\frac{R}{h_2}} \ln \frac{h_n}{h_2} + \frac{1}{2} \sqrt{\frac{1-r}{r}} \sqrt{\frac{R}{h_2}} \ln \left(\frac{1}{1-r} \right) \right] \quad (3.23)$$

According to Sims, Q_p in Eq. 3.23 provides the contribution due to friction and the inhomogeneity of deformation.

Finally, the specific roll torque may be calculated from the following equation:

$$G = 2 R^2 \int_0^a s \phi d\phi \quad (3.24)$$

3.3.4. Effect of Friction

Although Sims pointed out that the geometrical factor Q_p includes the contribution of the inhomogeneity of deformation as well as that of friction, his solution must be regarded as an approximation, especially when the friction coefficient changes during rolling. Sparling [71] reviewed the various methods available to determine this coefficient and concluded that there is no reliable method that can be used for this purpose. However, he was able to estimate the friction coefficient during hot rolling as varying from 0.23 for highly scaled material between smooth rolls to 0.38 when the material is scale free between rough rolls. Regarding the effect of varying the coefficient of friction on the rolling load, El-Kalay and Sparling [72] found that changes in the roll separating force of up to 44% occurred when the degree of scaling and the roll roughness were changed.

3.4. SIMPLIFIED EMPIRICAL-ANALYTICAL EQUATIONS FOR CALCULATION OF THE DEFORMATION RESISTANCE

In order to satisfy demands for high accuracy and efficient rolling, it is necessary to develop accurate mathematical models of the roll force. The reliability of such a mathematical model is important with respect to decisions regarding the mill configuration. Several models have been established; these can be separated into four categories : table "look-up" methods, empirical formulae, formulae derived from empirical modifications to existing theories, and formulae based on physical principles. Very little published data are available regarding the numerical accuracy of these models. However, there

seems to be agreement that the empirical models are the most accurate and the easiest to implement on-line.

Since the predominant term in the roll force is the deformation resistance, the latter must be predicted with sufficient accuracy. The deformation resistance is affected by many factors, such as temperature, accumulated strain and strain rate. At high temperatures, microstructural changes have strong effects on the resistance to hot deformation. Thus, in order to control the microstructure and to predict the roll force with accuracy, the effect of the microstructural changes on the deformation resistance must be accounted for. However, these factors are not completely understood in the case of plate and particularly strip rolling, and considerable further investigation into proper mathematical models is therefore required.

Most current models calculate the deformation resistance or the rolling force taking into account only the mean strain, strain rate, and temperature, and not the deformation history. The measured and calculated values differ mainly on the last stands of the mill. To achieve better accuracy, it is necessary to describe precisely the stress/strain behavior and to involve the influence of the restoration processes on the flow stress of the material in the mathematical model [73].

The mathematical model must consist of two different parts [74] :

- i) The fundamental equations which describe the behavior of the workpiece in the roll gap. This must include models of deformation resistance as a function of temperature, strain and strain rate, and composition; models of heat transfer via radiation, convection and conduction, and models relating laboratory experiments to rolling theory,
- ii) Equations describing the progress of static restoration during the interpass interval.

A comprehensive model for hot mills should therefore include algorithms to describe: the rolling load, the evolution of temperature in the rolled material,

the progress of restoration, and the evolution of the metallurgical properties. To accomplish these objectives, the computer model should be universal (can be applied to the maximum number of existing mills), accurate in simulation and in extrapolation, use the minimum number of empirical coefficients, and be verifiable and applicable to typical rolling mill configurations using standard test equipment.

In the roll gap, equations describing the stress/strain behavior can be used to compute the deformation resistance. Most of the equations describing flow curves are empirical in nature, however, and not based on any theoretical approach. The Hollomon equation is widely used to approximate the plastic behavior of materials [75]. It is a simple power law of the form $\sigma = K_H \epsilon_p^{n_H}$, where σ is the true stress, ϵ_p is the true plastic strain, K_H the strength coefficient and n_H the strain hardening coefficient. This equation is easy to use and is sufficiently accurate to represent the stress/strain curve at small strains. A disadvantage of the Hollomon equation is that the flow stress is zero at zero plastic strain, which is not realistic.

Other empirical equations for the stress/strain curve, such as those of Ludwik [76], Swift [77] and Voce [78] have been suggested. However, these models are not popular in practice because they need non-linear fitting techniques.

With regard to the effect of restoration between passes on the deformation resistance, an interesting mathematical model of the softening process based on physical assumptions was proposed recently by Saito et al. [74] and applied with success in the Japanese rolling industry. The differential equation of deformation during the restoration is given by:

$$\frac{d\epsilon}{dt} = -f(\epsilon) g(T) \quad (3.25)$$

where $g(T)$ is an Arrhenius type function ($\exp(Q/RT)$). By assuming that $f(\epsilon)$ is approximated by a second order polynomial, and by integrating directly, they obtained a hyperbolic equation for ϵ . The final equation is:

$$\frac{\Delta \epsilon}{\epsilon} = \frac{C_1}{(C_2 \epsilon_1 + C_1) \exp(C_2 t \exp(-Q/RT)) - C_2 \epsilon_1} \quad (3.26)$$

where $\Delta \epsilon$ is the strain accumulated by the first deformation, ϵ_1 is the prestrain and t is the interruption time. The coefficients C_1 , C_2 and Q were determined by regression analysis, using data from two-stage tensile tests with t varying between 1 and 300s, prestrains of 0.05 to 0.3, and deformation temperatures of 800 to 1000°C. The strain rate was 8 s^{-1} .

This model has a theoretical basis and is very simple (Fig. 3.4). However, it takes into account only the effect of recovery even though, in the temperature range used, partial recrystallization can occur and modify the structure and therefore the flow stress.

3.5. SUMMARY

In the light of the literature review presented in this chapter, it can be concluded that the problem of predicting thermomechanical history during hot rolling is far from completely solved. Considerable work is needed to describe the flow behavior of steels at high temperatures and to investigate the associated metallurgical changes. This will lead to the accurate control of both the gauge and the microstructure. It is only by linking computer modelling with laboratory experiments, and eventually plant trials, that these goals can be achieved. The experimental and numerical methods used in this study will be described in the next two chapters.

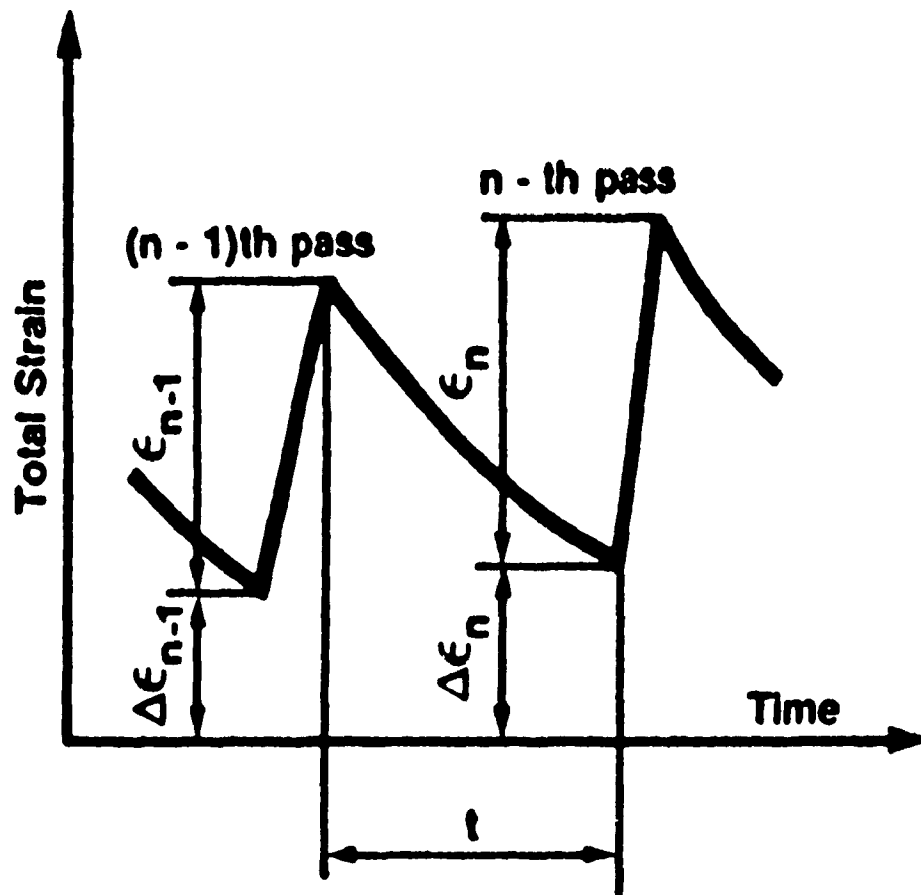


Figure 3.4 Illustration of softening by recovery [74].

Chapter FOUR

EXPERIMENTAL MATERIALS AND METHODS

4.1. INTRODUCTION

The literature review presented in Chapters Two and Three has described the theoretical concepts used to study the thermomechanical and structural changes taking place during hot deformation. However, to deal with complicated events such as hot rolling operations, it is necessary to have a set of "concrete" relationships for the high temperature flow stresses of steels, as well as constants for the equations associated with the microstructural changes. A series of laboratory hot compression tests was therefore carried out to determine these parameters. Some experimental rolling schedules were also simulated, either to test the predictive capabilities of the temperature, deformation resistance and microstructural models developed, or for the production of a new generation of tough high strength steels, destined for low temperature applications.

The procedure and equipment used for these experiments are described in this chapter.

4.2. EXPERIMENTAL MATERIALS

To study the high temperature flow and recrystallization behavior, four low carbon steels were used. The chemical compositions of these grades are shown in Table 4.1. These steels were cast and hot rolled to plates of 12 mm final thickness at the Metals Technology Laboratories (MTL) of Energy, Mines and Resources in Ottawa.

Table 4.1 Chemical compositions of the experimental steels.

wt% →	C	Mn	Si	P	S	Ti	Nb	B	Al	Cu	N	C _{EQ} ^{*1)}	P _{CM} ^{*2)}
Steel →													
Base	0.03	1.54	0.19	0.008	0.005	0.02	---	---	0.020	---	0.0048	0.287	0.113
Nb	0.026	1.42	0.16	0.007	0.007	0.02	0.055	---	0.020	---	0.0063	0.263	0.102
Nb-B	0.026	1.56	0.15	0.007	0.007	0.02	0.055	0.003	0.025	---	0.0064	0.286	0.124
Cu-Nb-B	0.026	1.38	0.18	0.007	0.006	0.017	0.058	0.003	0.019	2.03	0.0060	0.391	0.217

$$*1) C_{EQ} = C + Mn/6 + (Ni + Cu)/15 + (Cr + Mo + V)/5$$

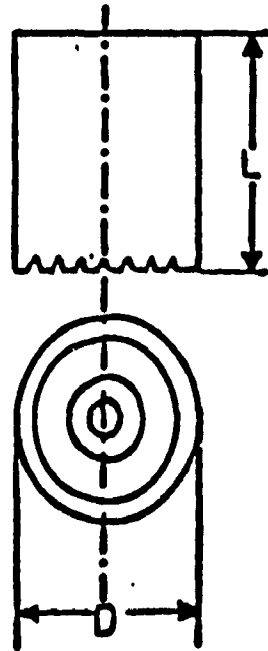
$$*2) P_{CM} = C + (Mn + Cu + Cr)/20 + Si/30 + V/10 + Mo/15 + Ni/60 + 5B$$

The first steel in Table 4.1 was selected as a reference steel. The low carbon content in the other materials is typical of high toughness weldable steels. For two reasons, considerable caution was exercised to lower the nitrogen level and to satisfy the relation $\%Ti - 3.4\%N \geq 0$. The first is the great stability of TiN, which enables it to act as a grain growth inhibitor at high preheating temperatures [37]. The second is to prevent boron nitride formation (in the boron-containing steels), since titanium has a stronger affinity for nitrogen than boron. In this way, the hardening effect of boron is ensured [79]. The relatively high concentration of copper was added to investigate possible solute effects on the flow stress and on the austenite recrystallization kinetics. Also, the high precipitation strengthening potential of copper at lower temperatures is an advantage of such compositions because of its beneficial effect on the final mechanical properties in terms of strength and toughness, both in the base plate and in the heat affected zone (HAZ) [80].

4.3. SPECIMEN PREPARATION AND DIMENSIONS

Two types of specimen were used in this work, depending on the equipment employed. In the case of low strain rates ($\dot{\epsilon} \leq 2 \text{ s}^{-1}$), small cylindrical compression specimens were machined out of the as-received hot rolled plates, with the deformation axis parallel to the rolling direction. A height-to-diameter ratio of 1.5 was selected to ensure homogeneous deformation [81]. Care was exercised to minimize friction between the compression anvils and the specimen surface by machining flat-bottomed grooves on the end faces of the samples, as shown in Fig. 4.1. These grooves are effective for reducing the friction and the associated barreling by retaining the glass lubricant during deformation [82, 83]. A powdered glass lubricant manufactured by the Corning Glass Co. Ltd., of 10^4 poise viscosity has been shown to be suitable for such experiments [84] and was used in the present study.

In the case of the higher strain rates, a second type of specimen was used. An example is shown in Fig. 4.2. The shape of compression specimen known as Rastegav's design is also effective for reducing barreling when a high cumulative deformation is applied [85]. A boron nitride lubricant was used to



Specimen Dimensions (mm)		
size	Length (L)	Diameter (D)
1	11.9	7.9

Groove Dimensions (mm)				
size	A	B	C	E
1	0.18	0.15	0.36	0.10

Tolerance	0.02
-----------	------

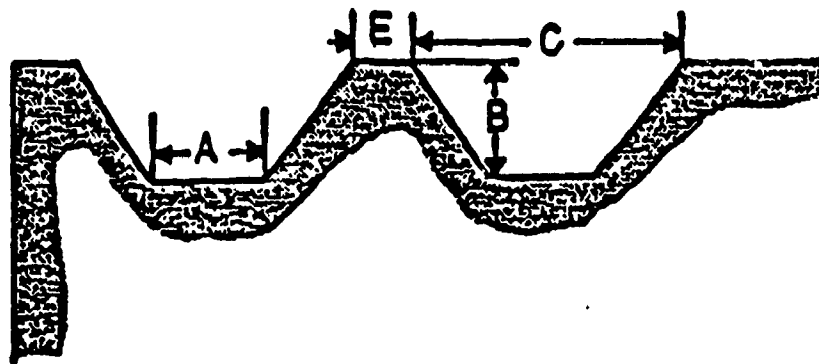


Figure 4.1 MTS compression test sample geometry and groove design [81].

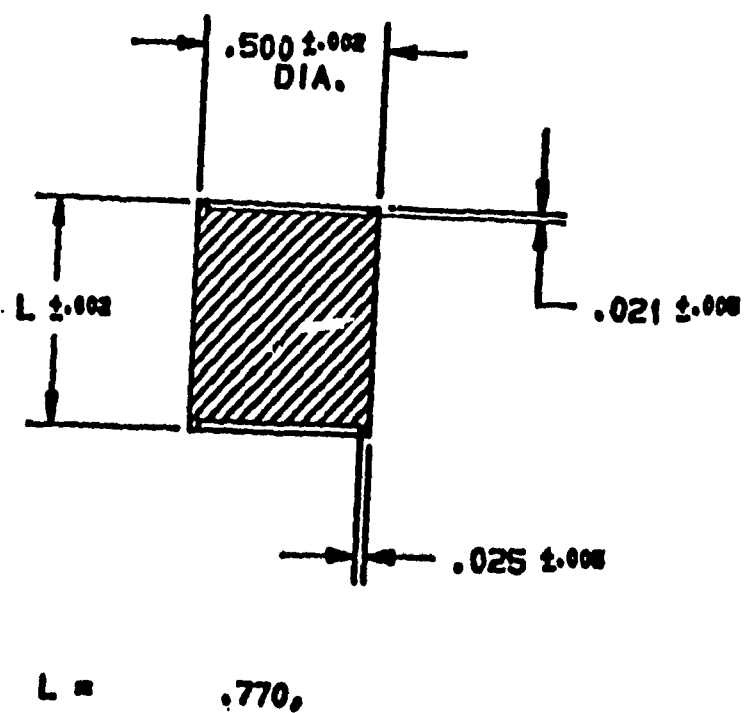


Figure 4.2 Cam plastometer compression test sample geometry.

reduce friction between the tools and the sample, especially during the two hit tests, where the total deformation is large [86].

4.4. SOLUTION TREATMENT

Immediately before testing, the specimens were solution treated at a given temperature. The first objective of selecting these temperatures is to cover the range of soaking temperatures used in practical hot forming operations. In this case, it is necessary to estimate the amount of niobium in solution at each reheating temperature. To be effective during finishing, the niobium carbonitrides should be dissolved in the austenite during reheating prior to deformation. In this way, the maximum of precipitation occurs at lower temperatures which can result in a considerable improvement in the strength and toughness [40, 87]. The second objective, which is no less important, is to produce approximately the same starting grain structure when the flow behavior of two steels deformed at high temperatures is to be compared. Finally, the highest solution temperature is controlled by the grain coarsening temperature; a reheating temperature higher than the GCT produces mixed grain structures because of abnormal grain growth.

4.4.1. Solubility Product for Nb(C,N)

Several equations exist in the literature concerning the solubility product of NbC in austenite [88-90]. These equations are of the type:

$$\log_{10}[\%C^x.\%Nb]=a-\frac{b}{T} \quad (4.1)$$

where x , a and b are empirical constants varying from one author to another, and T is the absolute temperature. The range of error introduced by such equations must be taken into account and can be overcome by overestimating the reheating temperature if the maximum amount of niobium in solution is desired.

For the first purpose, the following equation was used [91]:

$$\log_{10}[\%C.\%Nb]=2.96-\frac{7510}{T} \quad (4.2)$$

Eq. 4.2 leads to a solution temperature around 1020 °C for the three steels. Irvine et al. [92] have proposed the following equation, where the nitrogen level is introduced:

$$\log_{10}\left[\left(\%C+\frac{12}{14}\%N\right).\%Nb\right]=2.26-\frac{6770}{T} \quad (4.3)$$

Fig. 4.3 shows the equilibrium solubility of Nb for the three steels studied, estimated from the last two equations. It is evident that even if the nitrogen level is low, the solubility of niobium is lower when the nitrogen level is taken into account together with the carbon, leading to complete solution at a temperature around 1074 °C. In this study, the niobium carbonitride particles were considered to be in solution when a reheating temperature of 1100 °C or higher was used. Finally, due to the low level of Ti, titanium carbides are also considered to be in solution at that temperature [93].

4.4.2. Reheated Austenite Grain Size

A series of Cu-Nb-B steels was austenitized for different times and temperatures, and then quenched into water. The grain size was measured by means of optical microscopy, using the intercept method, on at least ten fields at several magnifications. A typical set of microphotographs is shown in Fig. 4.4 for the Nb-B and Cu-Nb-B steels and the temperature dependence of the mean grain size is depicted in Fig. 4.5. Data for a Nb-B steel taken from reference [94] are also included. It is interesting to note here that the copper steel exhibits a finer austenite grain size in the range of temperatures shown. It is difficult to state whether copper is responsible for this decrease. The most probable reason is that the level of titanium is slightly lower in the Cu-bearing steel. Thus, as the effectiveness in controlling the grain size at high temperatures is dictated more by the volume fraction of the fine TiN particles formed after solidification than by the amount of titanium available [37, 93], the lower Ti level may be

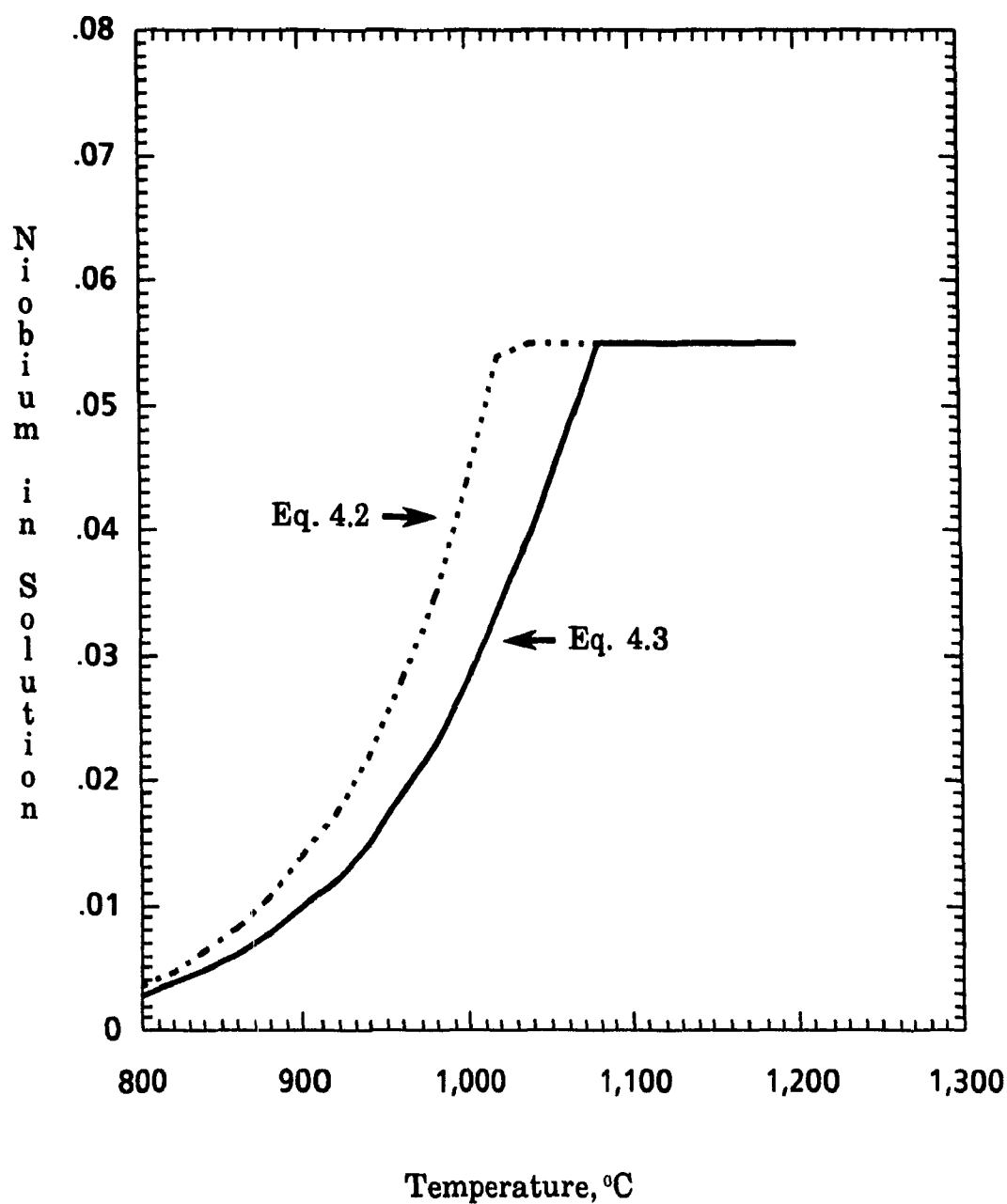


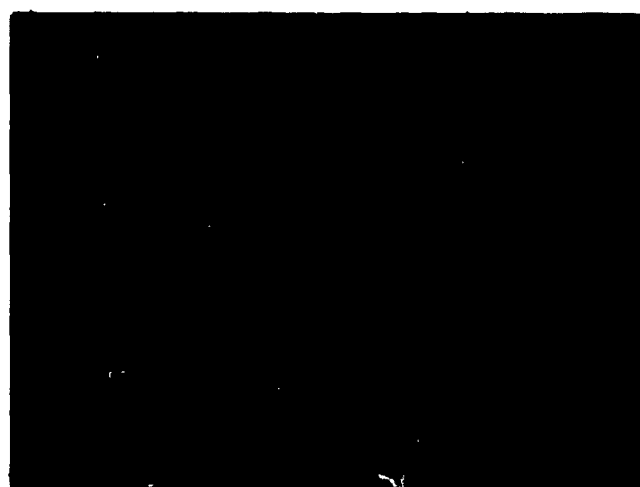
Figure 4.3. Dissolved niobium as a function of temperature for the Nb steels.



Nb-B
RT = 1100°C



Cu-Nb-B
RT = 1100°C



Cu-Nb-B
RT = 1200°C

Figure 4.4 Microstructures of the reheated samples prior to testing.
Magnification 400X.

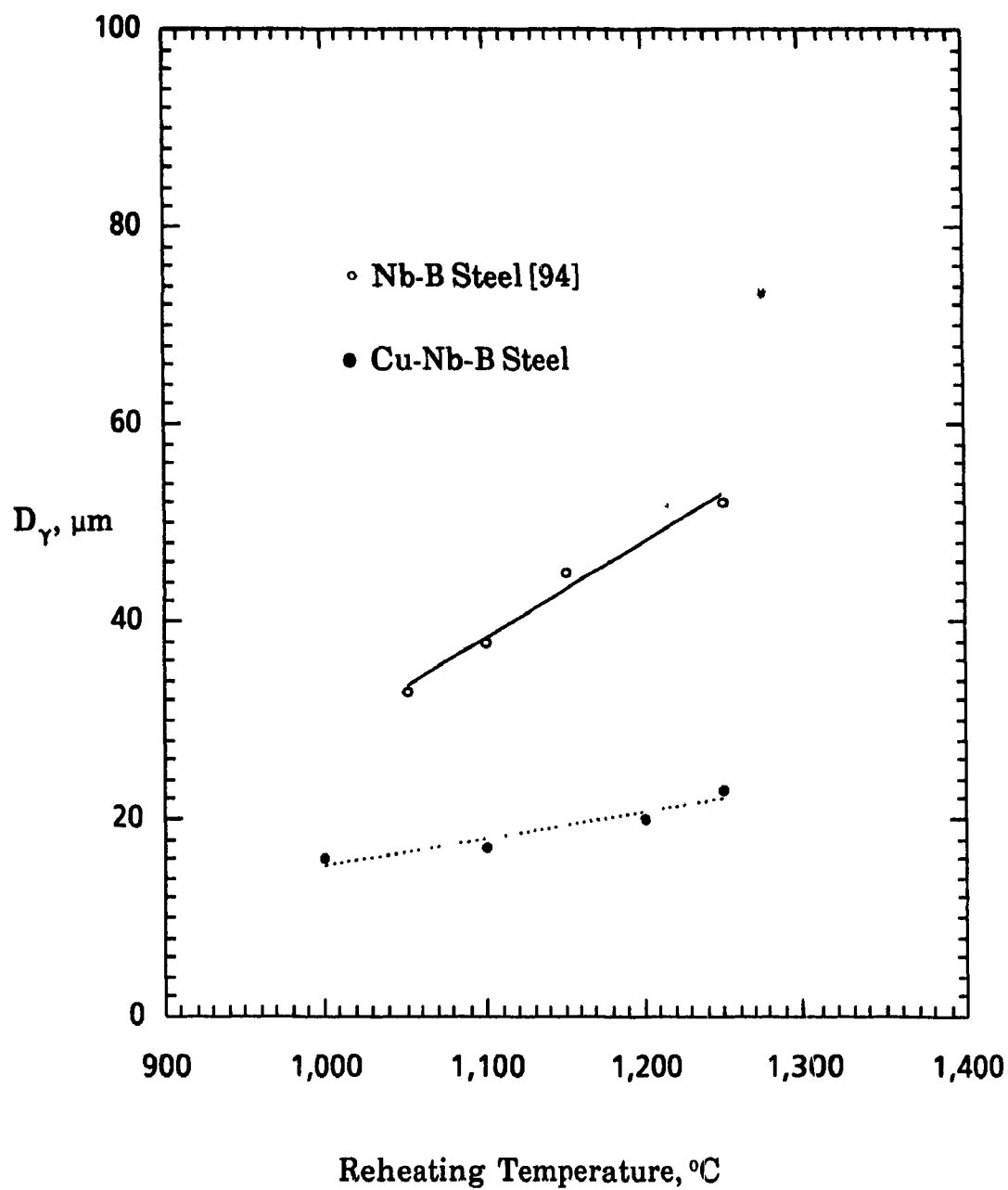


Figure 4.5. Dependence of austenite grain size on reheating temperature in the boron-containing steels.

responsible. Alternatively, copper in solution may be contributing a solute drag effect.

Finally, it is worth noting that the reheating temperatures studied in the case of the B-containing steels are lower than the grain coarsening temperature.

4.5. HOT COMPRESSION TESTING

4.5.1. Experimental Equipment

The hot compression tests were conducted on a McGill computerized servohydraulic MTS machine for strain rates lower than 2 s^{-1} , and on a cam plastometer at MTL in Ottawa for the higher strain rates.

4.5.1.1. MTS Automated Testing System

The MTS machine is a 100 kN closed loop unit capable of a maximum strain rate of 2 s^{-1} . Although a detailed description of this machine is given in reference [93], some important features and units will be described here.

The control sequences are monitored by a computer/433 subsystem which can perform the commands of function generation, data acquisition and real time decision making. This subsystem is a Digital Equipment PDP-11/04 minicomputer with a memory of 32 K in 16 bit words. It also includes a Tektronix graphics terminal, a 433 processor interface unit, a DEC RX01 disk system and a Tektronix hard copy unit (Fig. 4.6). The software used is MTS-BASIC /RT-11, which consists of a package of real time routines taking the form of external functions [95, 96].

The high temperature compression tests were carried out in a CENTORR model M60 front loading high temperature high vacuum furnace. The tested specimen is compressed between two tungsten anvils inside the chamber. After a vacuum of around 10^{-5} torr has been reached, the heating system, which consists of tungsten mesh resistances, can be started (Fig. 4.7).



Figure 4.6 View of the high temperature computerized MTS compression testing equipment.



Figure 4.7 View of the CENTORR high temperature furnace.

4.5.1.2. Cam Plastometer

The cam plastometer is a 0.45 MN high speed compression testing machine capable of simulating high strain rate deformation processing such as the hot rolling of plates and strips. The operating range of strain rate is between 0.5 and 150 s⁻¹ and schedules of up to four hits can be performed on the same sample (Fig. 4.8). In Fig. 4.9, a simplified design of the main components of the machine is shown†. For a deformation to occur, the pressurized piston (G) inserts the cam follower (I) between the cam lobe and the transfer block (J), and retracts it after exactly one revolution of the cam (H). During the test, the analog signal of the load transmitted to the strain gauge load cell is recorded continuously using a BAM (bridge amplifier meter). A Biomation transient recorder converts the analog signal to digital and stores the data. The displacement of the lower die (K) is given by a linear variable differential transducer (LVDT). A Minc PDP 11/23 microcomputer is used to monitor the automatic operations and to perform data acquisition by means of software written in Fortran. A detailed description of the design and operation of the cam plastometer can be found in references [86], [97] and [98].

To heat the sample to the desired testing temperature, a Lindberg induction heating unit was used and the control of heating and cooling was performed manually.

4.5.2. Continuous Tests

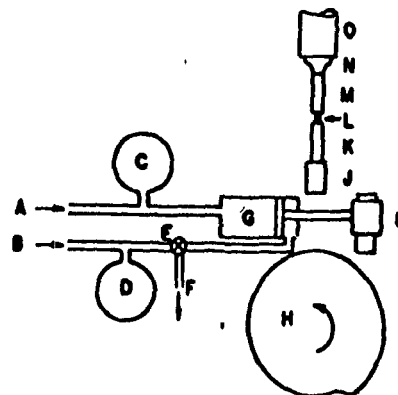
4.5.2.1. Stress/Strain Experiments

Single hit tests were carried out at a variety of temperatures and strain rates using the computer programs described above. Prior to testing, the specimens were austenitized for 10 to 15 minutes at a specific reheating temperature, cooled to the deformation temperature, held for 60 to 90 seconds to

† The cam shown in Fig. 4.9a is designed for one hit deformation.



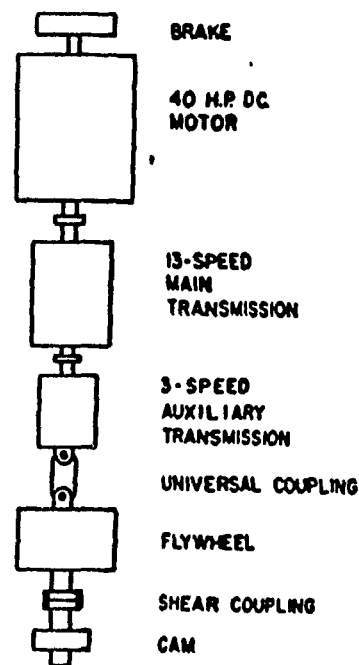
Figure 4.8 View of the cam plastometer machine used for high strain rate testing.



a)

A- LOW PRESSURE IN
B- HIGH PRESSURE IN
C- SURGE TANK
D- SURGE TANK
E- SOLENOID VALVE
F- EXHAUST
G- CYLINDER

H- CAM
I- CAM FOLLOWER
J- TRANSFER BLOCK
K- LOWER DIE
L- SPECIMEN
M- UPPER DIE
N- LOAD CELL
O- PRESS SCREW



b)

Figure 4.9 Schematic of:

- a) the cam follower insertion mechanism
b) the plastometer drive train [97].

eliminate thermal gradients, and finally deformed at a constant true strain rate; this was followed by water quenching in the case of the cam plastometer (Fig. 4.10a).

When the specimen was cooled from the reheating temperature to the deformation temperature by turning off the furnace, the cooling rate was dependent on the testing temperature. Fig. 4.11 shows that for the CENTORR furnace, the mean cooling rate decreases from 2°C/s at high temperatures, to approximately 1 °C/s below 900 °C. Similar cooling rates were attained in the induction furnace used in the cam plastometer.

Care was taken when the specimen was held at the testing temperature to allow the latter to stabilize. The total time of holding was not allowed to exceed 90 seconds at the lower temperatures where static precipitation can occur prior to deformation. As shown by Jonas and Weiss [28], the nose of the PTT diagram for undeformed Nb steels at 900 °C can correspond to times as short as 90 seconds.

During deformation, the temperature of the specimen was continuously monitored by a K-type Chromel-Alumel thermocouple attached to the specimen surface†. A few millimeters away from the sample, a second thermocouple was used as a reference to detect any abnormal reading. During normal operations, a constant temperature difference between the two thermocouple readings was maintained after the temperature had stabilized. Nevertheless, the two cooling rates are different because of the difference in the heat capacities of the specimen and the furnace [93].

Prior to starting a set of experiments, the testing system was calibrated for the desired deformation conditions by carrying out several initial tests. Special attention was given to the calibration of temperature. Dummy tests were repeated until the conditions of the previous set of tests were reproduced.

† During cam plastometer testing, the temperature was monitored using a 304 stainless steel sheathed Chromel-Alumel thermocouple inserted at the mid-height of the specimen to half its radius.

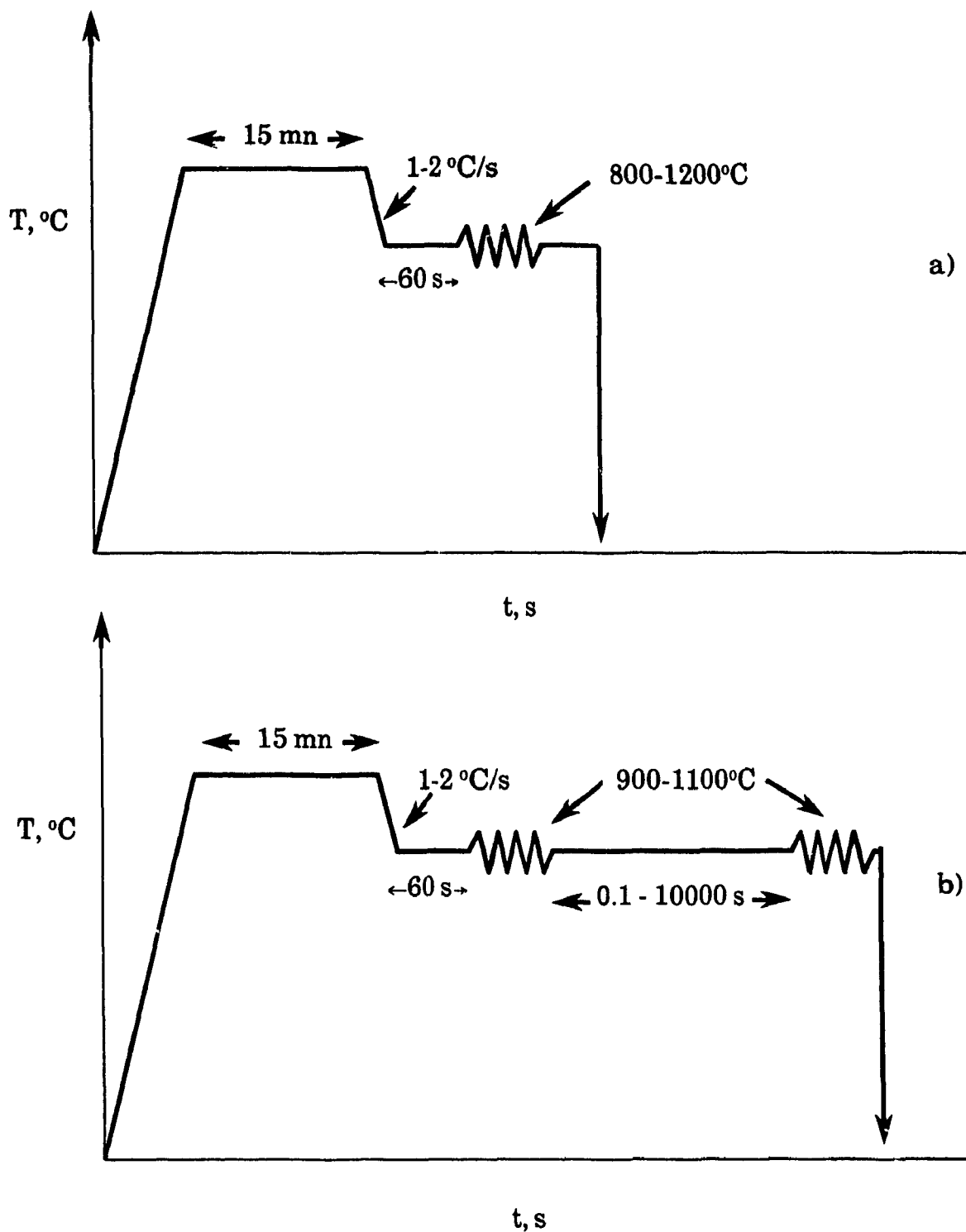


Figure 4.10 Schematic representation of the method used during:

a) single hit tests

b) double hit tests.

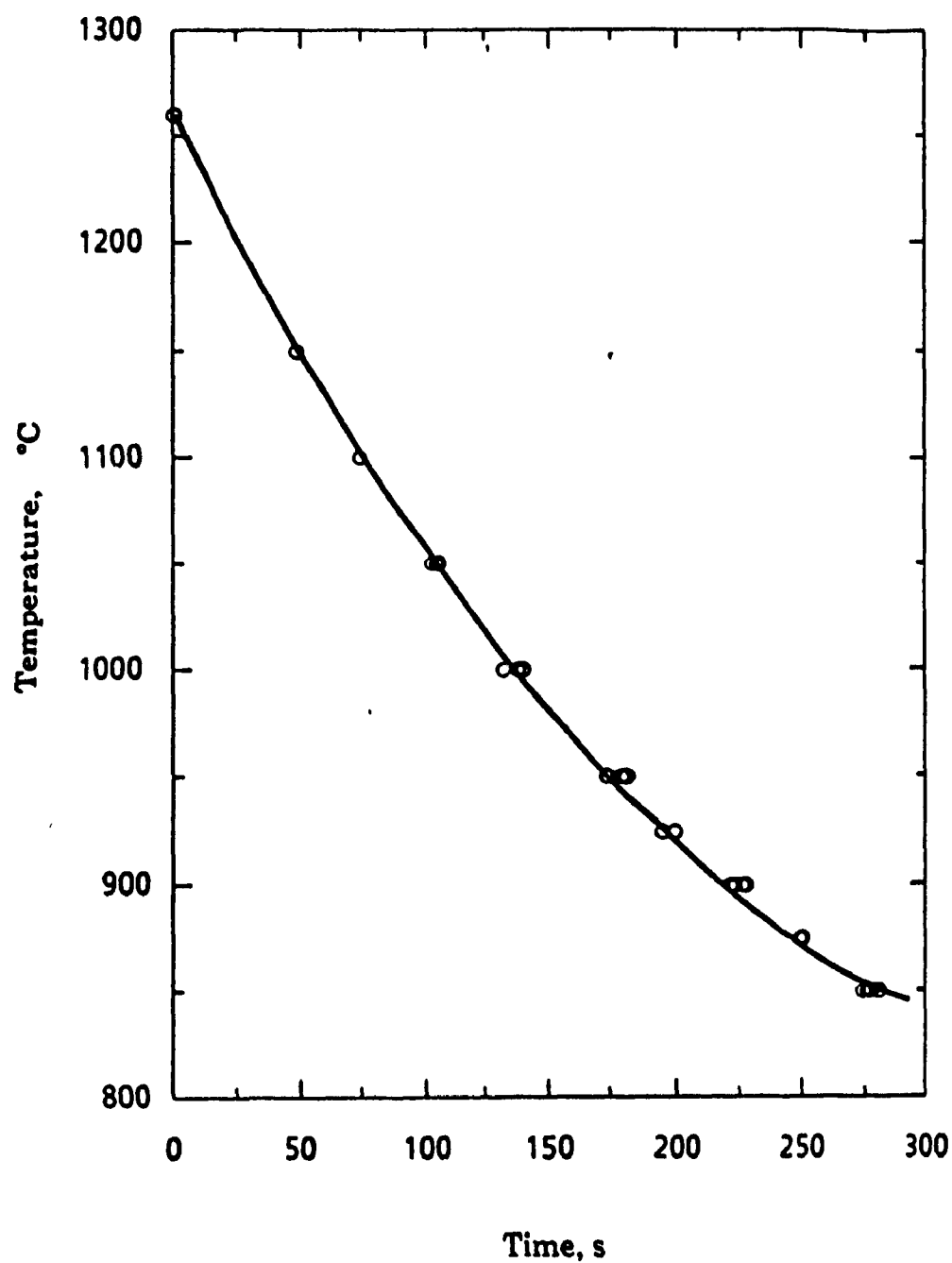


Figure 4.11 Dependence of the maximum cooling rate on testing temperature when the CENTORR furnace is turned off [93].

4.5.2.2. Strain Rate Control

In standard tensile or compression testing, the deformation speed is kept constant and the true strain rate decreases or increases, respectively, during deformation. For a strain of one, the true strain rate can decrease or increase by a factor of 2.3 during deformation [99]. To conduct monotonic compression tests at different rates, the true strain rate must be kept constant during the entire test. For this reason, the deformation speed must vary with the height of the sample, as described below:

$$\varepsilon = -\ln\left(\frac{h_o}{h}\right). \quad (4.4)$$

by differentiation

$$\dot{\varepsilon} = -\frac{1}{h} \cdot \frac{dh}{dt} \quad (4.5)$$

if $\dot{\varepsilon}$ takes a constant value $\dot{\varepsilon}_c$, the change in height is given by:

$$\Delta h = h_o [1 - \exp(-\dot{\varepsilon}_c t)] \quad (4.6)$$

where h_o is the initial sample height. In the case of the MTS servohydraulic machine, Eq. 4.6 can be discretized by dividing the deformation time into small steps Δt ; the anvil displacement can then be controlled according to this equation. In the case of the cam plastometer, the cam profile is designed so that the strain rate is kept constant during deformation [98].

4.5.2.3. Data Treatment

During each test, the output of the load cell and the displacement given by the LVDT were converted into true stress and true strain, respectively, using the following relations:

$$\sigma = \frac{P}{A} = \frac{P}{A_o (h_o/h)} \quad (4.7)$$

$$\epsilon = \ln\left(\frac{h}{h_0}\right) \quad (4.8)$$

where σ is the true stress, ϵ is the true strain, P is the recorded load, and h and A are the instantaneous height and area, respectively. The analog signals of load and displacement were converted to digital data using an analog-digital converter and stored in the memory as blocks to save space. Since the core memory of the minicomputer is limited, the stored data in the data acquisition system were converted into text. Then, a special software called KERMET was used to convert the data from text in the RT-11 operating system to ASCII. This was stored using a specific format in an IBM PC for further calculations. Corrections for the compliance of the machine and the temperature were then conducted and are described below.

4.5.2.4. Correction for Elastic Distortion†

The data obtained after the computerized compression test consists of the signal outputs (voltage) from the LVDT and load cell, and the time for each reading. When the specimen is strained in the test apparatus, the load is transmitted to the entire system, which consists mainly of the loading frame, the tungsten compression tools, the stainless steel extension rods, the load cell and the actuator (Fig. 4.12). Since it was not possible to measure the actual displacement of the ram relative to the lower anvil, the displacement readings were corrected for the machine compliance. This is necessary because the elastic strain of steels deformed at high temperatures is small (of the order of 10^{-3} if the Young's modulus is assumed to be around 100 GPa) and the apparent elastic deformation displayed at the beginning of each stress/strain curve is actually due to the elastic deformation of the machine.

† No corrections of this type were made for the data from the cam plastometer because the elastic deformation of the machine was taken into account during the design of the cam [98].

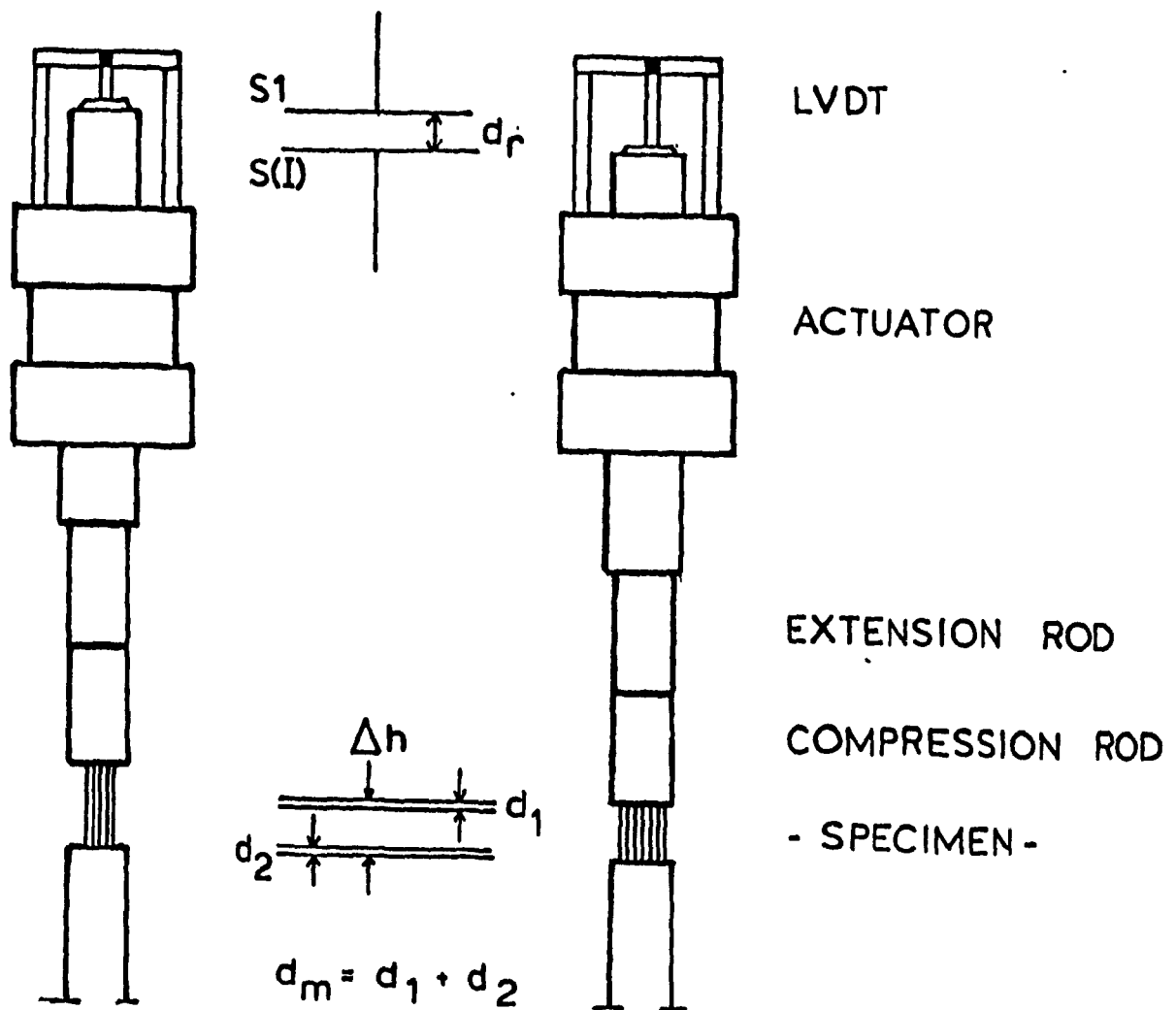


Figure 4.12 Determination of the actual height of a deformed specimen in the MTS machine [96].

Previous measurements have shown that for a range of deformation speeds and temperatures, the elastic distortion of the machine is independent of these two variables [100]. In such a case, the collected data were fitted by the following expression:

$$d_m = a(P + b)^c - d \quad (4.9)$$

where P is the instantaneous load, and a , b , c and d are constants.

Since the ram displacement d_r is the sum of the instantaneous change in height of the specimen Δh and the elastic distortion due to the machine, the instantaneous height of the specimen is given by :

$$h_i = h_o - d_r + d_m \quad (4.10)$$

d_m was determined for the MTS machine used for the present work by loading the system in the absence of a specimen, and collecting the displacement values for given loads [96]. The data in Fig. 4.13 show a linear dependence of the displacement on load, which is consistent with the elastic behavior of the machine. In this work, when stress/strain data are used in calculations, they have always been submitted to this correction. This results in a shift of the stress/strain curve to the left.

4.5.2.5. Correction for Temperature

At high strain rates, the temperature rise due to deformation was estimated from the adiabatic stress/strain curves. The corresponding stress decrease was calculated at each strain increment by the following expression:

$$\delta\sigma = \left[\frac{\partial\sigma}{\partial(1/T)} \right]_{\epsilon, \dot{\epsilon}} \delta(1/T) \quad (4.11)$$

and the isothermal stress/strain curves were reconstituted by adding the $\delta\sigma$'s to the adiabatic stresses. Details of the method of correction for adiabatic heating will be given in the next chapter.

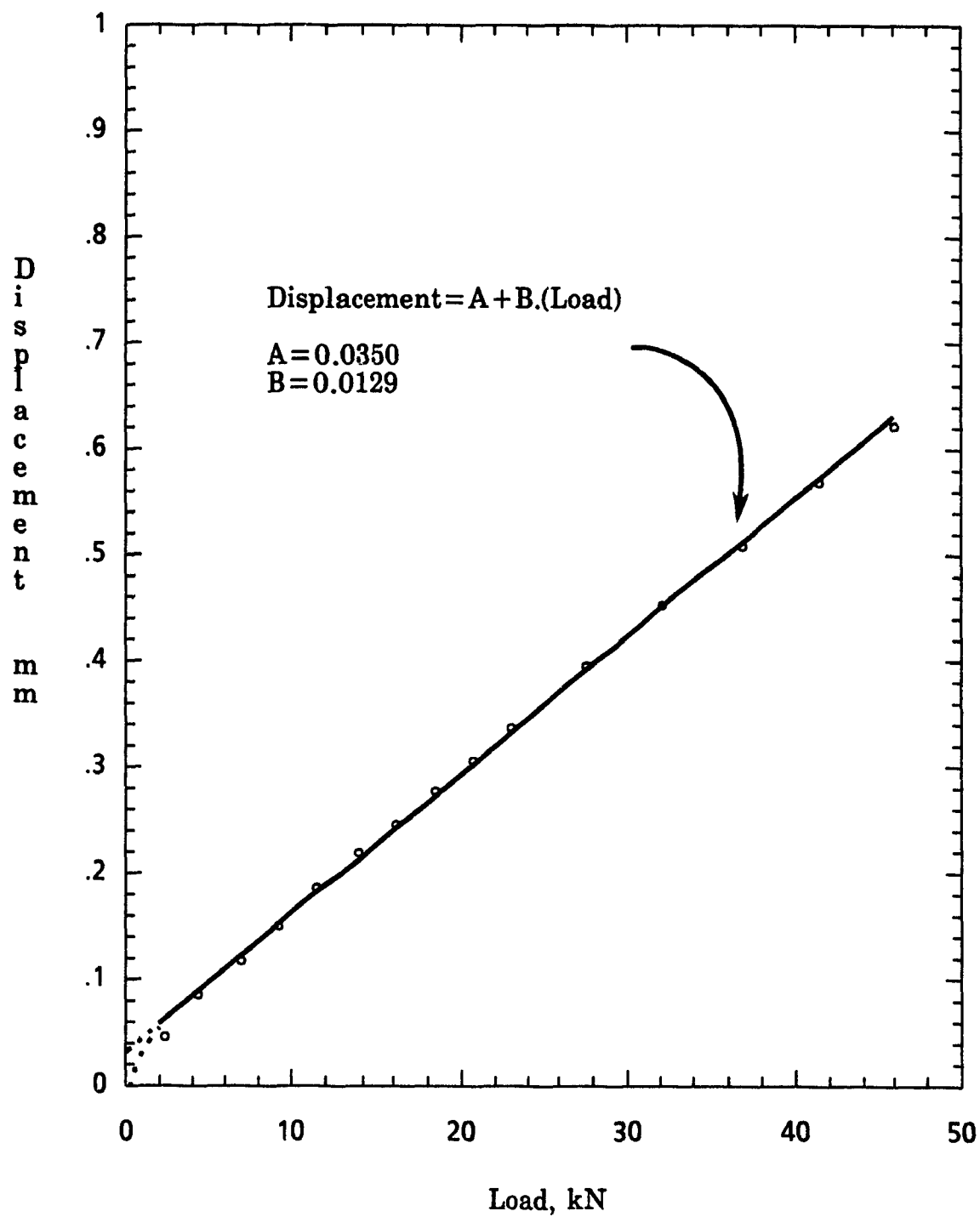


Figure 4.13 Elastic distortion of the MTS testing system.
(Data are from ref. [96])

4.5.3. Interrupted Tests

To follow the recrystallization kinetics of the steels at high temperatures, the technique of interrupted compression was employed. This technique was first developed by Wilber et al. [101] using a Gleeble machine and further by Petković [100]. It was later applied to measure static softening by several investigators [11, 15, 19, 23, 102-105].

In the interrupted compression technique, after being reheated to a given temperature and cooled to the deformation temperature, the specimen is prestrained at a constant strain rate, unloaded and held for increasing times. After the interruption, the specimen is reloaded at the same strain rate and temperature (Fig. 4.10b). A typical example of the data output immediately after an interrupted test is shown in Fig. 4.14.

Finally, Table 4.2 gives a summary of the experimental conditions for both continuous and interrupted tests.

Table 4.2 Range of experimental conditions.

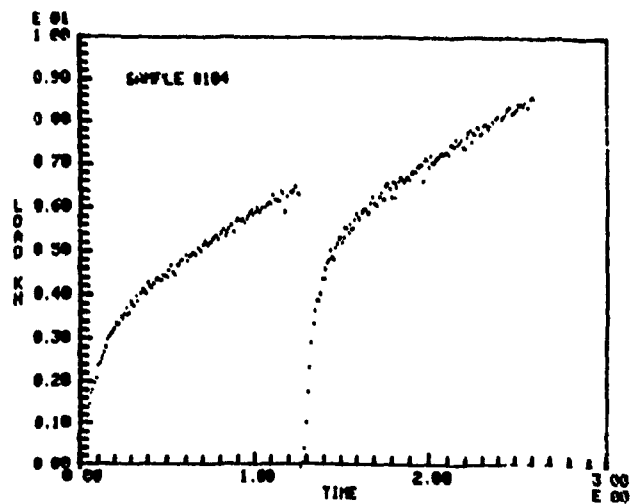
	Single Hit Tests	Two Hit Tests
RT (°C)	1100, 1200	1000-1200
DT (°C)	800- 1200	900- 1100
ϵ	Up to 1	0.12, 0.25, 0.5
$\dot{\epsilon}$ (s ⁻¹)	0.2, 2, 10*, 50*	0.2, 2, 10*, 50*
Hold t (s)	-	0.1-10,000

* cam plastometer tests

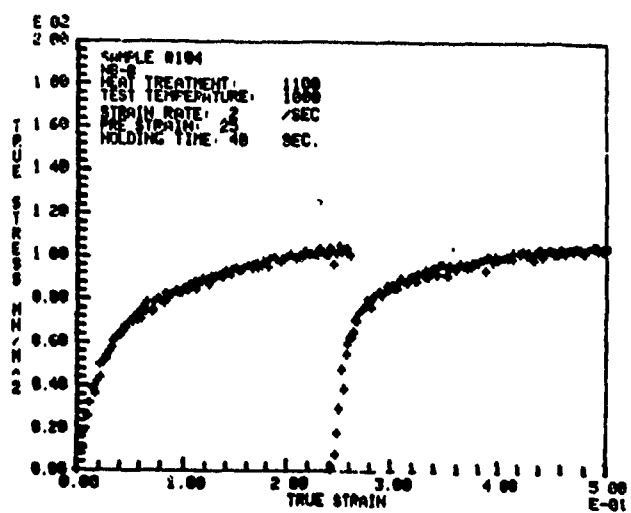
4.6. ROLLING

4.6.1. Rolling Mill

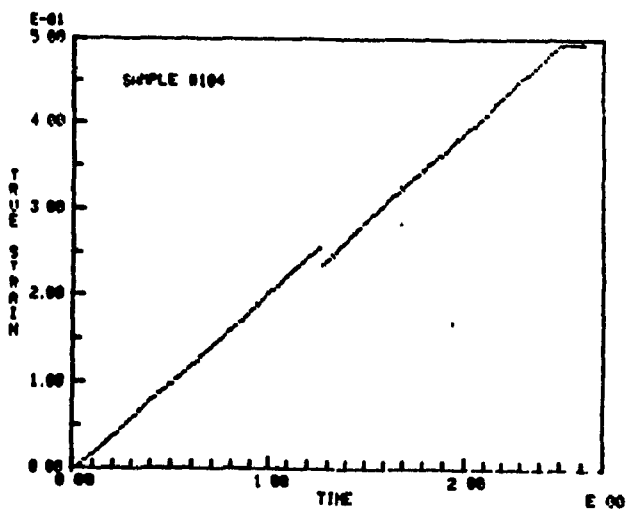
Controlled rolling experiments were carried out on an instrumented single-stand pilot scale rolling mill in its reversible configuration (Fig. 4.15).



a)



b)



c)

Figure 4.14 Typical outputs after MTS interrupted compression testing:

- a) load-time plot
- b) true stress/true strain curve
- c) true strain versus time.



Motor Speed:	150/300/450 rpm
Peripheral Roll Speeds:	0.5/1.0/1.5 m/s
Max. Load Capacity:	4.5MN
Roll Diam., Width:	470, 475 mm
Roll Gap Setting:	0-130 mm

Figure 4.15 MTL pilot-scale rolling mill with its design specifications [106].

The mill is driven by a motor having a capacity of 225 kW and operates at a roll speed of 45 rpm. The design specifications are shown in Fig. 4.15.

4.6.2. Temperature, Rolling Load and Roll Gap Measurements

Recent modernization of the MTL rolling mill permitted the completely automatic acquisition of the temperature, rolling load and roll gap [106]. During rolling, the temperature of the slab was continuously monitored by two thermocouples embedded in the mid-thickness and near the surface in the side of the plate. A detailed time-temperature profile throughout the complete processing and cooling cycle was obtained from the thermocouple readings and recorded on a strip chart recorder. The rolling load was recorded by cylindrical load cells under the roll positioning screws at each side of the stand. The readings correspond to the deformation resistance of the mid-length of the slab being rolled. Automatic digital control of the next pass draft is possible with a preprogrammed pass reduction schedule, using on-line measurement of the roll gap from the rotational positions of the roll positioning screws.

The collected analog d.c. signals of the rolling loads and roll gaps ranged from -5 to +5V d.c. and were converted to digital data and transferred to a DEC PDP 11/23 microcomputer.

4.6.3. Rolling Schedules

Slabs 75 mm thick and 127 mm wide were reheated for one hour in a Lindberg furnace and then taken out of the furnace for controlled rolling. The slabs were reduced to 11.5 mm plates in 9 or 10 passes according to the nominal schedule presented in Table 4. 3. Two reheating temperatures, 1100 and 1250°C, and two finish rolling temperatures, 830 and 750°C, were used, with water quenching being performed immediately after the last pass.

Table 4.3 Rolling schedules used for the Cu-Nb-B steel.

Pass N°	1 st Schedule		2 nd Schedule		3 rd Schedule	
	Setting mm	Temp. °C	Setting mm	Temp. °C	Setting mm	Temp. °C
1	64.5	1230	63	1100	63	1100
2	56.7	1120	51	1000	51	1000
3	49.9	1010	43.8	930	43.8	930
4	42.9	930	36.4	900	36.4	900
5	35.6	900	28.7	885	28.7	885
6	28.1	885	22.4	870	22.4	870
7	21.9	870	18.1	860	18.1	860
8	17.7	860	14.9	840	14.9	840
9	14.5	840	11.6	830	11.6	750
10	11.4	830	-	-	-	-

4.7. MICROSTRUCTURAL STUDIES

4.7.1 Optical Microscopy

Optical microscopy was carried out on both quenched compression and rolling specimens following standard metallographic procedures [107]; i.e. sectioning, mounting, grinding, polishing and etching. The compression samples were cut parallel to the deformation axis and examined in the center, far from the dead zone, while the rolling specimens were cut either parallel or perpendicular to the rolling direction.

Etching the compression samples to reveal the prior austenite grain boundaries was performed using several etchants. The most satisfactory solution consisted of saturated aqueous picric acid with 2 or 3 drops of hydrochloric acid. Etching at 80 °C for 10 to 30 seconds produced satisfactory results. To reveal the final ferritic or bainitic structure in the case of rolling, 2% nital was used.

The average grain size was determined by the standard intercept method of Abrams [108]. The method consists of overlaying three concentric circles of 50 cm total length on the micrographs obtained from different areas of the sample and counting the number of intercepts with the grain boundaries.

4.7.2. Electron Microscopy

For thin foil preparation, slices of 0.3 mm thickness were cut from the material, mechanically thinned, chemically polished in a solution of HF-H₂O-H₂O₂ and finally thinned using a JET thinning instrument (South Bay Technology Model 550B) and a solution of Na₂CrO₄-CH₃COOH [109]. The foils were observed in a JEOL-100 CX scanning transmission electron microscope at 120 kV (see Fig. 4.16).

4.8. MECHANICAL TESTING

To test the mechanical properties of the rolled plates of the Cu-Nb-B steel, both tensile and Charpy V-notch testing were performed.

Specimens of 6.4 mm diameter round bars were used in accordance with ASTM E8. Tests were conducted at CANMET on a 100 kN Instron servo-electric testing machine at a nominal speed of 0.5 mm/mn. Impact tests were performed according to ASTM E23 on standard V-notch specimens (55x10x10 mm). The notch was cut with a broach, especially designed for this purpose, giving a very good surface finish. The tests were then performed on a 360 Joule capacity Tinius Olsen impact tester. The load and energy curves were recorded and analyzed via an ETI 630 data acquisition and analysis system. To cool the specimens prior to testing, a bath of alcohol cooled by liquid nitrogen was used and maintained within 0.5°C of the desired temperature. For the transition temperature, the 27 Joule criterion was used.

4.9. SUMMARY

In the previous sections, the experimental procedures used during the present work were described. A simple schematic summary of these methods is

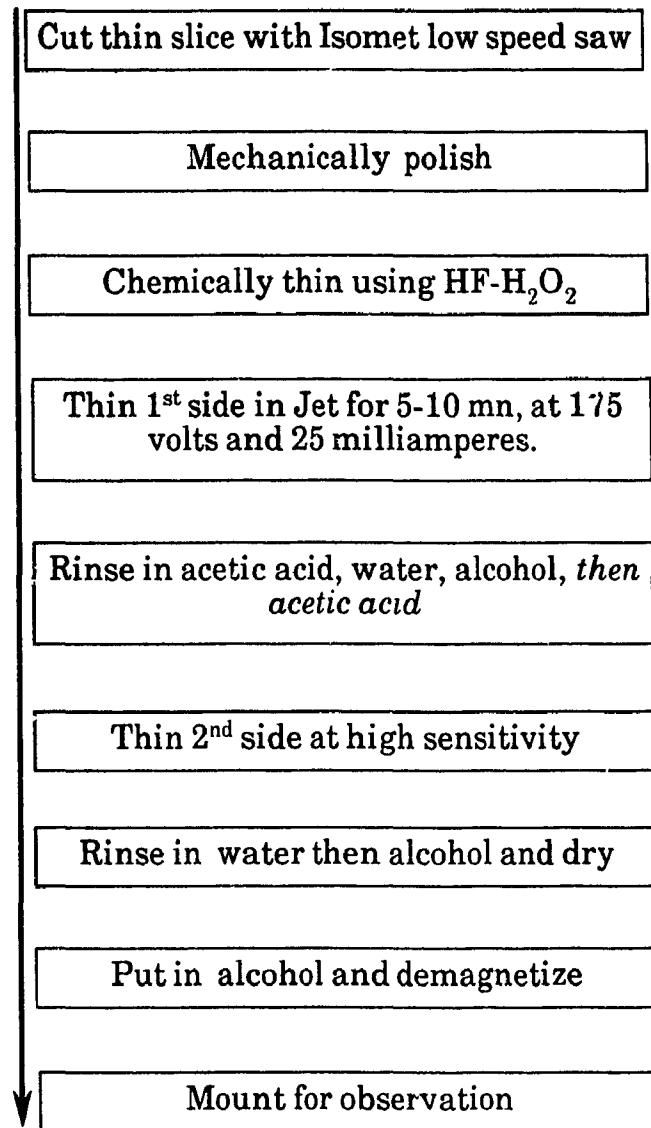


Figure 4.16 Method for thin foil preparation.

given in Fig. 4.17, together with the relationships existing between them. The numerical techniques employed to analyze the experimental data will be presented in the next chapter.

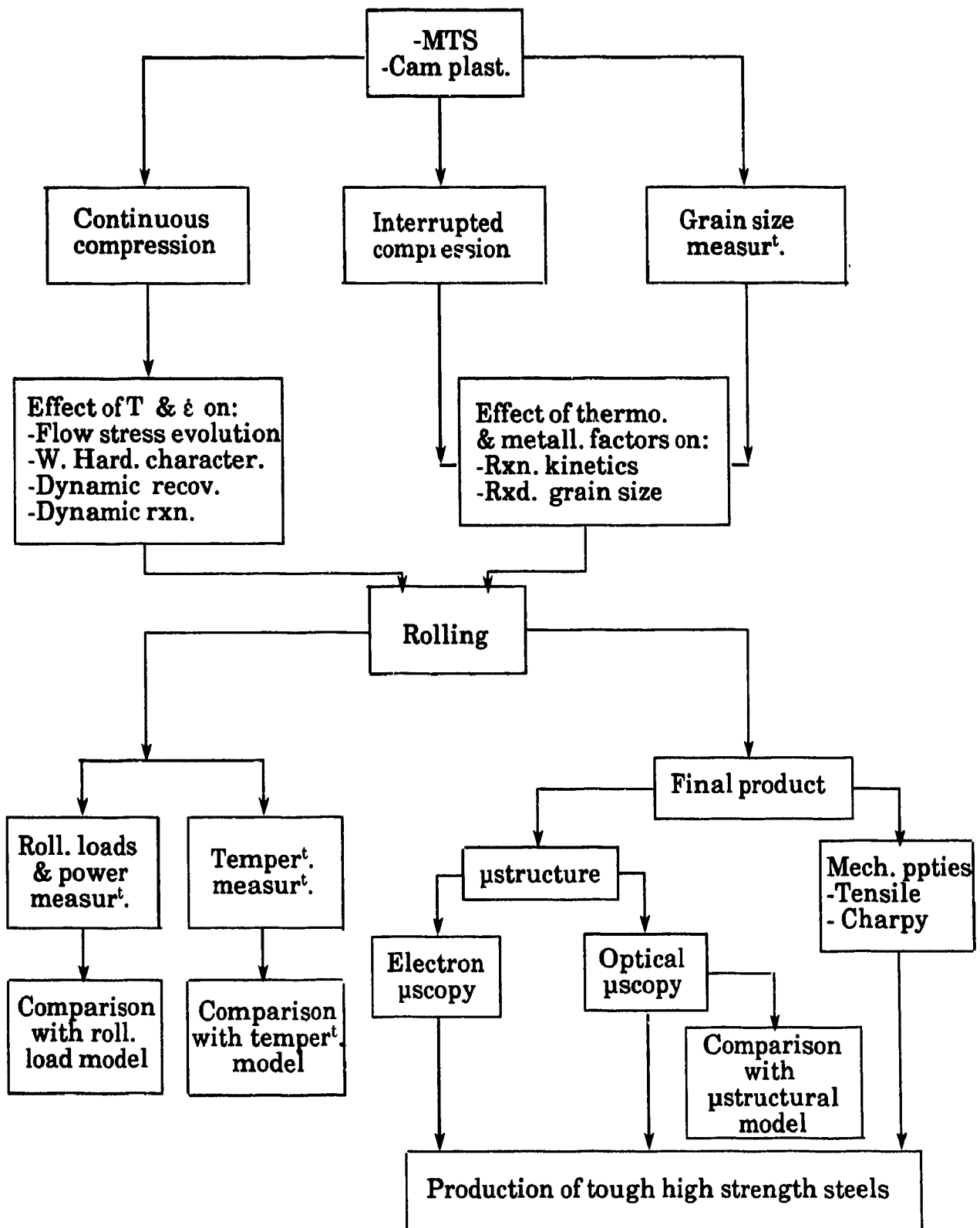


Figure 4.17 Summary of the experimental methods used.

Chapter FIVE

DATA ANALYSIS AND NUMERICAL TECHNIQUES

5.1. INTRODUCTION

The data available from the experiments described in the previous chapter were analyzed extensively by computer. The storage of these data in the IBM PC after each experiment permitted effective and accurate computations. In this chapter, some of the data analysis techniques and numerical methods employed during this study will be presented. The first section deals with the analysis of stress/strain curves using non-linear fitting. The second section treats the different methods that have been used for determination of the softening parameters after interrupted testing. In the third section, the procedure used during the correction of the stress/strain data for adiabatic heating, particularly at high strain rates, will be described. Finally, the finite difference method employed for temperature prediction during multipass hot rolling will be examined closely.

5.2. STRESS/STRAIN CURVE ANALYSIS

5.2.1. Smoothing Stress/Strain Curves

Although the true stress/true strain data obtained from the MTS and cam plastometer tests were relatively smooth (see Fig. 4.14), the noise present is sufficient to create significant scatter after differentiation. To correct the curves for this scatter without influencing the trend of the data, the following smoothing technique was used.

The general concept of smoothing is summarized in what follows. We assume that we have a set of "n" data points (x_1, y_1) , (x_2, y_2) , ..., (x_n, y_n) , not

necessarily equally spaced, where x is the reliable variable and y is the uncertain variable (strain and stress, respectively, in a compression test). To reduce the amount of noise in y , a linear combination of the readings is then taken symmetrically about x_i :

$$Y_S = a_{-k}y_{i-k} + a_{-k+1}y_{i-k+1} + \dots + a_k y_{i+k} \quad (5.1)$$

where $i+k \leq n$ and $i-k \geq 1$. The values of the constants a_{-k} to a_k can be found by fitting the data points $(x_{i-k}, y_{i-k}) \dots (x_{i+k}, y_{i+k})$ using the least squares method to obtain a straight line, for instance.

During this work, the number of points used in the smoothing was chosen to be 3 or 5, depending on the level of noise (this corresponds to $k=1$ and 2, respectively). The problem then becomes the minimization of the following expression with respect to α_i and β_i :

$$S(\alpha_i, \beta_i) = \sum_{m=i-k}^{i+k} (\alpha_i z_m + \beta_i - y_m)^2 \quad (5.2)$$

where:

$$z = x - x_i \quad (5.3)$$

When the set of constants α_i and β_i is determined for each pair of data points in the curve, the new "regressed" values constituting the smoothed curve are given by the Y_i 's, where:

$$Y = \alpha_i z + \beta_i \quad (5.4)$$

If the latter exhibits some remaining scatter, the procedure can be repeated until the smoothed points resemble the initial points. Finally, it should be pointed out that Eq. 5.1 is valid for all data points except those near the ends. For these points, off-center formulas similar to Eq. 5.1 can be used [110,111]. However, the strain intervals in the present stress/strain curves were too small for this purpose, thus the calculations at the ends were ignored.

5.2.2. Non-linear Fitting of the Bergström Model

Several equations describing the flow stress of metals have been employed throughout this work, with different degrees of success. These equations are those of Hollomon [75], Swift [77], Voce [78] and Bergström [112]. The curve fitting technique will be described only for the Bergström model because this represents a typical non-linear case, and also because of the difficulties that were encountered. In fact, the values of α and U cannot be determined separately by fitting the stress/strain curve and the solution of $\alpha^2 U = \text{constant}$ yields a hyperbole of points. The values of α can only be determined experimentally by measuring the dislocation density at high temperatures, which is quasi-impossible for steels because of the phase transformation. However, to provide an accurate description of the stress/strain curve, at least mathematically, the separate determination of the parameters α and U is not necessary (these are defined in p. 158 below). Thus, the Bergström equation was fitted in the following form:

$$\sigma = [(\alpha\mu b)^2 \frac{U}{\Omega} (1 - e^{-\Omega\epsilon}) + \sigma_o^2 e^{-\Omega\epsilon}]^{1/2} \quad (5.5)$$

where:

$$\sigma_o = \alpha\mu b \sqrt{\rho_o} \quad (5.6)$$

and ρ_o is the initial dislocation density. To determine $[(\alpha\mu b)^2 U]$, Ω and σ_o , the least squares fitting method was employed. This consisted of minimizing the following expression for the "n" data points of the stress/strain curve :

$$S[(\alpha\mu b)^2 U, \Omega, \sigma_o^2] = \sum_{i=1}^n [(\alpha\mu b)^2 \frac{U}{\Omega} (1 - e^{-\Omega\epsilon_i}) + \sigma_o^2 e^{-\Omega\epsilon_i} - \sigma_i^2]^2 \quad (5.7)$$

If we set $A = [(\alpha\mu b)^2 (U/\Omega)]$, $B = \Omega$ and $C = \sigma_o^2 - (\alpha\mu b)^2 (U/\Omega)$ and set the derivatives of S with respect to A , B and C equal zero, we end up with a non-linear system of three equations and three unknowns:

$$nA + C \sum_{i=1}^n e^{-B\epsilon_i} = \sum_{i=1}^n \sigma_i^2 \quad (5.8a)$$

$$A \sum_{i=1}^n e^{-B\epsilon_i} + C \sum_{i=1}^n e^{-2B\epsilon_i} = \sum_{i=1}^n \sigma_i^2 e^{-B\epsilon_i} \quad (5.8b)$$

$$A \sum_{i=1}^n \epsilon_i e^{-B\epsilon_i} + C \sum_{i=1}^n \epsilon_i e^{-2B\epsilon_i} = \sum_{i=1}^n \sigma_i^2 \epsilon_i e^{-B\epsilon_i} \quad (5.8c)$$

From Eqs. 5.8a and 5.8b, A and C were determined as functions of B , and when substituted in Eq. 5.8c, the non-linear equation for B was solved:

$$F(B) = A \sum_{i=1}^n \epsilon_i e^{-B\epsilon_i} + C \sum_{i=1}^n \epsilon_i e^{-2B\epsilon_i} - \sum_{i=1}^n \sigma_i^2 \epsilon_i e^{-B\epsilon_i} \quad (5.9)$$

where:

$$A = \left[\left(\sum_{i=1}^n \sigma_i^2 \right) \left(\sum_{i=1}^n e^{-2B\epsilon_i} \right) - \left(\sum_{i=1}^n e^{-B\epsilon_i} \right) \left(\sum_{i=1}^n \sigma_i^2 e^{-B\epsilon_i} \right) \right] / D \quad (5.10a)$$

$$C = \left[n \left(\sum_{i=1}^n \sigma_i^2 e^{-B\epsilon_i} \right) - \left(\sum_{i=1}^n \sigma_i^2 \right) \left(\sum_{i=1}^n \epsilon_i e^{-B\epsilon_i} \right) \right] / D \quad (5.10b)$$

$$D = n \sum_{i=1}^n e^{-2B\epsilon_i} - \left(\sum_{i=1}^n e^{-B\epsilon_i} \right)^2 \quad (5.10c)$$

Eq. 5.9 was solved for B (i.e. Ω) by iteration using the secant method and $[(\alpha\mu b)^2 U]$ and σ_0 were given by Eqs. 5.10a and 5.10b, respectively. The complete program used for these calculations is given in Appendix C.

Some stress/strain curves sometimes displayed non-monotonic behavior at low strains. To avoid this problem, the iteration procedure was performed over a range of starting strains, up to 5%. For each iteration, the correlation coefficient was calculated and the final values of $[(\alpha\mu b)^2 U]$, Ω , and σ_0 chosen were those corresponding to the best fit (i.e. to the highest correlation coefficient). The corresponding starting strain generally fluctuated around 2%.

5.2.3. Work Hardening Rate Calculation

For a given strain, the work hardening rate is the derivative of stress with respect to strain, which corresponds to the tangent at this value of strain. The numerical derivation calculation using the data points of the stress/strain curve is similar to the smoothing procedure described in section 5.2.1. The tangent at a given strain ϵ_i was taken as the slope of the straight line obtained by regressing three data points symmetrically around ϵ_i (i.e. α_i in Eq. 5.2.). Differentiation of a mathematical function fitted to the stress/strain curve was avoided for the reason that an actual discontinuous change can be masked by taking the derivative of this function.

5.3. SOFTENING PARAMETER DETERMINATION

5.3.1. Introduction

When the interrupted testing technique is used to investigate the static restoration behavior, the amount of softening taking place during an interval of unloading can be assessed by different means. These methods are based mainly on true stress/true strain data, or on hardness measurements after quenching the deformed samples [11, 15, 19, 23, 102-105, 113]. Since the techniques based on stress/strain data are the most frequently used, one of the aims of the present investigation is to compare these methods and to relate the softening rate and the recrystallization kinetics. A brief description of the techniques used to evaluate this parameter is given in the next two sections.

5.3.2. Offset, Back Extrapolation and Recovered Strain Fraction Methods

The offset method employs the following definition:

$$S_{Off} = \frac{\sigma_m - \sigma_{Off}}{\sigma_m - \sigma_o} \quad (5.11)$$

Here σ_m is the flow stress corresponding to the strain ϵ_1 in the first hit (Fig. 5.1), and σ_o and σ_{off} are the offset flow stresses (0.2%) in the first and second hits, respectively. According to this technique, the yield stress at high temperature is a sensitive measure of the structural state of the material tested. That is, the magnitude of the offset stress on reloading is controlled by the degree of change of the microstructure that has occurred during the holding time [100, 104, 114, 115].

In the back extrapolation method, the following definition is used:

$$S_{BE} = \frac{\sigma_m - \sigma_{BE}}{\sigma_m - \sigma_o} \quad (5.12)$$

where σ_{BE} is defined as the stress corresponding to the intersection of the vertical line with the prestraining curve after shifting it from O to O', in order to superimpose it on the reloading curve (Fig. 5.1). The back extrapolation method is based on the principle that after a small transient strain, the reloading stress/strain curve is close to the continuous curve of the fully annealed state. Although this last assumption is true only when recovery is the sole controlling mechanism during restoration, an extension to the case of recrystallization has been made [114].

A further way of describing the softening rate is to use the unrecovered strain fraction, which is defined as:

$$\lambda = \frac{\Delta\epsilon}{\epsilon_1} \quad (5.13)$$

where ϵ_1 is the strain in the first hit and $\Delta\epsilon$ is the accumulated strain after reloading (Fig. 5.1). This last method is based on the same principle as the back extrapolation method, but provides an easier and faster way of estimating the softening taking place after reloading.

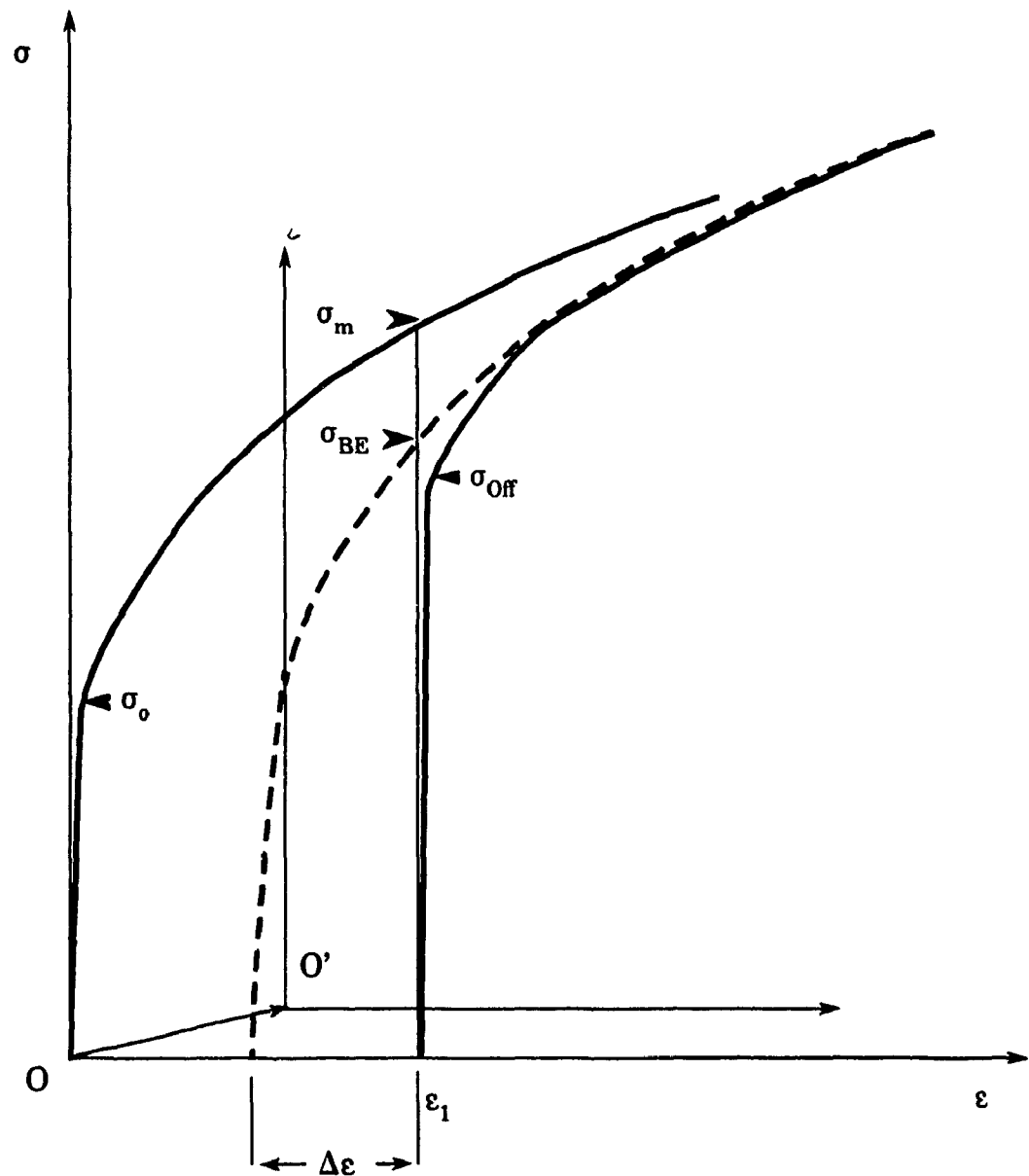


Figure 5.1 Determination of the flow stresses used in the evaluation of the softening rate by the offset and back extrapolation methods.

5.3.3. Mean Stress Method

Although the offset and back extrapolation methods described in the previous section have been used extensively to characterize softening after deformation, they involve many disadvantages. The measurement of yield stress is difficult and tends to be inaccurate at elevated temperatures. The lubricant and grooves used to minimize friction between the sample and the tools are another source of error in this measurement. In fact, the effect of lubricant and grooves is manifested particularly during the early stages of loading, which complicates the determination of the offset stress. For these reasons, the reduction in the overall level of the flow curve can be used instead to evaluate the fractional softening. This involves the mean flow stress, which is calculated by integrating the area under the stress/strain curve:

$$\bar{\sigma} = \frac{1}{\epsilon_2 - \epsilon_1} \int_{\epsilon_1}^{\epsilon_2} \sigma d\epsilon \quad (5.14)$$

The fractional softening is then defined as:

$$S_{\bar{\sigma}} = \frac{\bar{\sigma}_m - \bar{\sigma}}{\bar{\sigma}_m - \bar{\sigma}_0} \quad (5.15)$$

where $\bar{\sigma}_0$ and $\bar{\sigma}$ are the mean stresses in the first and second hits, respectively, and are taken at equal strains (Fig. 5.2). $\bar{\sigma}_m$ is the mean stress in the second hit using the continuous curve and corresponds to zero softening.

The data available from stress/strain curves permitted this softening parameter to be evaluated automatically. For this purpose, the maximum mean stress in the second hit, i.e. the area *ABCD*, is needed and a simple linear extrapolation between *A* and *B* would give inaccurate results, because of the occurrence of work hardening. For this reason the stress/strain curve in the first hit must be fitted to a non-linear mathematical function which is extrapolated and forced to pass through the point *B*. The choice of the following empirical relation is justified by the rapid determination of the constants A_0 , A_1 , A_2 and A_3 [116]:

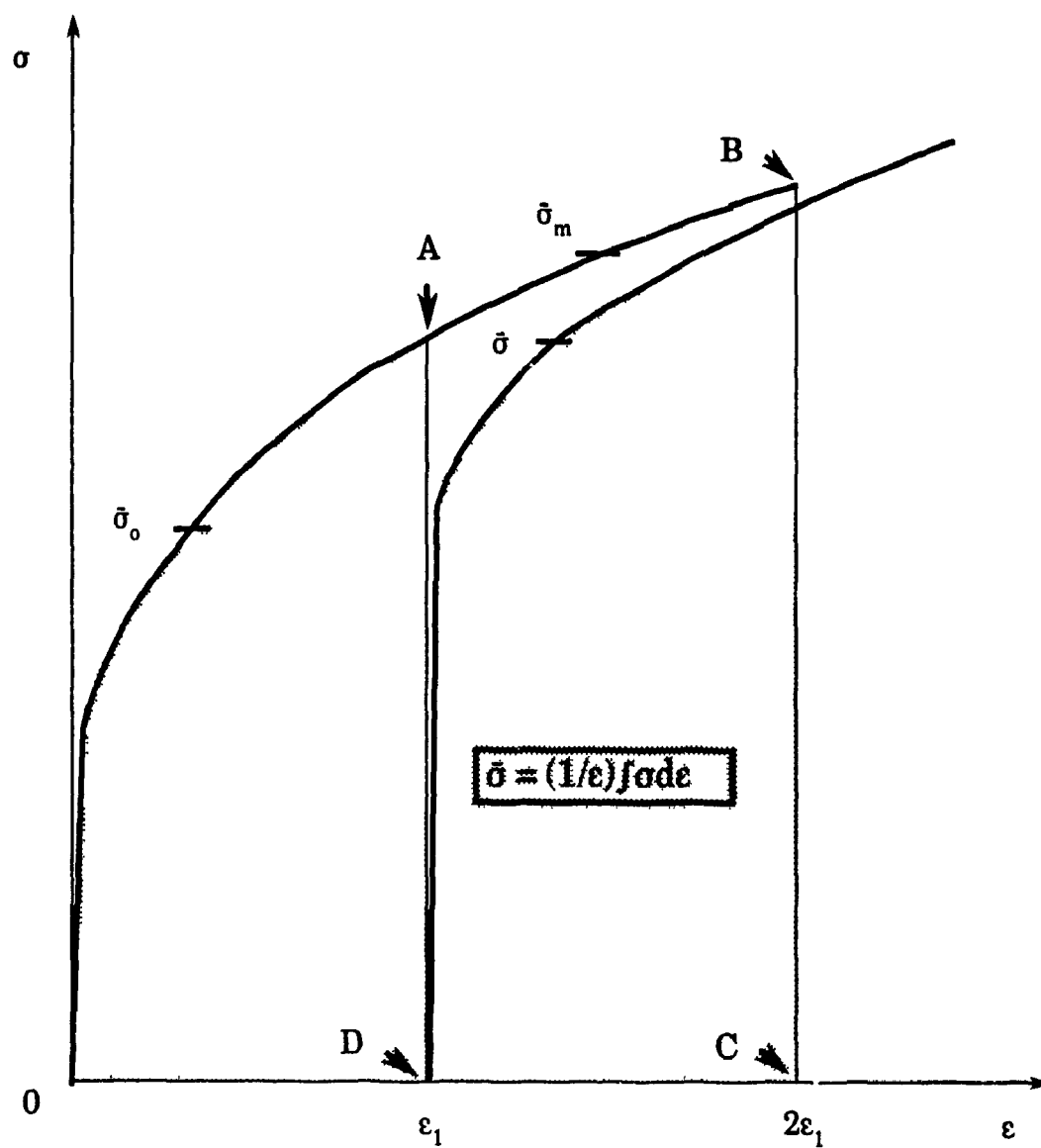


Figure 5.2 Determination of the mean stresses used in the evaluation of the softening rate by the mean stress method.

$$\sigma = A_0 + A_1 \varepsilon^{.4} + A_2 \varepsilon^{.8} + A_3 \varepsilon^{1.2} \quad (5.16)$$

The least squares method described in section 5.2.2 was employed together with the minimization of the following expression:

$$S(A_0, A_1, A_2, A_3) = \sum_{i=1}^n [(A_0 + A_1 \varepsilon_i^{.4} + A_2 \varepsilon_i^{.8} + A_3 \varepsilon_i^{1.2}) - \sigma_i]^2 \quad (5.17)$$

with respect to the A_i . This resulted in the following matrix:

$$\Sigma \begin{bmatrix} 1 & \varepsilon_i^{.4} & \varepsilon_i^{.8} & \varepsilon_i^{1.2} \\ \varepsilon_i^{.4} & \varepsilon_i^{.8} & \varepsilon_i^{1.2} & \varepsilon_i^{1.6} \\ \varepsilon_i^{.8} & \varepsilon_i^{1.2} & \varepsilon_i^{1.6} & \varepsilon_i^2 \\ \varepsilon_i^{1.2} & \varepsilon_i^{1.6} & \varepsilon_i^2 & \varepsilon_i^{2.4} \end{bmatrix} \begin{bmatrix} A_0 \\ A_1 \\ A_2 \\ A_3 \end{bmatrix} = \Sigma \begin{bmatrix} \sigma_i \\ \sigma_i \varepsilon_i^{.4} \\ \sigma_i \varepsilon_i^{.8} \\ \sigma_i \varepsilon_i^{1.2} \end{bmatrix} \quad (5.18)$$

where the Σ associated with the 4x4 matrix denotes the sum from 1 to n of each element in this matrix. To determine the A_i 's, the pivoting procedure [110, 111] was performed on the above matrix and the area $ABCD$ was calculated by integration of Eq. 5.16.

5.4. CORRECTION FOR ADIABATIC HEATING DURING HIGH STRAIN RATE COMPRESSION TESTING

During deformation and particularly at higher values of Z ($Z = \dot{\varepsilon} \exp(Q_{def}/RT)$), the deformation temperature does not remain constant. The increase in temperature due to adiabatic heating can lead to significant amounts of flow softening [117]. The resulting flow curve does not then correspond to isothermal conditions. Because isothermal flow stress data are essential for modeling, a correction for the temperature rise due to deformation

is necessary. A temperature correction was therefore applied to the data corrected for elastic distortion.

Under adiabatic heating conditions, the temperature increase δT can be calculated for each flow curve as follows:

$$\rho C dT = dw = \sigma d\epsilon \quad (5.19a)$$

ρ = density, Kg/m³

C = specific heat, J/Kg.K

w = mechanical work per unit volume, J/m³

If ρ and C are assumed to remain constant within the temperature interval δT , we obtain by integration:

$$\int_{T_o}^{T_o + \delta T} \rho C dT = \int_{\epsilon_o}^{\epsilon_o + \delta \epsilon} \sigma d\epsilon \Rightarrow \delta T = \frac{\bar{\sigma} \delta \epsilon}{\rho C} \quad (5.19b)$$

where $\bar{\sigma}$ is the mean stress calculated from the stress/strain curve over the strain interval $\delta \epsilon$ using the trapezoid formula:

$$\bar{\sigma} = \frac{1}{\delta \epsilon} \int_{\epsilon_o}^{\epsilon_o + \delta \epsilon} \sigma d\epsilon \quad (5.20)$$

For each flow curve determined at a given strain rate $\dot{\epsilon}$, δT was calculated incrementally at strain intervals of about 0.001 over the entire stress/strain curve. At a given value of $\delta \epsilon_i$, for instance, plots of σ versus $1/T$ (at constant $\dot{\epsilon}$) were constructed, and the corresponding δT_i was calculated using Eq. 5.19b (see Fig. 5.3a). The decrease in flow stress $\delta \sigma_i$ due to adiabatic heating during the strain interval $\delta \epsilon_i$ was estimated using the following equation:

$$\delta \sigma_i = \left[\frac{\partial \sigma}{\partial (1/T)} \right]_{\delta \epsilon_i, \dot{\epsilon}} \left[\frac{1}{T_{iso} + \delta T} - \frac{1}{T_{iso}} \right] \quad (5.21)$$

where T_{iso} is the temperature at the beginning of straining ($T_{iso} = T(\delta \epsilon_i = 0)$) and $\dot{\epsilon}$ is the strain rate (see Fig. 5.3b). The coefficient $\beta = [\partial \sigma / \partial (1/T)]_{\dot{\epsilon}}$ in the above

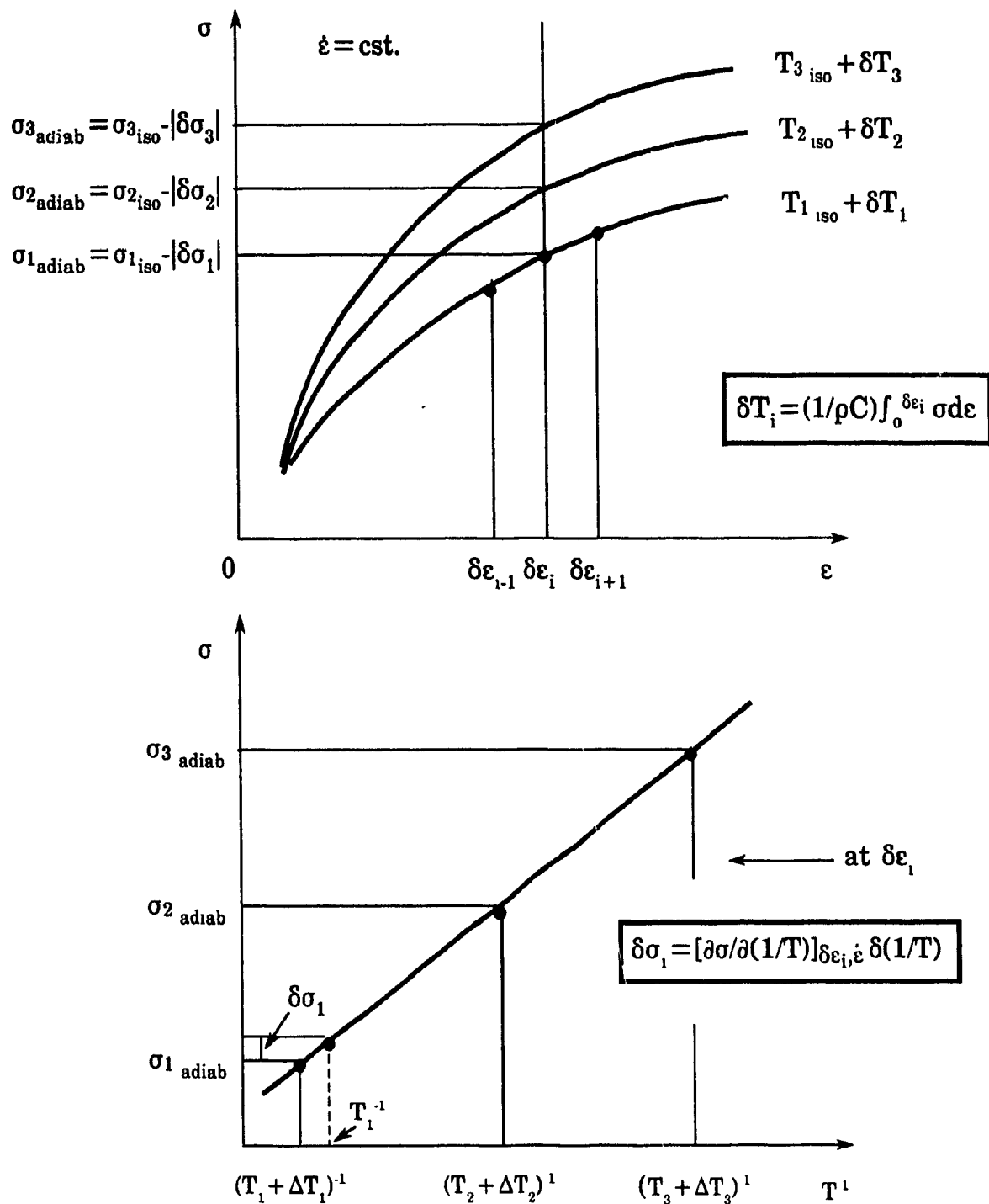


Figure 5.3 Procedure used for determination of the temperature increase and the corresponding flow softening during adiabatic compression.

relation was found to vary with strain (see next chapter). The calculation of β at each strain interval $\delta\epsilon_i$ all along the flow curve, at the strain rate of interest, permitted the accurate determination of $\delta\sigma_i$.

The calculated isothermal flow stress increase over the strain interval $\delta\epsilon_i$ can then be given in terms of the observed adiabatic stress increase as follows:

$$\Delta\sigma_{i, iso} = \Delta\sigma_{i, adiab} + |\delta\sigma_i| \quad (5.22)$$

The program used for the correction of temperature is given in Appendix C. At the end of the program, the stress/strain data were rewritten and stored to be used in subsequent calculations.

5.5. TEMPERATURE PREDICTION DURING HOT ROLLING

5.5.1. Introduction

To solve the differential equation for heat conduction (Eq. 3.1), several computing methods can be used. The finite element method, for example, is a useful technique for this purpose, but requires powerful computers and is time consuming so that it can only be employed for off-line applications. The finite difference method is another attractive technique which consists of transforming a differential equation into a system of linear algebraic equations. In contrast to FEM, the FDM is suitable for on-line calculations if the number of iterations carried out during execution of the algorithm is optimized. In this method, two different approaches exist to provide the numerical solution [56, 57, 118]:

- the *explicit* solution, which gives the future temperature of a particular node in terms of the current temperatures of the node and its neighbors;
- the *implicit* solution, which gives the future temperature of the node in terms of its current temperature and the future temperatures of its neighbors.

In the implicit method, the time step is not restricted by the size of the elements and the stability of the solution is ensured. In the explicit technique, if the time step is too large, the solution becomes unstable. The explicit solution is generally preferred due to its simplicity; however, the stability criterion must be respected.

During this study, the explicit technique was used, with the time step for stability varying from one stage of hot rolling to another. Also, instead of developing T in Eq. 3.1 in a Taylor series with respect to t and x , a heat balance was applied to each node. This method is equivalent to the usual mathematical one, but provides a physical derivation of Fourier's second law (Eq. 3.1)

5.5.2. Description of the Model

The model calculates the dynamic temperature distribution in the steel plate or strip during hot rolling. The determination of the temperature distribution within the deformed material is based on heat conduction, together with the boundary conditions characterizing each cooling zone (Fig. 5.4).

In hot rolling, temperature prediction is more important during finishing than roughing. At this stage, the width of the plate or strip is much greater than its thickness. It is therefore justified to neglect heat conduction in the width direction. This also applies to the length direction because of the relatively high speed of strip and plate in finishing mills. Thus, a one-dimensional analysis is sufficient to describe the temperature during hot rolling. A two-dimensional model in the thickness and width directions is not more complicated. It only implies a higher number of equations, which requires a spacious memory in the computer and takes a longer time for execution. Therefore, a unit section is considered for this purpose, of a thickness d which varies with the process time (Fig. 5.5). The temperature distribution for the complete workpiece can be computed if this section is taken to represent any position along the length and width of the transfer bar. During hot rolling, it is assumed that the top and bottom faces are subjected to identical cooling conditions. Because of symmetry, only half the material thickness is studied. For transfer bars less than 30 mm in thickness, acceptable results were obtained

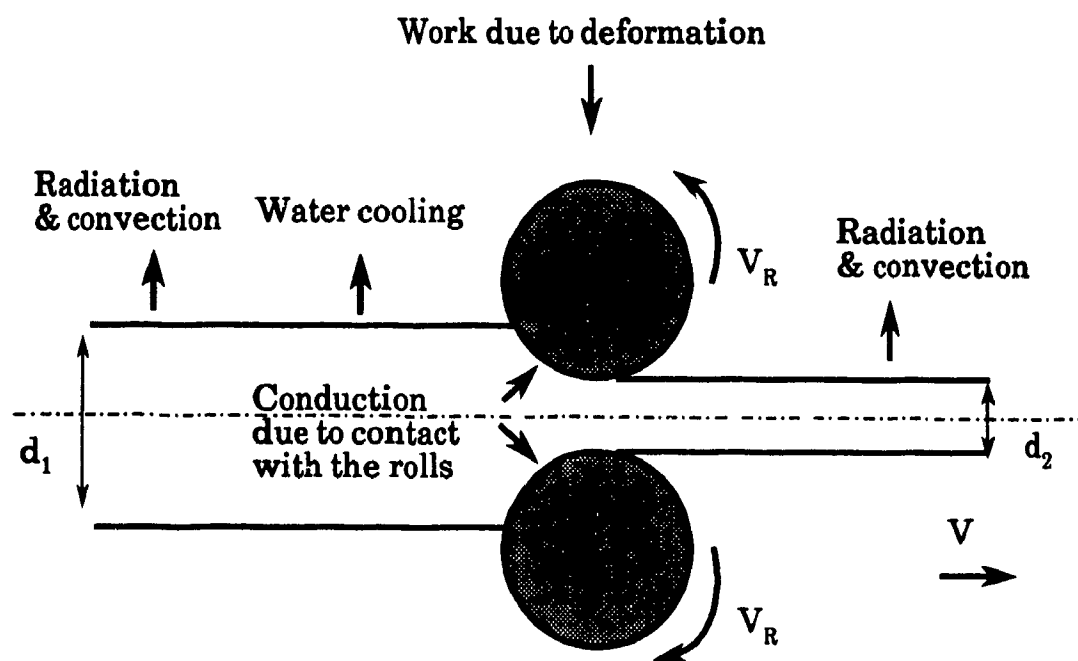


Figure 5.4 Heat transfer mechanisms during hot rolling.

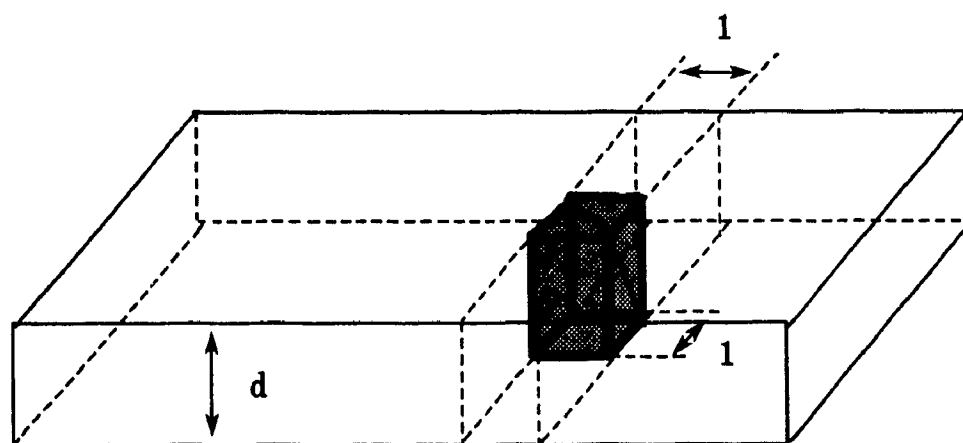


Figure 5.5 Representative section for the temperature distribution calculations.

by dividing the half thickness into 6 slices of thickness Δx each, so giving 7 nodes at which the temperature was calculated (Fig. 5.6).

For any node i different than 1 or 7, a heat balance across the thickness of the workpiece can be carried out by considering that the amount of heat accumulated at node i during a time Δt is equal to the difference between the heat lost to $i-1$ and gained from $i+1$. This can be written as follows :

$$k \frac{(T_{i+1} - T_i)}{\Delta x} (1^2) \Delta t - k \frac{(T_i - T_{i-1})}{\Delta x} (1^2) \Delta t = \rho C (T_i' - T_i) (1^2 \Delta x) \quad (5.23)$$

where T is the temperature and k is the thermal conductivity. One can express T_i' explicitly in terms of T_{i-1} , T_i and T_{i+1} :

$$T_i' = (1 - 2M)T_i + MT_{i+1} + MT_{i-1} \quad (5.24)$$

where $M = \alpha \Delta t / \Delta x^2$ and α is the thermal diffusivity ($\alpha = k / \rho C$). Thermodynamically speaking, the old temperature must have a positive effect on the new one. To ensure stability of the solution, the term $(1 - 2M)$ in Eq. 3. 24 must then be positive, i.e.:

$$\Delta t \leq \frac{\Delta x^2}{2\alpha} \quad (5.25)$$

The first and last (1 and 7) nodes are only half nodes and since they are subject to different boundary conditions, a different heat balance must be employed for each these nodes.

5.5.2.1. Radiation and Convection

For Node 7, adiabatic conditions are assumed:

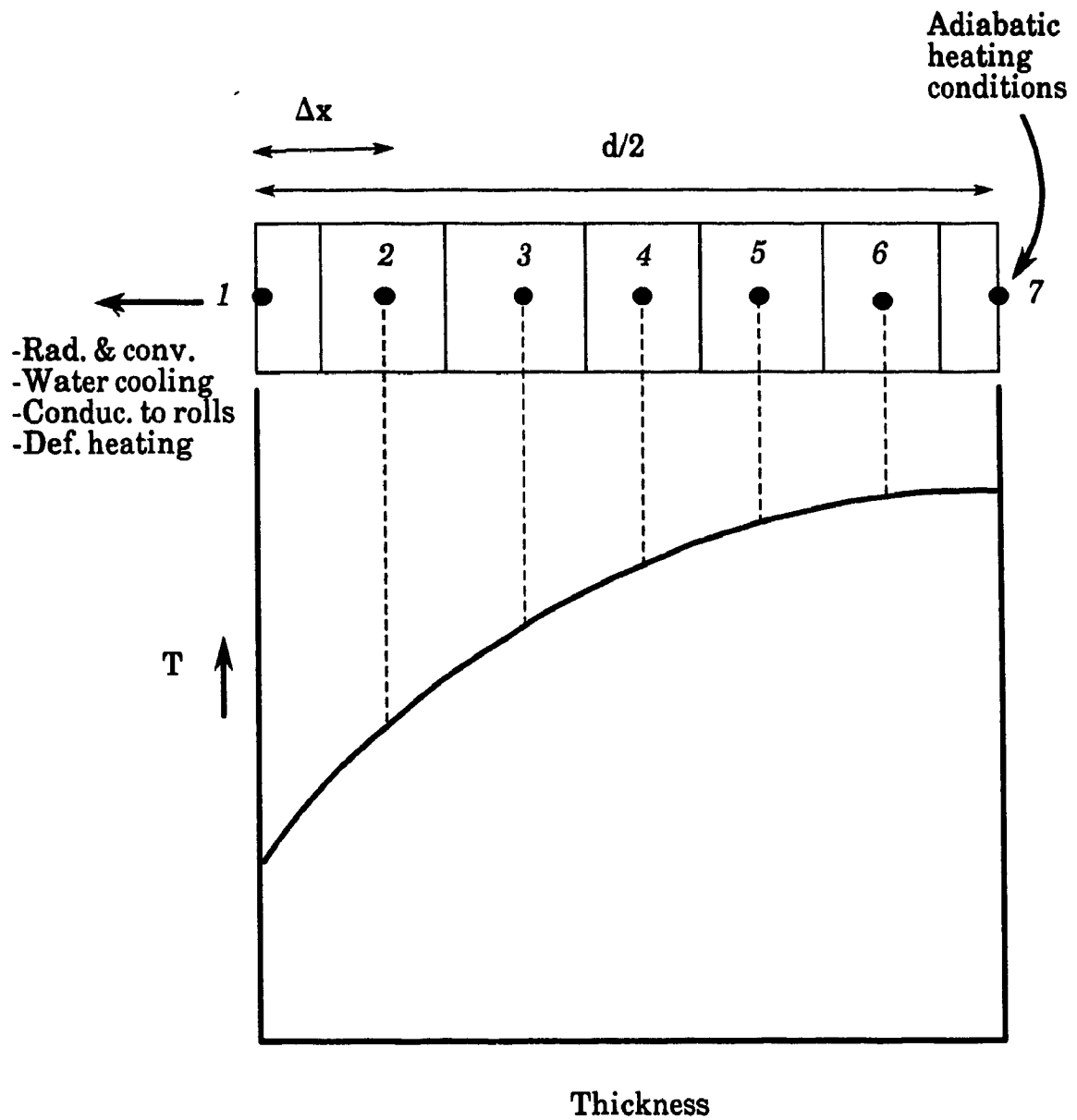


Figure 5.6 Discretization of slab half thickness into nodes for finite difference analysis.

$$T_7' = (1 - 2M)T_7 + 2MT_6 \quad (5.26)$$

When the slab is outside the stands, the surface loses heat by radiation and convection. For node 1, the heat balance is as follows:

$$k \frac{(T_2 - T_1)}{\Delta x} (1^2) \Delta t - \varepsilon_m(T) \sigma_{SB} (1^2) (T_1^4 - T_A^4) \Delta t - H_{CVC} (T_1 - T_A) \Delta t = \rho C (T_1' - T_1) (1^2 \frac{\Delta x}{2}) \quad (5.27)$$

where $\varepsilon_m(T)$ is the emissivity, σ_{SB} is the Stefan-Boltzmann constant and T_A is the ambient temperature. The above equation becomes:

$$T_1' = (1 - 2M - 2N_{RC}T_1^3 - 2H_{RC})T_1 + 2MT_2 + 2N_{RC}T_A^4 + 2H_{RC}T_A \quad (5.28)$$

where:

$$M = \alpha \Delta t / \Delta x^2$$

$$N_{RC} = \varepsilon_m(T) \sigma_{SB} \Delta t / \rho C \Delta x$$

$$H_{RC} = H_{CVC} / \rho C \Delta x$$

The stability criterion is as follows:

$$\Delta t \leq 1 / [2(\frac{\alpha}{\Delta x^2} + \frac{\sigma_{SB} \varepsilon_m(T) T_1^3}{\rho C \Delta x} + \frac{H_{CVC}}{\rho C \Delta x})] \quad (5.29)$$

The stability time varies with T_1^3 . The highest surface temperatures lead to the lowest Δt 's.

5.5.2.2. Cooling Due to Water

When the slab is water cooled outside the roll gap, convective losses determine the boundary conditions:

$$-k \left(\frac{\partial T}{\partial x} \right)_{surf} = H_{WAT} (T_1 - T_A) \quad (5.30)$$

where H_{WAT} is the appropriate heat transfer coefficient for water cooling. The temperature at the surface is given by :

$$T_1' = (1 - 2M - 2N_{WAT})T_1 + 2MT_2 + 2N_{WAT}T_A \quad (5.31)$$

where $N_{WAT} = H_{WAT}/\rho C \Delta x$. For a stable solution, we must have:

$$\Delta t \leq 1 / [2(\frac{\alpha}{\Delta x^2} + \frac{H_{WAT}}{\rho C \Delta x})] \quad (5.32)$$

5.5.2.3. Contact with the Rolls

During contact of the steel with the rolls, the surface is being cooled and conversely the work rolls are gaining heat. Two different approaches were used in this study to estimate the temperature drop at the surface of the slab.

Before describing these approaches, it is necessary to distinguish between perfect and imperfect contact. For perfect contact between two infinite bodies at different and uniform temperatures T_1^∞ and T_2^∞ , a boundary temperature T_p is defined to provide continuity of the temperature profile through the interface (Fig. 5.7a). The assumption of perfect contact is not realistic and does not simulate actual contact conditions in industrial processes.

In the present work, the *first approach* assumed a thermal resistance between the steel and the rolls. The heat conduction equation was then solved in the manner described above, using the finite difference method. The boundary condition at the surface is:

$$-k(\frac{\partial T}{\partial x})_{surf} = H_{CTC}(T_1 - T_A) \quad (5.33)$$

where H_{CTC} is the heat transfer coefficient at the slab/work roll interface. The expressions for T_1' and Δt are similar to Eqs. 5.31 and 5.32, respectively, with H_{WAT} replaced by H_{CTC} .

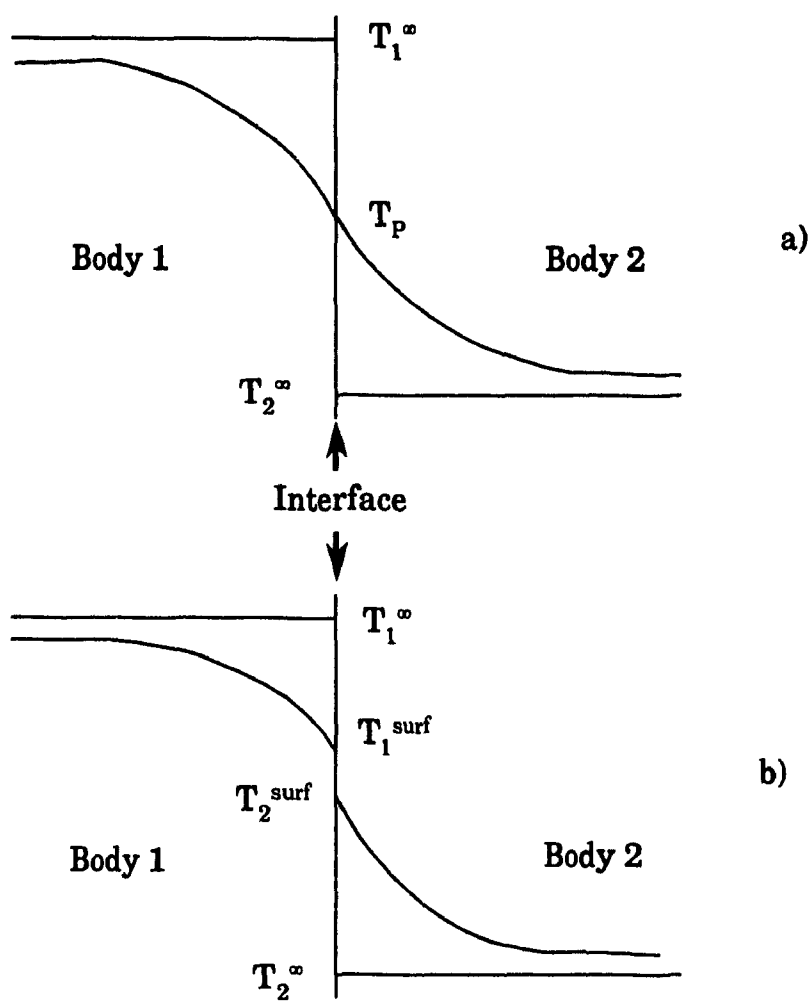


Figure 5.7 Temperature profile with:
a) perfect contact
b) imperfect contact.

In the *second roll gap approach*, it was assumed that the workpiece and roll have the same surface temperature at the point of contact. In such a case, the heat flux can be computed from the solution of the differential equation describing the temperature distribution for unsteady state conditions. This approach assumes the absence of thermal resistance (perfect contact), so that the heat flux is given by :

$$q = \frac{-k(T_{BLK} - T_{BND}) \exp\left(-\frac{x^2}{4\alpha t}\right)}{\sqrt{\pi\alpha t}} \quad (5.34)$$

where

q = heat flux density, $\text{J m}^{-2} \text{s}^{-1}$

x = distance from the boundary plane, m

T_{BLK} = bulk temperature, K (T_1^∞ or T_2^∞ in Fig. 5.7)

T_{BND} = boundary plane temperature, K (T_p in Fig. 5.7)

For $x=0$:

$$q_{Slab} = \frac{-k(T_{BLK,S} - T_{BND})}{\sqrt{\pi\alpha t}} \quad (5.35a)$$

$$q_{Roll} = \frac{-k_R(T_{BLK,R} - T_{BND})}{\sqrt{\pi\alpha_R t}} \quad (5.35b)$$

Since $q_{Slab} = q_{Roll}$, T_{BND} can be calculated. The total heat loss during a contact time t_c is :

$$Q = \int_0^{t_c} q_{slab} dt = \frac{2k(T_{BLK,S} - T_{BND})}{\sqrt{\pi\alpha}} \sqrt{t_c} \quad (5.36)$$

The drop in surface temperature of the *element* under consideration of thickness d_o is simply calculated from the expression:

$$\Delta T = \frac{Q}{d_o \rho C} \quad (5.37)$$

5.5.2.4 Heat Due to Deformation

The temperature rise due to deformation is calculated at each node by considering that each element has a different initial temperature. The temperature increase at node i is given by:

$$\Delta T_i = \frac{\bar{\sigma}_i(T)}{\rho C} \cdot \ln\left(\frac{h_1}{h_2}\right) \quad (5.38)$$

where $\bar{\sigma}_i(T)$ is the mean flow stress of the material and is strongly dependent on temperature. h_1 and h_2 are the initial and final thicknesses, respectively. Because of the temperature differences, each node is heated to a different degree. In particular, the surface being colder gains more heat than the center.

5.5.3. Temperature Calculation Algorithm

This program was written in True Basic and the corresponding flow chart is shown in Fig. 5.8. For each condition, a subroutine is called to calculate the temperature distribution during the process time. During reduction, no temperature distribution is calculated; the temperature profile is simply transferred from the thickness before the pass to the new thickness. Then, the temperature drop due to contact with the rolls is computed during the contact time using the subroutine based on the heat balance. To allow comparison with the last subroutine, the one based on the perfect contact assumption is used. Finally, the temperature rise due to deformation is computed at each element and added to the previous profile. The simplification of not computing the temperature during deformation is reasonable, since the contact times during hot rolling are very short.

5.6. SUMMARY

The basic techniques used frequently throughout the present investigation were described in detail in this chapter. It should be mentioned that only typical cases were examined here to provide the reader with an understanding of the interpretation of the results described in subsequent chapters. Also, some of the algorithms will only be described later, because they

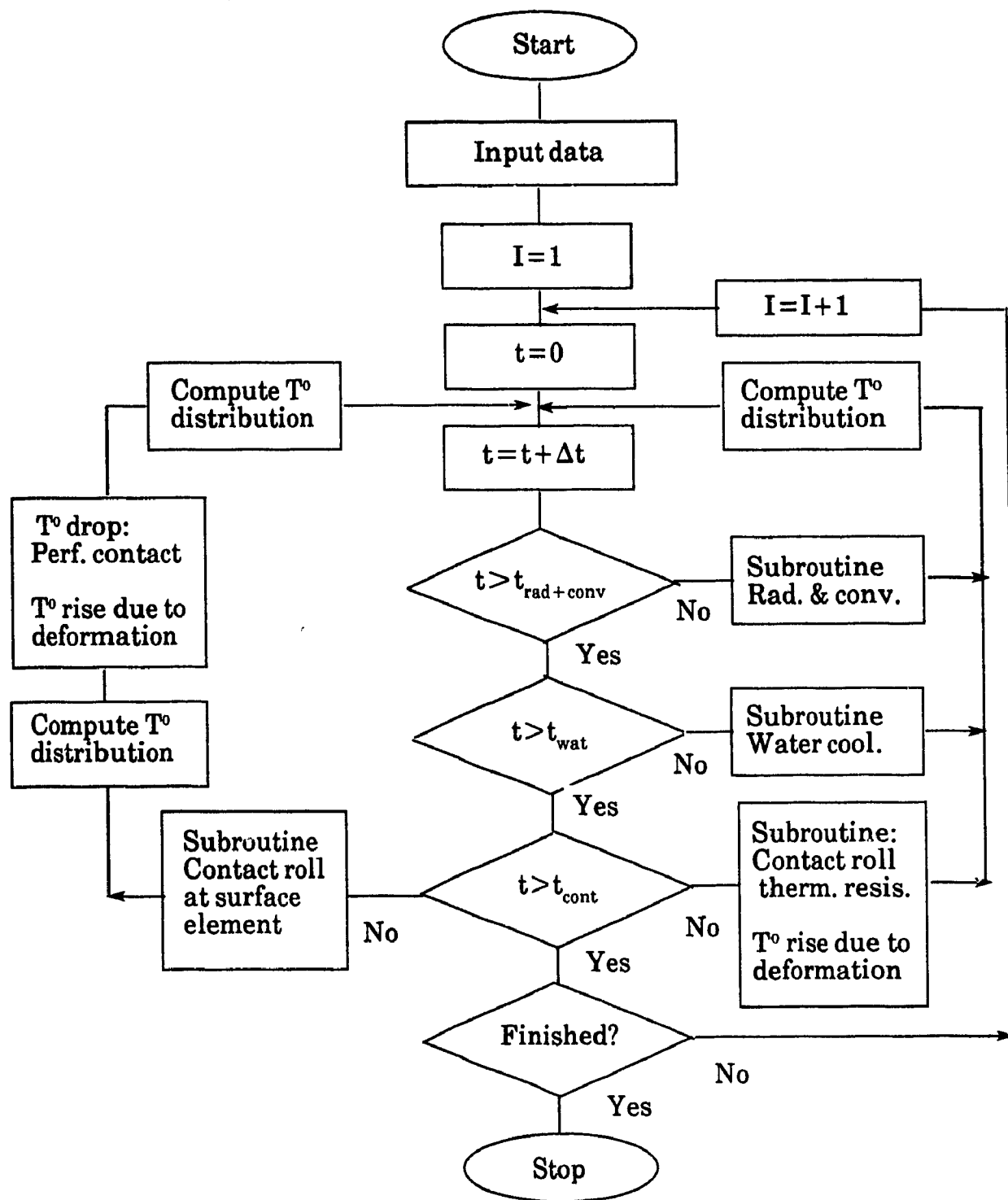


Figure 5.8 Flow chart of computer program for calculating workpiece temperature distribution.

concern other components of the present investigation.

Chapter SIX

MODELLING THE EFFECT OF HIGH TEMPERATURES AND STRAIN RATES ON THE FLOW BEHAVIOR OF STEEL

6.1. INTRODUCTION

The technology of deformation processing is based on an understanding of advanced process modelling techniques and on experience with forming operations. While many sophisticated numerical methods have recently been developed, the application of this technology depends on accurate descriptions of the flow behavior of the material, using constitutive equations in terms of strain, strain rate and temperature. These equations are required as inputs to the computer models which predict the deformation history of the material being formed at any time. The effective use of computers together with a thorough understanding of the plastic behavior of metals can result in considerable reductions in the costs of production, process design and of the analysis of hot forming processes.

With regard to modelling the flow behavior of metals during hot working operations such as rolling, forging or extrusion, the complexity is due to the evolution of the internal structure with time, which in turn involves mechanisms such as work hardening, dynamic recovery and dynamic recrystallization. This behavior can, however, be described by constitutive relations consisting of rate and evolution equations which have the form:

$$\epsilon = f(\sigma, T, S_t) \quad (6.1)$$

$$\frac{dS_t}{dt} = g(\sigma, T, S_t) \quad (6.2)$$

where $\dot{\epsilon}$ is the strain rate, σ the stress, T the temperature and S_0 is a structure parameter.

The objective of the present chapter is to study the plastic behavior of steels at high temperatures and strain rates, by formulating constitutive equations which can be used in subsequent applications such as hot rolling. A one-internal-variable formulation is adopted where the structural parameter is taken as the dislocation density and where dynamic recovery is the only softening mechanism. The topics that will be discussed include the effects of adiabatic heating, testing temperature and strain rate on the flow stress. This is followed by a description of the rate equation and of the activation parameters employed in its formulation. A phenomenological model for the evolution equation will be presented with some mechanistic interpretations. Finally, the effect of dynamic recrystallization on flow softening will be modelled and discussed briefly.

6.2. TRUE STRESS/TRUE STRAIN CURVES

6.2.1. General Characteristics

Typical true stress/true strain curves are shown in Figs. 6.1 to 6.4 for the four steels studied as a function of testing temperature and strain rate. Here it can be seen that the two types of test are complementary; the MTS machine performs compressions to strains of one but with some limitations in strain rate ($\dot{\epsilon} \leq 2 \text{ s}^{-1}$), while the cam plastometer deforms samples at relatively high strain rates (e.g. 50 s^{-1}), but is limited in terms of maximum strain.

The shapes of the flow curves are classical in nature, with the work hardening rate at a given strain and the strain to the peak increasing with decreasing temperature and increasing strain rate. This is typical of materials which recrystallize dynamically when deformed at temperatures above half their melting points. A peak strain would also have been reached at the higher strain rates ($\geq 10 \text{ s}^{-1}$) in the boron-containing steels if higher strains had been attained. However, it is of interest that at the strain rates pertaining to hot strip mill conditions, only dynamic recovery took place in the latter steels at strains up to 0.5, even at temperatures as high as 1100°C . This behavior is attributed to the retarding effect of niobium and boron on dynamic

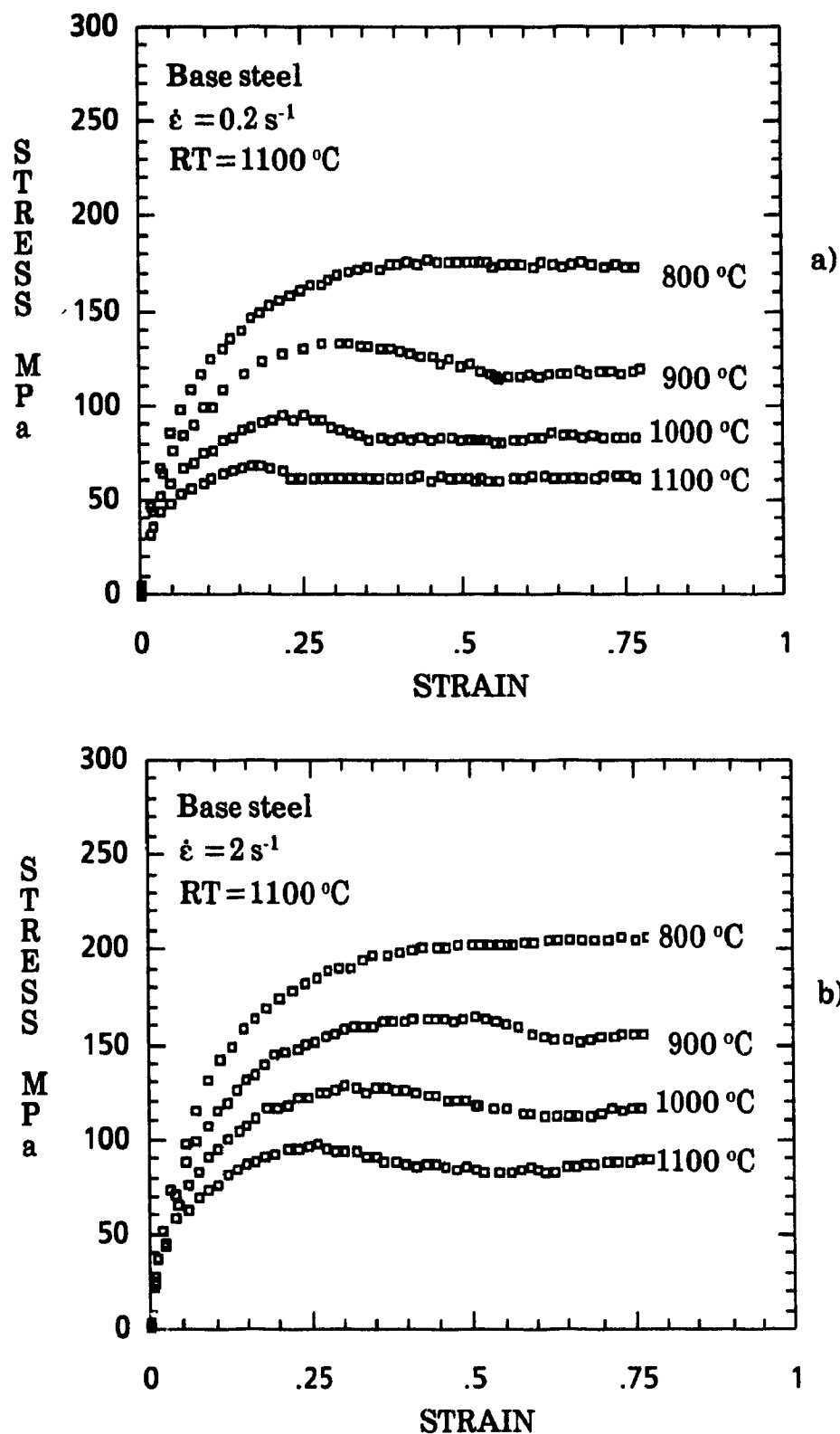


Figure 6.1 Effect of temperature on flow stress in the base steel deformed at
a) 0.2 s^{-1} , b) 2 s^{-1} .

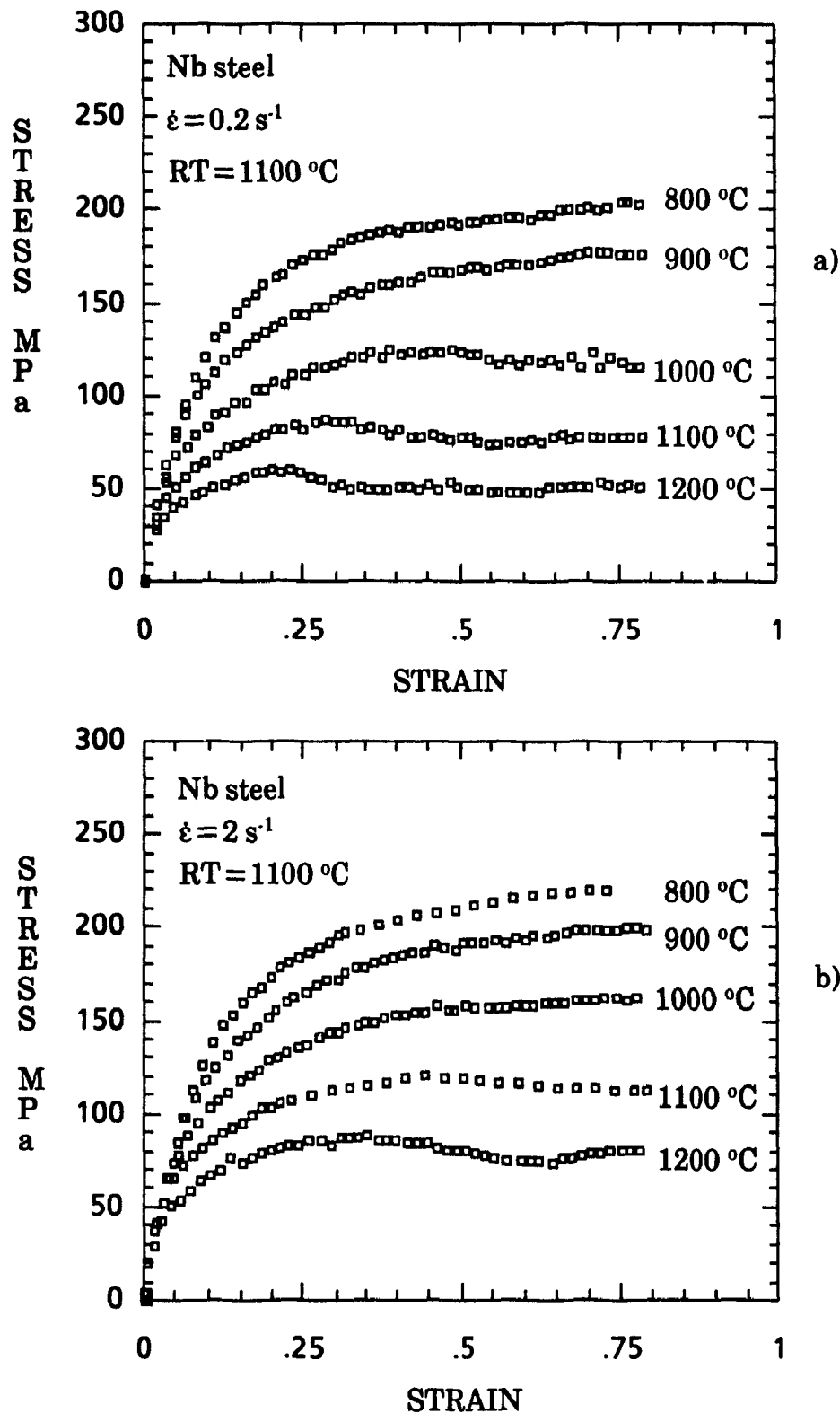


Figure 6.2 Effect of temperature on flow stress in the Nb steel deformed at
a) 0.2 s^{-1} , b) 2 s^{-1} .

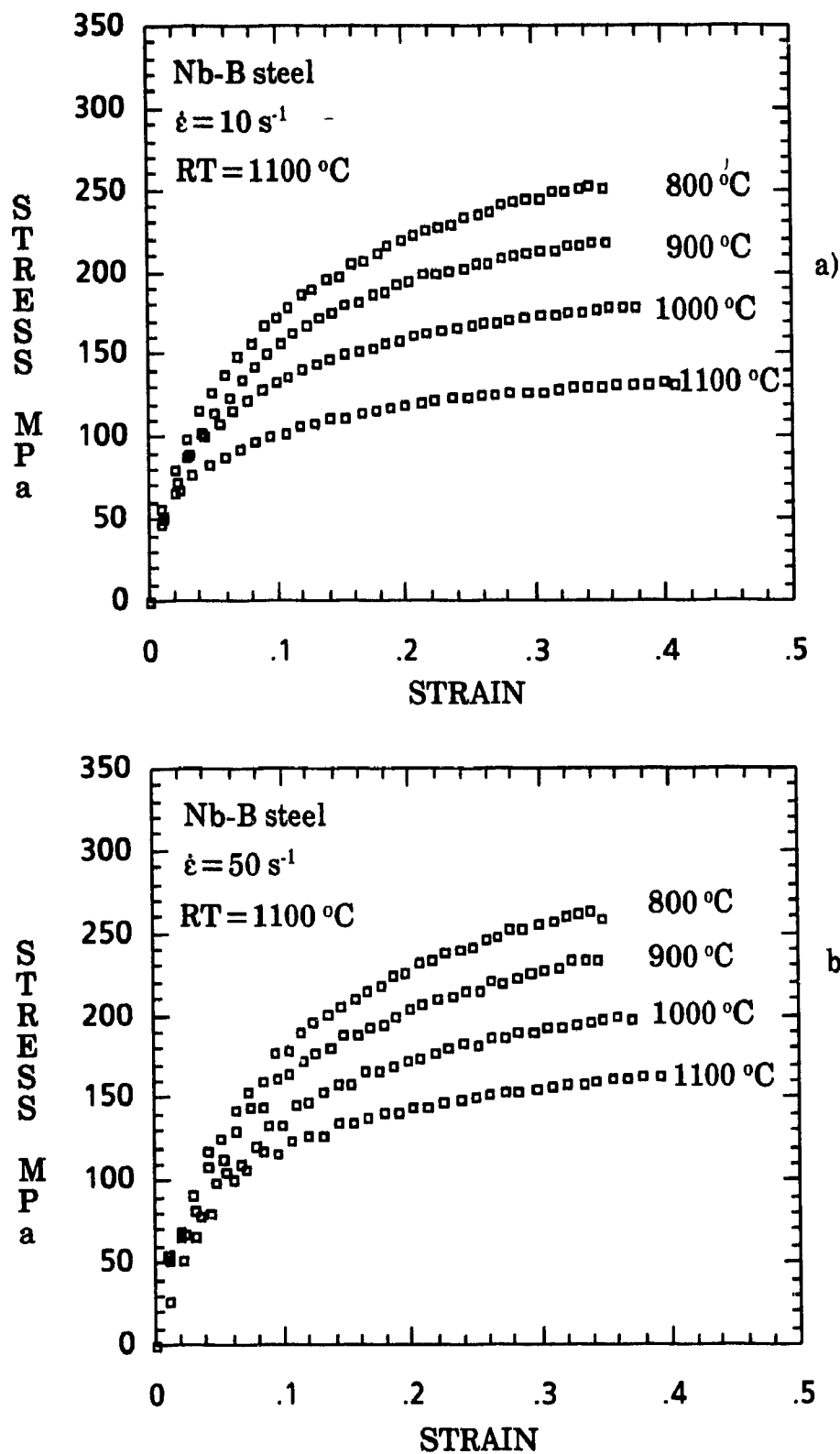


Figure 6.3 Effect of temperature on flow stress in the Nb-B steel deformed at a) 10 s^{-1} , b) 50 s^{-1} .

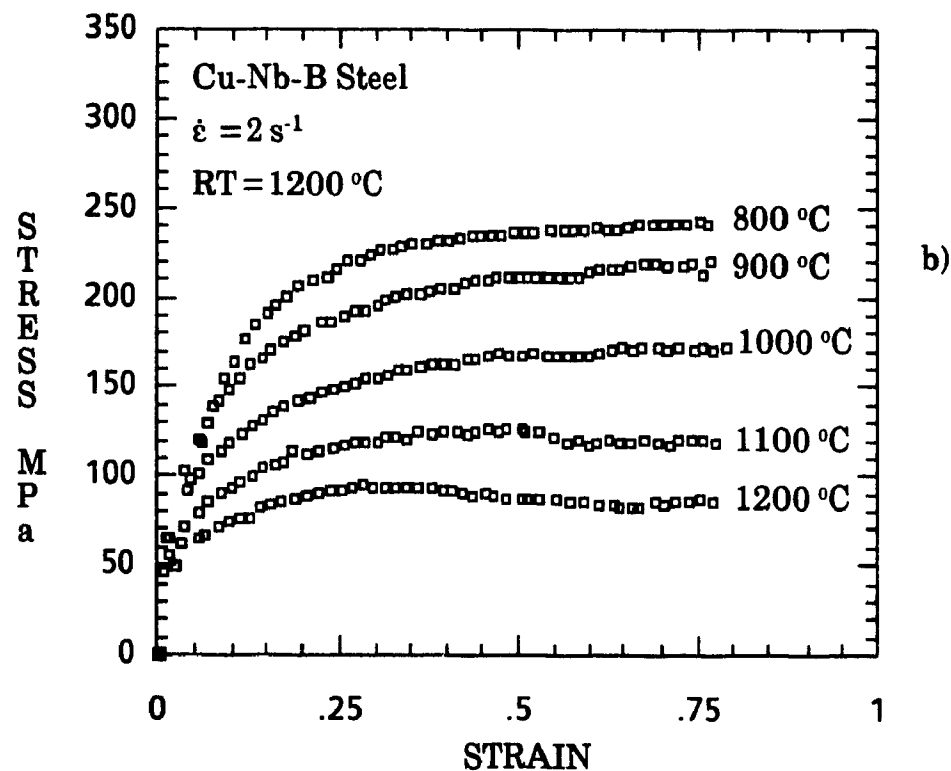
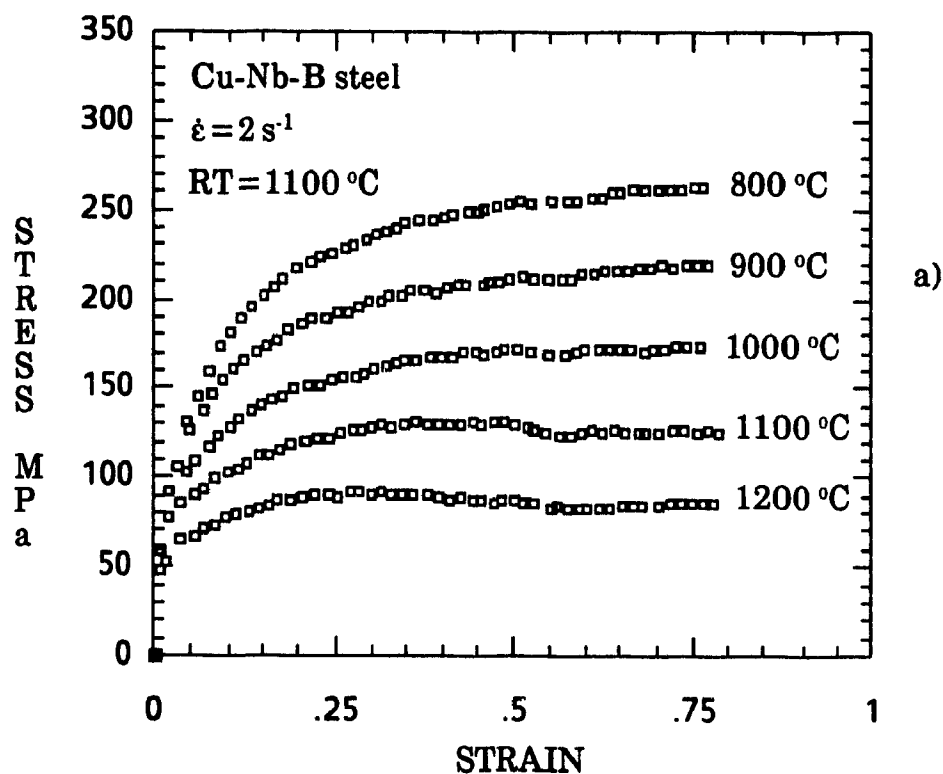


Figure 6.4 Effect of temperature on flow stress in the Cu-Nb-B steel reheated at a) 1100°C, b) 1200°C (Contd.).

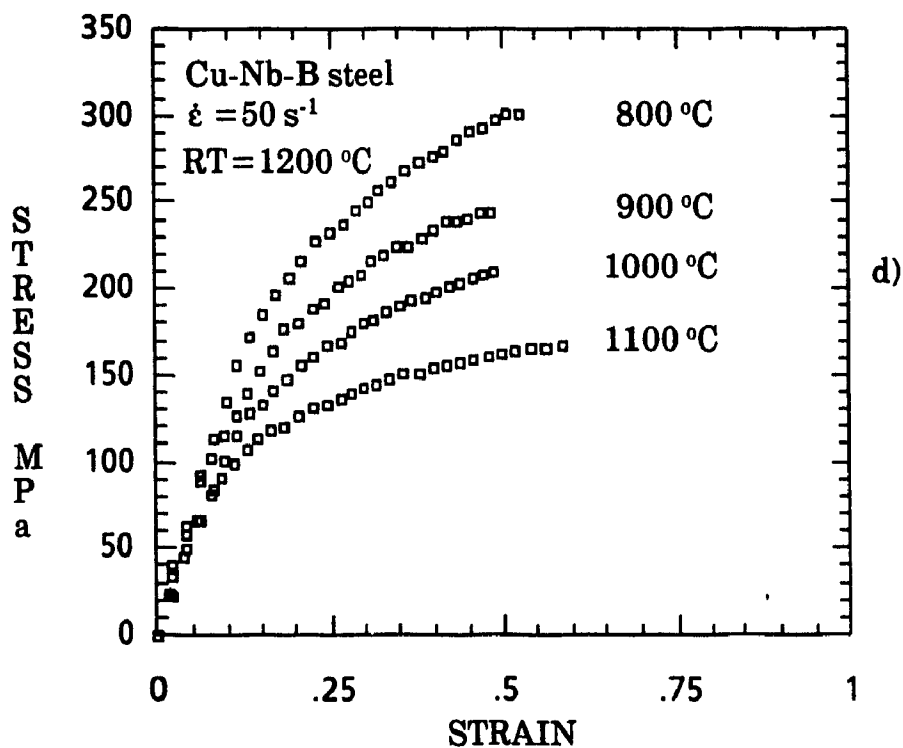
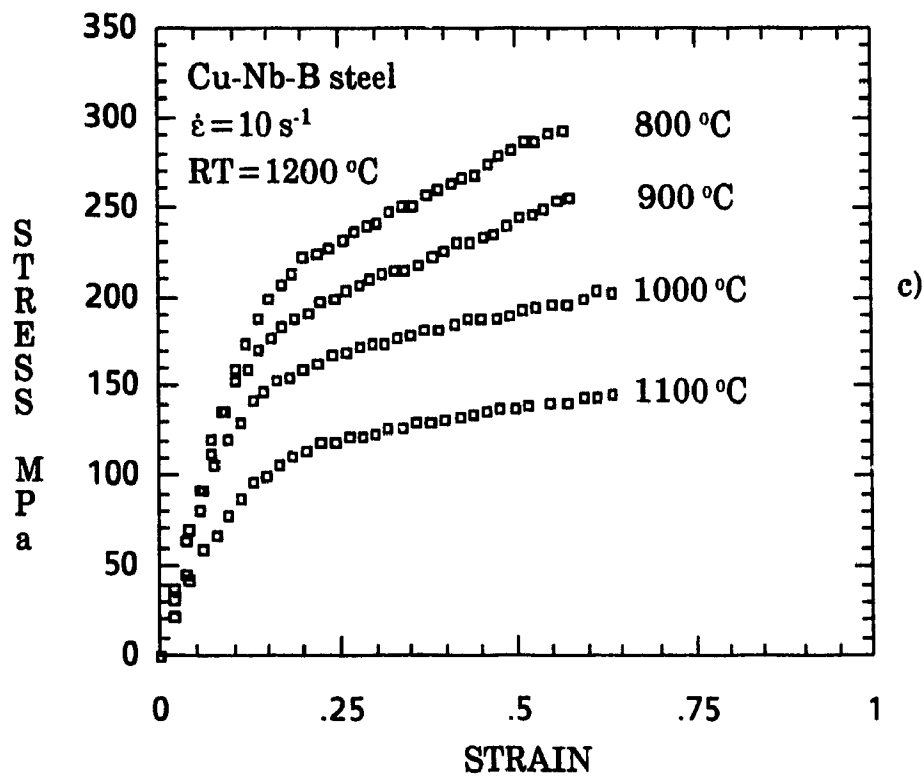


Figure 6.4 Effect of temperature on flow stress in the Cu-Nb-B steel reheated at 1200 °C and deformed at c) 10 s^{-1} , d) 50 s^{-1} .

recrystallization [119]. By contrast, in the base steel, the flow curves show signs of dynamic recrystallization at temperatures as low as 900°C. In this material, dynamic recrystallization occurs earlier because of the absence of the retarding effect of the alloying elements.

In the copper steel, changing the reheating temperature from 1100 to 1200°C did not result in any significant variation in the stress level when the steel was deformed between 900 and 1200°C (Figs. 6.4a and b). This is simply explained by *i*) the similar initial grain sizes obtained at these two reheating temperatures (Fig. 4.4), and *ii*) the fact that at reheating temperatures of 1100°C and above, all the niobium is in solution (section 4.4.1).

6.2.2. Temperature Rise Due to Adiabatic Heating

All the curves presented in the last section are based on the initial specimen temperature. However, due to the conversion of plastic work into heat and losses by conduction, convection and radiation from the specimen to its surroundings, the actual specimen temperature differs from the initial one.

The heat losses by conduction, convection and radiation can be computed using the appropriate heat transfer coefficients. Wright and Sheppard [120] calculated the heat losses during torsion testing by employing a three-dimensional finite difference model on the torsion specimen and found significant radial and axial temperature profiles. During the present work, the heat losses were not evaluated for two reasons. The first is because of the difficulty of measuring the heat transfer coefficient during contact of the tools with the sample, particularly in the CENTORR furnace. The second reason is that attention was paid to homogenizing the temperature prior to deformation, thereby avoiding any thermal gradients in the specimen. Furthermore, the deformation time was very short at high strain rates, so that little heat loss can be assumed to have occurred during deformation.

While the heat losses during a test can be calculated or minimized, the temperature rise at higher strain rates cannot be ignored. Unfortunately, most research workers have assumed that the temperature rise during deformation is negligible and the data reported in the literature are usually based on adiabatic

rather than isothermal temperatures. Although this is of lesser importance at low strain rates, in general, it is not the case when the material exhibits high flow stresses or if the strain rates are high. The assumption that the temperature rise due to plastic work can be ignored then leads to considerable error. Up to a 100°C increase in temperature has been observed during the deformation of a specimen, both in torsion and compression [121- 123].

The procedure described in section 5.4 is then used to assess the temperature increase during compression testing. It is assumed that this rise is uniform throughout the specimen and the changes in ρ and C with temperature are not taken into account. The actual change in temperature normalized by the strain interval is given in Fig. 6.5 at different initial testing temperatures and strain rates. In this figure, data from Baragar [116] and Samanta [124] are included for comparison purposes. It is clear that the normalized increase in temperature during deformation is greater at low testing temperatures and higher strain rates because of the higher flow stresses developed. Similar behavior has been observed for other steels and aluminum alloys [120, 123-126]. The increase in $\delta T/\delta \epsilon$ with increasing strain rate and decreasing temperature is to be expected. Assuming that the process is adiabatic at high strain rates because of the short deformation times involved, it is obvious from Eq. 5.19 that an increase in strain and strain rate and a decrease in temperature will result in an increase in the mean stress and consequently in $\delta T/\delta \epsilon$. If plots of the mean stress versus temperature, strain and strain rate can be prepared for a material, it is easy to estimate the temperature rise under any conditions of ϵ , $\dot{\epsilon}$, and T during deformation.

Korhonen and Kleemola [127] have used the following expression for the flow stress to calculate the temperature increase during tensile testing:

$$\sigma = K_K \epsilon^{m_K} \dot{\epsilon}^{n_K} [1 - a(T - T_o)] \quad (6.3)$$

where K_K , m_K , n_K and a are constants and T_o is the initial temperature. They assumed that the temperature dependence of the flow stress is linear because of the limited operating range, which seems to be reasonable. Introducing Eq. 6.3

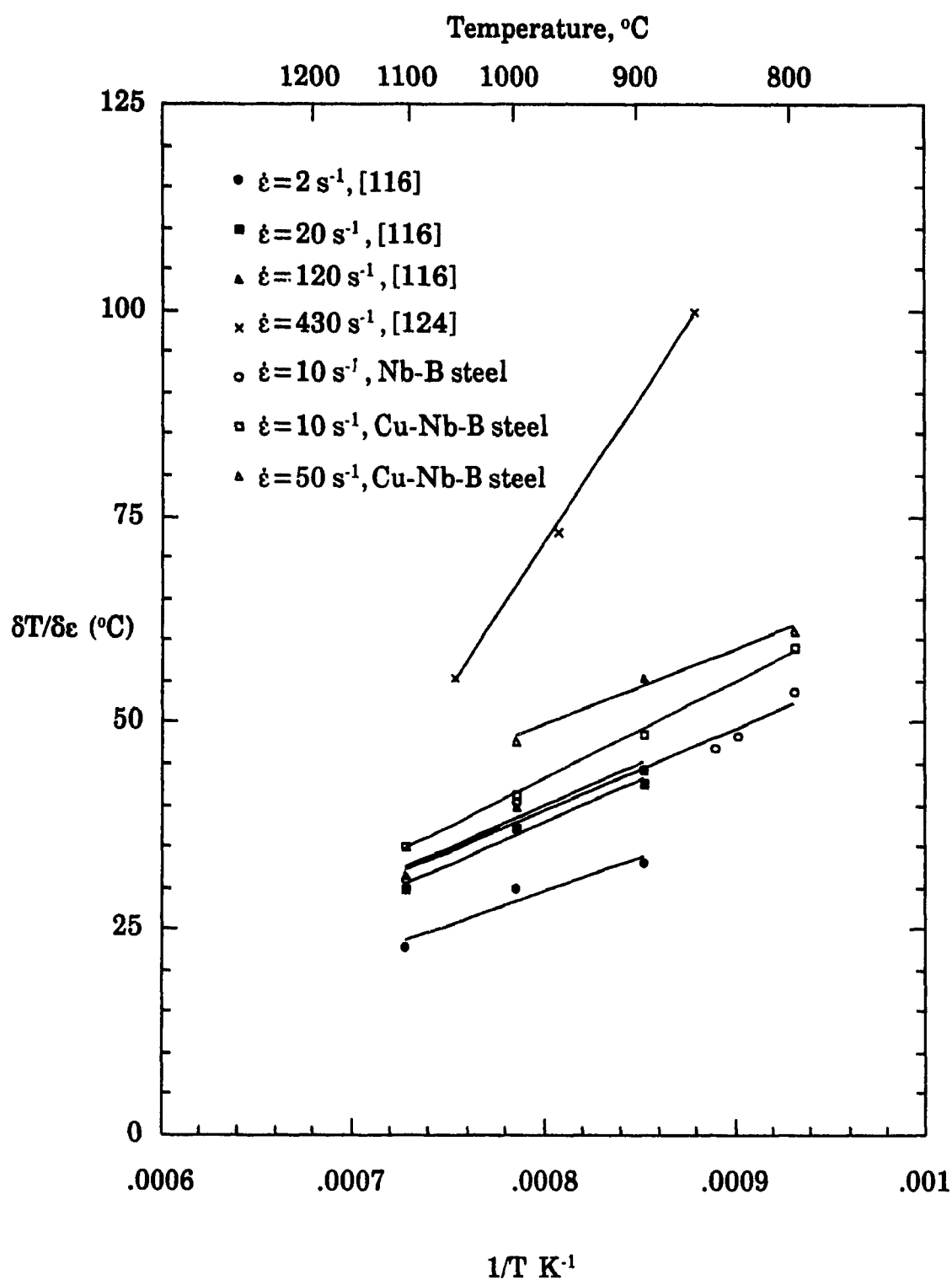


Fig. 6.5 Effect of testing temperature and strain rate on the temperature increase per unit strain during deformation.

into 5.19 and integrating from $\epsilon_0 - \delta\epsilon$ to ϵ_0 , they found that the instantaneous temperature during the test had the following form:

$$T = T_o + \frac{1}{a} \{1 - \exp[-\frac{K_K a}{\rho C} \frac{\dot{\epsilon}^{m_K}}{n_K + 1} (\epsilon_o^{n_K + 1} - (\epsilon_o - \delta\epsilon)^{n_K + 1})]\} \quad (6.4)$$

The above generalization derived by these authors leads to estimation of the temperature rise due to adiabatic heating for a combination of ϵ , $\dot{\epsilon}$, and T by differentiation of Eq. 6.4 with respect to *strain*.

As will be shown in a later section, the form of the dependence of stress on strain in Eq. 6.3 is not very accurate, particularly at large strains. However, for small strain increments, it is a good example of how the temperature rise due to adiabatic heating can be estimated from stress/strain data. Other forms for the dependence of flow stress on strain, strain rate and temperature can be employed and the adiabatic temperature can be computed by numerically integrating the following general equation:

$$\rho C \int_{T_o}^{T_o + \delta T} \frac{dT}{f(T)} = \int_{\epsilon_o}^{\epsilon_o + \delta\epsilon} \sigma(\epsilon, \dot{\epsilon}) d\epsilon \quad (6.5)$$

where $f(T)$ is any type of function that represents the temperature dependence of the flow stress at constant strain and strain rate (e.g. $\exp(Q/RT)$)

The effect of temperature rise on flow stress was estimated using Eq. 5.21 when the coefficient $\beta = \partial\sigma/\partial(1/T)|_{\epsilon}$ is not constant. Since the flow stress decrease is calculated at each strain increment, the corresponding β was evaluated point by point. An example of a corrected flow curve and the corresponding variation of β with strain are shown in Figs. 6.6a and b, respectively. Tables 6.1a, b and c give the calculated decreases in flow stresses normalized by the stress and strain levels. For the steels investigated in the present work, the corrected flow stress values differ from the initial flow stress data by up to 11 pct. for a strain of one. The agreement with the values calculated from the data in reference [116] is satisfactory, as the flow stress decreases are similar. Some of the values of $\delta\sigma/\sigma\delta\epsilon$ obtained from this reference are lower than in the present case, which is

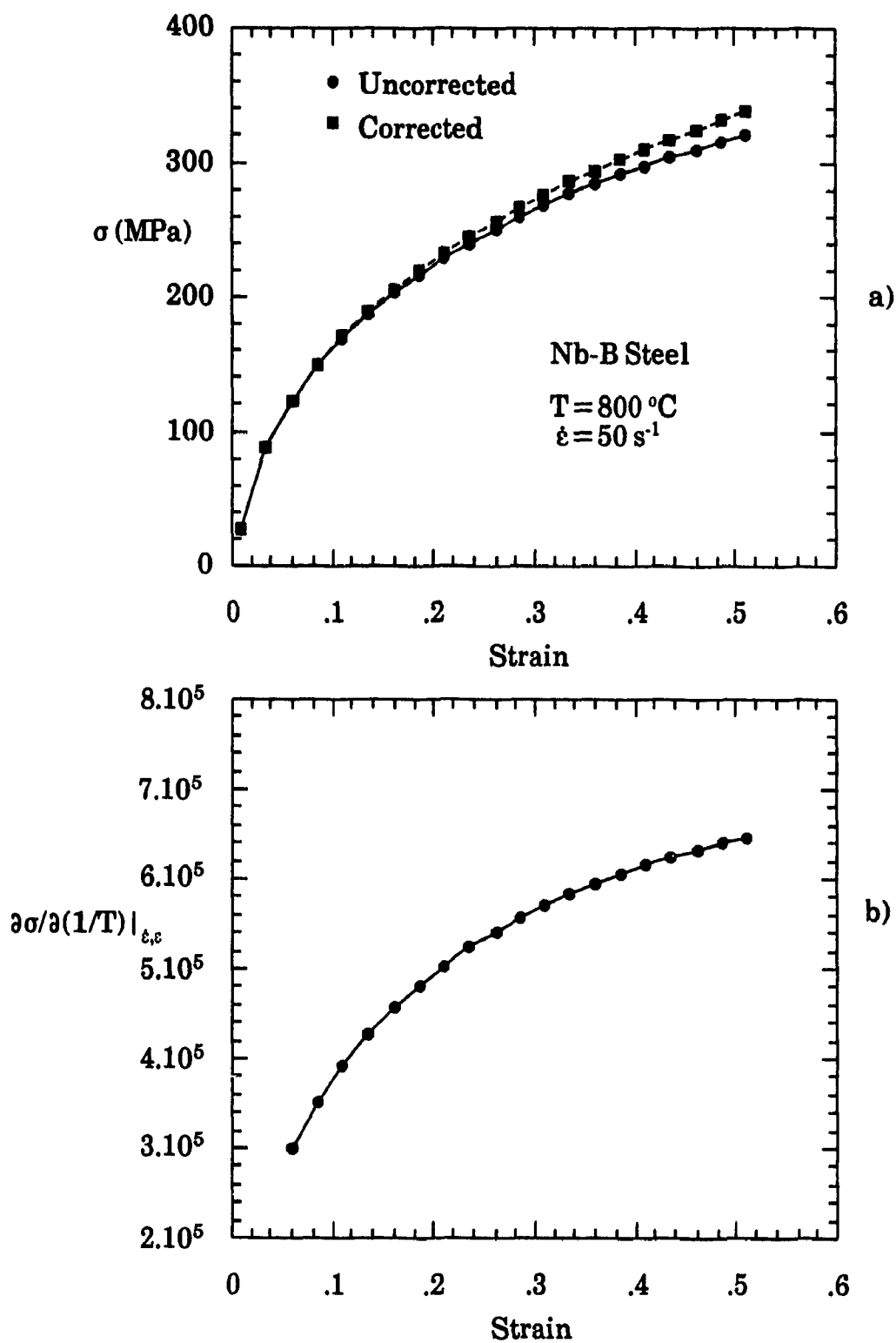


Figure 6.6 a) Effect of adiabatic heating on flow stress during deformation of the Nb-B steel.

b) Strain dependence of the coefficient $\partial\sigma/\partial(1/T)|_{\epsilon, \dot{\epsilon}}$.

Table 6.1a Calculated temperature increases and the corresponding stress decreases in the Nb-B steel deformed at 10 s^{-1} .

ϵ	T (°C)	δT (°C)	$\delta \sigma$ (MPa)	$\delta T/\delta \epsilon$ (°C)	$-\delta \sigma/\sigma \delta \epsilon$
.36	800	19.4	10.1	53.8	.112
.39	835	18.8	8.9	48.3	.099
.36	850	17.2	7.8	47.7	.096
.39	900	17.4	7.4	44.3	.092
.38	1000	15.3	5.8	40.3	.086
.40	1100	12.4	4.1	30.9	.078
.41	1100	12.4	3.8	30.5	.073

Table 6.1b Calculated temperature increases and the corresponding stress decreases in the Cu-Nb-B steel.

$\dot{\epsilon}$ (s^{-1})	ϵ	T (°C)	δT (°C)	$\delta \sigma$ (MPa)	$\delta T/\delta \epsilon$ (°C)	$-\delta \sigma/\sigma \delta \epsilon$
	.53	800	31.4	17.3	59.3	.107
10	.48	900	23.7	10.8	48.8	.907
	.48	1000	20.1	7.8	41.3	.077
	.61	1100	21.4	7.5	35.1	.073
	.57	800	34.3	21.9	59.9	.129
20	.57	900	30.4	16.3	52.9	.111
	.64	1000	28.6	13.4	44.8	.103
	.58	800	35.2	18.7	61.1	.106
50	.59	900	33.0	14.8	55.6	.092
	.65	1000	30.9	12.0	47.9	.085

mainly due to the occurrence of flow softening around 0.7 strain. It is also because the efficiency of deformation heating ζ [117, 126, 128] was taken as

Table 6.1c Calculated temperature increases and the corresponding stress decreases in the HSLA steels ^[116].

$\dot{\epsilon}$ (s ⁻¹)	ϵ	T (°C)	δT (°C)	$\delta \sigma$ (MPa)	$\delta T/\delta \epsilon$ (°C)	$-\delta \sigma/\sigma \delta \epsilon$
	.70	1100	16.0	6.8	22.9	.088
2	.70	1000	21.0	3.8	30.0	.031
	.70	900	23.0	4.9	32.9	.035
	.70	1100	21.0	6.7	30.0	.056
20	.70	1000	26.0	8.0	37.2	.054
	.70	900	30.0	11.4	42.8	.068
	.70	1100	22.0	9.2	31.5	.076
120	.70	1000	28.0	11.0	40.0	.069
	.70	900	31.0	15.0	44.3	.081

one, which means that 100% of the plastic work is assumed to be converted into heat. This is not of course true, as many other complicated mechanisms of heat transfer operate during deformation of the specimen.

6.3. RATE EQUATION

6.3.1. Effect of Temperature and Strain Rate on the Saturation Stress

During the hot compression experiments, when the steady state was reached, the saturation stress was measured directly from the stress/strain curves. If the flow curve does not display a steady state regime due to continuous work hardening or to softening by dynamic recrystallization, the work hardening rate $\partial \sigma / \partial \epsilon|_{T, \dot{\epsilon}}$ can be extrapolated to a hypothetical saturation stress σ_{ss}^* due to dynamic recovery alone [129-132] corresponding to $\partial \sigma / \partial \epsilon = 0$ (see Fig. 6.7). This saturation stress σ_{ss}^* provides a measure of the additional softening taking place after the peak when dynamic recrystallization occurs (see section 6.6 for more details). The values of σ_{ss}^* reported in this chapter thus

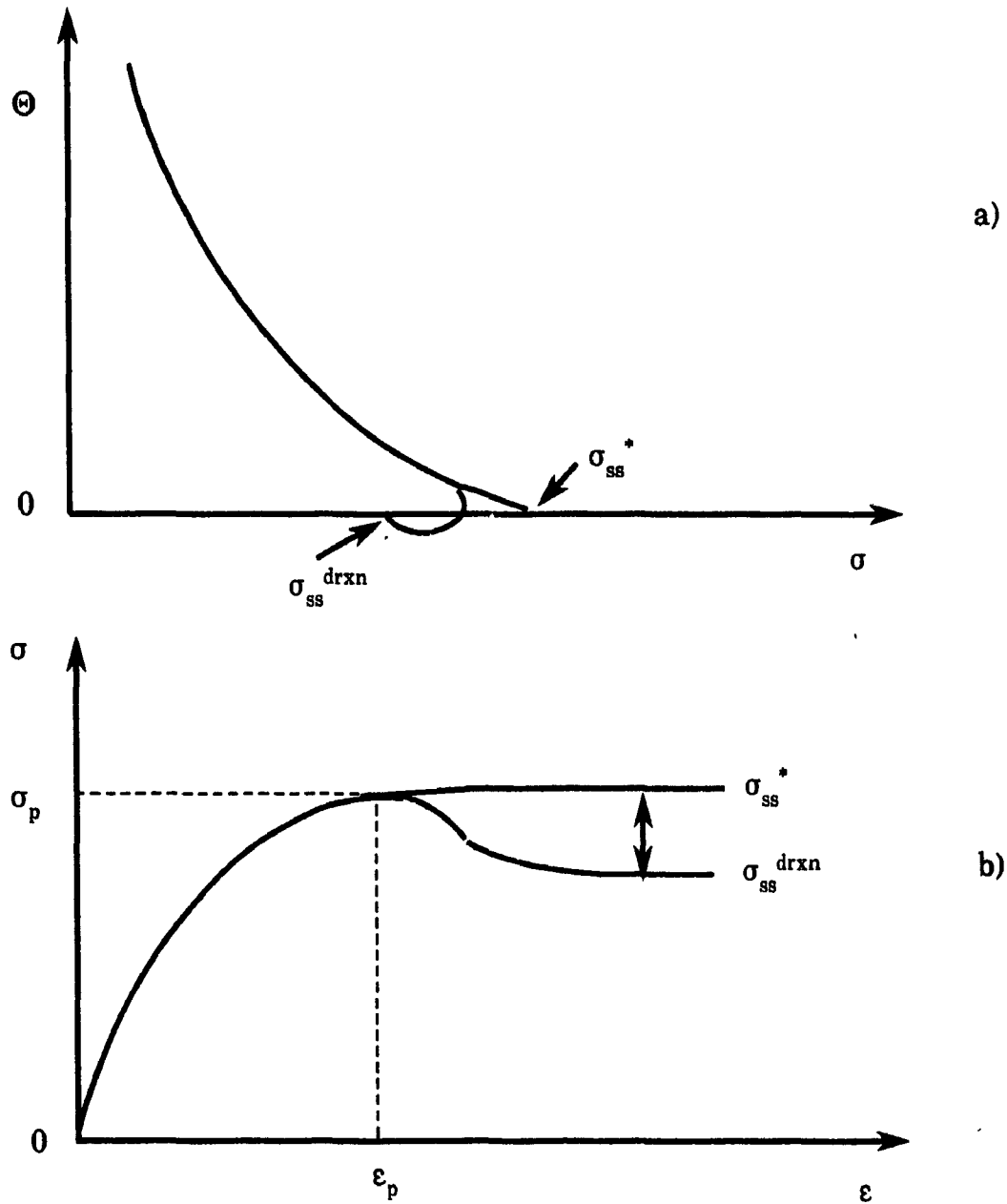


Figure 6.7 a) Schematic representation of the change in Θ with stress.
 b) Definition of the hypothetical saturation stress σ_{ss}^{*} .

correspond to the saturation stress without considering the additional softening brought about by dynamic recrystallization.

For the four steels studied, the temperature and strain rate dependence of σ_{ss}^* was modeled using the following hyperbolic sine law [2, 133-135]:

$$\dot{\epsilon} = A [\sinh(\alpha \sigma_{ss}^*)]^{n'} \exp\left(-\frac{Q}{RT}\right) \quad (6.6)$$

where Q is the apparent activation energy for deformation, R the gas constant, and A , α and n' are assumed to be constant. To determine n' and α , a method similar to that used by Uvira and Jonas [134] is adopted here. It consists of varying α over a narrow range which results in a variation in n' . The final value of α chosen is the one which gives the best correlation coefficient over the full range of temperature and strain rate.

In Fig. 6.8, $\sinh(\alpha \sigma_{ss}^*)$ is plotted versus Z ($Z = \dot{\epsilon} \exp(Q/RT)$) on a log-log scale with the values of α , n' and A indicated for each steel. The data support the validity of Eq. 6.6 first proposed by Sellars and Tegart [5] and used by many investigators to describe the change in the steady state stress with strain rate [56, 116, 134, 136, 137]. The value of α which gives the best fit is around 0.012 MPa^{-1} for the four steels investigated here, which compares very well with the values of 0.013 , 0.012 and 0.016 MPa^{-1} reported for HSLA steels, stainless steels and silicon steels, respectively [116, 129, 134]. The value of n' decreases slightly from 5.1 for the base steel to 4.2 for the Cu-Nb-B steel.

To provide a broad and clear picture of the effect of temperature and strain rate on the saturation stress, the following relation used by Kocks [131] can be considered:

$$\ln\left(\frac{\sigma_{ss}^*}{\sigma_0^*}\right) = -\frac{k_B T}{A} \ln\left(\frac{\dot{\epsilon}_0}{\dot{\epsilon}}\right) \quad (6.7)$$

where k_B is the Boltzmann constant and A is another constant. The semi-logarithmic form relating σ_{ss}^* and T is suggested by the similarity with the

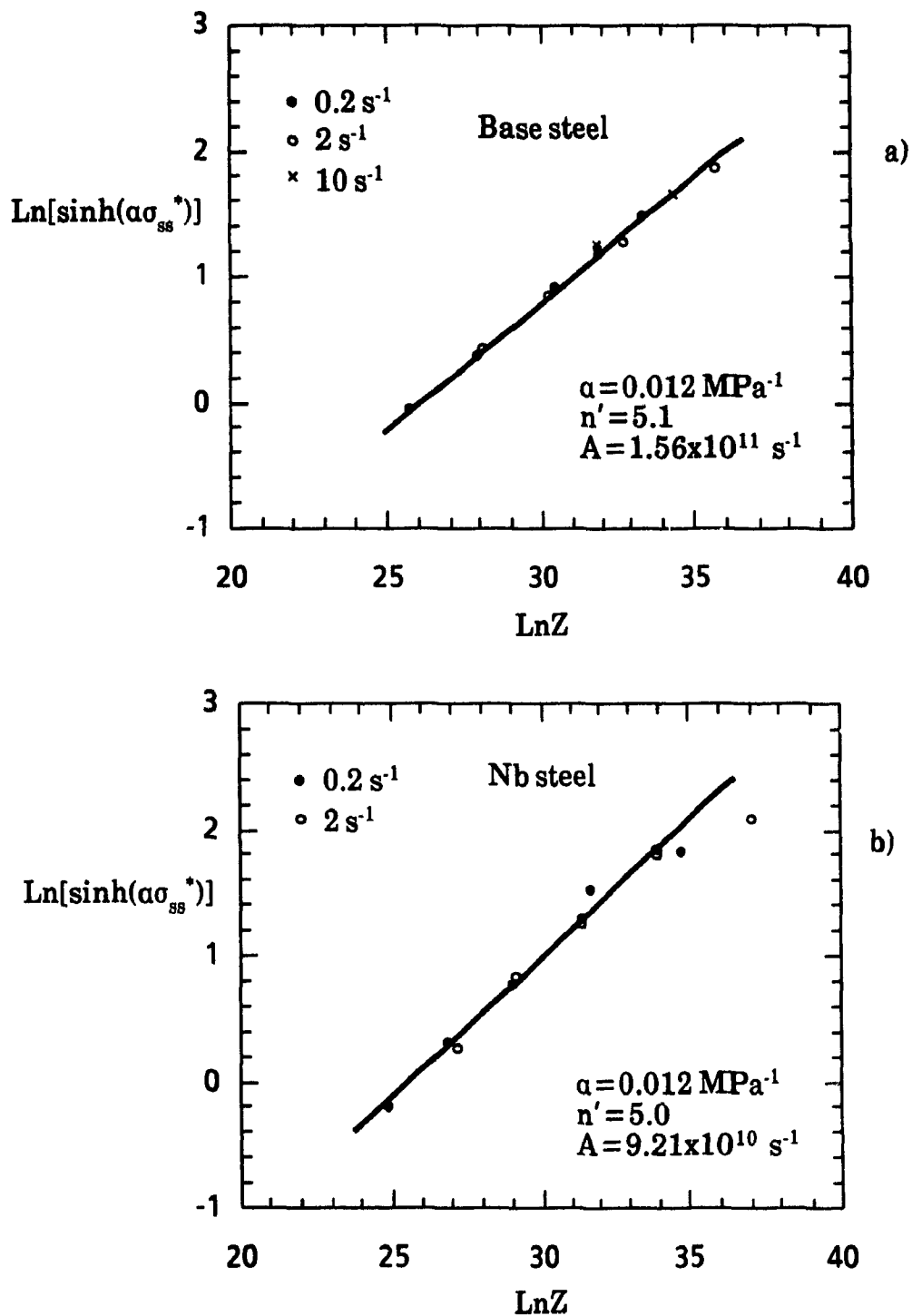


Figure 6.8 Strain rate and temperature dependences of the saturation stress σ_{ss}^* using Eq. 6.6: a) base steel b) Nb steel (contd.).

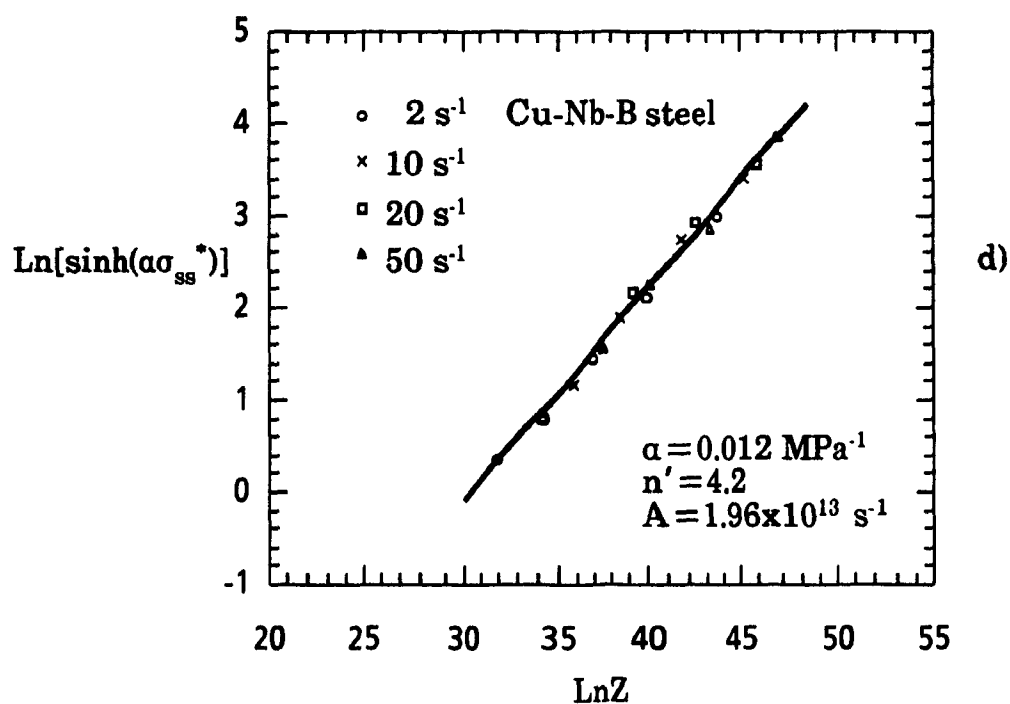
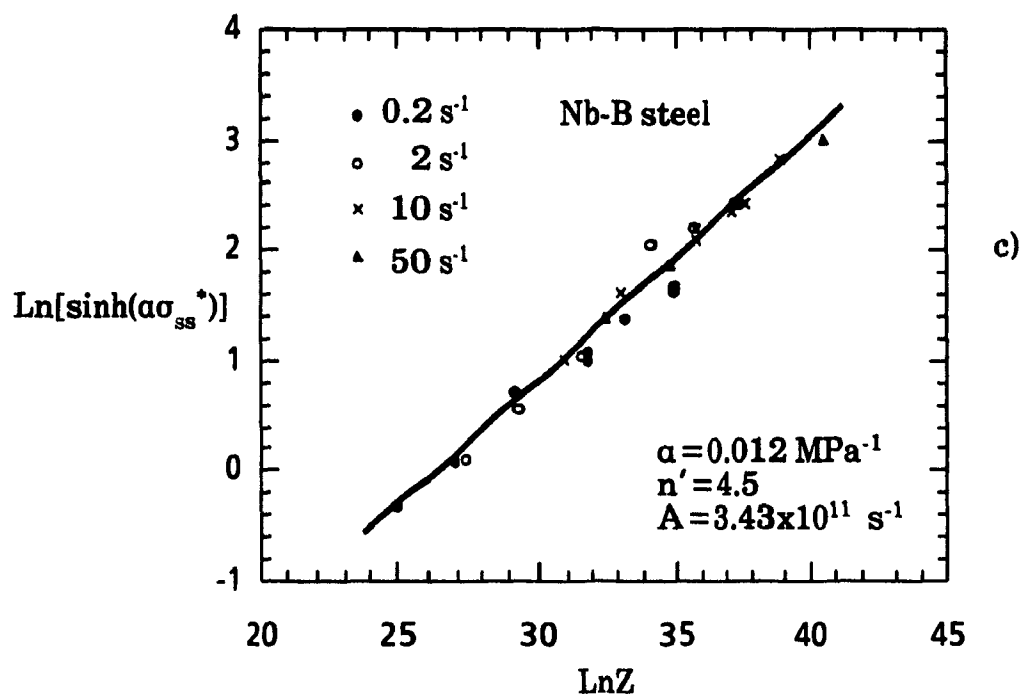


Figure 6.8 Strain rate and temperature dependences of the saturation stress σ_{ss}^* using Eq. 6.6:

c) Nb-B steel

d) Cu-Nb-B steel.

temperature dependence of the stress at the beginning of stage III work hardening in single and polycrystals, as reported by Kocks [131].

Plots of $\ln(\sigma_{ss}^*)$ versus T are shown in Fig 6.9 for the four steels studied. Slight variations from straight line fits are probably caused by the temperature dependence of the shear modulus μ , a well known physical dependence [138]. To eliminate this temperature effect via μ , the values in Fig. 6.9 were normalized as shown in Tables 6.2a to c and will be considered in this form for subsequent calculations.

Table 6.2a Normalized variables shown in Fig. 6.9a for the base steel.

T (K)	T/T _M	μ (GPa)	$10^2 \times kT/\mu b^3$	$10^3 \times \sigma_{ss}^*/\mu$		
				$\dot{\epsilon} = 0.2$ (s ⁻¹)	$\dot{\epsilon} = 2$ (s ⁻¹)	$\dot{\epsilon} = 10$ (s ⁻¹)
1073	0.59	54.0	1.713	3.368	3.960	-
1173	0.65	48.5	2.086	2.844	3.442	4.081
1273	0.70	42.5	2.582	2.303	3.126	3.808
1373	0.76	36.1	3.282	1.966	2.285	-

The values of σ_{ss}^* at 0 K, i.e., σ_0^* , which is independent of strain rate, fall between $3.92 \times 10^{-2} \mu$ and $5.8 \times 10^{-2} \mu$ for the four steels. This is consistent with the values found by Kocks [131] for aluminum, copper and stainless steel (S.S.) (see Table 6.3), higher values of σ_0^*/μ being characteristic of materials with lower stacking fault energies.

Similarly, when $\ln(\sigma_{ss}^*)$ is plotted versus $\ln \dot{\epsilon}$, the straight lines fitting the data at each temperature converge to a strain rate where the saturation stress is independent of temperature (Fig. 6.10). The apparent strain rate sensitivities corresponding to the slopes of the plots in these figures increase with increasing temperature according to Eq. 6.7, where the apparent strain rate sensitivity is given by $k_b T/A$. The mean normalized values of the inverse of the slopes $\mu b^3/A$ are given for the four steels in Table 6.4 and are also plotted against σ_0^*/μ in Fig.

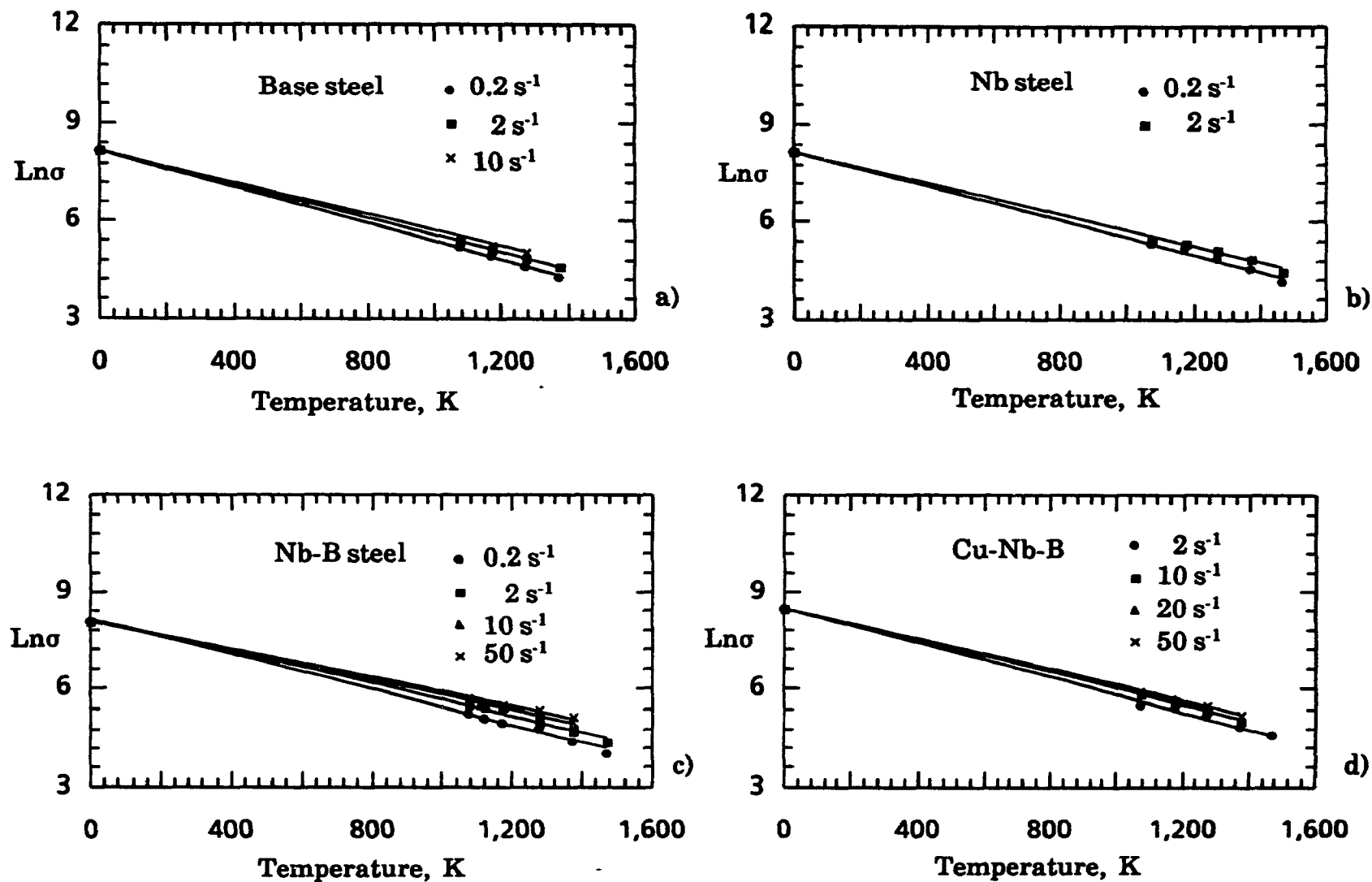


Figure 6.9 Dependences of the saturation stress σ_{ss}^* on temperature in the
a) base steel, b) Nb steel, c) Nb-B steel, d) Cu-Nb-B steel.

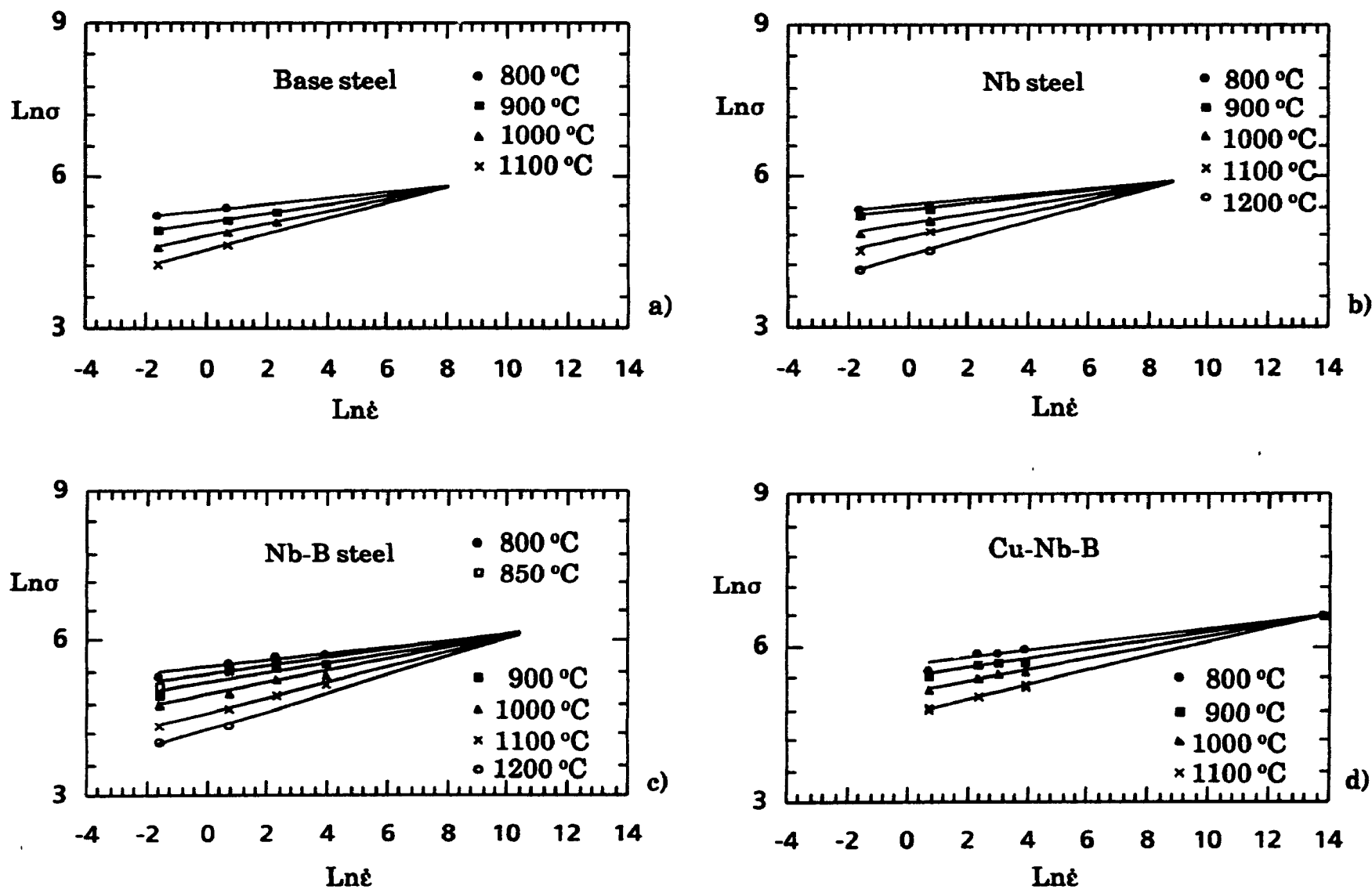


Figure 6.10 Dependences of the saturation stress σ_{ss}^* on strain rate in the
a) base steel, b) Nb steel, c) Nb-B steel, d) Cu-Nb-B steel.

Table 6.2b Normalized variables shown in Fig. 6.9b for the Nb steel.

T (K)	T/T _M	μ (GPa)	$10^2 \times kT/\mu b^3$	$10^3 \times \sigma_{ss}^*/\mu$	
				$\dot{\epsilon}=0.2$ (s ⁻¹)	$\dot{\epsilon}=2$ (s ⁻¹)
1073	0.59	54.0	1.713	3.905	4.294
1173	0.65	48.5	2.086	3.833	4.369
1273	0.70	42.5	2.582	2.962	3.949
1373	0.76	36.1	3.282	2.576	3.656
1473	0.81	29.2	4.353	2.157	3.082

Table 6.2c Normalized variables shown in Fig. 6.9c for the Nb-B steel.

T (K)	T/T _M	μ (GPa)	$10^2 \times kT/\mu b^3$	$10^3 \times \sigma_{ss}^*/\mu$			
				$\dot{\epsilon}=0.2$ (s ⁻¹)	$\dot{\epsilon}=2$ (s ⁻¹)	$\dot{\epsilon}=10$ (s ⁻¹)	$\dot{\epsilon}=50$ (s ⁻¹)
1073	0.59	54.0	1.713	3.683	4.831	5.459	5.719
1123	0.62	51.3	1.888	3.389	4.714	4.968	-
1173	0.65	48.5	2.086	3.071	4.741	4.823	5.359
1273	0.70	42.5	2.582	2.867	3.479	4.561	5.054
1373	0.76	36.1	3.282	2.188	3.075	4.044	4.875
1473	0.81	29.2	4.353	1.917	2.739	-	-

6.11 for comparison with Kocks' data [131]. The values obtained from the present study are in satisfactory agreement with the linear dependence of σ_o^*/μ and $\mu b^3/A$ on stacking fault energy, which is of the following form [131]:

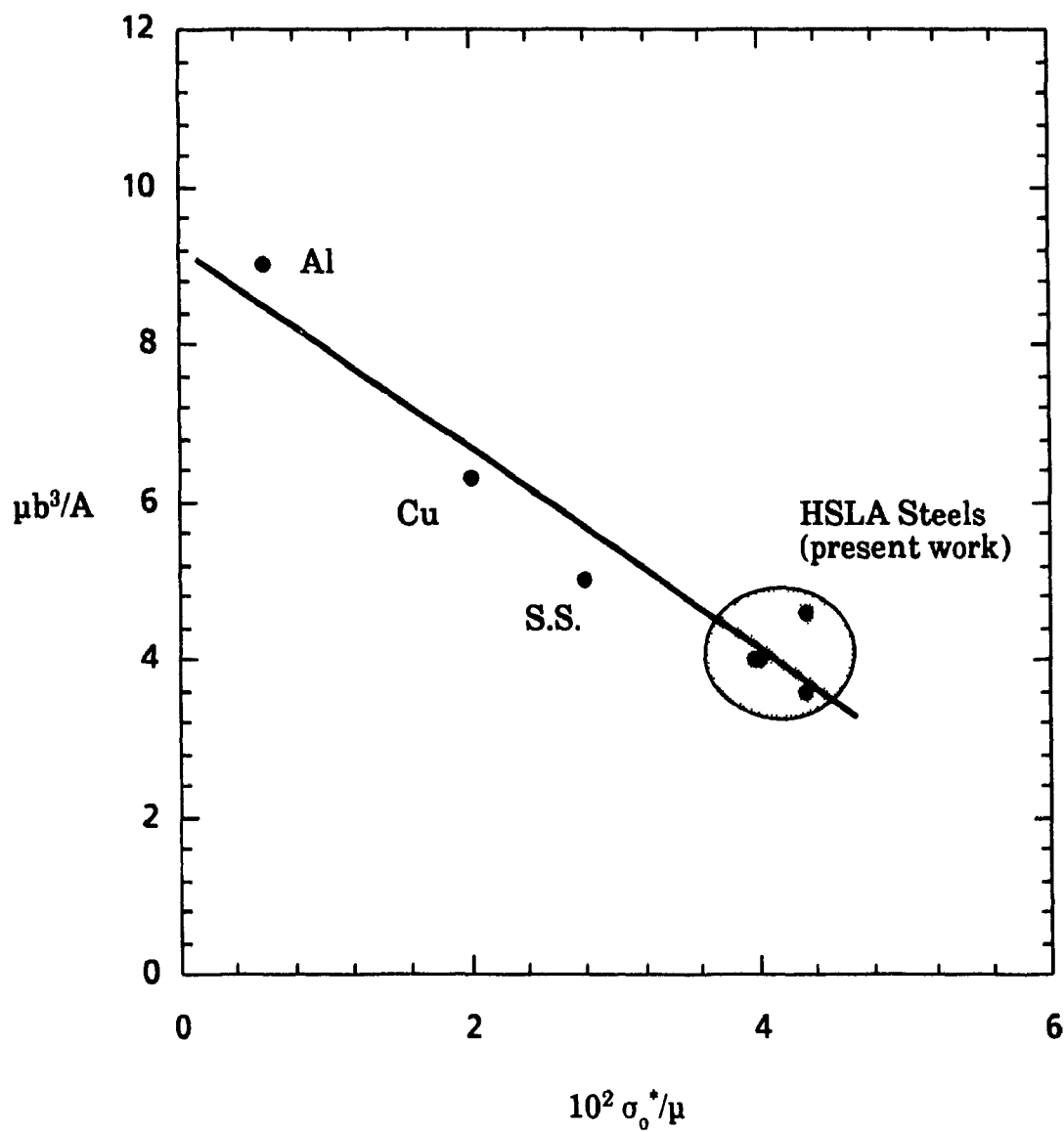


Figure 6.11 Relation between the normalized strain rate sensitivity and saturation stress at 0 K for different materials. Data for Al, Cu and S.S. are taken from reference [131].

Table 6.2d Normalized variables shown in Fig. 6.9d for the Cu-Nb-B steel.

T (K)	T/T _M	μ (GPa)	$10^2 \times kT/\mu b^3$	$10^3 \times \sigma_{ss}^*/\mu$			
				$\dot{\epsilon}=2$ (s ⁻¹)	$\dot{\epsilon}=10$ (s ⁻¹)	$\dot{\epsilon}=20$ (s ⁻¹)	$\dot{\epsilon}=50$ (s ⁻¹)
1073	0.59	54.0	1.713	4.627	6.366	6.588	7.032
1173	0.65	48.5	2.086	4.823	5.936	6.245	6.142
1273	0.70	42.5	2.582	4.231	5.125	5.665	5.806
1373	0.76	36.1	3.282	3.518	4.349	-	5.291
1473	0.81	29.2	4.353	3.322	-	-	-

Table 6.3 Numerical values of the parameters in Eq. 6.7 pertaining to the four steels investigated. Data for Al, Cu and stainless steel (S.S.) are included for comparison.

Material	Base	Nb	Nb-B	Cu-Nb-B	Al*	Cu*	S.S.*
$10^2 \times \sigma_0^*/\mu$	4.3	4.3	3.9-4.1	3.96	0.6	2.0	2.8
$\dot{\epsilon}_0$ (s ⁻¹)	3.8×10^3	8.1×10^3	4.0×10^4	9.8×10^5	5×10^4	5×10^4	5×10^4
$\mu b^3/A$	4.6	3.6	4.0	4.0	9.0	6.3	5.0

* from Ref. [131]

$$\frac{\mu b^3}{A} = C_1 + C_2 \frac{\chi}{\mu b} \quad (6.8a)$$

$$\frac{\sigma_0^*}{\mu} = C_3 - C_4 \frac{\chi}{\mu b} \quad (6.8b)$$

where C_1 to C_4 are positive constants and χ is the stacking fault energy. When combined together, Eqs. 6.8a and b yield a linear relationship between σ_0^*/μ and $\mu b^3/A$, as shown in Fig. 6.11.

Table 6.4 Normalized apparent strain rate sensitivities for the four steels studied.

T K	Base		Nb		Nb-B		Cu-Nb-B	
	kT/A	$\mu b^3/A$	kT/A	$\mu b^3/A$	kT/A	$\mu b^3/A$	kT/A	$\mu b^3/A$
1073	.066	3.82	.055	3.23	.058	3.40	.065	3.79
1123	-	-	-	-	.071	3.73	-	-
1173	.094	4.50	.067	3.21	.084	4.03	.083	3.98
1273	.128	4.96	.100	3.87	.110	4.24	.106	4.09
1373	.163	4.97	.129	3.92	.146	4.43	.131	3.99
1473	-	-	.169	3.87	.175	4.01	-	-

Although the HSLA steel data are in reasonable agreement with the data presented by Kocks, it should be borne in mind that the data he collected for stainless steel were obtained at one strain rate only, and do not therefore allow any conclusions to be drawn about the accuracy of the values obtained in the present work.

As mentioned above, the exponent in Eq. 6.7, i.e.:

$$n = \frac{\partial \ln(\dot{\epsilon})}{\partial \ln(\sigma_{ss}^*)} = \frac{A}{k_B T} \quad (6.9)$$

varies with temperature. Kocks [131] has shown that the steady state stress exponent n is temperature dependent through the isostructural strain rate sensitivity m according to the following equation:

$$\frac{1}{n} = \frac{k_B T}{A'} + \frac{1}{m} \quad (6.10)$$

where A' is a constant. Figure 6.12 shows the dependence of $1/n$ on T for the HSLA steels investigated in the present work and for 316 stainless steel from reference [129]. Although the contribution of the isostructural strain rate

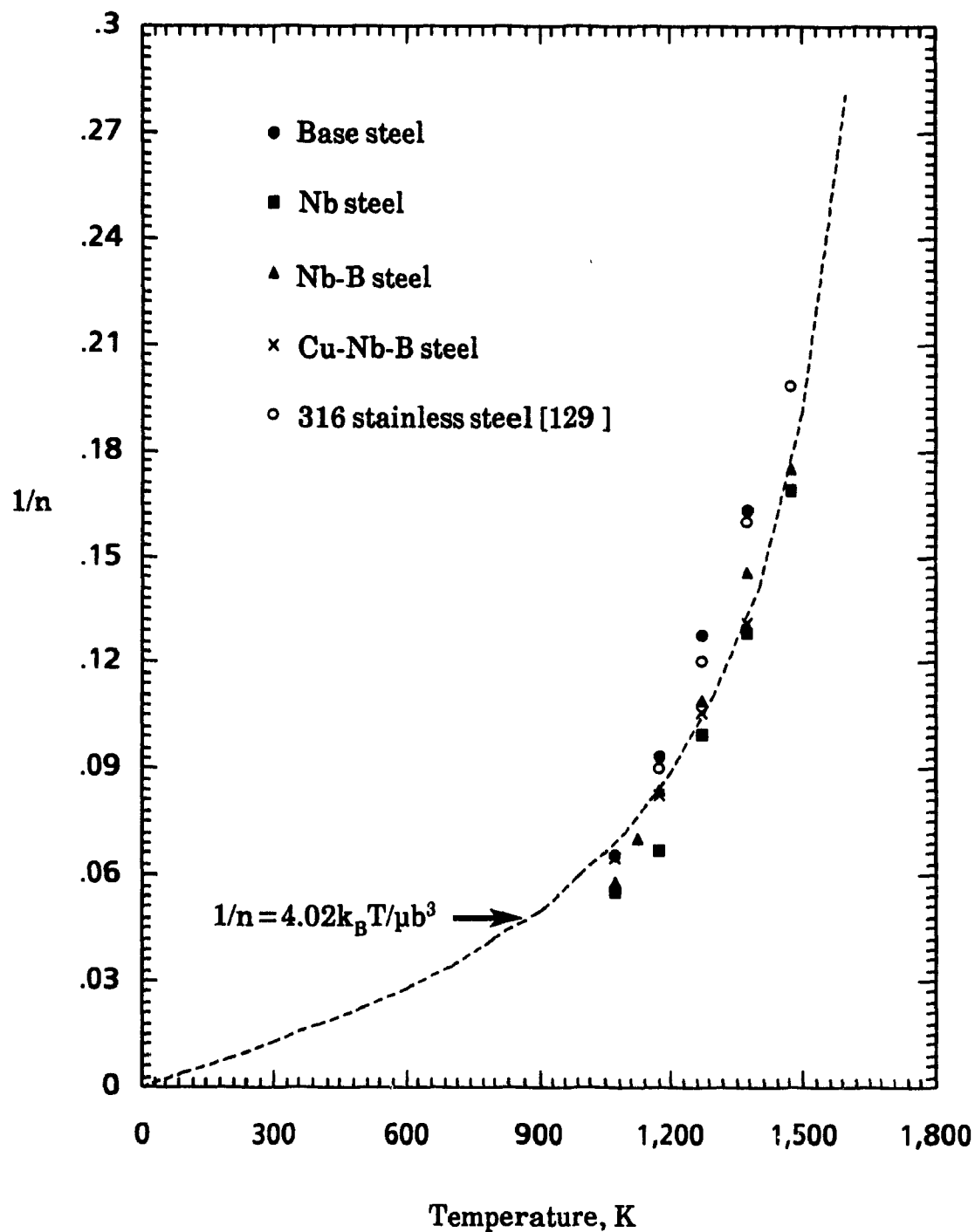


Figure 6.12 Dependence of the coefficient $\partial \ln(\sigma_{SS}^*) / \partial \ln \dot{\epsilon} |_T$ on temperature for the HSLA and 316 stainless steels.

sensitivity m has been shown to be negligible at higher temperatures for aluminum, it is not reasonable to anticipate that this applies to the case of steels. Also, although Kocks has reported that no additional mechanisms are involved at high temperatures in addition to those operating in the low temperature regime, the identification of the rate controlling mechanisms associated with deformation at high temperatures is necessary. This is because the activation parameters associated with σ_{ss}^* are characteristic of these mechanisms [1], which include diffusion controlled climb and node unpinning [133]. Knowledge of these activation parameters and their dependencies on temperature and strain rate permits the identification of the actual deformation mechanism which controls the plastic behavior at different temperatures and strain rates. This will be dealt with in the next section.

6.3.2. Activation Analysis

6.3.2.1 Apparent Activation Enthalpy

Before going further, it is important to make some comments regarding the activation parameters associated with high temperature deformation. The experimentally measurable quantities are termed the *apparent* activation parameters, because they differ from the true activation values which are directly related to the mechanisms controlling the deformation. That is, the measured activation enthalpy (also called activation energy in the literature) and volume are called apparent activation enthalpy and apparent activation volume, respectively. The word "true" is dropped when the true activation parameters are dealt with; i.e. the true activation enthalpy and true activation volume are simply called the activation enthalpy and volume. Finally, the Gibbs free energy of activation ΔG is called the activation free enthalpy.

Figs. 6.13a and b show Arrhenius plots of the strain rate plotted at constant saturation stress against the inverse absolute temperature for the base and Nb-B steels. It should be noted that the points shown on these graphs do not represent the experimental values of Figs. 6.1 and 6.3; they are the constant saturation stress intercepts taken at different temperatures from the $\ln \sigma$ versus $\ln \dot{\epsilon}$ plots of Figs. 6.10a and c. The experimental ranges of strain rate are shown by the two horizontal lines.

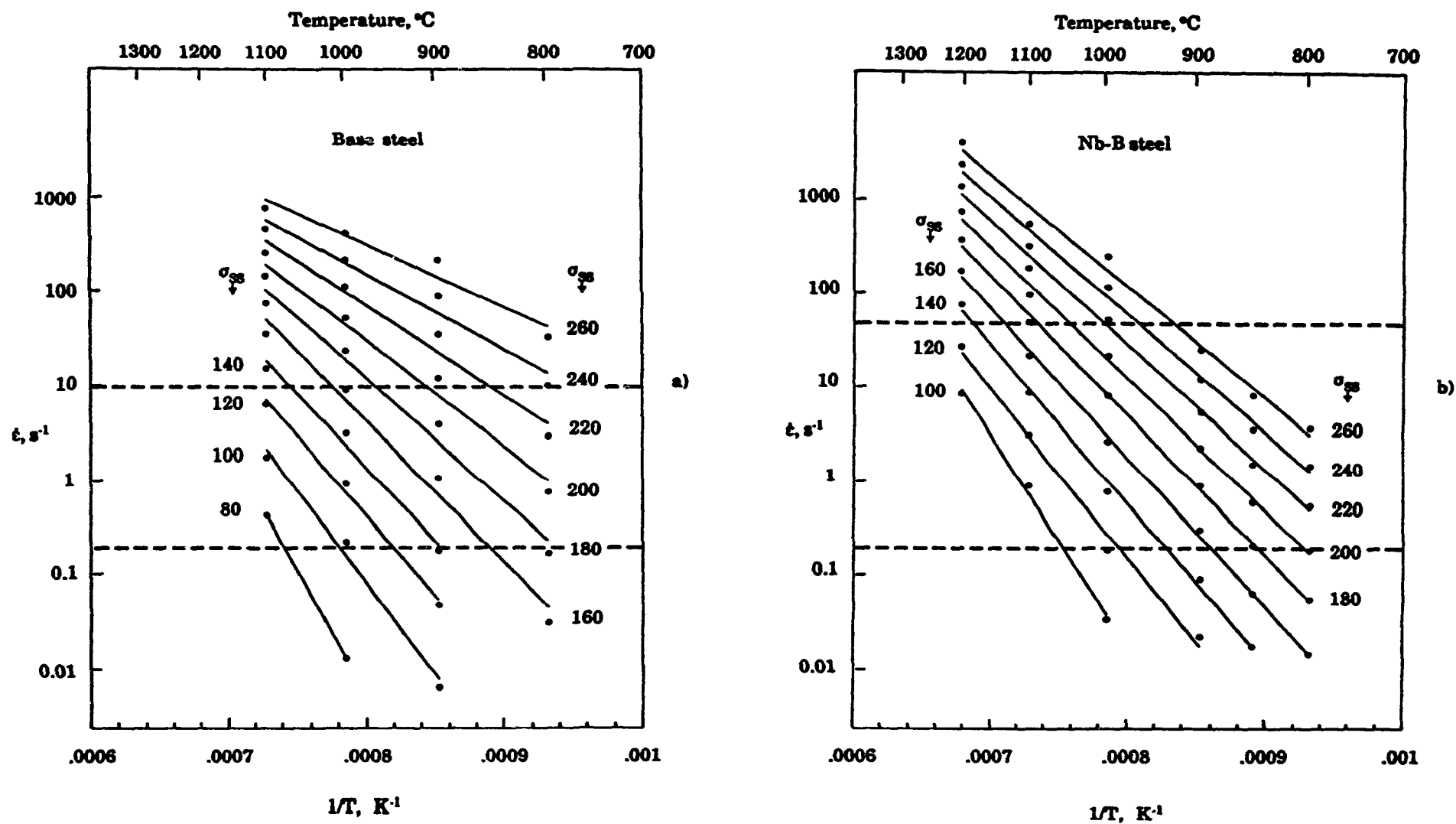


Figure 6.13 Temperature dependence of the strain rate at constant saturation stress in the a) base steel and b) Nb-B steel.

It is clear from the Arrhenius plots that the slopes are not constant but decrease with increasing saturation stress. The apparent activation enthalpies are determined from these slopes as follows:

$$Q = -k_B \left. \frac{\partial \ln(\dot{\epsilon})}{\partial (1/T)} \right|_{\sigma_{SS}} \quad (6.11)$$

Although some change in the constant stress slope occurs in the case of the plain carbon steel, particularly at lower temperatures, reasonable averages of the apparent activation enthalpy can be taken within the experimental ranges of strain rate and temperature. It is apparent from Fig. 6.13 that Q is strongly stress dependent, especially at low stress levels, and decreases with increasing stress. This behavior has been observed for Armco iron and silicon steel [99, 139], and stainless [129] and HSLA [133] steels.

It is important to note here that the values of Q at the lower stresses may have been overestimated due to the way they were calculated by the computer program. The latter determines the number of intercepts between the $\sigma = \text{constant}$ and $\ln \sigma / \ln \dot{\epsilon}$ lines, which leads to sets of data pairs ($\ln \dot{\epsilon}$, $1/T$) at constant stress. At the lower stresses, the $\ln \dot{\epsilon}$ values determined in this way can be very low; they were therefore eliminated from the calculation of the slope in the Arrhenius plot. The number of points for regressing the data pairs at constant stress was reduced in this way, so that the remaining points were insufficient for the accurate determination of the slope.

For the steels used in the present study, most of the error associated with the determination of the slope occurs out of the range of the experiments. Since mean values of the apparent activation energy are required in process modelling, the low stress problem can be overcome by taking average values of Q over the experimental strain rate and temperature range. These values turned out to be 312, 325, 326 and 382 kJ/mole for the base, Nb, Nb-B and Cu-Nb-B steels, respectively. The mean values of Q for the first three steels are close to that of self-diffusion and compare well with values found in the literature for steels, both in the creep and in the hot working ranges [116, 134, 137]. However, the value of 382 kJ/mole obtained for the copper steel is

somewhat higher than Q_{SD} . This is probably due to the high level of copper in solution. Values of Q up to 435 kJ/mole in the hot working range have been reported in HSLA steels and up to 508 kJ/mole for stainless steel [137]. In the latter steels, alloying additions clearly raise the apparent activation energy, a phenomenon which is manifested by the increase in flow stress.

The strong dependence of Q on stress reflects the strong dependence of the steady state stress on structure. In fact, the values of σ_{ss} in Fig. 6.10 do not correspond to isostructural values. After a small value of microstrain, the structure changes and evolves rapidly with strain to a stable state corresponding to the saturation stress. The dependence of σ_{ss} on structure is the reason for the convergence of the slopes in Fig. 6.10 to a value which corresponds to $\dot{\epsilon}_0$, a behavior that was also observed by Kocks [131] and Ryan and McQueen [129, 130]. The $\ln\sigma/\ln\dot{\epsilon}$ slopes would have been parallel had the *isostructural* saturation stress been used, which would have resulted in a constant value of Q . To evaluate the correct value of Q , one must account for the structure in the rate equation. If the state of the structure S_t (S_t can be the dislocation density, subgrain size, grain size,...) is introduced into this equation, in the following form† for instance [140]:

$$\dot{\epsilon} = B\sigma_{SS}^p S_t^q \exp\left(-\frac{Q}{RT}\right) \quad (6.12)$$

by differentiation we obtain:

$$Q = -k_B \left. \frac{\partial \ln(\dot{\epsilon})}{\partial (1/T)} \right|_{\sigma_{SS}, S_t} + k_B q \left. \frac{\partial \ln(S_t)}{\partial (1/T)} \right|_{\sigma_{SS}} \quad (6.13)$$

The term $q \partial \ln S_t / \partial (1/T)|_{\sigma_{SS}}$ contributes to the dependence of $\partial \ln \dot{\epsilon} / \partial (1/T)|_{\sigma_{SS}, S_t}$ on stress, and Q can be calculated if the dependence of S_t on temperature is known. Finally, it should be added that part of the apparent stress dependence of Q can be attributed to the nature of the rate controlling obstacle itself [138].

† Use of the hyperbolic sine rate equation with any functional form of S_t leads to similar conclusions.

To separate the effect of structure from the other effects, strain rate change experiments could be performed to determine the change of stress with strain rate at constant structure. However, recovery effects associated with the sudden change in strain rate at high temperatures affect the results considerably [140]. Furthermore, the curve after the strain rate change is too smooth to permit the ready determination of the instantaneous stress [141]. Another alternative to employing the saturation stress is to use the *effective* stress, which can be arranged to correspond to a constant structure. However, the same problem remains because of the difficulty of defining the effective stress at high temperatures; this is associated with the rapid change of structure at the initiation of flow.

6.3.2.2. Apparent Activation Volume

The apparent activation volume was determined using the following expression† [2, 125, 138]:

$$V_{app} = k_B T \left. \frac{\partial \ln(\dot{\epsilon})}{\partial \tau} \right|_T = \frac{2nk_B T}{\sigma_{SS}} \quad (6.14)$$

where n is given by Eq. 6.9.

The stress dependence of the activation volume at constant temperature is exemplified in Figs. 6.14a and b for the base and Nb-B steels. At each temperature, the apparent activation volume decreases rapidly with increasing stress. This behavior is similar for all the steels. It is also clear that the V_{app} values derived in this work are lower than those pertaining to pure iron [99, 139]. This can be linked to the higher dislocation densities expected to be present in alloyed steels.

† The average Taylor factor was taken as 2.

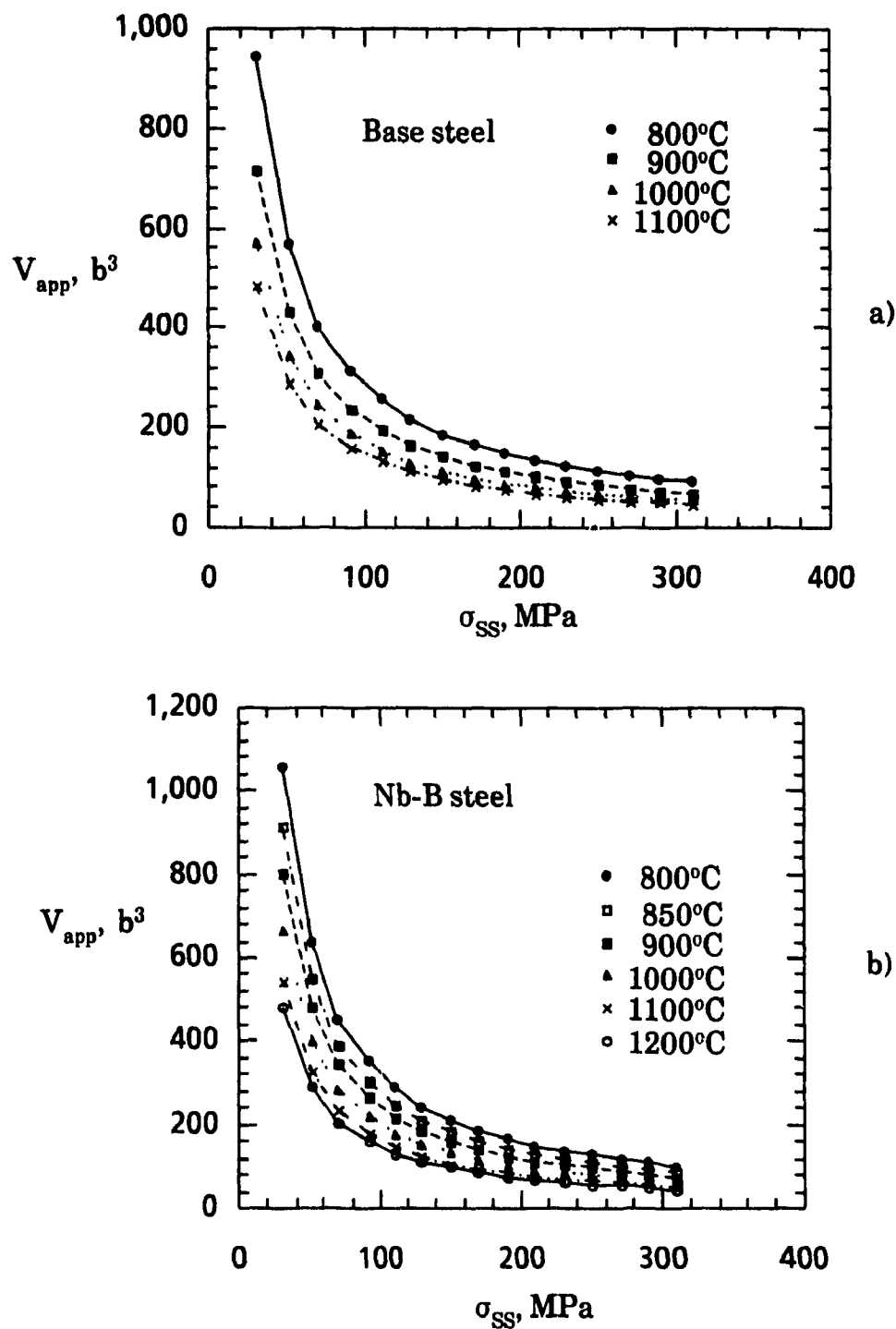


Figure 6.14 Stress dependence of the apparent activation volume in the
a) base steel, b) Nb-B steel.

The effect of temperature on the apparent activation volume is evident from Fig. 6.14. At a given stress, an increase in temperature leads to a decrease in the apparent activation volume. To illustrate this effect, the data have been replotted as a function of the modulus-corrected term σ/μ , where μ is the shear modulus†. Fig. 6.15 shows that the apparent activation volumes corresponding to different temperatures fit the same curve for the base steel. The temperature dependence of V_{app} is thus due to the temperature dependence of μ ; V_{app} itself is solely a function of the shear modulus-reduced stress.

6.3.2.3. Activation Free Enthalpy

To calculate the activation free energy ΔG , one can use the general rate equation [131, 138, 144]:

$$\Delta G = k_B T \ln \left(\frac{\dot{\epsilon}_0}{\dot{\epsilon}} \right) \quad (6.15)$$

which is only possible when the stress and temperature dependence of the pre-exponential factor $\dot{\epsilon}_0$ is known. For the evaluation of ΔG , this factor can be assumed to be either constant or a function of σ/μ only. For the derivation of the expression for the activation free energy ΔG in terms of the experimental activation quantities Q and V_{app} , the reader is referred to Appendix A.

Fig. 6.16a shows the stress and temperature dependence of ΔG calculated from Eq. A.8 in the appendix for the Nb-B steel. At a constant temperature, ΔG depends strongly on the stress. This dependence is similar to that of the apparent activation enthalpy. At constant stress, however, the temperature dependence of ΔG is also strong; decreasing the temperature results in an increase in the activation free enthalpy.

† Data for μ as a function of temperature are taken from references [138, 142, 143].

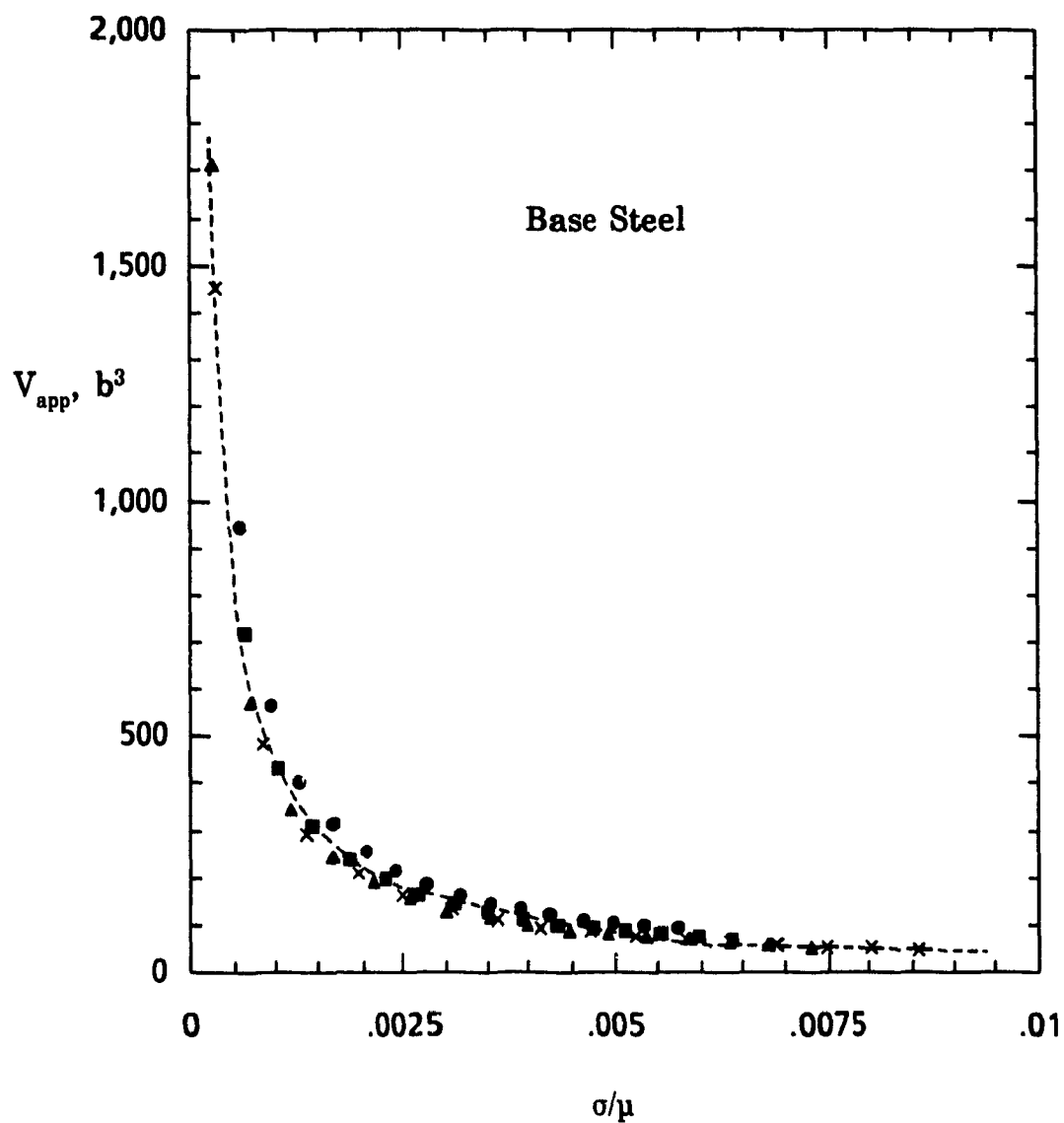


Figure 6.15 Dependence of the apparent activation volume on the modulus-reduced stress in the base steel.

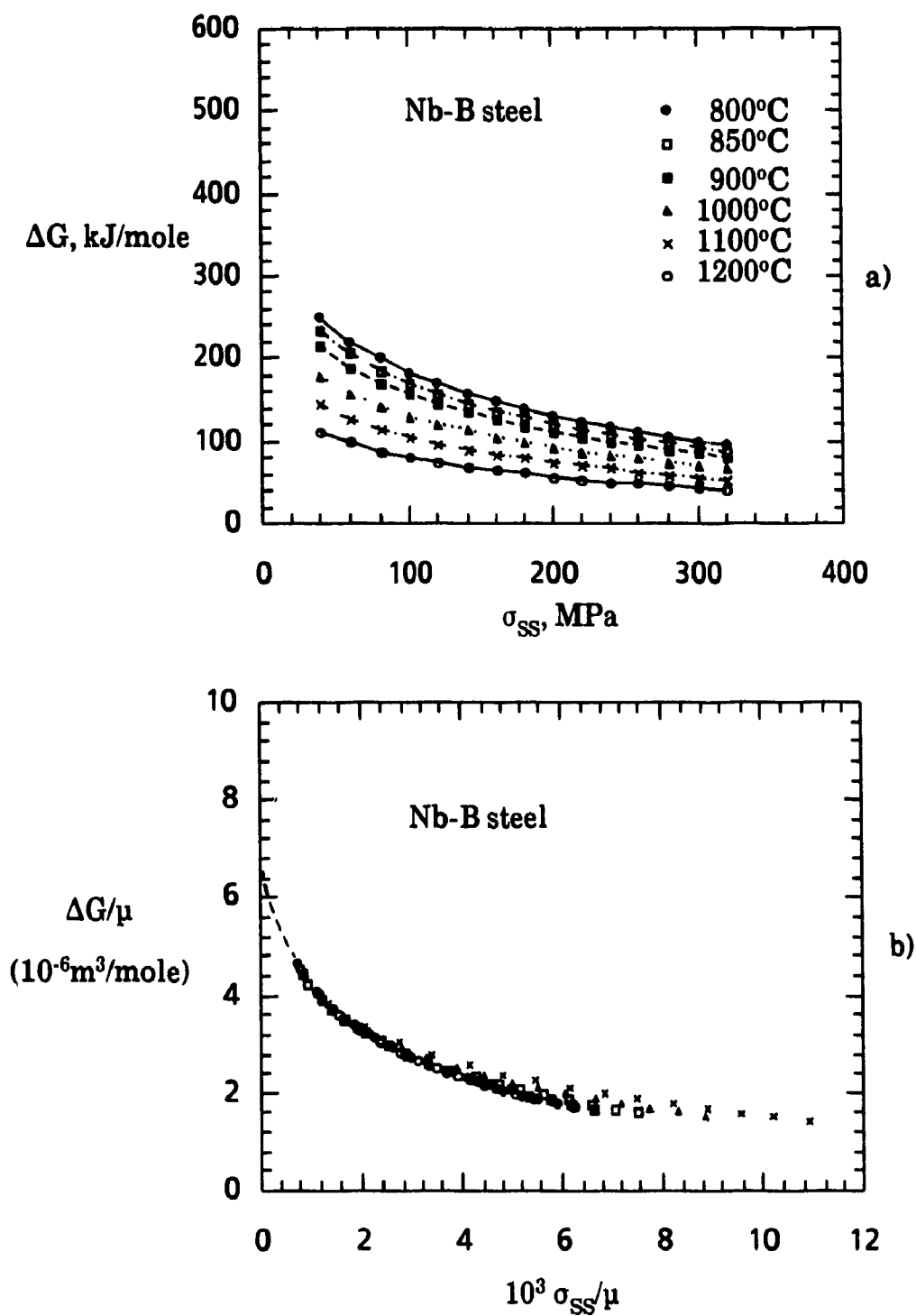


Figure 6.16 a) Stress dependence of the activation free energy in the Nb-B steel.
 b) Dependence of the modulus-reduced activation free energy on σ_{SS}/μ in the Nb-B steel.

To eliminate the temperature dependence of ΔG , plots of shear modulus-reduced ΔG and σ_{ss} were attempted (Fig. 6.16b). It is clear that by normalizing the variables by μ , the activation free enthalpy is no longer temperature dependent. Furthermore, above a certain stress level, ΔG approaches a near constant value without much further decrease. When ΔG plot is back-extrapolated to zero σ_{ss}/μ , it leads to the characteristic value of the activation free energy, ΔG_o [138]. Although such extrapolations are not very accurate, they nevertheless give a good indication of the nature of the rate controlling obstacle. At $\Delta G_o/\mu = 6.5 \times 10^{-6}$ m³/mole, this could be attractive intersection, for example, with the ΔG_o value corresponding to the energy required to unpin the attractive nodes [1].

Once ΔG is known, the pre-exponential factor $\dot{\epsilon}_o$ can be determined from Eq. 6.15; this leads to values between 8 and 16. These are similar to the values quoted by Kocks et al. [138] for the strain rate range 10^{-2} - 10^2 s⁻¹. The scatter in the data do not permit a conclusion to be drawn regarding whether $\dot{\epsilon}_o$ is constant or proportional to σ_{ss}/μ . Nevertheless, even if $\dot{\epsilon}_o$ could be determined accurately, the evaluation of the true activation parameters (such as the activation enthalpy ΔH , the activation volume V and the activation entropy ΔS), would unduly extend our treatment of this subject. Immarigeon [99] and Immarigeon and Jonas [139] have shown that the activation enthalpy, the activation volume and entropy are given by the following expressions:

$$\Delta H = Q + m_o \frac{T^2}{\mu(T)} \frac{d\mu(T)}{dT} \quad (6.16a)$$

$$V = V_{app} - 2m_o \frac{k_B T}{\sigma} \quad (6.16b)$$

$$\Delta S = - \frac{1}{\mu} \frac{d\mu}{dT} (\Delta G + V \frac{\sigma}{2}) \quad (6.16c)$$

where m_o is a constant (see Appendix A). At a given temperature, since $d\mu/dT$ is negative in Eq. 6.16 a, the stress dependence of the activation enthalpy is parallel to that of the apparent activation enthalpy, with lower values. The same remarks apply to the activation volume versus the apparent activation

volume. While V and V_{app} can differ by almost a factor of two [139], there is much less difference between ΔH and Q . If we assume that this generalization applies to the present case, knowledge of the apparent activation parameters for steel is sufficient for a qualitative check of the rate controlling mechanism.

Most of the high temperature deformation theories have the common characteristic that the activation energy for deformation is approximately equal to that for self-diffusion. These theories include the cross-slip, dislocation climb and recovery models. However, cross-slip is unlikely to be the rate controlling mechanism at homologous temperatures above 0.5 [145]. Dislocation climb theories, on the other hand, have been called upon to explain steady state flow. However, since they are associated with activation volume values of about $1 b^3$ [99, 125, 146], the present activation parameters are not consistent with the climb models. To account for a ΔH which is stress dependent and V values of $100 b^3$ or higher, Immarigeon and Jonas [139] suggested a recovery model. The latter has the advantage that it includes the concept of internal stress and allows for both work hardening and recovery; thus it can apply to steady state flow as well as to transient deformation.

6.4. EVOLUTION EQUATION

6.4.1. Work Hardening Rate

6.4.1.1. Stress, Strain Rate and Temperature Dependence of the Work Hardening Rate

In the flow curves determined at constant true strain rate and temperature, the slope of the stress versus plastic strain relation corresponds to the work hardening rate, i.e.:

$$\Theta = \left. \frac{\partial \sigma}{\partial \epsilon} \right|_{\dot{\epsilon}, T} \quad (6.17)$$

The hardening rate during deformation can be analyzed by considering plots of the hardening rate Θ versus the true stress σ [131]. From the form of the

Θ - σ curve, accurate information can be extracted concerning the relationship between stress and strain.

Figs. 6.17 to 6.20 show typical Θ - σ curves converted from the present stress/strain data using the procedure described in section 5.2.3. It is evident from these curves that the work hardening rate decreases rapidly with stress under all conditions of strain rate and temperature; this decrease is more pronounced at high strain rates and low temperatures. It is of interest that when the temperature is decreased, the dependence of stress on temperature at constant work hardening rate (i.e. the term $\partial \ln \sigma / \partial T|_{\Theta, \dot{\epsilon}}$) decreases, particularly when the strain rate is increased. This is evident if we compare Figs. 6.17a, b and c, or 6.18a and b, etc... . At relatively high strain rates, the Θ - σ curves overlap showing less sensitivity to temperature. This behavior can be explained in terms of Eq. 6.7, which can be assumed to also hold during transients [131]. According to this equation, the temperature sensitivity at constant work hardening rate is then equal to $(k_B/A) \ln(\dot{\epsilon}/\dot{\epsilon}_0)$. Since $\dot{\epsilon}_0 > \dot{\epsilon}$, $\partial \ln \sigma / \partial T|_{\Theta, \dot{\epsilon}}$ decreases when the strain rate is increased.

Extrapolation of the initial range of the Θ - σ diagram by straight lines to $\sigma=0$ yields values of the initial athermal work hardening rate Θ_0 . For the steels investigated in the present work, the behavior differs from that of pure aluminum and copper reported by Kocks [131] and Ferron and Mliha-Touati [141] in the sense that the extrapolated lines at different strain rates and temperatures do not converge to a constant value of Θ_0/μ . In particular, when the temperature is high, the work hardening rate back extrapolated to zero stress can take very high values. This behavior was observed by Mliha-Touati [147] and by Diercks and Burke [148] in 304 stainless steel, and was believed to be due to the contribution of solution and/or precipitation hardening to the flow stress. Although the extrapolated lines for the HSLA steels converge before the Θ/μ axis, most of the intercepts fluctuate around a value of Θ_0 between $\mu/15$ and $\mu/10$. These values are similar to those for other materials (Table 6.5).

6.4.1.2. Phenomenological Formalism of the Θ - σ Law

To model the dependence of work hardening rate on stress, a relation of the form :

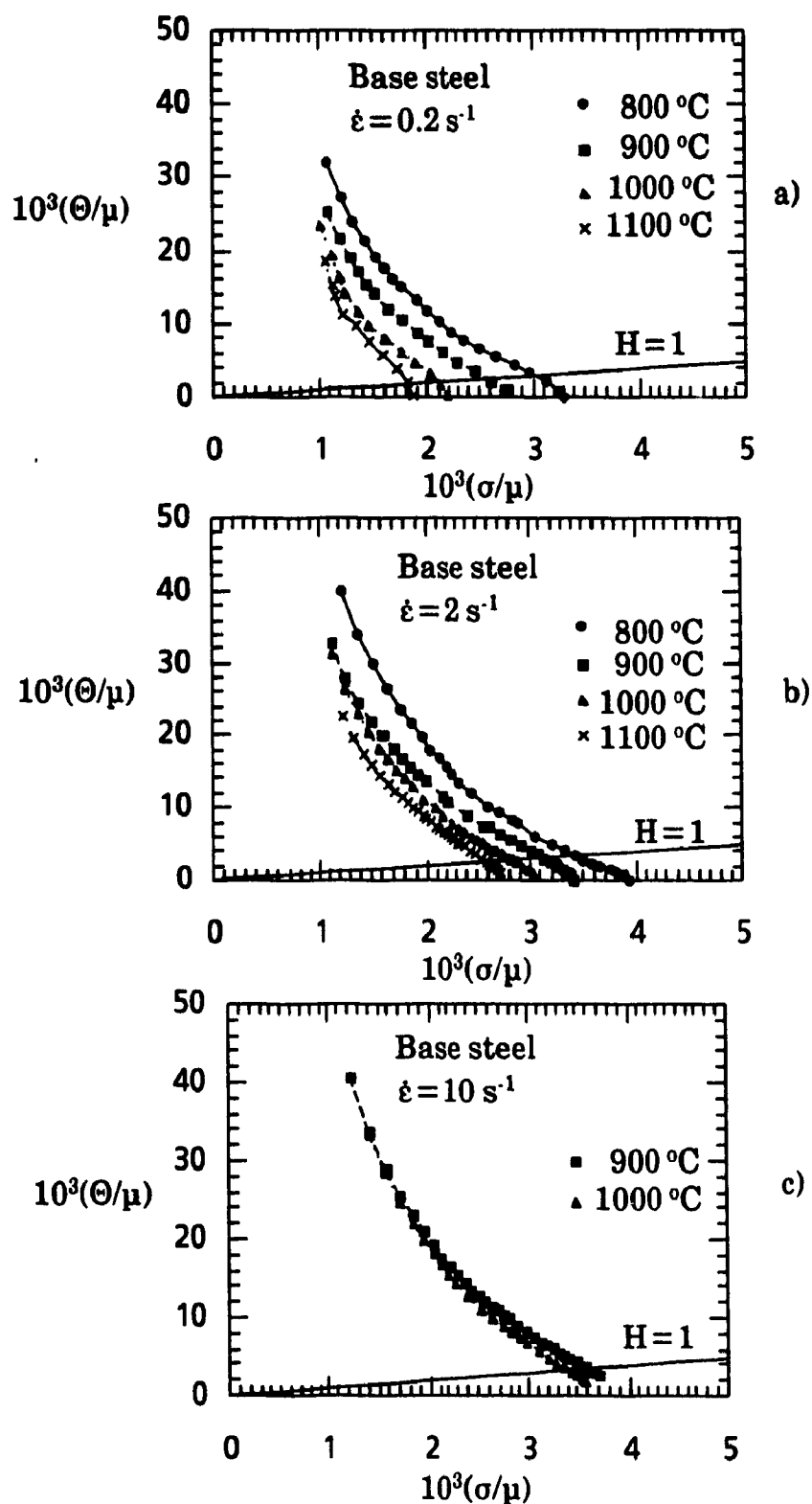


Figure 6.17 Stress dependence of the work hardening rate at different temperatures in the base steel: a) $\dot{\epsilon} = 0.2 \text{ s}^{-1}$, b) $\dot{\epsilon} = 2 \text{ s}^{-1}$, c) $\dot{\epsilon} = 10 \text{ s}^{-1}$.

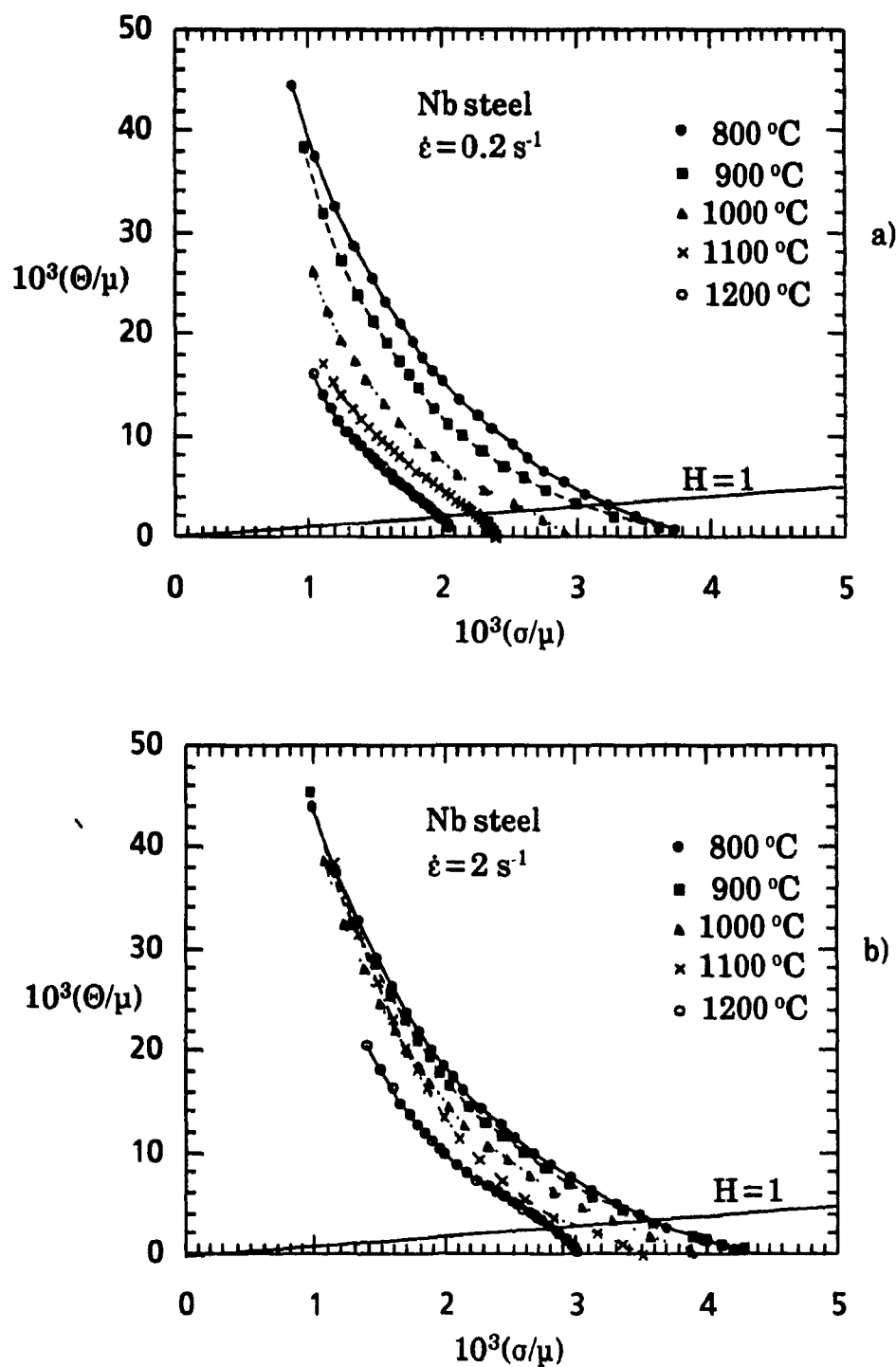


Figure 6.18 Stress dependence of the work hardening rate at different temperatures in the Nb steel. a) $\dot{\epsilon} = 0.2 \text{ s}^{-1}$, b) $\dot{\epsilon} = 2 \text{ s}^{-1}$.

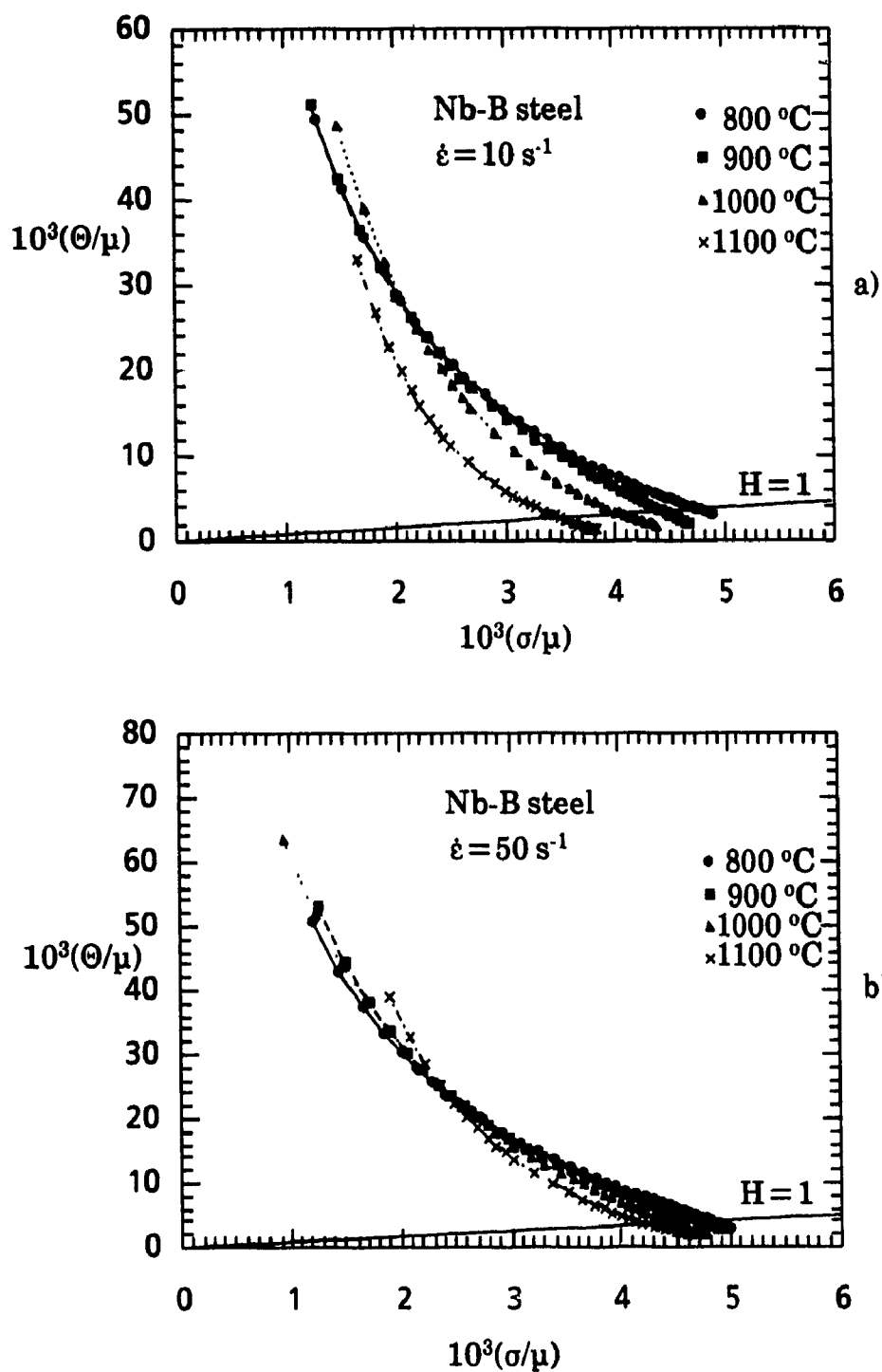


Figure 6.19 Stress dependence of the work hardening rate at different temperatures in the Nb-B steel. a) $\dot{\epsilon} = 10 \text{ s}^{-1}$, b) $\dot{\epsilon} = 50 \text{ s}^{-1}$.

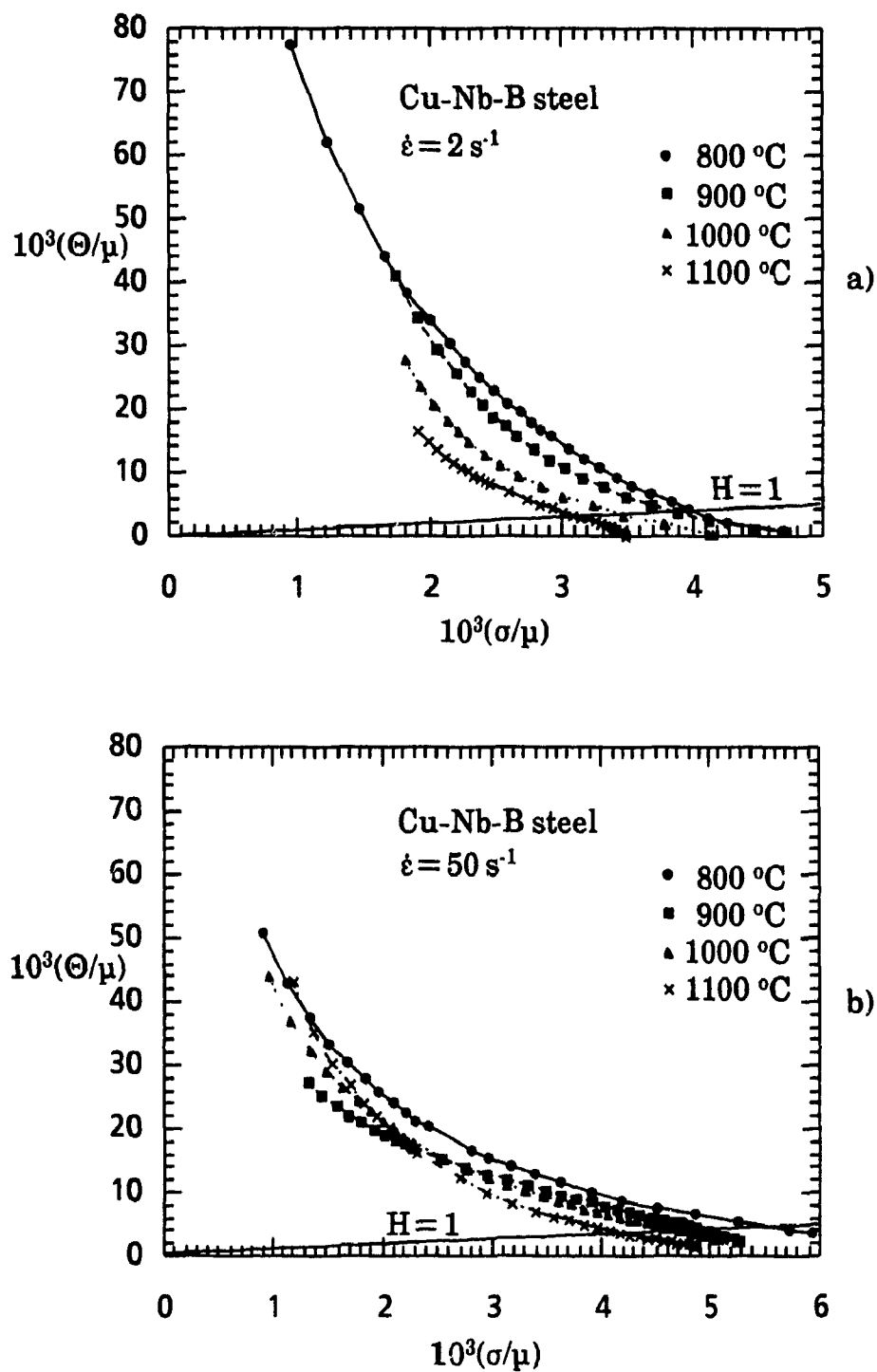


Figure 6.20 Stress dependence of the work hardening rate at different temperatures in the Cu-Nb-B steel. a) $\dot{\epsilon} = 2 \text{ s}^{-1}$, b) $\dot{\epsilon} = 50 \text{ s}^{-1}$.

Table 6.5 Comparison of numerical values of the modulus-reduced initial work hardening rate Θ_0/μ .

Material	Base & Nb	Nb-B & Cu-Nb-B	Pure Al ^[131]	99.5% Al ^[141]
$10^2 \times \Theta_0/\mu$	6.0-8.0	9.0-10.0	6.0	9.7
Material	Cu ^[131]	S.S. ^[131]	Nb-V-Mo ^[149]	Fe-Si ^[150]
$10^2 \times \Theta_0/\mu$	6.0	5.5	6.2-6.5	5.0

$$\Theta = \Theta_0 \left(1 - \frac{\sigma}{\sigma_{ss}^*}\right) \quad (6.18)$$

has been used by many authors [78, 131, 141]. According to the above equation, for a given temperature and strain rate, the work hardening rate varies linearly with stress from Θ_0 to 0. If this is approximately true at low homologous temperatures ($T_H \sim 0.1-0.2$), it is certainly not the case for the rather higher temperatures used here. Examination of the work hardening data in Figs. 6.17 to 6.20 indicates clearly that Θ is not linear with respect to σ . Brown [150] and Brown et al. [151] found similar non-linear dependencies of Θ on σ in silicon steel over the same ranges of temperature as were used in the present work. They modified Eq. 6.18 by adding an exponent to $(1 - \sigma/\sigma_{ss}^*)$ to account for the non-linearity. However, the accuracy in fitting the Θ - σ curves was not significantly improved.

Roberts [133] found that Eq. 6.18 gave an excellent fit to the compression data obtained on pure aluminum between 450 and 600 K, but only over a limited strain range. At higher stresses (strains), he observed that the data deviated considerably from this linear law when the saturation stress was approached. This led Choquet et al. [132] to divide the Θ - σ diagram into three successive linear regions from $\Theta = \Theta_0$ to $\Theta = 0$. Although this partitioning procedure reduces the errors involved in estimating the work hardening rate as a function of stress, the number of constants involved in the integration of Eq. 6.18 becomes too large to provide a meaningful description.

For deformations higher than 0.05, Roberts observed that Θ was linearly related to $1/\sigma$ instead of σ . In his work, plots of the work hardening rate versus the inverse stress were almost straight, with slopes that increased with increasing temperature and decreasing strain rate, as does $1/\sigma_{ss}^*$. To examine the validity of the relation proposed by Roberts, such plots are portrayed in Fig. 6.21 for selected strain rates and temperatures. It is evident that this formalism is a good way of describing the work hardening rate as a function of stress.

With the aid of the above description of the work hardening rate, i.e., the linear Θ - σ relation considered by Kocks and the linear dependence of Θ on $1/\sigma$ found by Roberts, and supported by the high initial values of the work hardening rate observed here, one can assume that the work hardening law has the following form:

$$\Theta = \frac{A}{\sigma} - B\sigma \quad (6.19)$$

which is a combination of a linear and a non-linear function of σ . This form is justified by the experimental data in the present work, and is similar to the work hardening rate that can be derived from the Bergström equation, which describes the dependence of flow stress on strain [112, 152, 153]. Fig. 6.22 shows that Eq. 6.19 represents the decrease in the work hardening rate with increase in stress very well. It will be instructive to attempt to account for Eq. 6.19 in mechanistic terms. This will be treated in the next section.

6.4.2. Model of the Stress/Strain Curve

6.4.2.1. Mechanistic Interpretation

During deformation, the evolution of the dislocation density with strain (or time) is generally considered to consist of two components [131, 154, 155]:

$$\frac{d\rho}{d\varepsilon} = \left. \frac{d\rho}{d\varepsilon} \right|_{\text{storage}} - \left. \frac{d\rho}{d\varepsilon} \right|_{\text{recovery}} \quad (6.20)$$

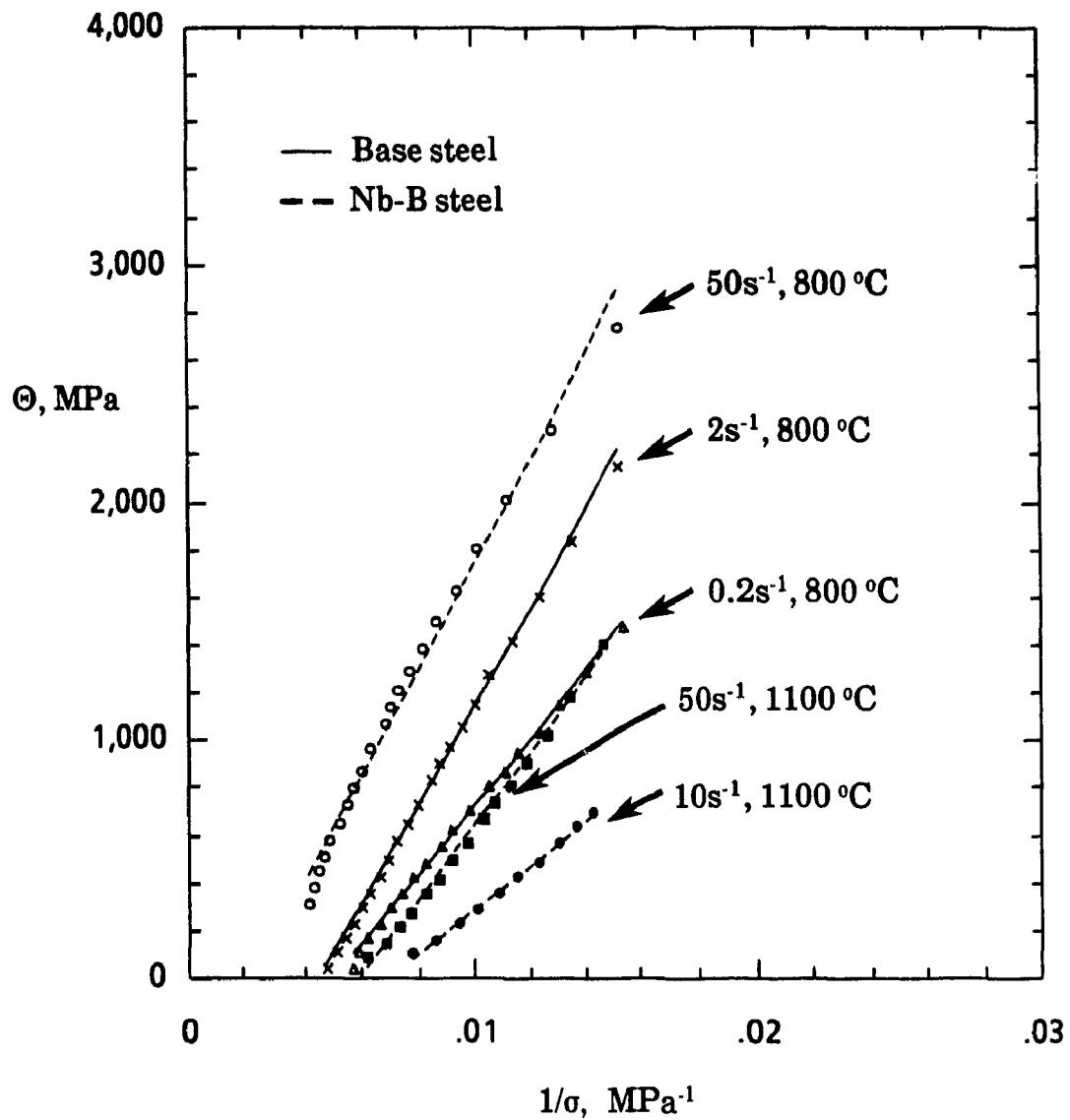


Figure 6.21 Dependence of the work hardening rate Θ on the inverse stress for the base and Nb-B steels.

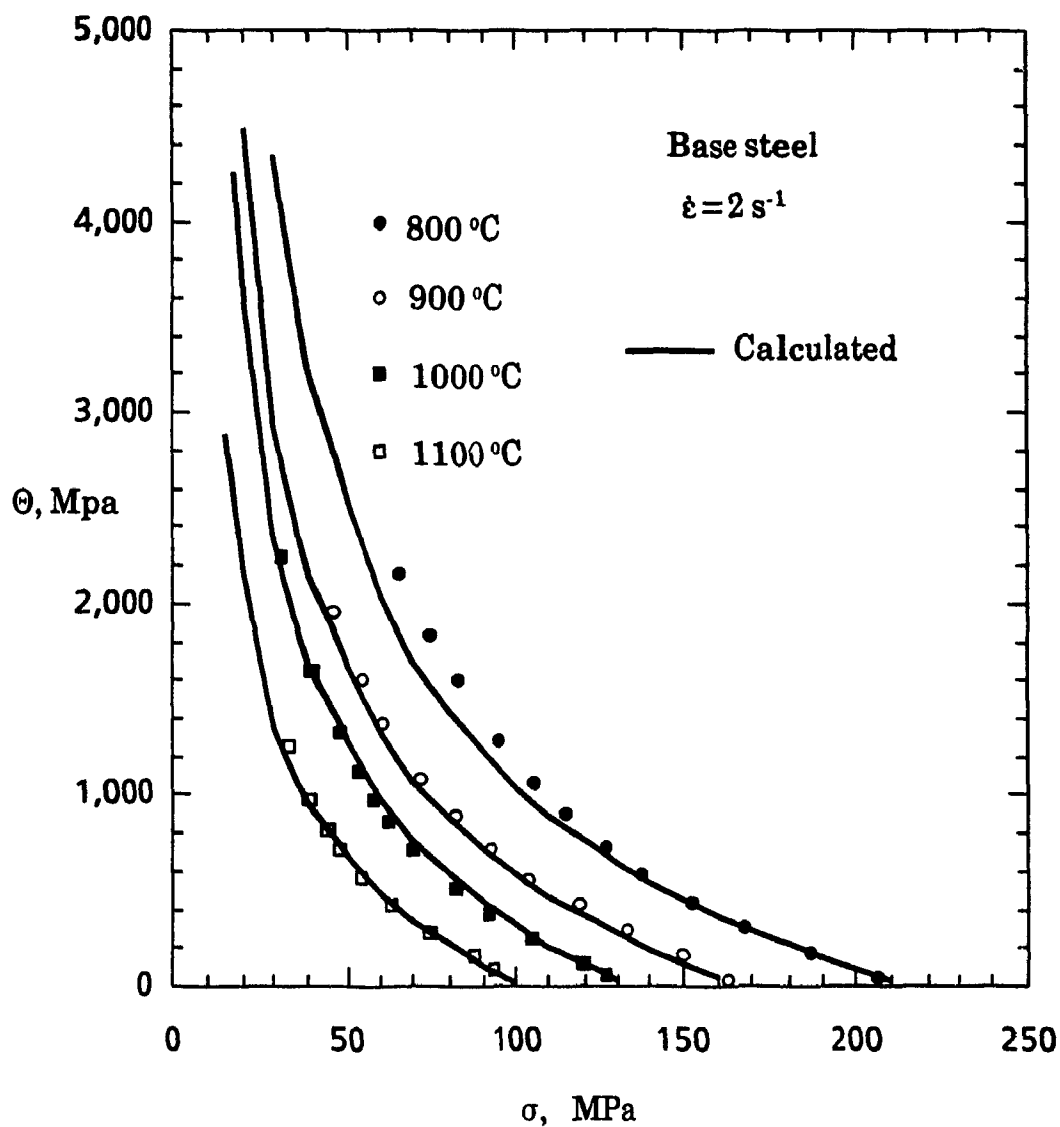


Figure 6.22 Comparison between Θ evaluated according to Eq. 6.19 and measured from the stress/strain curves.

Phenomenologically, Kocks [131] has shown that the linear work hardening law (Eq. 6.18) is consistent with the following relation for the rate of increase of dislocation density with strain:

$$\frac{d\rho}{d\varepsilon} = \frac{1}{b}(k_1\sqrt{\rho} - k_2\rho) \quad (6.21a)$$

where k_1 and k_2 are constants which are related to microscopic parameters and b is the burgers vector. By contrast, when the work hardening rate is assumed to vary linearly with $1/\sigma$, Roberts [133] rationalized the Θ - σ relation in terms of the following dependence of dislocation density on strain:

$$\frac{d\rho}{d\varepsilon} = k_{R1} - k_{R2}\sqrt{\rho} \quad (6.21b)$$

In a similar way, Eq. 6.19 can be interpreted in terms of the following equation:

$$\frac{d\rho}{d\varepsilon} = U - \Omega\rho \quad (6.21c)$$

Here U is a multiplication term and can be regarded as constant with respect to strain [112, 133, 145, 154, 156, 157]. $\Omega\rho$ is the contribution due to dynamic recovery through dislocation annihilation and rearrangement [152, 154, 157]. The integration of Eq. 6.21c gives:

$$\rho = \rho_0 e^{-\Omega\varepsilon} + \frac{U}{\Omega}(1 - e^{-\Omega\varepsilon}) \quad (6.22)$$

where ρ_0 is the initial dislocation density. Previous studies have shown that, at high temperatures, the effective stress is negligible compared to the internal stress [145, 156, 158, 159], so that the applied stress can be related directly to the square root of the dislocation density:

$$\sigma = \alpha\mu b\sqrt{\rho} \quad (6.23)$$

where α is constant for a given material and is of the order of unity. Combining Eqs. 6.22 and 6.23, the flow stress can be given by the following expression in terms of the strain:

$$\sigma = [\sigma_o^2 e^{-\Omega \epsilon} + (\alpha \mu b)^2 \frac{U}{\Omega} (1 - e^{-\Omega \epsilon})]^{0.5} \quad (6.24a)$$

or

$$\sigma = [\sigma_{ss}^{*2} + (\sigma_o^2 - \sigma_{ss}^{*2}) e^{-\Omega \epsilon}]^{0.5} \quad (6.24b)$$

where the initial and saturation stresses are:

$$\sigma_o = \alpha \mu b \sqrt{\rho_o} \quad (6.25a)$$

$$\sigma_{ss}^* = \alpha \mu b \sqrt{(U/\Omega)} \quad (6.25b)$$

Relation 6.24a is similar to the Bergström equation derived from dislocation theory and applied with success at low homologous temperatures to FCC and BCC materials. It is also similar to the expression derived by Yoshie et al. [145], who formulated the change of dislocation density as follows†:

$$d\rho = \frac{d\rho}{d\epsilon} d\epsilon + \frac{d\rho}{dt} dt \quad (6.26)$$

where t is the time. Eq. 6.24a was fitted to the stress/strain data over the full range of experimental conditions corresponding to the absence of dynamic recrystallization, using the procedure described in section 5.2.2. An excellent fit was obtained and correlation coefficients of up to .999 were achieved. When dynamic recrystallization takes place, the simultaneous use of the above σ - ϵ relation and the dynamically recrystallized fraction makes it possible to predict the flow stress after the peak. Such modelling is described in section 6.6.

† The derivation of Eq. 6.26 below and its integral are given in Appendix B.

6.4.2.2. Effect of Temperature and Strain Rate on Ω

Figure 6.23 shows typical plots of the strain rate and temperature dependence of Ω for the base and Nb-B steels. It is clear from these graphs that increasing the strain rate or decreasing the temperature results in a decrease in the value of Ω . This is consistent with the fact that Ω is a measure of the ease of dynamic recovery, which is a thermally activated process.

To quantify the effect of $\dot{\epsilon}$ and T on Ω , Yoshie and coworkers [145] used the following power function:

$$\Omega = A_{\Omega} d_0^{n_{\Omega}} \dot{\epsilon}^{m_{\Omega}} \exp\left(\frac{Q_{\Omega}}{RT}\right) \quad (6.27)$$

where d_0 is the initial grain size, Q_{Ω} an apparent activation energy in Joules/mole, and A_{Ω} , n_{Ω} and m_{Ω} are constants. Regression analysis was performed on the above equation in the temperature range 800 to 1100°C for the Nb-B steel at strain rates of 2 to 50 s⁻¹ and A_{Ω} , m_{Ω} and Q_{Ω} turned out to be about 157, -0.2 and -27,400 J/mol, respectively. By performing compression experiments on a 0.07C-0.01Nb steel in the temperature range between 800 and 1000 °C, Yoshie et al. determined m_{Ω} to be about -0.1. However, the value of -0.1 reported by the above authors and that of 0.2 found here are mean values over the temperature ranges used. They did not take the temperature dependence of m_{Ω} into account.

As shown earlier, the steady state stress is inversely proportional to the square root of Ω (Eq. 6.25 b). The strain rate and temperature dependence of σ_{ss}^* is mainly due to that of Ω . This is supported by the weak variation of U with $\dot{\epsilon}$ and T , as will be shown in the next section. The form of expression 6.7 suggested by the experimental data is equivalent to assuming that Ω is proportional to $(\dot{\epsilon}/\dot{\epsilon}_0)^{2k_B T/A}$. A similar expression for Ω in terms of $\dot{\epsilon}$ and T has been suggested by Klepaczko [157] for FCC materials.

Estrin and Mecking [154] associated the inverse of Ω with the relaxation strain by analogy with relaxation times in creep. That is, $1/\Omega$ determines the rate (in terms of strain) at which the flow stress can achieve the steady state.

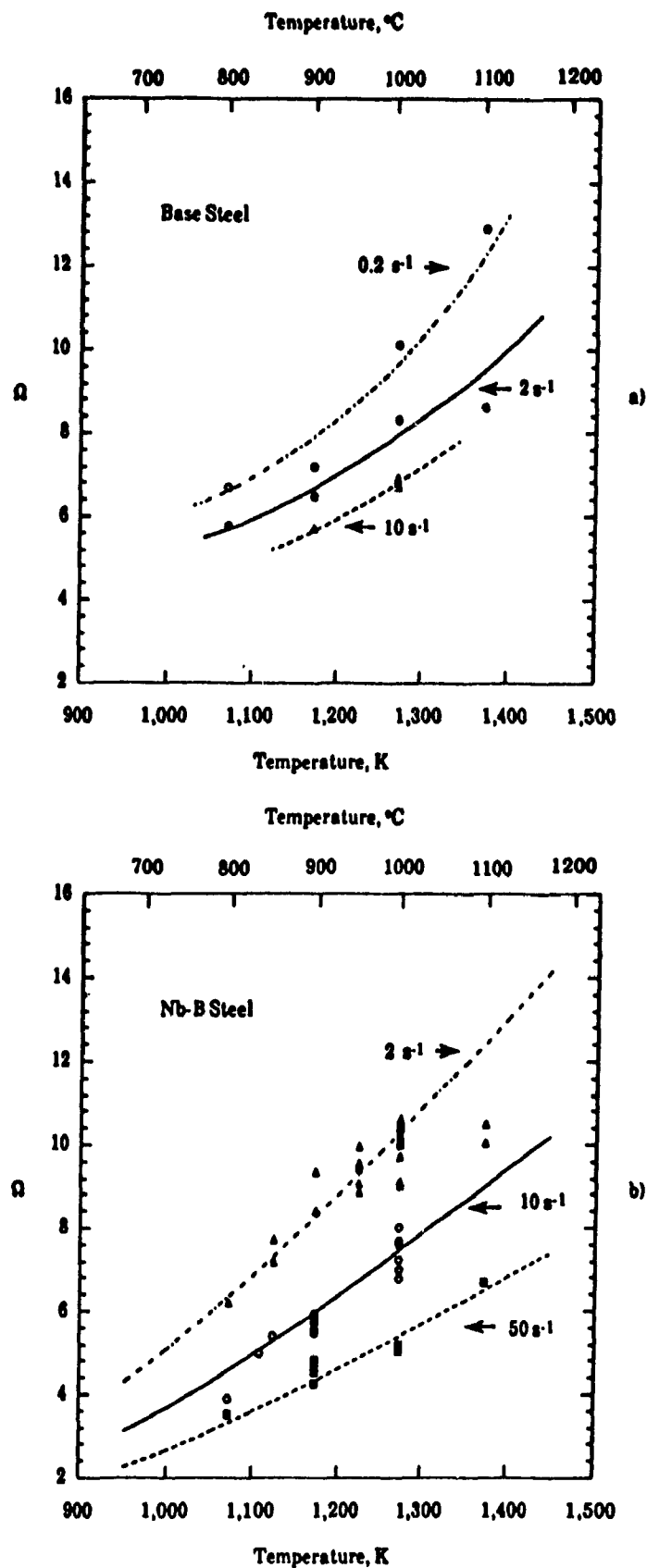


Figure 6.23 Dependence of Ω on temperature and strain rate in the
 a) base steel
 b) Nb-B steel.

Bergström considered Ω as the probability that immobile dislocations can become remobilized. This physical interpretation was considered by the above author to be satisfied at low temperatures in α -Fe and Al.

On the basis of the present results and discussion, it is difficult to retain the physical interpretation that Ω is the probability of dynamic recovery. At high temperatures, the deformation mechanisms are more complex due to the occurrence of diffusion controlled climb and to the dependence of the mobile dislocation density on strain [160]. Clarifying the effect of these parameters on U and Ω could constitute the subject of a complete study.

6.4.2.3. Effect of Temperature and Strain Rate on U

In Fig. 6.24a, $(\alpha\mu b)^2 U$ is plotted as a function of strain rate and temperature for the Nb-B steel. In contrast to Ω , the strain rate dependence of $(\alpha\mu b)^2 U$ is weak and can be neglected. However, its temperature dependence is not and a decrease in temperature results in a significant increase in $(\alpha\mu b)^2 U$. An important contribution to the variation of $(\alpha\mu b)^2 U$ with temperature is attributable to the temperature dependence of the shear modulus μ . Normalizing the former by $(\mu b)^2$ leads to a near constant value of $\alpha^2 U$ over the temperature and strain rate range (Fig. 6.24b). Similar temperature and strain rate independence of the multiplication term U has been reported by Bergström [153] and pointed out later by Estrin and Mecking [154]. In their interpretation, the last authors assumed that U (or $\alpha^2 U$) is related to the mean free path λ by the following relation:

$$U = \frac{1}{b\lambda} \quad (6.28)$$

where λ is the average distance traveled by each dislocation.

The assumption that U is constant and that therefore λ is constant constitutes the main difference with respect to Kocks' mechanistic interpretation of the Voce law (Eq. 6.21a, where the mean free path λ is assumed to be proportional to $1/\sqrt{\rho}$). The constancy of λ was believed to be more

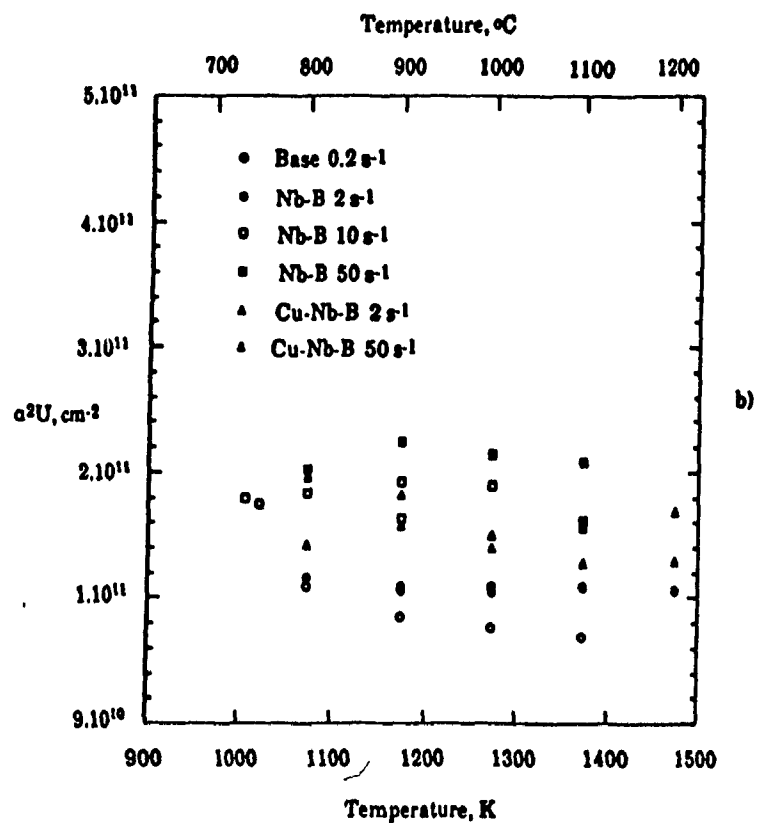
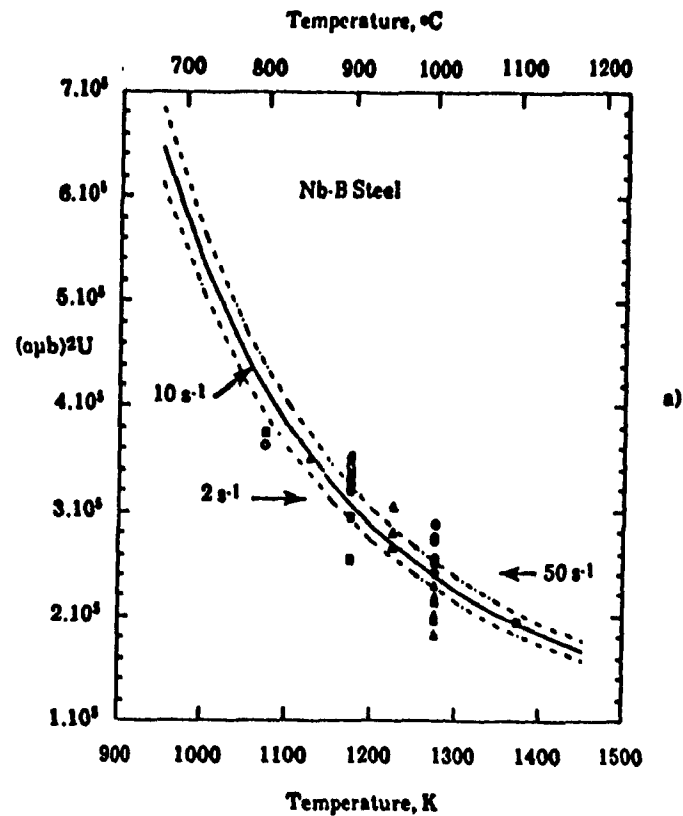


Figure 6.24 a) Dependence of $(\alpha pb)^2 U$ on temperature and strain rate.
 b) Dependence of $\alpha^2 U$ on temperature and strain rate.

realistic at high temperatures by Roberts [133], where a subgrain structure is established early during deformation.

Finally, it should be noted that there are considerable inadequacies in the physical interpretations of the constants discussed above. The difficulty in understanding the mechanisms of dislocation storage and dynamic recovery at high temperatures has led investigators to several different formalisms based on phenomenology rather than physics. The Bergström model, however, has many advantages for modeling the flow behavior of steels at high temperatures, particularly when compared to other existing models. It includes a saturation stress and describes the stress/strain curve accurately at a given strain rate and temperature using only two parameters, Ω and U . The detailed physical interpretation of these parameters is not impossible but needs more systematic study.

6.4.2.4. Relationship Between Ω , U , and the Hollomon Coefficients

Several empirical relations describing stress/strain curves for iron and steel exist in the literature. One of these relations which has been widely applied is the Hollomon equation, i.e.:

$$\sigma = K_H \varepsilon^{n_H} \quad (6.29)$$

where K_H is the strength coefficient and n_H the strain hardening index equal to $d \ln \sigma / d \ln \varepsilon$.

In Fig. 6.25a, $\ln \sigma$ is plotted against $\ln \varepsilon$ for the present niobium steel deformed at 900°C at a strain rate of 2 s⁻¹. It is evident that the data cannot be approximated by a straight line, indicating that the strain hardening index is not a constant. Similar decreases of n_H with ε were reported recently by Perdrix [161] for steels deformed at high temperatures and strain rates. Over a limited range of strain and because of the occurrence of necking during tensile testing, two or three straight lines were used to fit the data [162]. This has been called

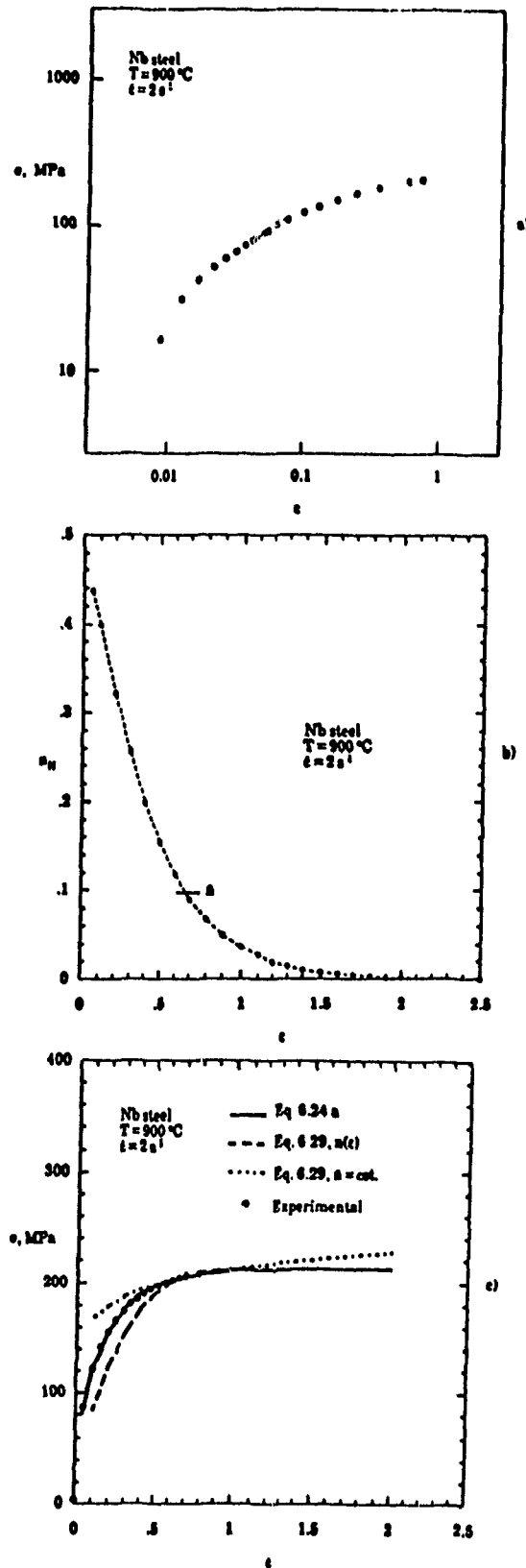


Figure 6.25 a) Log stress versus log strain for the Nb steel deformed at 900°C at a rate of 2 s^{-1} , b) Strain dependence of the coefficient n_H in the Hollomon equation and c) Comparison of calculated $\sigma(\epsilon)$ relations using the Hollomon (Eq. 6.29) and Bergström (Eq. 6.24) equations with measured data.

double or triple "n" behavior and was observed in ferrite at room and subzero temperatures.

The non-linear behavior of the $\ln\sigma/\ln\epsilon$ plot, and therefore the non-constant nature of n_H can be explained in terms of the Bergström equation. In fact, after differentiation of Eq. 6.24a, n_H can be expressed as:

$$n_H = \frac{\epsilon}{\sigma} \frac{d\sigma}{d\epsilon} = \frac{\Omega}{2} \left[\frac{\epsilon e^{-\Omega\epsilon}}{\sigma_{SS}^{*2}(\sigma_{SS}^{*2} - \sigma_0^2) - e^{-\Omega\epsilon}} \right] \quad (6.30)$$

where $\sigma_{SS}^{*2} = (\alpha\mu b)^2 U/\Omega$

In Fig. 6.25b, n_H is plotted versus strain according to Eq. 6.30 for the conditions of temperature and strain rate shown. It is clear that n_H decreases continuously with strain until it vanishes at deformations corresponding to steady state flow. In Fig. 6.25c, the poor representation of the stress/strain data by Eq. 6.29 is demonstrated, whether an average value of n_H is employed, or when account is taken of the continuous decrease of the exponent with strain. This is very important in modelling the flow behavior of steels at high temperatures, particularly if the strains are high, such as in strip rolling. Thus the use of Eq. 6.29 can lead to considerable error in estimating the rolling load. By contrast, very good fits are obtained when Eq. 6.24a is used (Fig. 6.25c).

6.5. HART ANALYSIS

In the last three decades, the flow behavior of metals has been analyzed using two different approaches. The first employs microscopic variables to describe the deformation. On the basis of theoretical considerations such as dislocation glide, this approach can lead to constitutive equations. The second, which is a phenomenological one, uses macroscopic parameters such as stress, strain rate and strain to describe the mechanical behavior of the deformed metal.

In the phenomenological approach, the integrated form of the plastic strain is not an appropriate state variable, because it does not correspond in a

unique way to the current structure (dislocation density, subgrain size,...) [138, 163]. Hart [163] was the first to introduce the notion of a "hardness state"† to be used as an evolutionary variable instead of the plastic strain. He assumed that the deformation history at a given temperature can be described incrementally by the following differential equation:

$$d\ln(\sigma) = H d\epsilon + M d\ln(\dot{\epsilon}) \quad (6.31)$$

where $H = d\ln\sigma/d\epsilon|_{T,\dot{\epsilon}}$ is the work hardening coefficient and $M = d\ln\sigma/d\ln\dot{\epsilon}|_{T,state}$ is the strain rate sensitivity at constant mechanical state. To be able to integrate Eq. 6.31, H and M must depend only on σ and $\dot{\epsilon}$. In this way, knowledge of the stress and strain rate dependence of H and M is sufficient to describe completely the mechanical response of a deformed material. Fig. 6.26 is schematic diagram illustrating different constant hardness lines "y" on a $\ln\sigma/\ln\dot{\epsilon}$ plot. These lines are necessarily parallel if an equation of state is to exist [163].

Various constant work hardening rates H can also be represented by analogy with the constant structure lines. The equation for the line $H=1$, for instance, can be written as follows:

$$\sigma_1 = \beta \dot{\epsilon}^N \quad (6.32)$$

where β is a constant at a given temperature. It is easily verified from Fig. 6.26 that the equation for the lines of constant "y", is given by:

$$\sigma = \beta [y^{(N-M)}] \dot{\epsilon}^M \quad (6.33)$$

It is the aim of this section to relate the parameters in Eq. 6.31 to those of the evolution and rate equations in sections 6.3 and 6.4 and to investigate their stress, strain rate and temperature dependencies. This constitutes a way of

† The term hardness is not the same as the one commonly employed in testing.

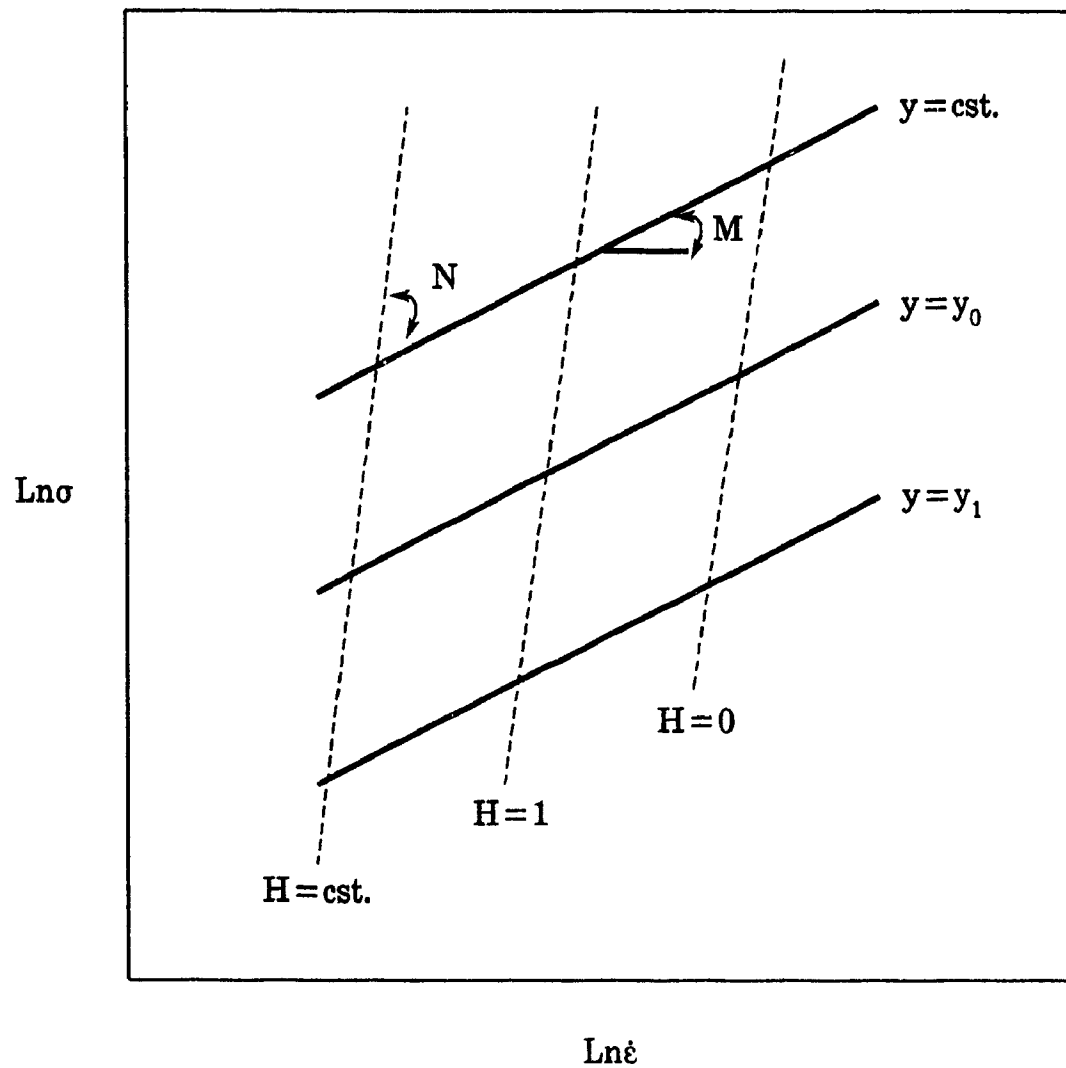


Figure 6.26 Schematic representation of constant hardness curves "y" and constant work hardening rate curves "H".

checking the coherence of the rate and evolution equations developed in the previous sections.

From Eq. 6.24b, the work hardening rate coefficient is expressed as follows:

$$H = \frac{d \ln(\sigma)}{d \epsilon} = \frac{\Omega}{2} \left[\left(\frac{\sigma_{SS}^*}{\sigma} \right)^2 - 1 \right] \quad (6.34)$$

In Fig. 6.27, the dependence of H on σ and $\dot{\epsilon}$ is shown at different temperatures for the base and Nb-B steels. It is evident that, for a given strain rate, H is a decreasing function of σ , as can be expected from Eq. 6.34. The effect of strain rate on the H - σ curves is similar to its effect on the Θ - σ diagrams. The rate dependence of H as given by $\partial H / \partial \ln \dot{\epsilon} |_o$ decreases at low stresses and increases when the work hardening curves start to deviate at higher stresses. This behavior has been observed in Al and Cu [164, 165] and $\partial H / \partial \ln \dot{\epsilon} |_o$ has been found to increase with temperature, as is the case in the present work.

To determine M and N , the following procedure is used. Eq. 6.24b can be rewritten in the following form:

$$\sigma = \sigma_{SS}^* \left[1 - \left(1 - \left(\frac{\sigma_o}{\sigma_{SS}^*} \right)^2 \right) e^{-\Omega \epsilon} \right]^{0.5} \quad (6.35)$$

For $H=0$, from Eqs. 6.32 and 6.33:

$$\sigma_{SS}^* = \beta_S \dot{\epsilon}^N \quad (6.36a)$$

$$\sigma_o = \beta_S y_o^{(N-M)} \dot{\epsilon}^M \quad (6.36b)$$

Combining Eqs. 6.36a and 6.36b :

$$\left(\frac{\sigma_o}{\sigma_{SS}^*} \right)^2 = \left(\frac{y_o}{\dot{\epsilon}} \right)^{2(N-M)} \quad (6.37)$$

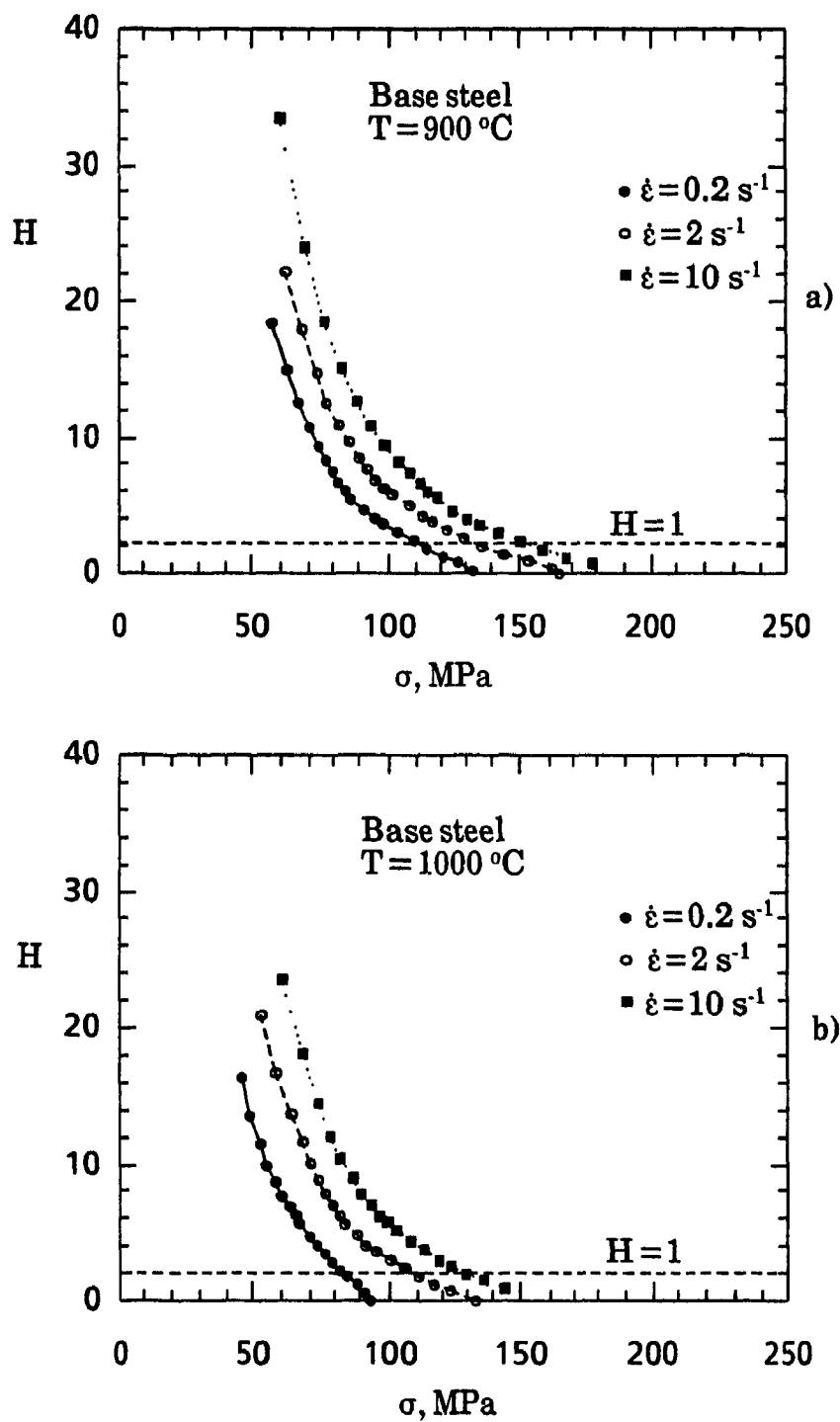


Figure 6.27 Dependence of the work hardening coefficient H on stress and strain rate in the base steel deformed at a) 900°C , b) 1000°C .(contd.)

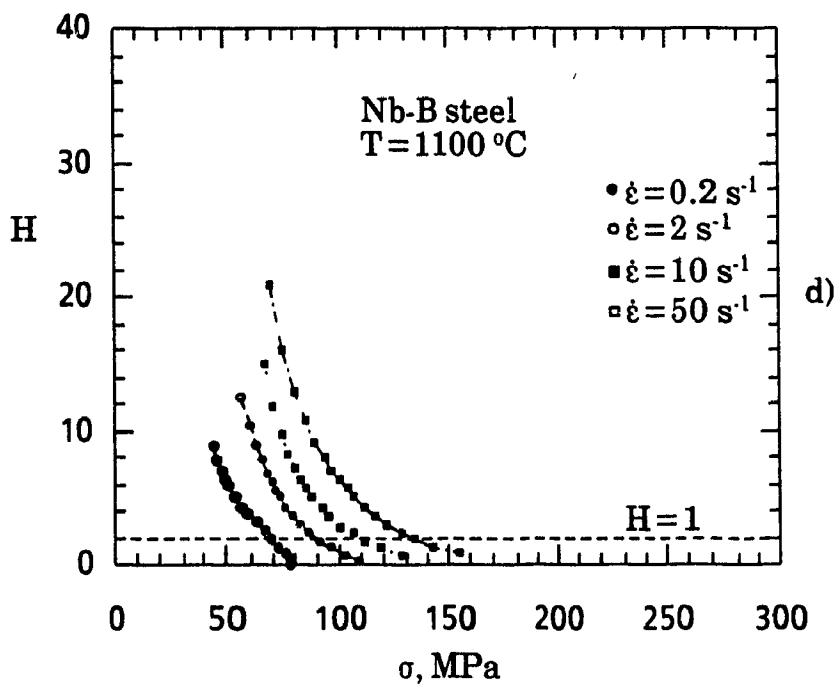
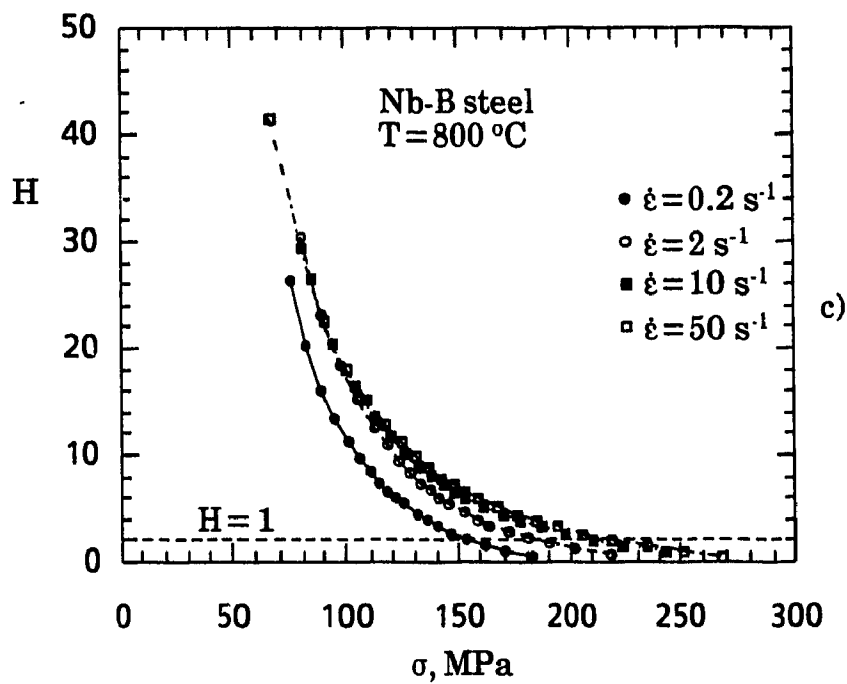


Figure 6.27 Dependence of the work hardening coefficient H on stress and strain rate in the Nb-B steel deformed at c) 800°C, d) 1100°C.

Introducing Eqs. 6.36a and 6.37 into Eq. 6.35 gives:

$$\sigma = \beta_S \dot{\epsilon}^N \left[1 - \left(1 - \left(\frac{y_o}{\dot{\epsilon}} \right)^{2(N-M)} \right) e^{-\Omega \dot{\epsilon}} \right]^{0.5} \quad (6.38)$$

From Eq. 6.24a we obtain:

$$\sigma = (\alpha \mu b) \sqrt{U/\Omega} \left[1 - \left(1 - \left(\frac{\sigma_o}{\alpha \mu b \sqrt{U/\Omega}} \right)^2 \right) e^{-\Omega \dot{\epsilon}} \right]^{0.5} \quad (6.39)$$

and finally, Eqs. 6.38 and 6.39 lead to:

$$\sigma_{SS}^* = (\alpha \mu b) \sqrt{U/\Omega} = \beta_S \dot{\epsilon}^N \quad (6.40a)$$

$$\frac{\sigma_o}{\alpha \mu b \sqrt{U/\Omega}} = \left(\frac{y_o}{\dot{\epsilon}} \right)^{(N-M)} \quad (6.40b)$$

Assuming that N and M are constant over a small range of strain rate [141, 163], one can calculate N and M from Eqs. 6.40a and 6.40b as follows:

$$N = \frac{\ln(\sigma_{SS1}^* / \sigma_{SS2}^*)}{\ln(\dot{\epsilon}_1 / \dot{\epsilon}_2)} \quad (6.41a)$$

$$M = \frac{\ln(\sigma_{o1} / \sigma_{o2})}{\ln(\dot{\epsilon}_1 / \dot{\epsilon}_2)} \quad (6.41b)$$

The strain rate sensitivity at constant work hardening rate N was calculated for the Nb-B and Cu-Nb-B steels over the strain rate range $2\text{-}10\text{s}^{-1}$ and $10\text{-}50\text{s}^{-1}$. The values found were close to $1/n$ in Fig. 6.12, with, however, a trend to a decrease with an increase in the strain rate. This is to be expected since the strain rate sensitivity at constant work hardening N as given by Eq. 6.41a is similar to the one in Eq. 6.7, and the strain rate sensitivity $k_b T/A$ in the latter equation is no other than an average N taken over the total range of strain rate. The decrease of N with strain rate is clear from the $\ln\sigma/\ln\dot{\epsilon}$ plots at 900 and 1000°C in the Cu-Nb-B steel, for instance (Fig. 6.10d). If each data pair between two successive strain rates were joined by a line, the slope of this line would decrease when the strain rate range is increased. Similar decreases in

the rate sensitivity with strain rate have been reported by Hart et al. [166] and Mliha-Touati [147], where the shapes of the $\ln\sigma/\ln\dot{\epsilon}$ plots were concave downwards at high temperatures, in contrast to the low temperature regime.

The strain rate sensitivity at constant structure M , given by Eq. 6.41b, was not evaluated due to the problems related to the determination of the stress at the beginning of flow, as explained in section 6.3.2.1. However, it has been shown by Christodoulou and Jonas [165] that the ratio between the strain rate sensitivity at constant state M and the apparent strain rate sensitivity $d\ln\sigma/d\ln\dot{\epsilon}|_{\epsilon}$ is between 0.4 and 0.6 for Al and Cu. Ferron and Mliha-Touati [141] have reported a ratio of 0.64 between M and N in Al. Although the apparent strain rate sensitivity $d\ln\sigma/d\ln\dot{\epsilon}|_{\epsilon}$ varies with strain, as illustrated in Fig. 6.28, it evolves rapidly to a constant value corresponding to that of N at large strains. It is then possible to have an estimate of the strain rate sensitivity at constant structure M by taking half the value of N .

6.6. EFFECT OF DYNAMIC RECRYSTALLIZATION ON FLOW SOFTENING

During deformation, when dynamic recovery is slow, the dislocation density increases and rapidly attains a critical value ρ_c at which dynamic recrystallization is initiated. Roberts [167] has reported that, at the critical strain ϵ_c corresponding to ρ_c , the nucleation of recrystallized grains occurred by the mechanism of strain-induced grain boundary migration.

Although it is unlikely that the critical strain for dynamic recrystallization can be attained during plate rolling, it can indeed be initiated in strip rolling. In the latter case, during rolling at low temperatures (finishing), the strain in a single pass may not exceed ϵ_c , but the strain accumulated over several passes can do so. This is due to several factors: the first is the absence of static recrystallization at low temperatures when the interpass time is short. The second is the decrease in grain size due to the complete cycles of static recrystallization taking place between the previous passes (roughing). As observed by Sellars and Whiteman [168], the critical strain ϵ_c decreases as the grain size is decreased. The other factors contributing to the occurrence of dynamic recrystallization are the absence of strain-induced

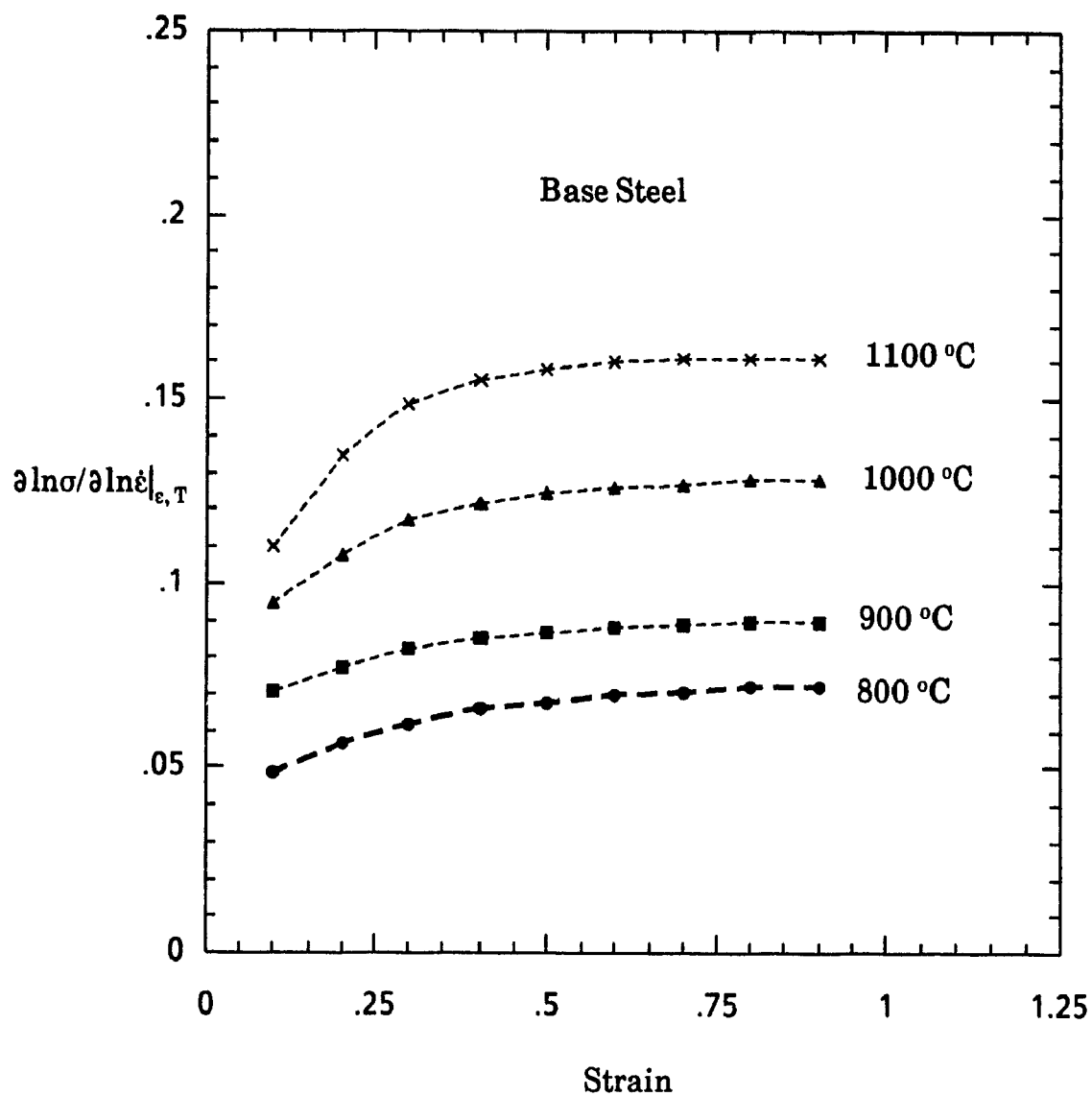


Figure 6.28 Dependence of the apparent strain rate sensitivity on temperature and strain.

precipitation when the interpass times involved are short, and the presence of solutes which retard static recrystallization. This type of softening via dynamic recrystallization can lead to several benefits. In addition to lowering the rolling loads in comparison to those involved when pancaking occurs, it produces a very fine grain structure, which cannot be achieved by conventional controlled rolling techniques. It was therefore decided during the present work to model the flow softening brought about by dynamic recrystallization, and to derive typical relationships that can provide the mean strength for later rolling load calculations.

The stress/strain curves for the base steel described in section 6.2.1 were analyzed. This steel was chosen because it is typical of those rolled in large quantities. When dynamic recrystallization contributes to softening, the following equation can be used:

$$\sigma^{drec} = [\sigma_o^2 e^{-\Omega \epsilon} + (\alpha \mu b)^2 \frac{U}{\Omega} (1 - e^{-\Omega \epsilon})^{0.5}] \quad \epsilon < \epsilon_p \quad (6.42a)$$

$$\sigma = \sigma^{drec} - \left[\sigma_{ss}^* - \sigma_{ss}^{drxn} \right] \left[1 - \exp \left(-K_D (\epsilon - \epsilon_p)^{n_D} \right) \right] \quad \epsilon \geq \epsilon_p \quad (6.42b)$$

Here σ^{drec} is the flow stress when dynamic recovery is the only softening mechanism, σ_{ss}^{drxn} is the steady state stress after dynamic recrystallization has progressed through the material, and K_D and n_D are constants. While σ_{ss}^* and the parameters in Eq. 6.42a were defined in terms of $\dot{\epsilon}$ and T in the previous sections, it is necessary to know how σ_{ss}^{drxn} , ϵ_p , K_D and n_D change with the thermomechanical conditions. The original structure (grain size) is another factor that affects these parameters, but will not be investigated here, simply because the compression tests were performed at constant initial grain size for the base steel.

Figure 6.29 shows the dependence of σ_{ss}^{drxn} on the Zener-Hollomon parameter Z . The hyperbolic sine function was found to give a good fit to the data, and the constants α , A , n' and Q are shown. In particular, the slope n' is close to that when $\ln[\sinh(\alpha \sigma_{ss}^*)]$ is plotted versus $\ln(Z)$ (Fig. 6.8a). The resulting equation for σ_{ss}^{drxn} is given by:

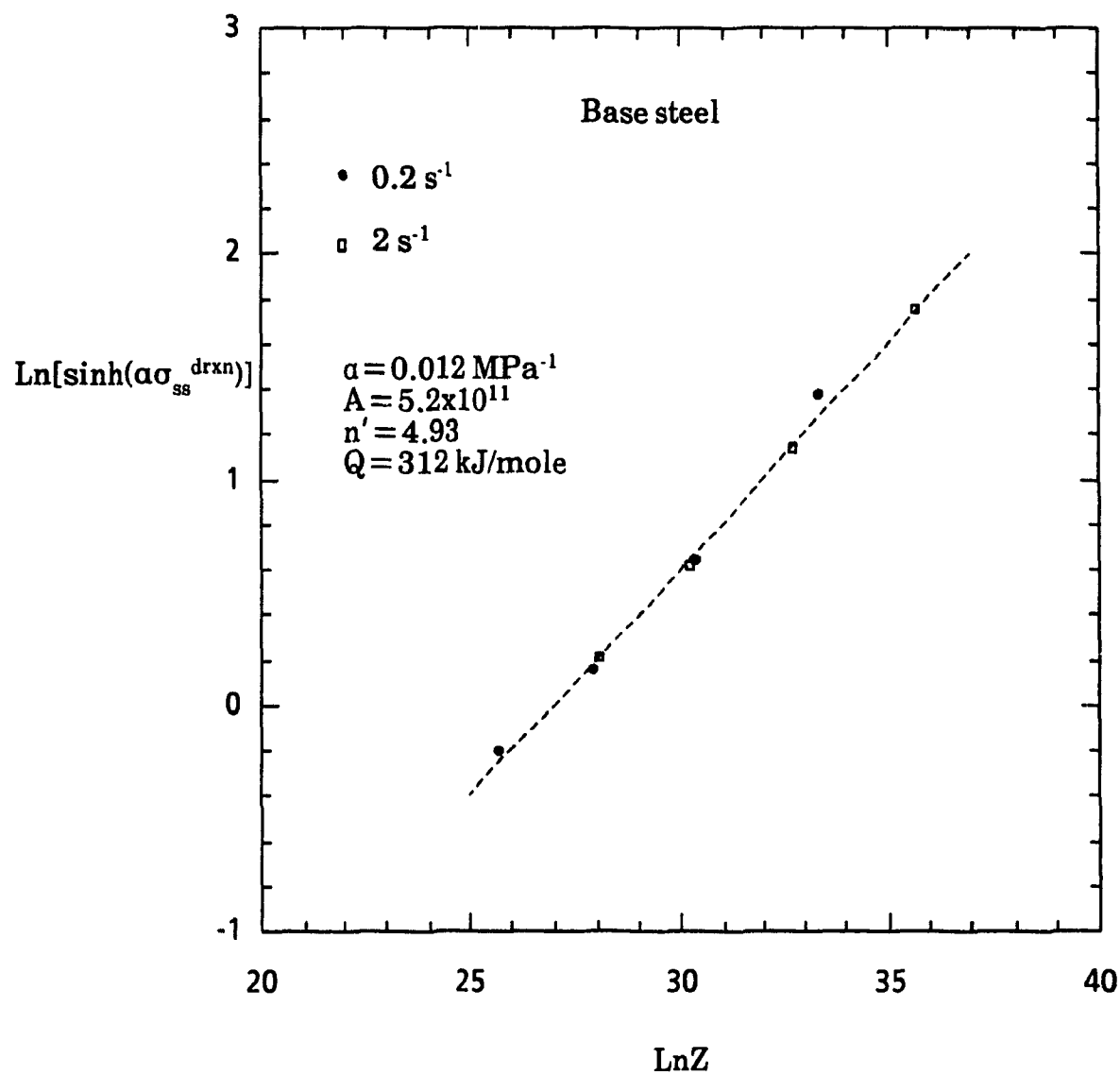


Figure 6.29 Effect of temperature and strain rate on the steady state stress $\sigma_{ss}^{\text{drxn}}$ associated with dynamic recrystallization.

$$\sigma_{ss}^{drxn} = 83.34 \sinh^{-1} \left[(Z/5.2 \cdot 10^{11})^{0.2} \right] \quad (6.43)$$

The following relation suggested by Sellars [17] was used to express the peak strain ε_p as a function of the thermomechanical parameters:

$$\varepsilon_p = A d_o^{0.5} Z^p \quad (6.44)$$

Figure 6.30 shows how well the present data fit the above expression. The value of 0.13 for p in Eq. 6.44 is within the range 0.12-0.17 reported by Sellars for steels [17].

To determine the values of K_D and n_D , plots of $\ln[\ln(1/(1-X_D))]$ versus $\ln(\varepsilon - \varepsilon_p)$ were used and are shown in Fig. 6.31 for selected conditions of $\dot{\varepsilon}$ and T , where X_D is given by:

$$X_D = \frac{\sigma^{drec} - \sigma}{\sigma_{SS}^* - \sigma_{SS}^{drxn}} \quad (6.45)$$

The values of n_D were found to be independent of $\dot{\varepsilon}$ and T , and fall between 1.5 and 1.6. They seem to be slightly higher than the values between 1.2 and 1.4 reported by Roberts [167] for stainless steel. The reason for this is that the critical strain for dynamic recrystallization, ε_c , must normally be taken instead of ε_p . However, due to the difficulty of estimating the ratio $\varepsilon_c/\varepsilon_p$, ε_p was used in Eq. 6.42b as a practical solution. Fig. 6.32 shows that Eq. 6.42a combined with Eq. 6.42b gives good descriptions of stress/strain curves in the range of strain rate and temperature examined, even when softening occurs by dynamic recrystallization. Such modelling can be employed for any composition provided the deformation conditions are known. Finally, it would be interesting to account for metallurgical factors such as the original grain size and carbon and the niobium levels. This requires extensive stress/strain data if on-line application to strip rolling is desired.

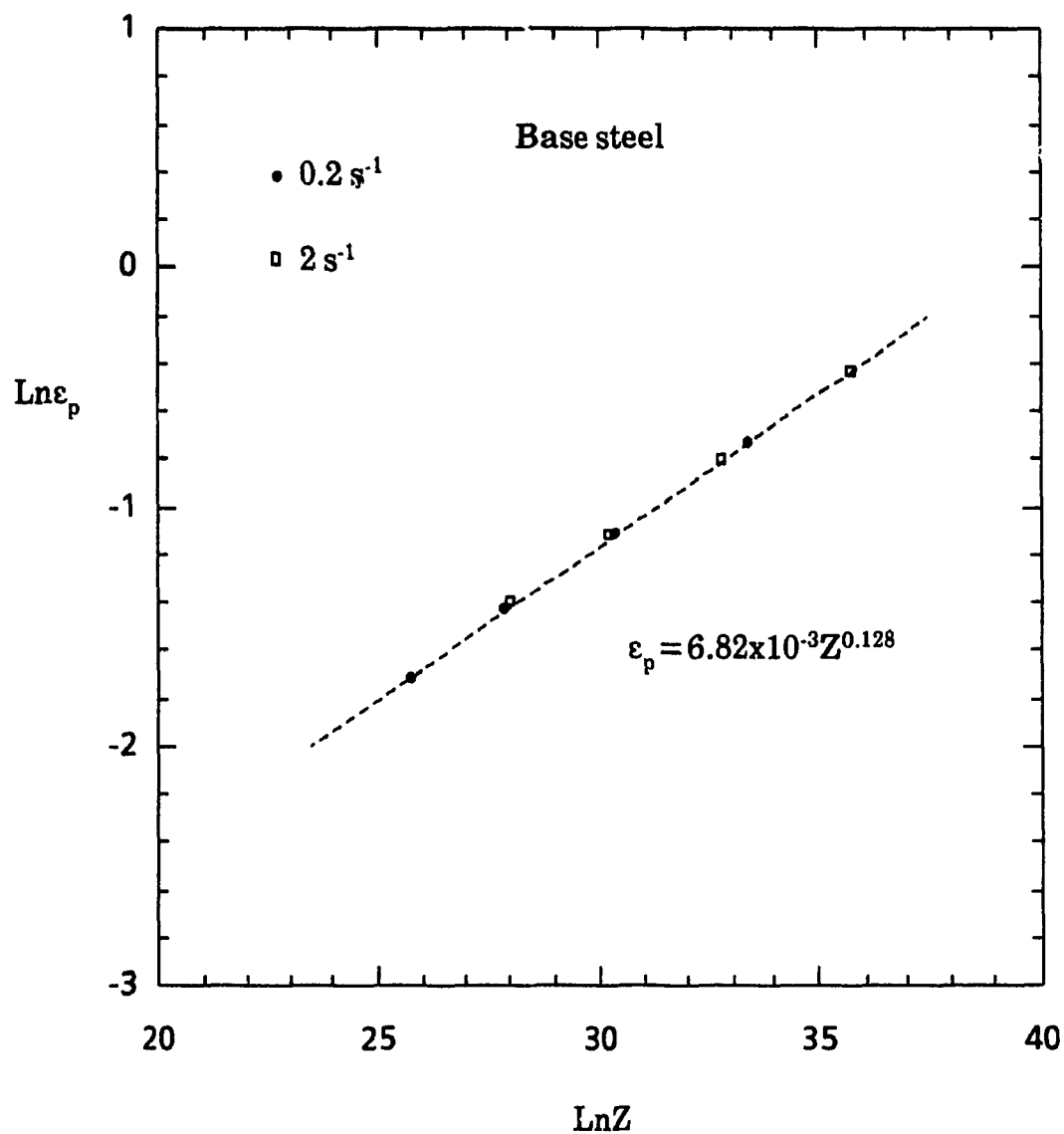


Figure 6.30 Effect of temperature and strain rate on the peak strain for dynamic recrystallization.

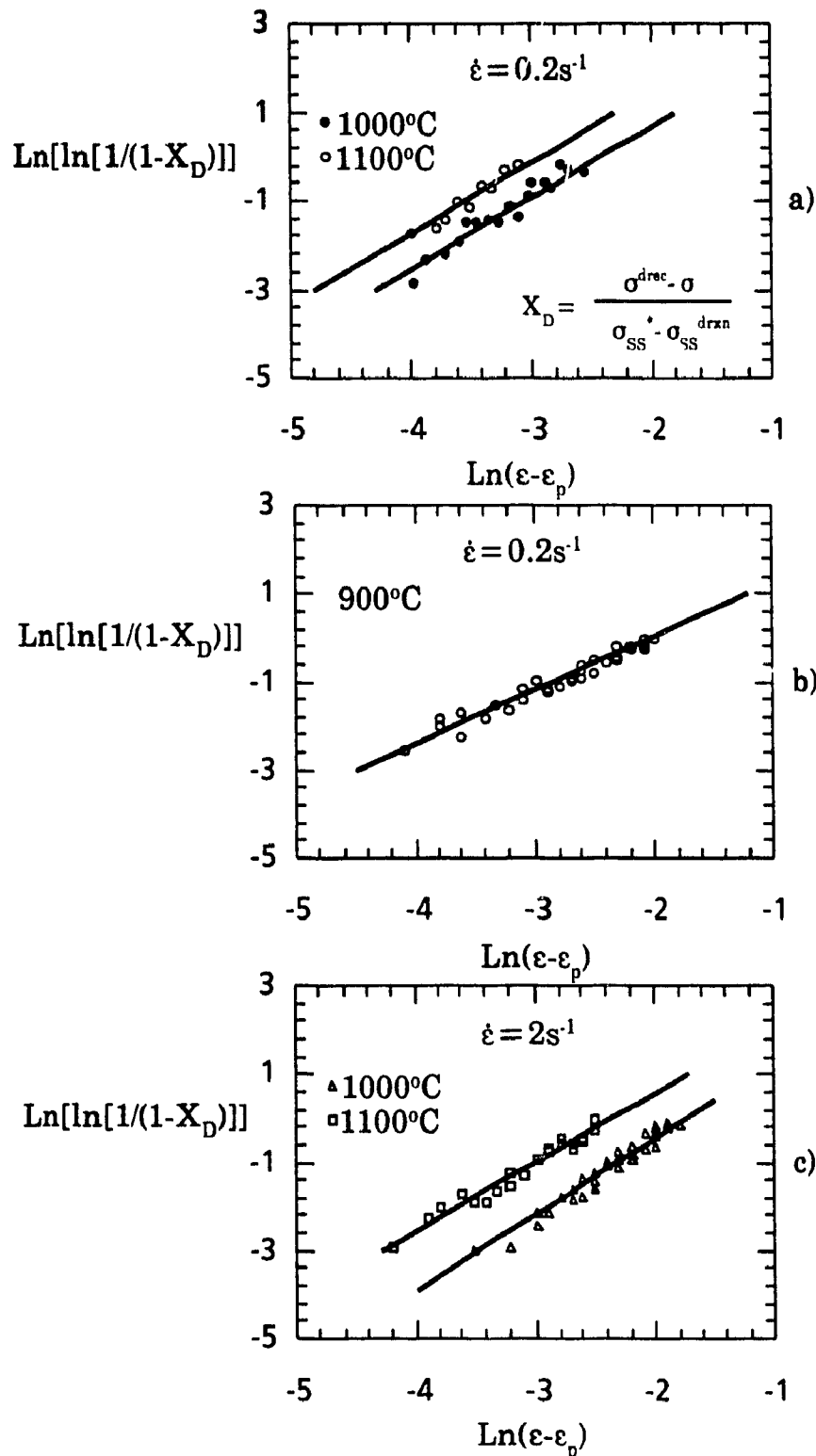


Figure 6.31 Determination of the constants n_D and K_D in Eq. 6.42b for the base steel at different temperatures and strain rates.

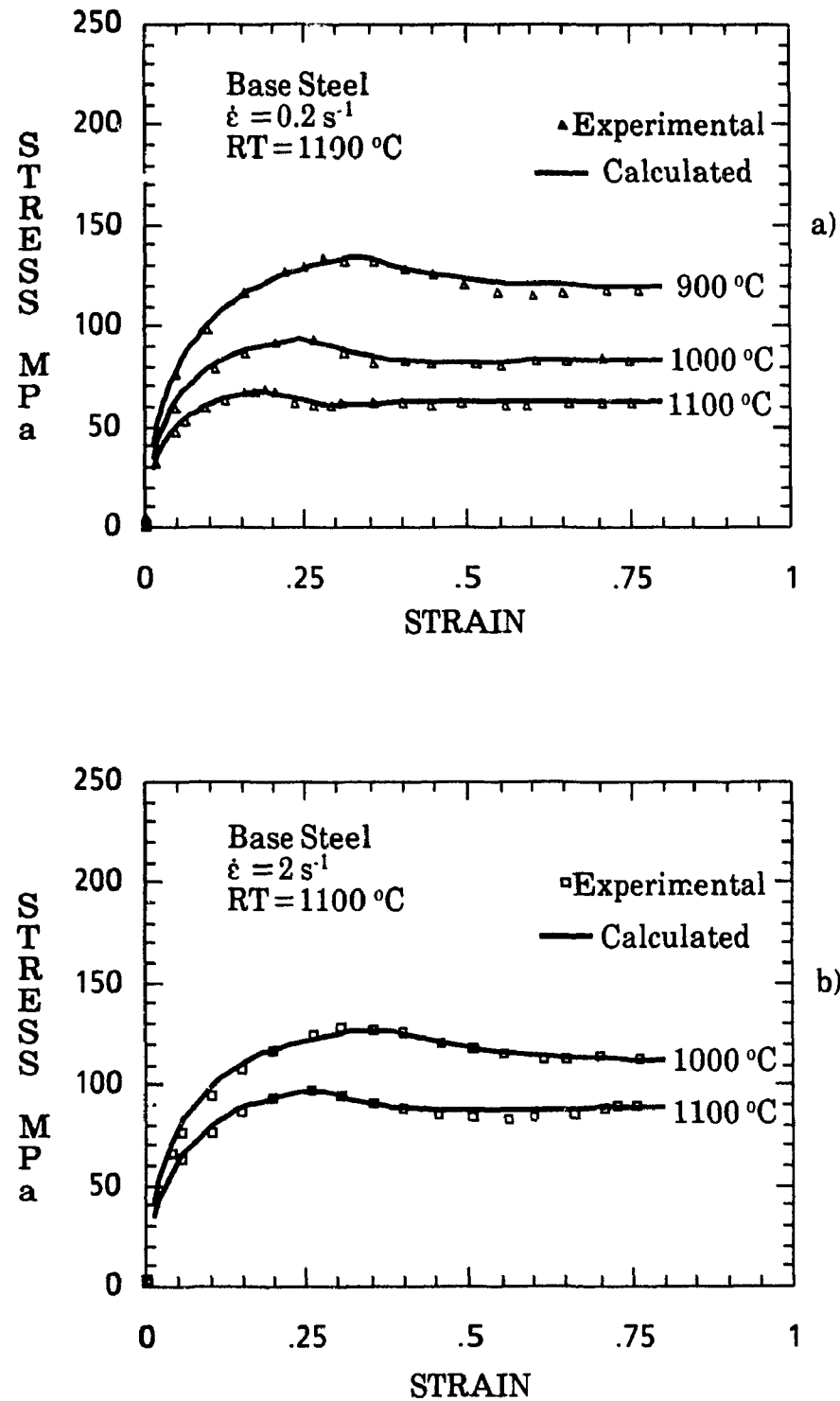


Figure 6.32 Comparison between predicted (Eq. 6.42a and b) and experimental stress/strain curves in the base steel deformed at a) 0.2 s^{-1} , b) 2 s^{-1} .

6.7. SUMMARY

In this chapter, constitutive equations were formulated describing the flow behavior of steels at high temperatures and strain rates; these were divided into two types: a rate and an evolution equation. When these two types of equations are combined together, the stress level can be determined under any conditions of temperature, strain and strain rate. These can then be used to compute the rolling load during hot rolling. However, up to now, the equations developed here have only been applied to fully annealed steels. During rolling, the microstructure changes between passes, affecting the flow behavior of the material considerably. This evolution of the structure, which is mainly due to the occurrence of static recrystallization, will be treated in the next chapter.

Chapter SEVEN

EFFECT OF THERMOMECHANICAL AND METALLURGICAL PARAMETERS ON THE MICROSTRUCTURAL EVOLUTION OF AUSTENITE AFTER DEFORMATION

7.1. INTRODUCTION

In Chapter 6, constitutive equations in terms of deformation conditions were described for a fully annealed steel. During hot forming operations, however, there is an important factor which can dramatically change the flow stress level and which was not treated in the last chapter. It is the evolution of structure when the steel is load free. This can be described by the state of the grain microstructure, i.e. whether it is deformed, recrystallized, or partially recrystallized. The deformation resistance can only be determined with confidence if the recrystallization kinetics after deformation are accurately known.

The objective of this chapter is therefore to develop appropriate relations for the recrystallization kinetics and for the evolution of grain size for the steels under investigation. These relations will be used together with the constitutive equations given in Chapter 6 for a complete description of the flow behavior. In the first part of the present chapter, the different methods used to assess the softening rate during interrupted compression testing (see section 5.3) will be compared. In the second part, the recrystallization kinetics of the different steels studied will be described in detail and modelled in terms of the processing parameters. The modelling of grain size will be treated in the third section and, finally, the influence of alloying elements such as niobium, boron

and copper on the recrystallization kinetics will be discussed in the last section.

7.2. STATIC SOFTENING MEASUREMENT METHODS

7.2.1. Comparison of the Mean Stress, Offset, Back Extrapolation and Recovered Strain Fraction Methods

The structural evolution of austenite after deformation can be followed by optical metallography. Although this method can be accurate, it involves several disadvantages. First, it cannot be employed for low hardenability steels in which it is difficult to reveal the prior austenite grain boundaries. Second, this method is long and tedious and requires the construction of special quenching systems. For this reason, the interrupted compression testing technique described in Chapter 4 was used to measure the amount of static softening taking place between the two hits.

The offset, back extrapolation, recovered strain fraction ($1-\lambda$) and mean stress methods of describing the softening in a Nb steel are compared in Figs. 7.1a and b†. Fig. 7.1a shows that the softening rates determined by the offset and fractional recovered strain methods are similar. The unrecovered (retained) strain $\Delta\epsilon$ can thus be estimated in partially recrystallized structures when λ is known. It is of interest that, on the basis of the results shown in Figs. 7.1a and b, the softening rate evaluated by the mean stress method lies between those of the offset and back extrapolation methods. This behavior was observed for both the Nb and Nb-B steels, and for various conditions of prestrain and temperature. Accordingly, it appears that the mean stress method is highly suitable for evaluation of the softening rate and therefore for the prediction of rolling load. In addition to its simplicity, accuracy and rapidity when stress/strain curves are available, it avoids the errors associated with the so-called "transient" during reloading [104].

† Some of the data in Fig. 7.1 have been taken from reference [94]. They have been adjusted for temperature differences during testing with respect to the present work.

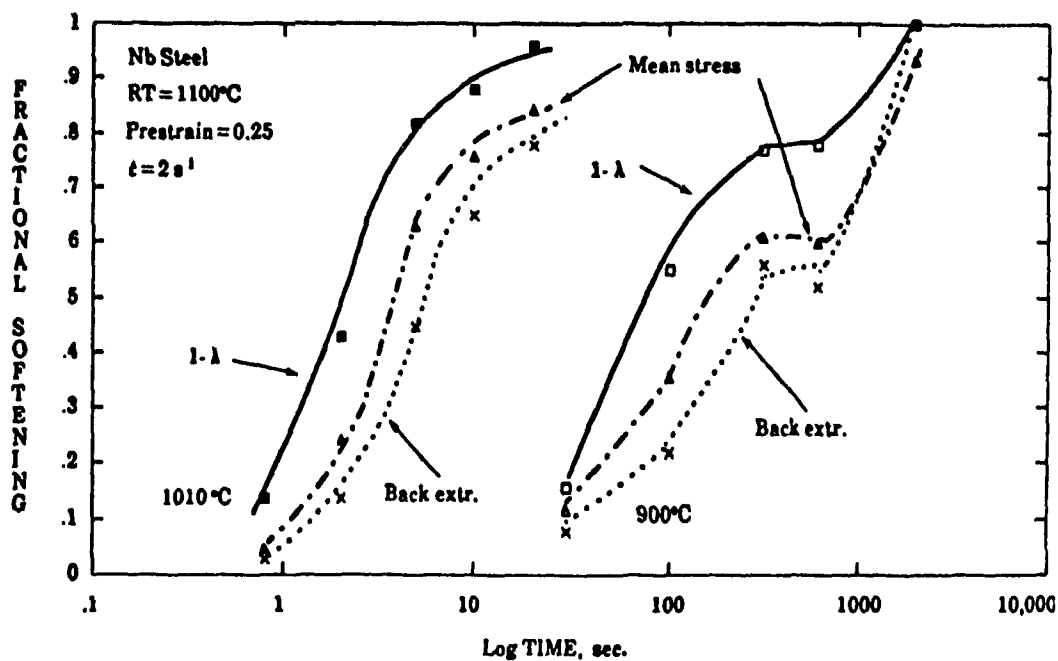
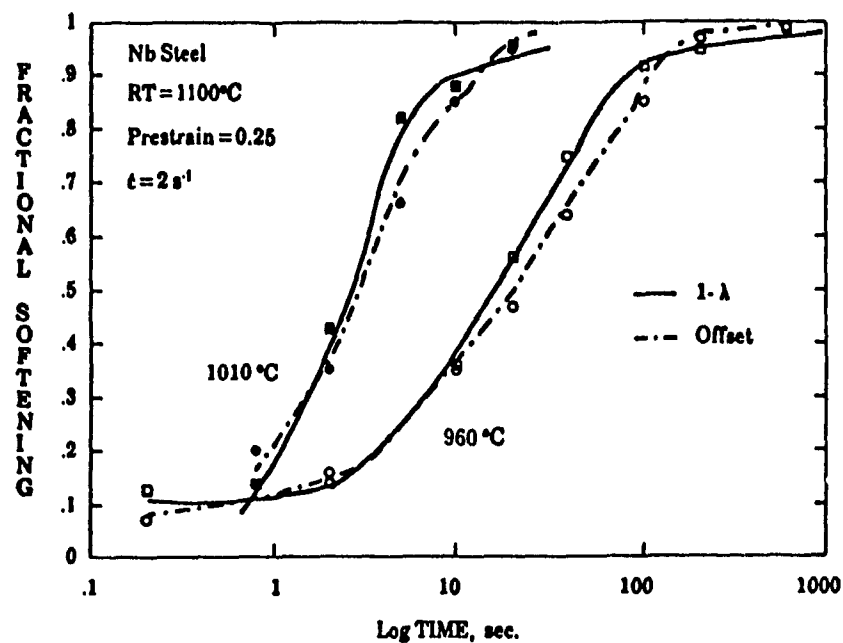


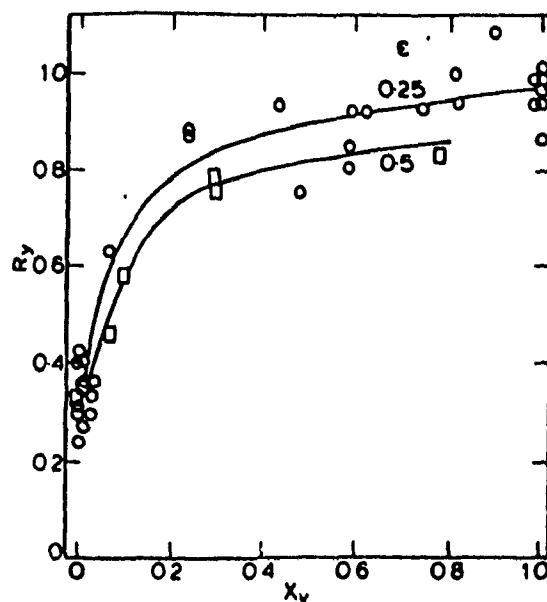
Figure 7.1 Comparison of different softening parameters.

7.2.2. Relationship Between Static Softening and Recrystallization

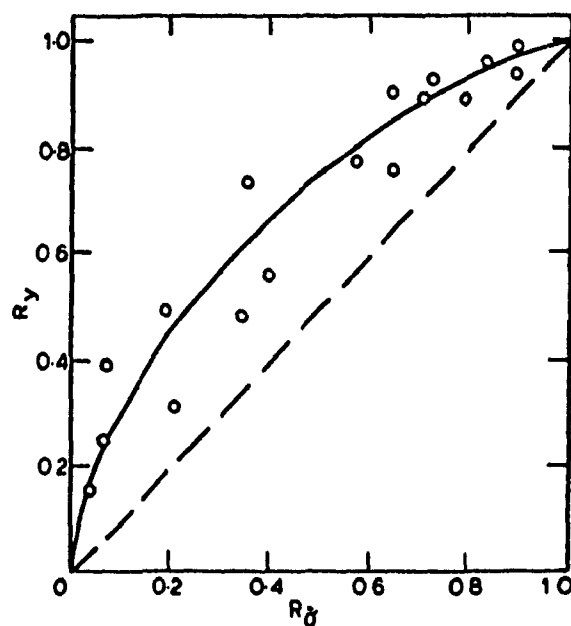
The static softening determined by mechanical testing techniques such as the offset method has been shown to be related non-linearly to the volume fraction of recrystallized grains. This non-linear behavior was demonstrated by Barraclough and Sellars [105] using torsion testing and optical metallography in stainless steel. The fractional softening, R_y , based on the offset flow stress, was generally higher than the recrystallized volume fraction, as can be seen from Fig. 7.2a. Their results also display an apparent recovery of 0.2 at the shortest times of interruption. In the case of the mean stress technique, such recovery only has a minor effect on the fractional softening (Fig. 7.2b).

In the present work, when X_{Off} or X_{BE} was plotted against X_δ (Figure 7.3), the same type of non-linear behavior was found, at all temperatures. However, the softening rate X_δ is approximately linear with respect to the recrystallized fraction X_v . The same finding was reported by the above authors and a plot from their work which is similar to that of Fig. 7.3 was presented above in Fig. 7.2b. In addition to static recovery, the non-linearity shown in Fig. 7.2a can be attributed to the heterogeneity of recrystallization and the concentration of further deformation in the softer recrystallized areas [105]. This behavior is less likely to occur in compression than in torsion where the concentration of strain and strain rate in the recrystallized regions leads to lower flow stresses and hence to more apparent softening. The radial strain and strain rate gradient present in torsion samples also contributes to the lower apparent fractional softening at short interruption times. It can therefore be concluded that, in addition to static recovery, the the transient effect also contributes to raising the restoration index X_{Off} above that for the fraction recrystallized.

Fig. 7.3 also shows that both X_δ and X_{BE} are close to zero for the shortest interrupted times. This is an indication that the mean stress and back extrapolation methods both avoid the transient which occurs during reloading. However, as recrystallization proceeds, the non-linear relationship between X_δ and X_{Off} also develops between X_δ and X_{BE} . Andrade et al. [104] showed that the area under the curve in the second compression was usually overestimated when the extrapolated curve was used instead of the actual one. This led to



a)



b)

Figure 7.2 a) Relationship between the restoration index based on offset flow stress and recrystallized fraction at prestrains of 0.25 and 0.5.

b) Relationship between the restoration indices based on offset and mean flow stress at a prestrain of 0.25 ^[105].

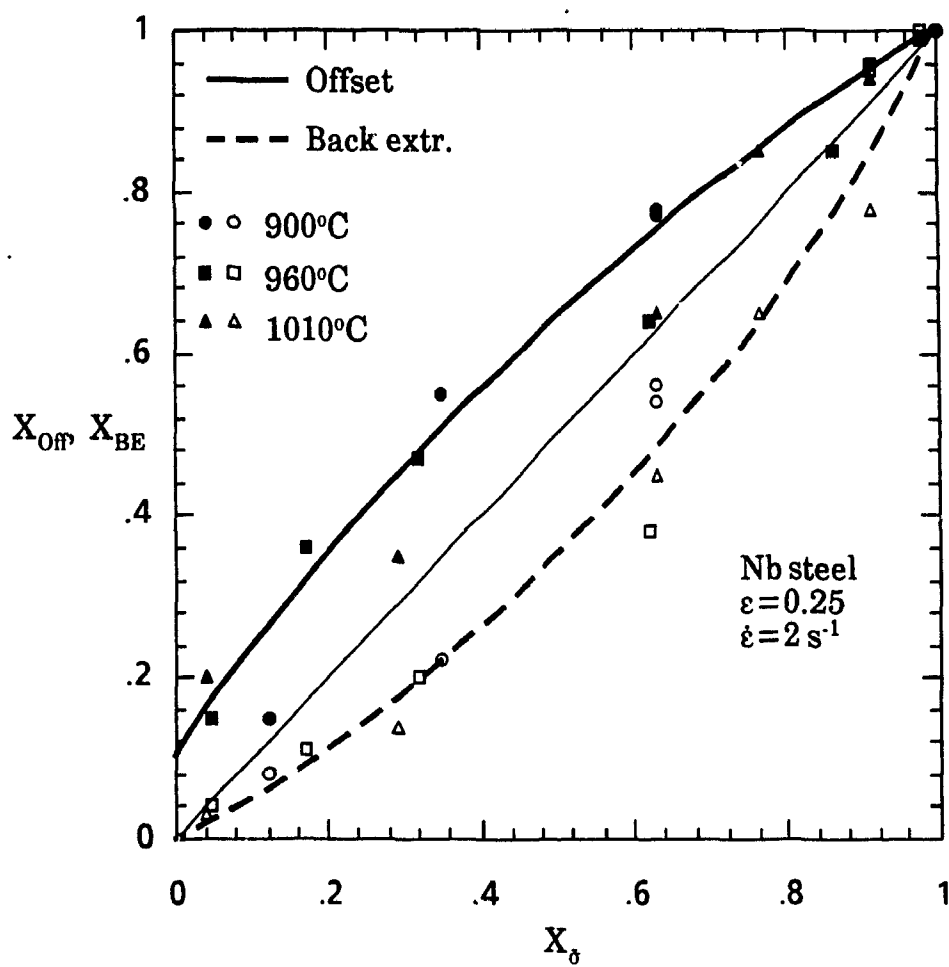


Figure 7.3 Relationship between the softening parameters determined by the mean stress, offset and back extrapolation methods.

lower values of fractional softening when the back extrapolation technique was employed.

In the rolling industry, it has long been reported that the static recovery occurring between stands only has a minor effect on the rolling load in subsequent passes, and that the major contributor to softening is static recrystallization. By using the offset method, Djaic and Jonas [19] showed that the softening taking place by recovery can account for up to 50% of the total softening. However, Luton et al. [169] demonstrated that, during reloading, and before the completion of recovery, a transient (represented by the dotted line in Fig. 7.4) is displayed, during which the flow stress abruptly increases. Since the area under continuous curve 1 in Fig. 7.4 is almost the same as the one under the rapid transient (dotted line), the rolling loads should be insensitive to this flow stress transient, even though the static 'softening' assessed by the offset method can be as high as 50%.

Finally, Barraclough and Sellars [17] made an important observation which supports the use of the mean stress method in the present work. In their paper, they stated that "*In rolling, it is mean flow stress rather than initial yield stress that determines the rolling forces....It would be expected that the rolling forces would correlate in a more nearly linear manner with fraction recrystallized. The linearity would also be expected to improve as the strain in the rolling pass increased*". Accordingly, in what follows, the mean stress method will be used to characterize the softening rate and the restoration by static recrystallization will be considered equal to X_0 .

7.2.3. Correction of the Softening Rate for Adiabatic Heating

During compression testing, particularly at high strain rates, the heat generated by deformation can change the specimen temperature considerably. The procedure for correcting the flow curve data for adiabatic heating during a single deformation was described and discussed in detail in sections 5.4 and 6.2.2. During interrupted compression testing, the change in temperature during the first and second hits affects the flow curves and therefore the softening rate measured by the mean stress method. The correction of X_0 is therefore necessary. It should be noted that the procedure described below is

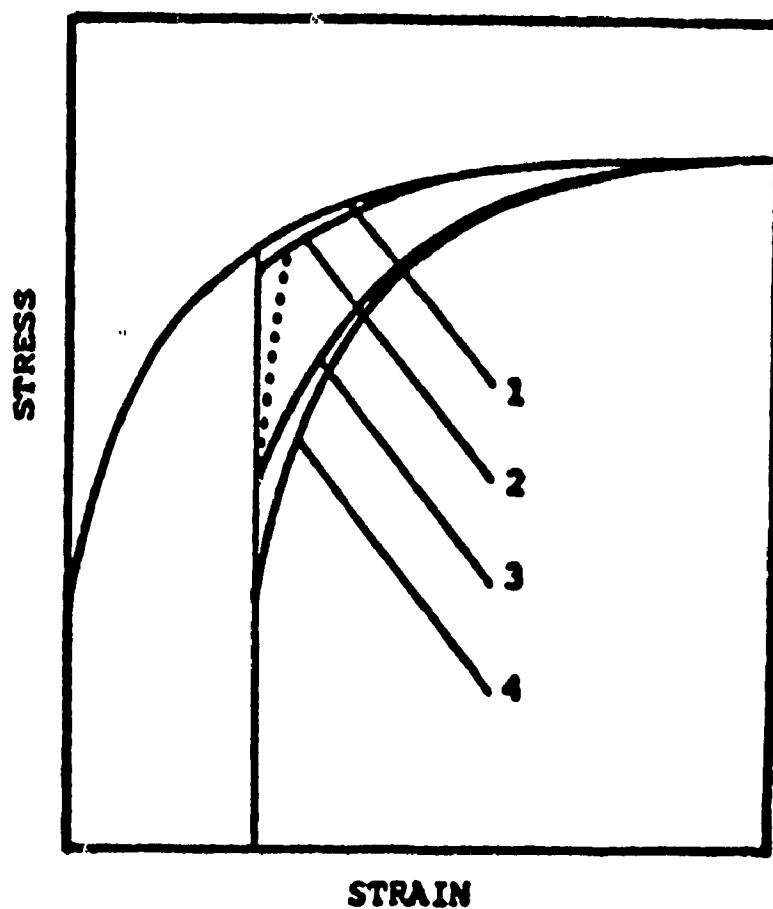


Figure 7.4 Schematic representation of interrupted compression flow curves showing continuous deformation (1), softening by static recovery (2), softening by static recrystallization (3) and full softening (4) ^[100].

not restricted to the situation where the changes in temperature are solely due to adiabatic heating. It can also be employed to calculate the anisothermal softening rate in situations where the temperature is decreasing continuously, as in hot rolling.

In an isothermal test, the original (i.e. full) and residual strengthening \bar{S}_O and \bar{S}_R are defined as follows:

$$\bar{S}_O = \frac{\bar{\sigma}_m - \bar{\sigma}_o}{\bar{\sigma}_o} \quad (7.1a)$$

$$\bar{S}_R = \frac{\bar{\sigma} - \bar{\sigma}_o}{\bar{\sigma}_o} \quad (7.1b)$$

where the $\bar{\sigma}$'s are the mean stresses defined in Fig. 7.5a. The softening rate $X_{\bar{\sigma}}$ can then be defined in terms of \bar{S}_O and \bar{S}_R in the following manner:

$$X_{\bar{\sigma}} = \frac{\Delta \bar{S}}{\bar{S}_O} = \frac{\bar{S}_O - \bar{S}_R}{\bar{S}_O} = \frac{\bar{\sigma}_m - \bar{\sigma}}{\bar{\sigma}_m - \bar{\sigma}_o} \quad (7.2)$$

During anisothermal compression, where the testing temperature increases from T_o to T_1 due to conversion of the plastic work to heat, the measured values are $\bar{\sigma}_o(T_o)$, $\bar{\sigma}_m(T_1)$ and $\bar{\sigma}(T_1)$ (see Figs. 7.5a and b). At T_1 , the full strengthening is given by the following:

$${}_A \bar{S}_O(T_1) = \frac{\bar{\sigma}_m(T_1) - \bar{\sigma}_o(T_1)}{\bar{\sigma}_o(T_1)} \quad (7.3)$$

Now $\bar{\sigma}_o(T_1)$ can be expressed in terms of the measured mean flow stress $\bar{\sigma}_o(T_o)$. This is possible if one assumes that the temperature interval between T_o and T_1 is small so that the σ - T plot can be approximated by a straight line (tangent), as displayed in Fig. 7.5c. In such a case, $\bar{\sigma}_o(T_1)$ is equal to $\bar{\sigma}_o(T_o)/K_S$, where K_S is a conversion factor. Eq. 7.3 can be written as follows:

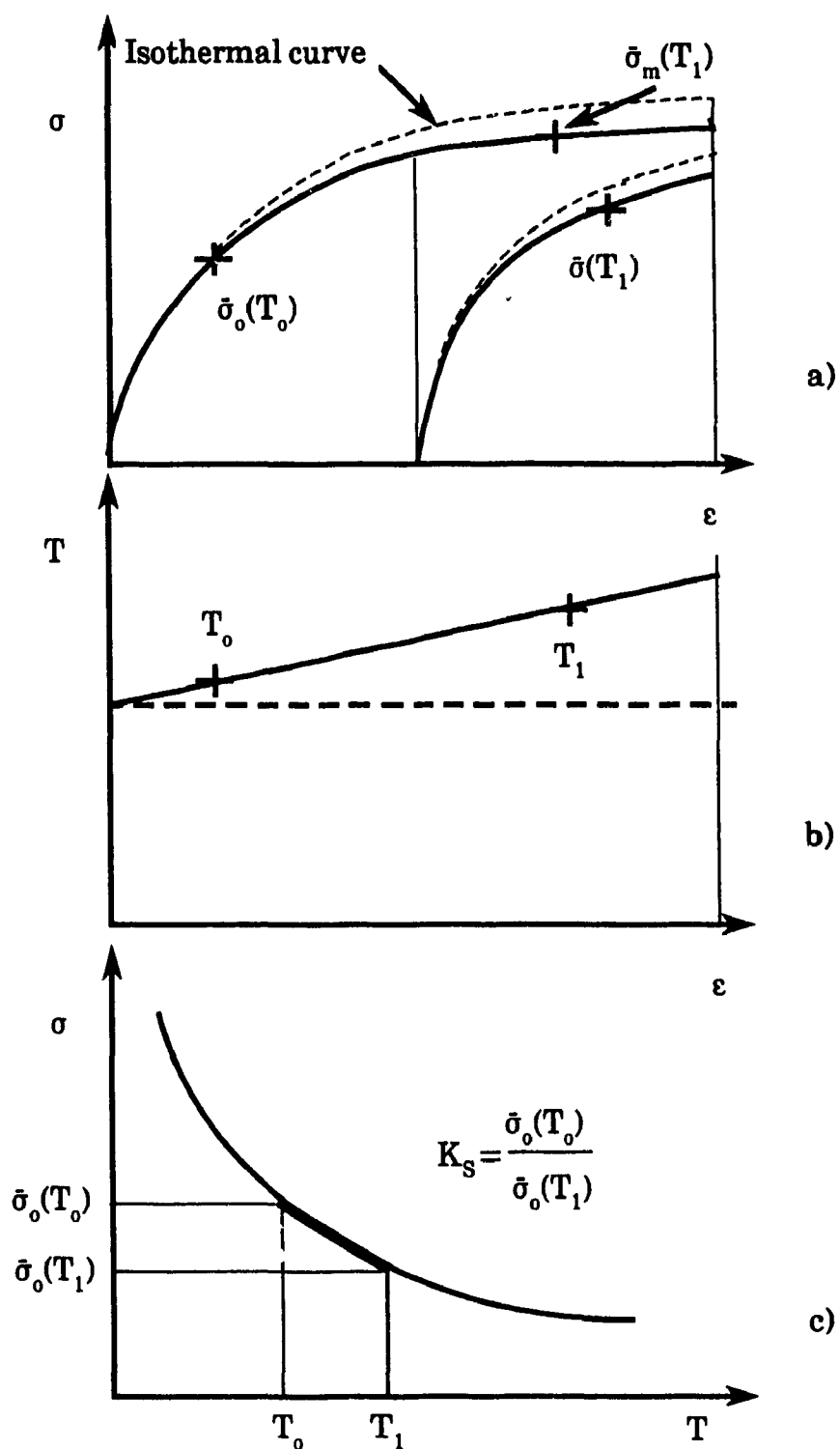


Figure 7.5 Description of the method used to correct the softening parameter for adiabatic heating.

$${}_A\bar{S}_O(T_1) = \frac{\bar{\sigma}_m(T_1)}{\bar{\sigma}_o(T_o)/K_S} - 1 \quad (7.4a)$$

Similarly:

$${}_A\bar{S}_R(T_1) = \frac{\bar{\sigma}(T_1)}{\bar{\sigma}_o(T_o)/K_S} - 1 \quad (7.4b)$$

and finally, the anisothermal softening rate can be written as:

$${}_A X_{\sigma} = \frac{\Delta_A \bar{S}}{{}_A \bar{S}_O} = \frac{\bar{\sigma}_m(T_1) - \bar{\sigma}(T_1)}{\bar{\sigma}_m(T_1) - \bar{\sigma}_o(T_o)/K_S} \quad (7.5)$$

Note that for $K_S = 1$, we retrieve the isothermal softening rate defined by Eq. 5.15.

Table 7.1 Corrected and uncorrected values of fractional softening during the interrupted compression testing of Nb-B steel deformed at 900°C and 10s⁻¹ with a prestrain of 0.25.

t	$X_o(\text{Uncorr.})$	$X_o(\text{Corr.})$	ΔX_{σ}	$100\Delta X_{\sigma}/X_o$
10	0.449	0.374	0.075	16.7
30	0.421	0.349	0.072	17.1
100	0.454	0.371	0.083	18.2
300	0.520	0.431	0.089	17.3
1000	0.612	0.506	0.106	17.3
5000	1.000	0.833	0.167	16.7

An example of corrected and uncorrected softening rates is given in Table 7.1. Fig. 6.5 was used to estimate the increase in temperature during the test performed at 900°C and the plot in Fig. 7.6 was employed to determine the mean stresses at the adiabatic and isothermal temperatures, and therefore the conversion factor K_S . The latter turned out to be about 1.1. Table 7.1 shows

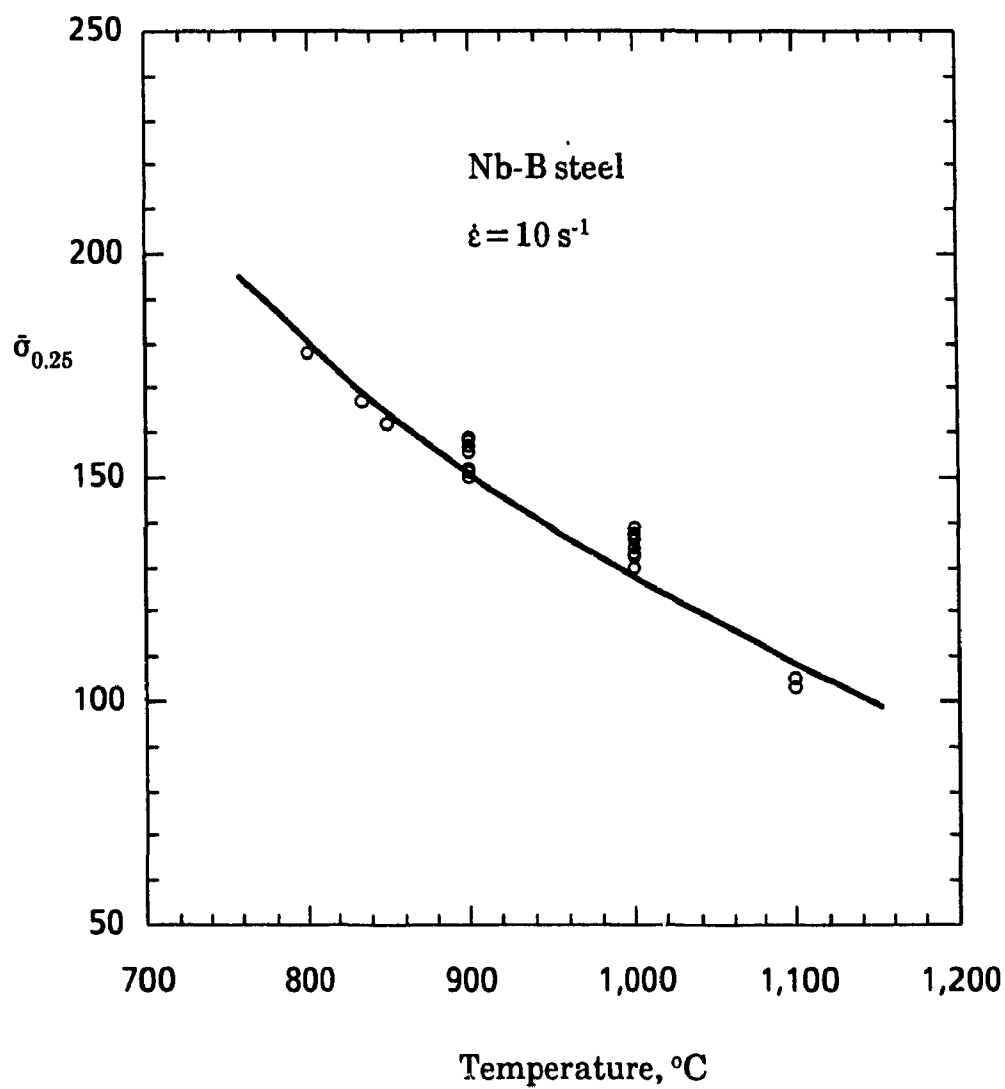


Figure 7.6 Temperature dependence of the mean flow stress determined at a strain of 0.25.

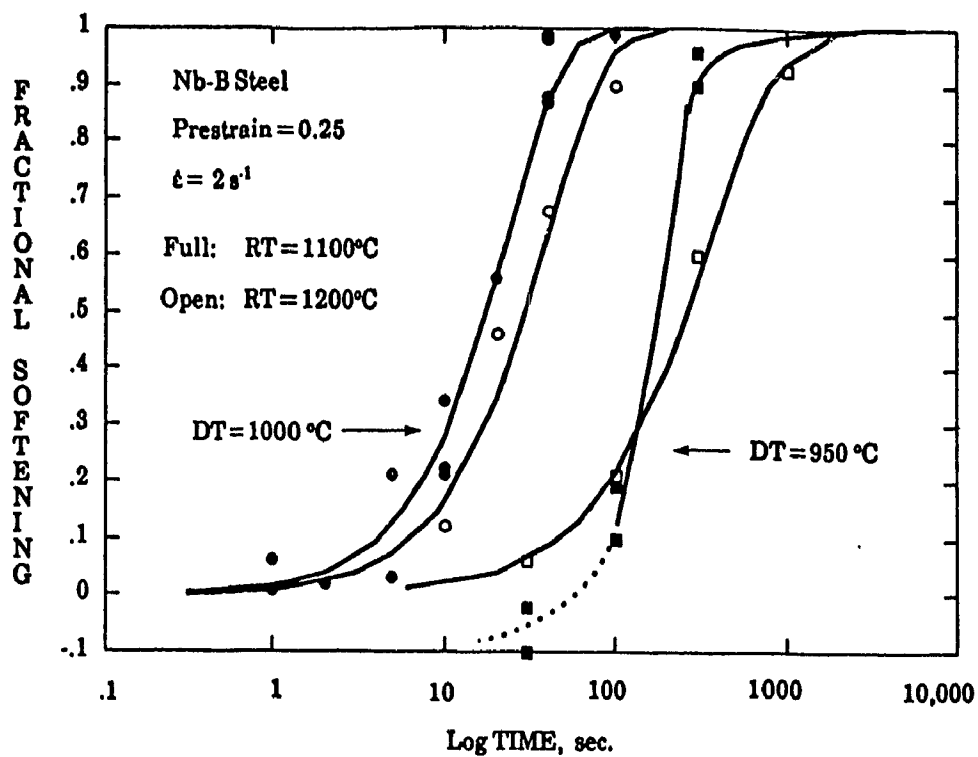
that the corrected values of fractional softening are actually lower than the uncorrected ones, with the difference ΔX_o increasing with the fractional softening itself. This was also reported by Pawelski and coworkers [170] using a similar technique to correct the softening rate determined by the offset method. In their work, when the restoration index X_{off} was about 0.9, they found that the difference between the corrected and uncorrected fractional softening was about 0.2, leading to an error of 2%. However, the temperature changes they considered also included the heat losses due to radiation and contact with the tools in addition to adiabatic heating. This explains why their errors in fractional softening are slightly higher than the ones shown in Table 7.1.

In conclusion, a simple way of correcting the softening rate for adiabatic heating which is based on the mean stress method was used and described. It was shown that this correction is necessary when the testing temperature is low or the strain rate is high, because errors of up to 18% can occur in measuring the restoration index.

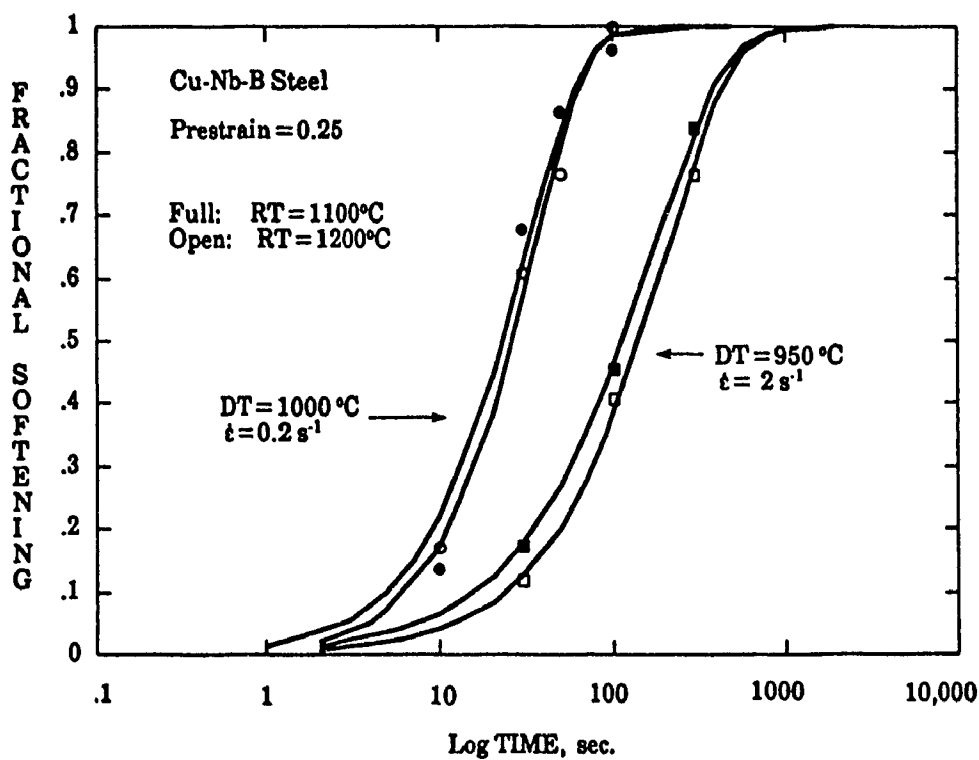
7.3. INFLUENCE OF DEFORMATION CONDITIONS ON RECRYSTALLIZATION KINETICS

7.3.1. Effect of Reheating Temperature

The effect of reheating temperature on the recrystallization curves is illustrated in Fig. 7.7a for the Nb-B steel. When the reheating temperature is increased from 1100 to 1200°C, the recrystallization kinetics are slightly delayed due to the slightly larger initial grain size (see Fig. 4.5), and probably because of the slightly greater amount of niobium in solution. Although it was assumed that the niobium is completely dissolved at 1100°C (see Fig. 4.3), the solution temperature is not a sufficient indicator of the complete dissolution of the niobium carbonitrides. For a 0.06C-0.04Nb steel, extraction replicas of specimens reheated to 1100°C, cooled to lower temperatures and quenched revealed the presence of undissolved niobium carbonitrides [171]. The coarse form of these precipitates suggested that they did not form during cooling but remained undissolved during reheating. Also, there is a contribution from alloying elements other than niobium. All these factors, together with the



a)



b)

Figure 7.7 Effect of reheating temperature on the softening rate in the
a) Nb-B steel
b) Cu-Nb-B steel.

effect of grain size, explain the retardation of the recrystallization kinetics observed at 1000°C and the acceleration of precipitation at 950°C when the reheating temperature is increased from 1100 to 1200°C (Fig. 7.7a).

Perdrix [161] found that the effect of initial grain size becomes less important when the deformation conditions are such that dynamic recrystallization is favored, as the static recrystallization kinetics then become independent of deformation rate and temperature. For the present steel, the effect of initial grain size and therefore the influence of reheating temperature are expected to be less important when the strain rate is decreased or the temperature is increased.

In the Cu-Nb-B steel, practically no effect of reheating temperature on recrystallization kinetics was observed between 1000 and 1200°C. Figure 7.7b gives an example of the behavior at two different testing temperatures and strain rates. For this steel, the absence of a reheating temperature effect can be explained in the same manner as for the Nb-B steel. In fact, Fig. 4.5 shows that the initial grain size remains almost constant as RT is raised from 1000 to 1250°C. Since the initial grain size affects the density of nucleation sites [172], equal grain sizes can be expected to lead to identical recrystallization kinetics.

7.3.2. Effect of Deformation Temperature and Prestrain

The softening parameter determined by the mean stress method at different testing temperatures is plotted against the logarithm of the holding time in Figs. 7.8a, b and c for the base, Nb and Nb-B steels, respectively. In the first steel, the effect of temperature on the recrystallization kinetics is evident from Fig. 7.8a, where the fractional softening goes from 12% at 900°C to almost 70% at 1000°C within a holding time of 1 second. It is of interest to note that, at 1000°C, the fractional softening does not go to completion, even at holding times greater than 100 seconds. Examination of the continuous true stress/true strain curves (Fig. 6.1b) shows that, at this temperature, dynamic recrystallization is already under way at a strain of 0.25, which leads to softening by metadynamic recrystallization after deformation. Such incomplete softening at long holding times has been observed in hot deformed

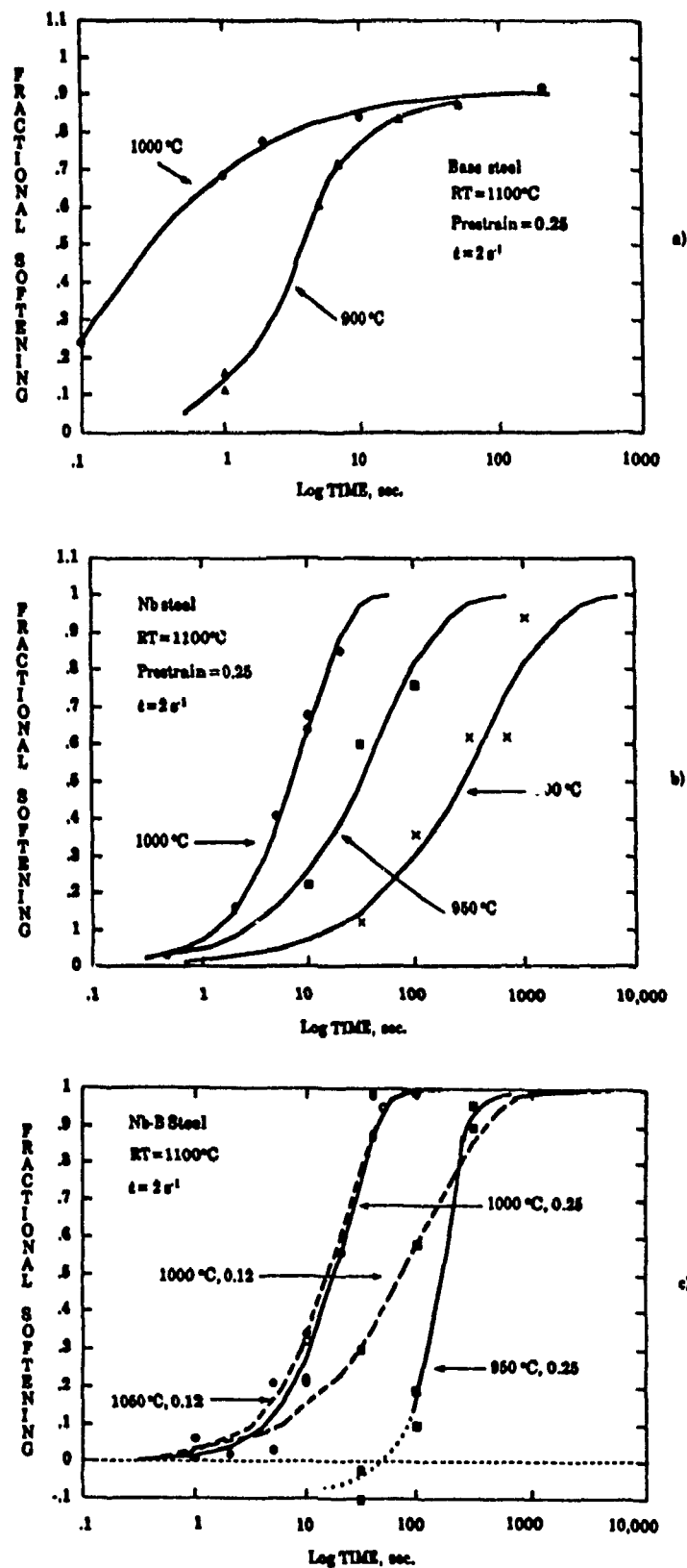


Figure 7.8 a) Effect of temperature on softening in the base steel prestrained to 0.25.
 b) Effect of temperature on softening in the Nb steel prestrained to 0.25 at 2 s^{-1} .
 c) Effect of temperature on softening in the Nb-B steel.

polycrystalline nickel by Sakai et al. [173, 174], who attributed it to the presence of metadynamically recovered grains. These grains are stable at high temperatures because they have a dislocation density which is below the critical level, so that there is insufficient driving force for nucleation.

In the Nb steel (Fig. 7.8b), the deformation temperature has the same effect on fractional softening, showing that the recrystallization kinetics are delayed by more than an order of magnitude in time when the temperature is decreased from 1000°C to 900°C. Similar trends are displayed by the Nb-B steel, as can be seen from Fig. 7.8c.

In Figs. 7.9a,b and c, the effect of strain prior to holding is illustrated for the base, Nb-B and Cu-Nb-B steels, respectively, over the temperature range from 900 to 1100°C. Here also, a reduction in the prestrain results in the strong retardation of recrystallization. During the past few years, systematic studies concerning the effect of temperature and prestrain on the restoration behavior after high temperature deformation have been carried out [17, 19, 100, 105, 119, 161, 167, 169, 172, 175]. The results given here are in agreement with the ones reported in the literature. In the above investigations, the acceleration of the softening rate with increasing temperature or prestrain has been described extensively for a considerable range of steel chemistries.

7.3.3. Effect of Strain Rate

While the effects of temperature, strain and initial grain size have been extensively studied and clarified by many authors, no systematic study has yet been conducted on the effect of strain rate on recrystallization kinetics in HSLA steels. Until now, the effect of strain rate on recrystallization has been neglected and evaluation of the softening rate at a single strain rate has been considered to be sufficient for modelling purposes. However, the systematic data collected during the present work show that the recrystallization kinetics are significantly accelerated when the strain rate is increased. Such behavior is observed in both the base and microalloyed steels and is illustrated in Figs. 7.10a to d.

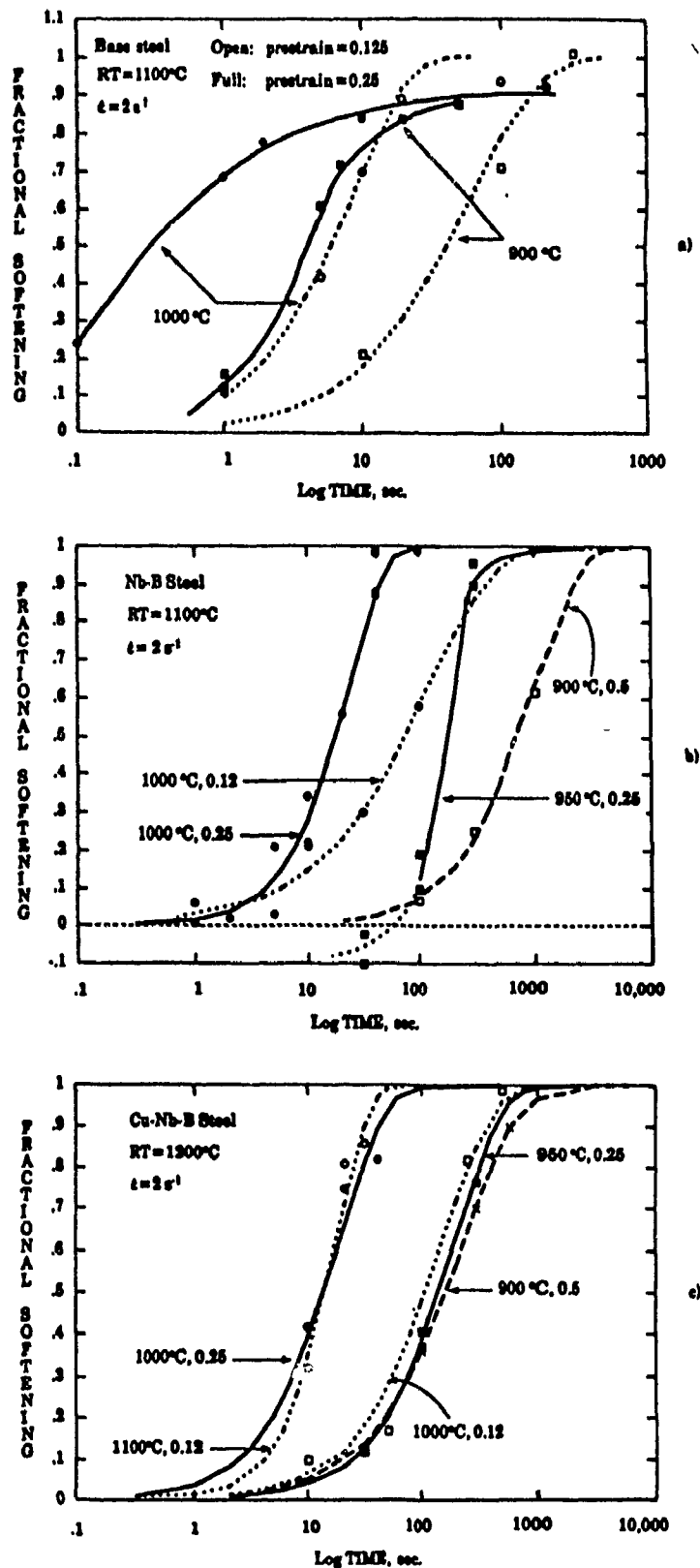


Figure 7.9 a) Effect of prestrain on softening in the base steel prestrained to 0.125 and 0.25.
 b) Effect of prestrain on softening in the Nb-B steel.
 c) Effect of prestrain on softening in the Cu-Nb-B steel deformed at different temperatures.

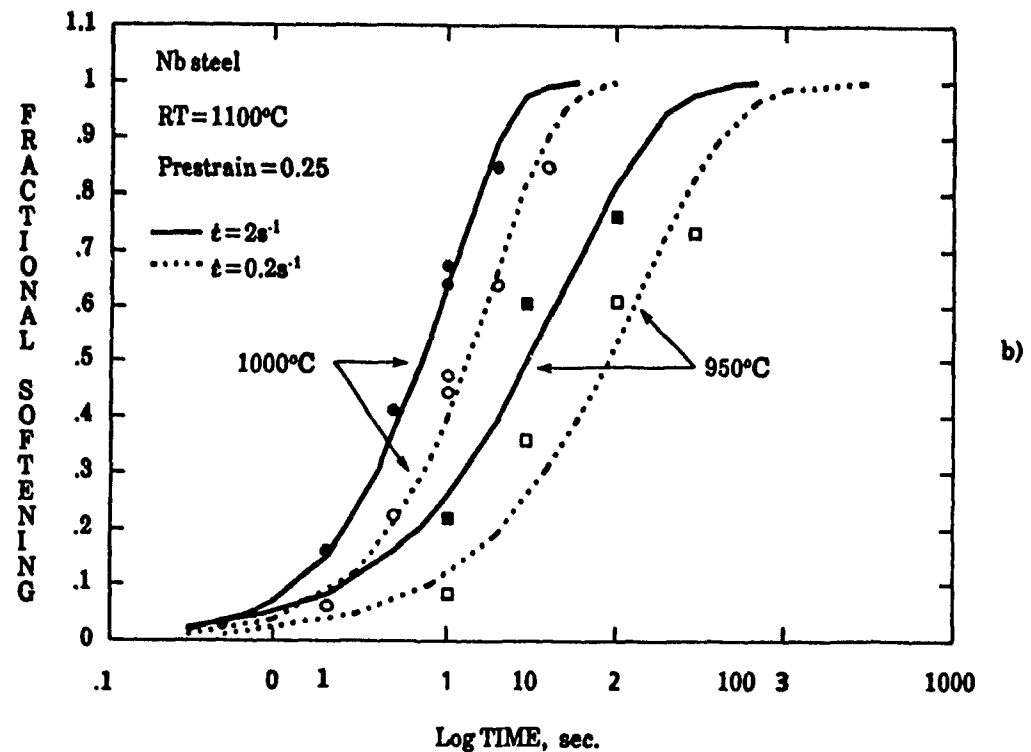
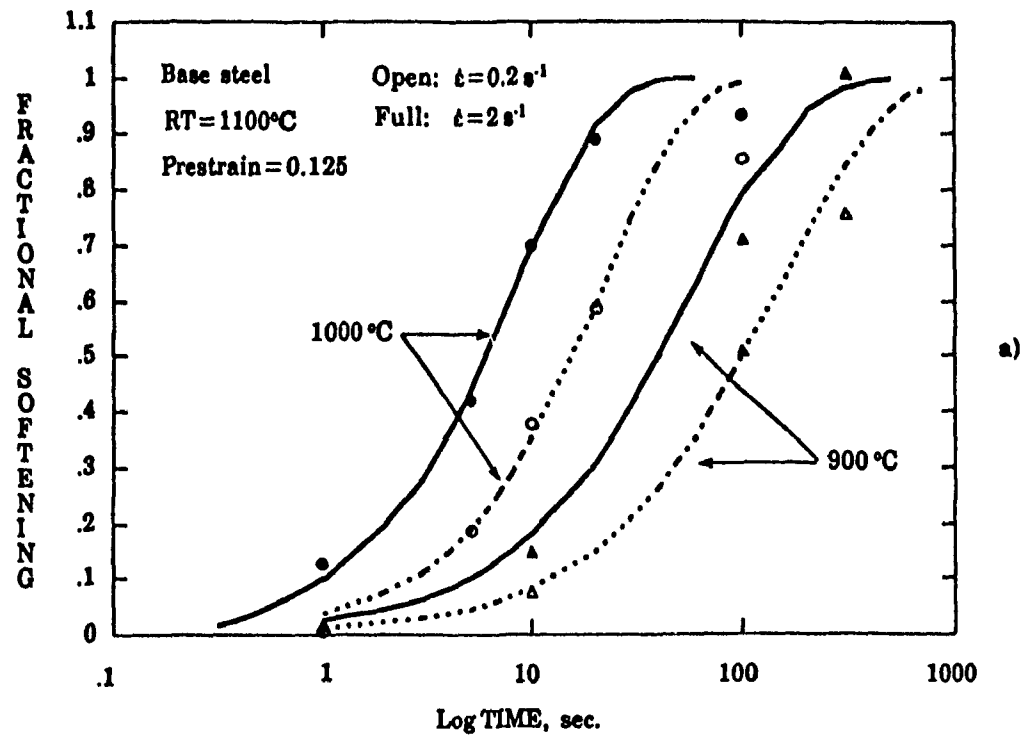
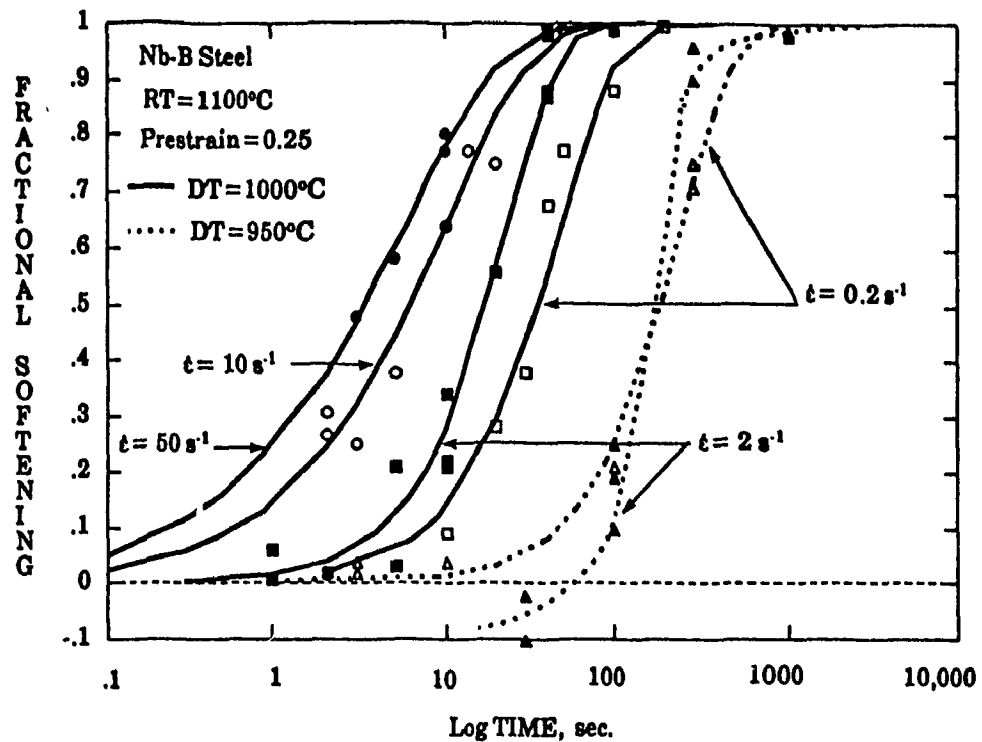
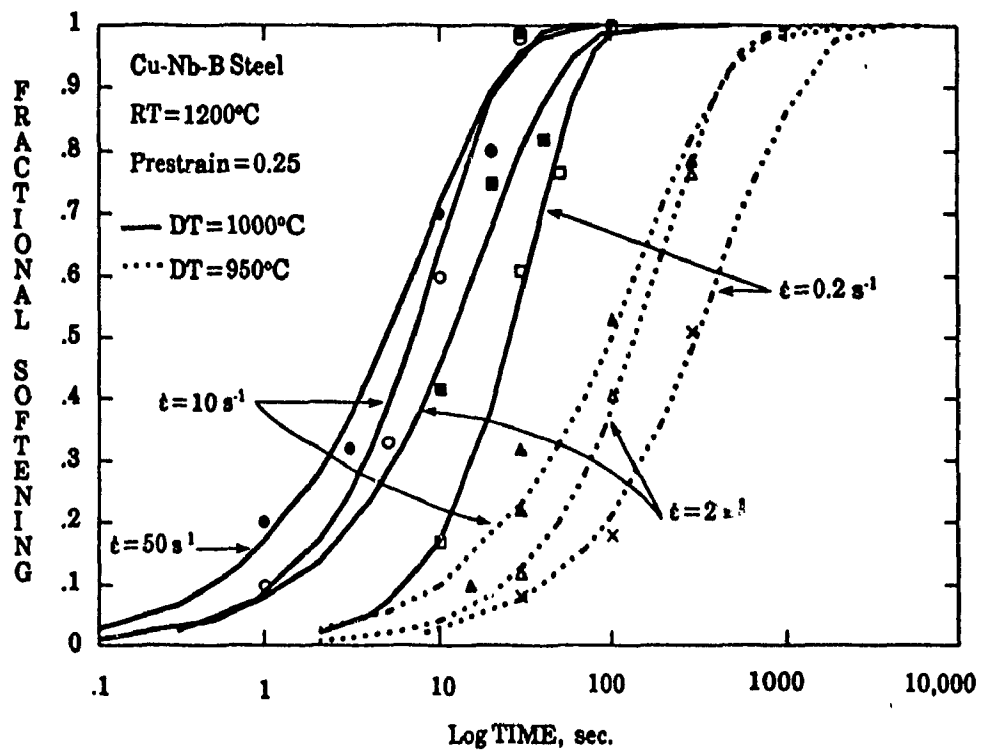


Figure 7.10 a) Effect of strain rate on softening in the base steel prestrained to 0.125.
b) Effect of strain rate on softening in the Nb steel prestrained to 0.25 (contd.).



c)



d)

Figure 7.10 c) Effect of strain rate on softening in the Nb-B steel.

d) Effect of strain rate on softening in the Cu-Nb-B steel.

C In the absence of strain-induced precipitation, raising the strain rate by two orders of magnitude increases the softening rate by at least one order of magnitude. This acceleration in softening rate is due to the increase in dislocation density and the decrease in subgrain size prior to holding, both of which increase the stress level and therefore the stored energy. This energy constitutes the driving force for recrystallization. In the range of temperatures where strain-induced precipitation is likely to occur, such as in the Nb-B steel deformed at 950°C (Fig. 7.10c), the strain rate effect is manifested by the acceleration of both recrystallization and precipitation at higher strain rates, which leads to an interaction between these two processes.

The above results have fundamental implications with respect to hot rolling practices. Since the strain rates used in plate rolling are higher than those usually employed in laboratory simulations, this difference can lead to an underestimation of the softening occurring between stands and consequently to an overestimation of the rolling load. This is of even greater importance in hot strip mills, where the strain rates are still higher and increase with pass number. A simple application of the laboratory data obtained at lower strain rates thus leads to errors which can be about equal to those associated with changes in temperature or prestrain. Also, simple extrapolations are likely to be inaccurate, because the flow stress prior to holding, which constitutes the driving force for static recrystallization via the dislocation density, does not vary linearly with strain rate at the higher rates of deformation. As discussed in section 6.5, the strain rate sensitivity is not always constant but decreases with increasing strain rate. In conclusion, unless the experimental determination of the softening rate is performed at industrial strain rates, the extrapolation of the laboratory data determined at conventional strain rates to high speed mill conditions will lead to significant errors in rolling load prediction.

C In the literature, there seems to be a controversy about whether the effect of strain rate on the recrystallization kinetics is important or not. While Barraclough and Sellars [105], and Ruibal et al. [172] found a significant effect in stainless and low alloy steels, respectively, Migaud [176] and Morrison [177] did not observe any effect of strain rate over one and two orders of magnitude, respectively. According to Sellars [17], deformation reduces the subgrain size

and increases the sub-boundary misorientation. Since these boundaries provide the major contribution to the stored energy, the dependence of the characteristic recrystallization time $t_{0.5}$ on strain rate comes from both an increase in the density of nucleation sites and in the *nucleation rate*. He attributed the absence of the influence of strain rate on the recrystallization kinetics in Morrison's work to the compensating effects on stored energy and substructure development, because of the initiation of dynamic recrystallization after deformation at the lower strain rates used.

7.3.4. Modelling the Effect of Deformation Conditions on Recrystallization Kinetics

7.3.4.1. Static Recrystallization Rate

For transformation processes involving nucleation and growth, such as recrystallization, the recrystallized fraction X_v can be described by an Avrami equation, which is of the form [178]:

$$X_v = 1 - \exp \left[-B \left(\frac{t}{t_F} \right)^{n_A} \right] \quad (7.6a)$$

Here t_F is the time for a specified fraction of recrystallization F , n_A is a constant and B is equal to $-\ln(1-F)$.

Experimental results concerning the dependence of softening rate (or recrystallized fraction) on the deformation parameters were presented above for the four steels investigated. These softening curves have sigmoidal shapes and follow Eq. 7.6a. Since X_v can be approximated by X_{σ} (see section 7.2.2) and setting F arbitrarily equal to 0.5, one can use the following expression to describe the present results:

$$X_{\sigma} = 1 - \exp \left[-0.69 \left(\frac{t}{t_{0.5}} \right)^{n_A} \right] \quad (7.6b)$$

Knowledge of the dependence of n_A and $t_{0.5}$ on the thermomechanical and metallurgical parameters permits the complete description of the

recrystallization kinetics. Taking the logarithm twice of both sides of Eq. 7.6b, one can plot $\ln[\ln(1/(1-X_0))]$ versus $\ln(t)$, estimate the slope n_A and determine the characteristic time $t_{0.5}$. Such plots are portrayed in Figs. 7.11a to d for the four steels studied, under different conditions of temperature, strain rate and prestrain. Examination of the slopes shows that, within experimental error, the average value of n_A is independent of the deformation parameters and chemistry and is about 1. This is valid for all conditions except when structural changes in addition to static recrystallization take place, such as strain-induced precipitation or metadynamic recrystallization.

Similar values of n_A were reported by Mavropoulos and Jonas [119] for a Nb and a Nb-B steel using a different approach to assess the recrystallized fraction from mechanical testing data. Luton et al. [169] and Ruibal et al. [172] also found constant slopes within the experimental ranges they employed for copper and low alloy steels, respectively, but they reported n_A values of around 2. For a given initial grain size, Sellars [17] and Barraclough and Sellars [105] observed the same independence of the deformation parameters in stainless and C-Mn steels. However, the measured values of the slopes by the latter authors were sometimes higher than the ones determined in the present work. When they increased the grain size from 140 to 530 μm , n_A decreased from 2 to 1. This is surprising because the grain sizes used in the present study are low and span the range from 17 to 40 μm . However, it was observed recently by Sellars [179] that variations in the value of n_A in the range from 1 to 2 can be attributed mainly to grain size distributions during reheating rather than to differences in the average grain size.

Differences in the results concerning the time exponent n_A can also be attributed to the different modes of deformation employed by different investigators. This has been explained by Sellars [17], who attributed the differences in the recrystallization kinetics, and therefore in the coefficients n_A and $t_{0.5}$, to the influence of the strain rate history during deformation on recrystallization. He has also pointed out that much of the discrepancy can result from differences in the methods of observation, i.e., mechanical testing versus the direct measurement of recrystallization by metallography. The type of mechanical test used to evaluate the softening can be another cause of this difference. As shown by Jonas et al. [18], flow stresses in torsion are lower

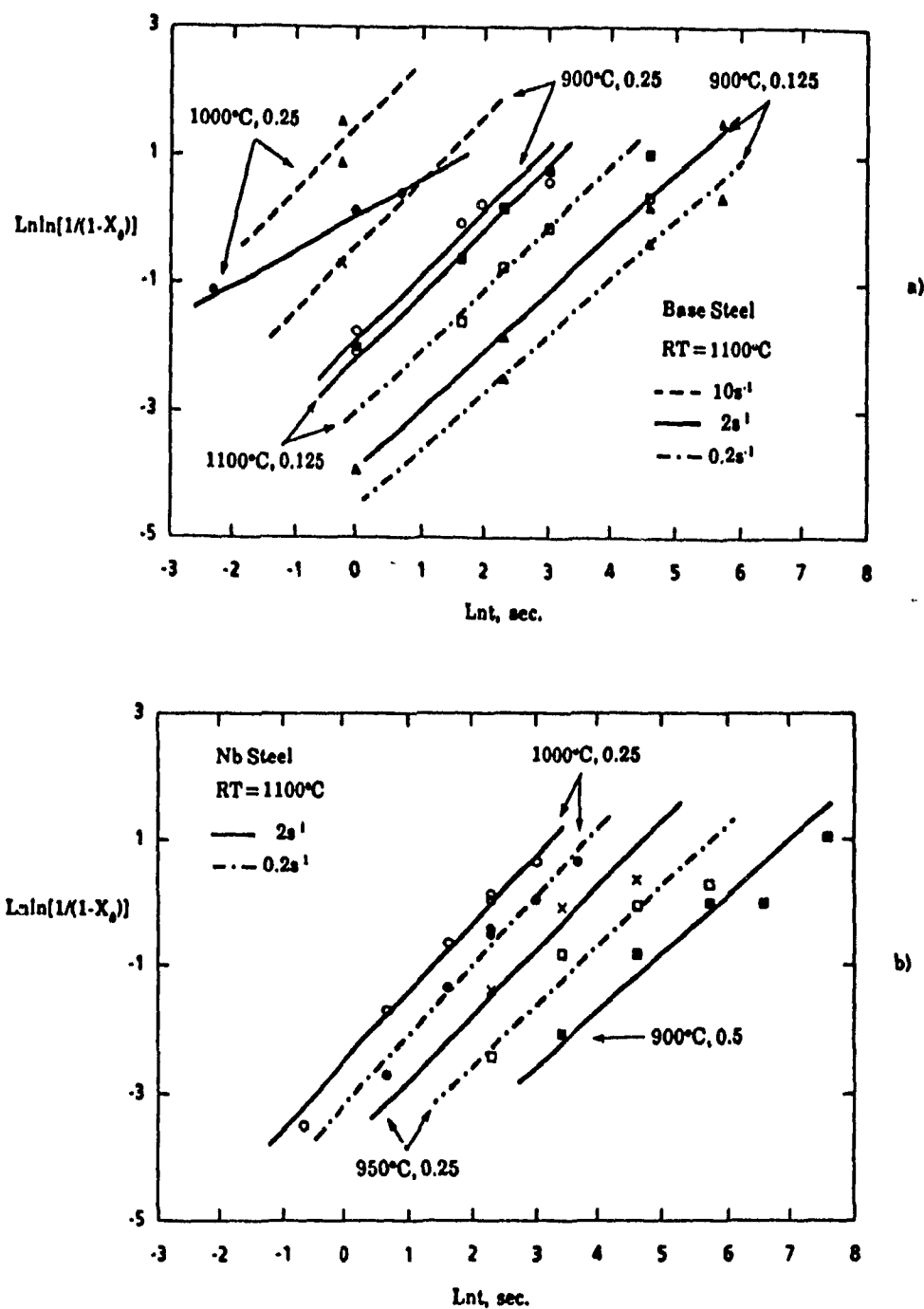


Figure 7.11 a) Dependence of $\ln \ln[1/(1-X_0)]$ on $\ln(t)$ under different conditions of prestrain, strain rate and temperature in the base steel.

b) Dependence of $\ln \ln[1/(1-X_0)]$ on $\ln(t)$ under different conditions of prestrain, strain rate and temperature in the Nb steel (contd.).

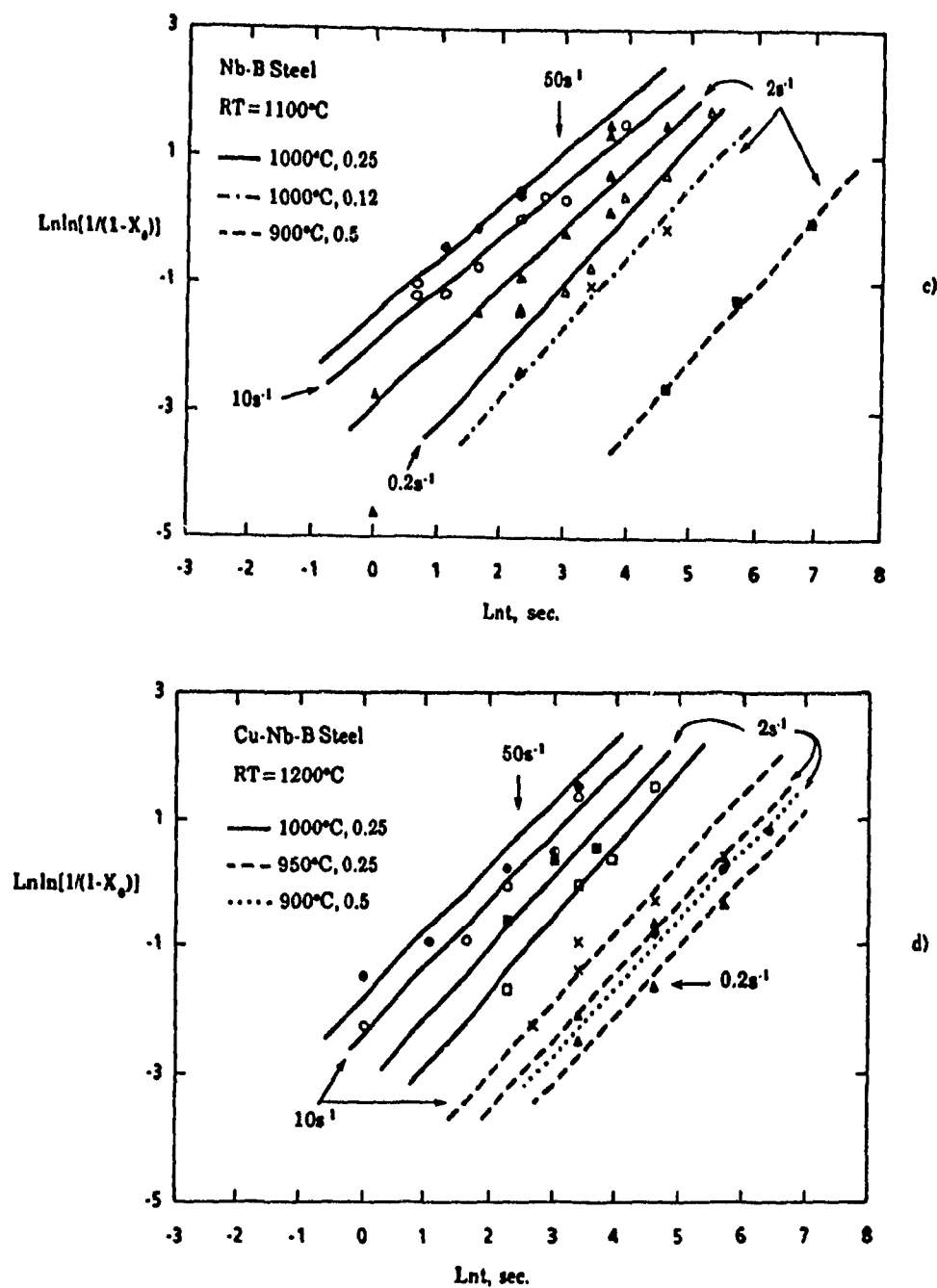


Figure 7.11 c) Dependence of $\text{Lnln}[1/(1-X_0)]$ on $\text{Ln}t$ under different conditions of prestrain, strain rate and temperature in the Nb-B steel.

d) Dependence of $\text{Lnln}[1/(1-X_0)]$ on $\text{Ln}t$ under different conditions of prestrain, strain rate and temperature in the Cu-Nb-B steel.

than in compression, so that a difference in the softening kinetics is to be expected, especially when the different geometries of the deformed grains are taken into account.

7.3.4.2. Dependence of $t_{0.5}$ on Initial Grain Size and Prestrain

An example of the strain dependence of the time for 50% recrystallization ($t_{0.5}$) is shown for the base and copper steels in Fig. 7.12. This plot shows that the strong dependence of the recrystallization kinetics on strain can be fitted by almost parallel lines on a log-log scale. This behavior supports the validity of the following empirical power law relationship:

$$t_{0.5} \propto \varepsilon^{-m_A} \quad (7.7)$$

where the mean value of m_A lies between 3.55 and 3.81, within the interval of prestrain used. This is in agreement with the values found in previous investigations on other ferrous alloys [9, 17, 94, 105, 172].

Perdrix [161] developed an empirical formula for the exponent m_A in Eq. 7.7 as a function of Nb content and initial grain size, which is as follows:

$$m_A = (0.86 + 0.037\sqrt{Nb}) d_o^{0.24} \quad (7.8)$$

where Nb is in 10^{-3} wt%. Perdrix showed that Eq. 7.8 is also valid for $Nb = 0$. From this equation, it is clear that an increase in niobium content results in a stronger dependence of $t_{0.5}$ on the amount of deformation. This is reasonable since the addition of niobium raises the flow stress level and consequently the stored energy prior to holding, which constitutes the driving force for recrystallization. However, the effect of initial grain size d_o does not predict the exponent m_A very well for the present steels. For a grain size between 20 and $40\mu\text{m}$, values between 2 and 2.8 are predicted for m_A by this equation. Care must therefore be exercised when applying empirical expressions to specific chemistries and ranges of experimental conditions.

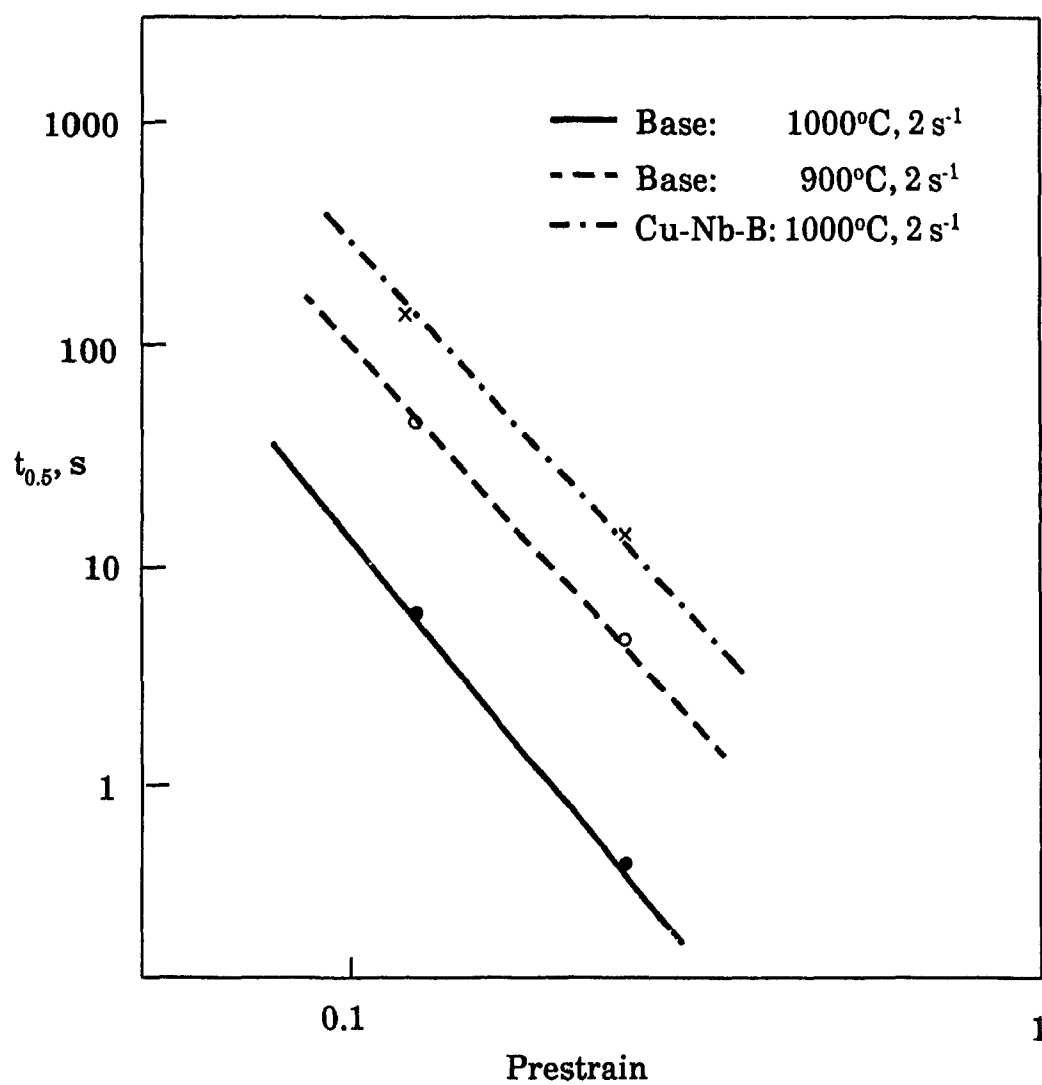


Figure 7.12 Dependence of $t_{0.5}$ on prestrain for the base and Cu-Nb-B steels.

Finally, it is worth emphasizing that Eq. 7.7 is only valid when the strain is below the critical strain for dynamic recrystallization [17]. This critical value is difficult to determine accurately and depends on several factors [15, 177]. The applicable strain must also be lower than the steady state or peak, strain where the strain dependence of $t_{0.5}$ approaches zero [105].

7.3.4.3. Apparent Activation Energies for Recrystallization

As in Figure 7.12, times for 50% softening ($t_{0.5}$) were estimated from Figs. 7.8 to 7.10 for the four steels, and then used to produce Fig. 7.13. Since static recrystallization is a thermally activated process, a plot of the characteristic recrystallization time $t_{0.5}$ versus the inverse absolute temperature leads to estimates of the activation energy for recrystallization. The temperature dependence of $t_{0.5}$ is illustrated in Fig. 7.13. Within the range of experimental conditions, $t_{0.5}$ varies linearly with the inverse temperature for the two steels shown, as well as for the Nb-B and Cu-Nb-B steels. The data conform to the well known expression for the temperature dependence of the time for 50% recrystallization, which is of the form:

$$t_{0.5} \propto \exp\left(\frac{Q_r}{RT}\right) \quad (7.9)$$

where Q_r is the activation energy that characterizes the recrystallization process.

In fact, Glover and Sellars [9] have shown that a true activation energy for recrystallization Q_r can only be estimated when the prior deformation conditions lead to equivalent flow stresses, and hence to similar driving forces at the different temperatures. This means that the strain rate and temperature must be adjusted in such a way that the deformation conditions, and therefore the state of the structure, are identical during the first deformation of each interrupted test. In other words, the Zener-Hollomon parameter Z must be constant. This problem is similar to that discussed in section 6.3.2.1, which concerns the determination of the activation energy of deformation.

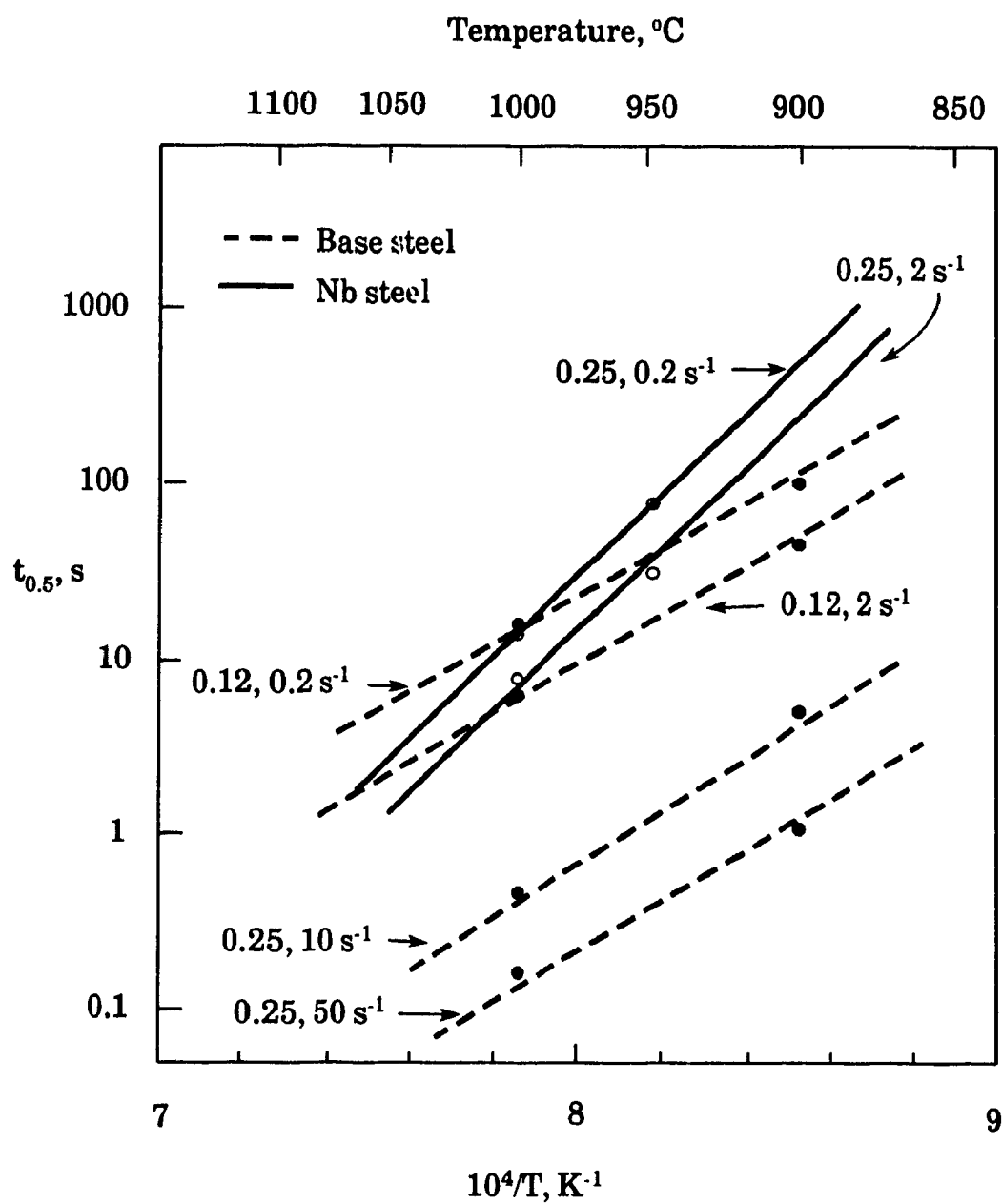


Figure 7.13 Temperature dependence of the time for 50% softening in the base and Nb steels.

In the literature, the values reported for Q_r are apparent and not true activation energies. They may characterize other processes in addition to recrystallization, such as precipitation for instance. The complexity of determining the true value of Q_r has prompted several investigators to discuss the recrystallization process in terms of an empirical constant which characterizes the overall process of softening. For this reason, and because mean values of Q_r in Eq. 7.9 are desirable for process modelling, only the apparent activation energies shown in Fig. 7.13 were determined in this investigation. For the base steel, an average value of about 252 kJ/mol was found. This is close to the 240 kJ/mol observed by Ruibal et al. [172] for a low alloy steel. Although Sellars [17] has reported slightly higher values of Q_r (between 272 and 300 kJ/mol) for C-Mn steels, the value of 252 kJ/mol found in the present investigation for the base steel appears to be normal because of the presence of titanium and the small initial grain size [94].

For the other steels, the mean values of Q_r turned out to be 404, 436 and 559 kJ/mol in the Nb, Nb-B and Cu-Nb-B steels, respectively. While additions of niobium and copper strongly increase the apparent activation energy, boron does not. In a 0.04% Nb steel, Sellars [17] reported values of Q_r of up to 780 kJ/mol in the temperature range 900-1000°C. Although he did not give a fundamental explanation of these observed values, he stated that the alterations in the activation parameter Q_r , as well as in the other constants, are due to the changes in the deformation conditions, which affect the kinetics of precipitation.

Finally, it should be noted that the above values of Q_r are mean values. A slight decrease in Q_r occurs when the strain or strain rate is increased. The low activation energies obtained at high strain rates for instance are due to the acceleration of recrystallization followed by the precipitation of Nb(C,N) particles, which stabilize the deformed structure of the austenite. The net driving force for recrystallization, however, in the form of stored energy remains relatively high.

7.3.4.4. Modelling the Effect of Strain Rate

The influence of strain rate on softening, and therefore on the recrystallization kinetics was described in Figs. 7.10a to d for the four steels, deformed at different temperatures to different prestrains. It was shown that the softening rate is clearly speeded up when the strain rate is increased in the range 0.2 to 50 s⁻¹. The effect of strain rate can be evaluated from the time for 50% softening using a simple expression. The data collected for each steel were plotted on log time scales for the temperatures and prestrains studied and the results are depicted in Figs. 7.14a and b. In the range of strain rates used, the points fit straight lines which are approximately parallel. It is clear that $t_{0.5}$ can be expressed by a power function of the form:

$$t_{0.5} \propto \dot{\epsilon}^{-p} \quad (7.10)$$

where p is about 0.41, 0.36, 0.42 and 0.33 for the base, Nb, Nb-B and Cu-Nb-B steels, respectively. These values show no special trend and are approximately constant. This is in good agreement with the constant value of 0.28 found by Perdrix [161] and Choquet et al. [132] for C-Mn and Nb steels. The values of p evaluated here are also close to that of 0.38 reported by Barraclough and Sellars [105] for a 304 stainless steel.

It is worth emphasizing that the values determined in the present work are valid only when Nb is in solution. When strain-induced precipitation occurs at low temperatures, the strain rate effect can be less pronounced due to the interaction between recrystallization and precipitation. An example of such a decrease in the effect of strain rate is illustrated for the Nb-B steel at 950°C in Fig. 7.14b. This behavior is difficult to model and needs more systematic study.

7.3.4.5. Mathematical Expressions for Recrystallization Kinetics

In process modelling, simple mathematical functions are useful as inputs into the computer program. During the hot rolling of steel, unified equations

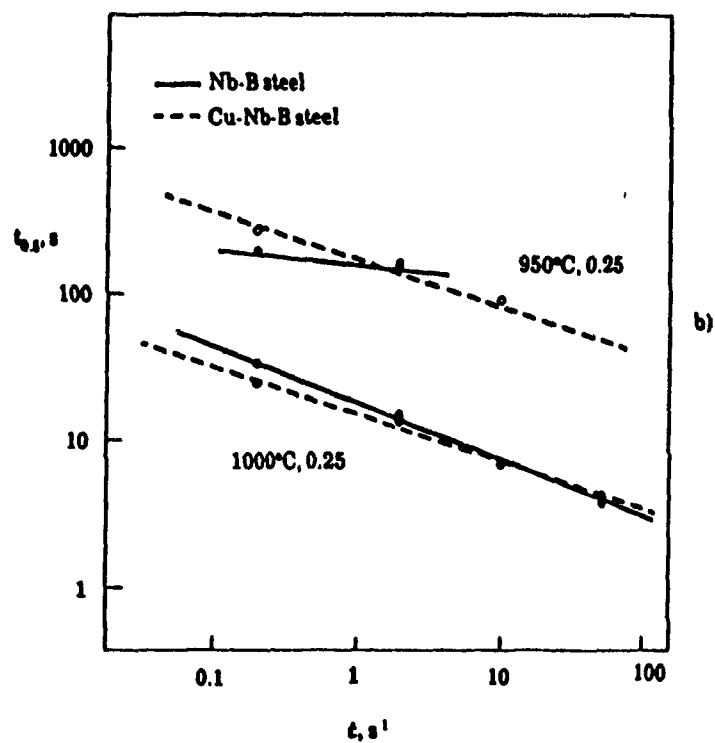
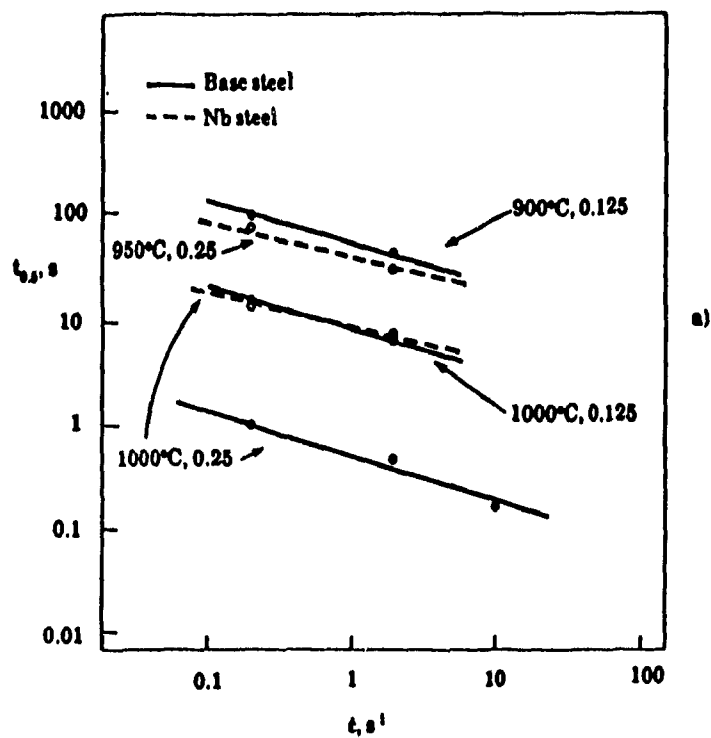


Figure 7.14 Dependence of the time for 50% softening on strain rate in the
 a) base and Nb steels
 b) Nb-B and Cu-Nb-B steels.

describing the recrystallization kinetics are highly desirable in order to predict the rolling forces with accuracy.

The data analysis performed in the above sections, including the effects of strain, strain rate and temperature, can be summarized in a single equation for each steel, in order to estimate X_v in Eq. 7.6b. Since n_A is found to be constant (around 1), the accuracy of prediction of X_v depends on how precisely $t_{0.5}$ can be predicted for given conditions of strain, strain rate and temperature. Table 7.2 gives the final mathematical expression for $t_{0.5}$ for each steel.

Table 7.2 Summary of the strain, strain rate and temperature dependencies of the time for 50% recrystallization for the four steels investigated.

Steel	Equation
Base	$t_{0.5} = 1.14 \cdot 10^{-13} \varepsilon^{-3.80} \dot{\varepsilon}^{-0.41} \exp(252\,000/RT)$ (7.11a)
Nb	$t_{0.5} = 1.27 \cdot 10^{-18} \varepsilon^{-3.81} \dot{\varepsilon}^{-0.36} \exp(404\,000/RT)$ (7.11b)
Nb-B	$t_{0.5} = 2.86 \cdot 10^{-19} \varepsilon^{-3.80} \dot{\varepsilon}^{-0.42} \exp(436\,000/RT)$ (7.11c)
Cu-Nb-B	$t_{0.5} = 1.06 \cdot 10^{-24} \varepsilon^{-3.55} \dot{\varepsilon}^{-0.33} \exp(559\,000/RT)$ (7.11d)

To test the accuracy of prediction of $t_{0.5}$ over the range of experimental conditions studied, plots of $t_{0.5}$ versus $[\varepsilon^{-m_A} \dot{\varepsilon}^{-p} \exp(Q_r/RT)]$ were prepared for each steel. Figs. 7.15a to d illustrate the extent to which the times for 50% softening can be predicted by the respective equations in Table 7.2. This accuracy is at a maximum when the deformation conditions are such that all the niobium is in solution (high temperatures or short holding times). When strain-induced precipitation occurs, the predicted $t_{0.5}$'s are underestimated (see

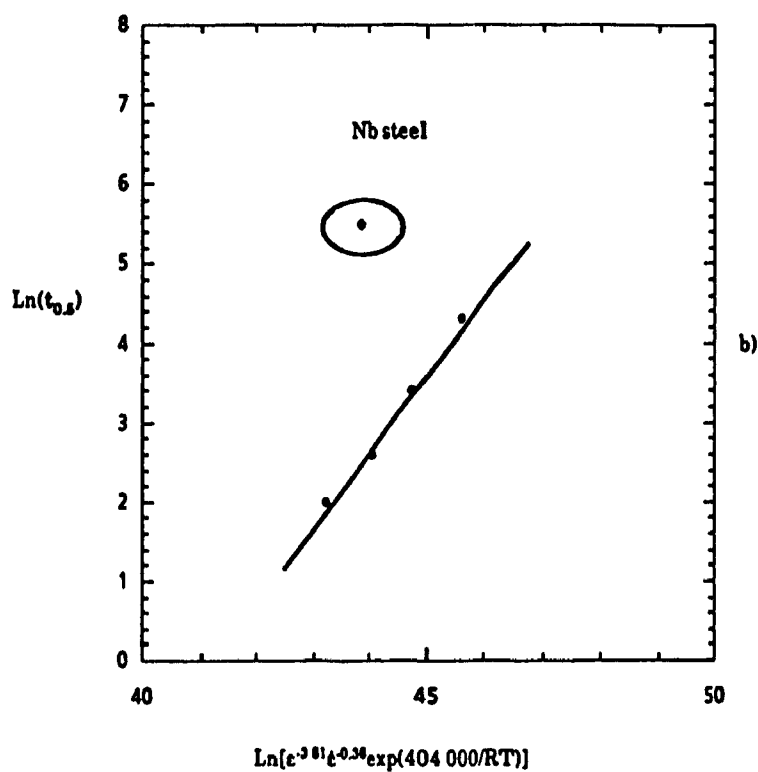
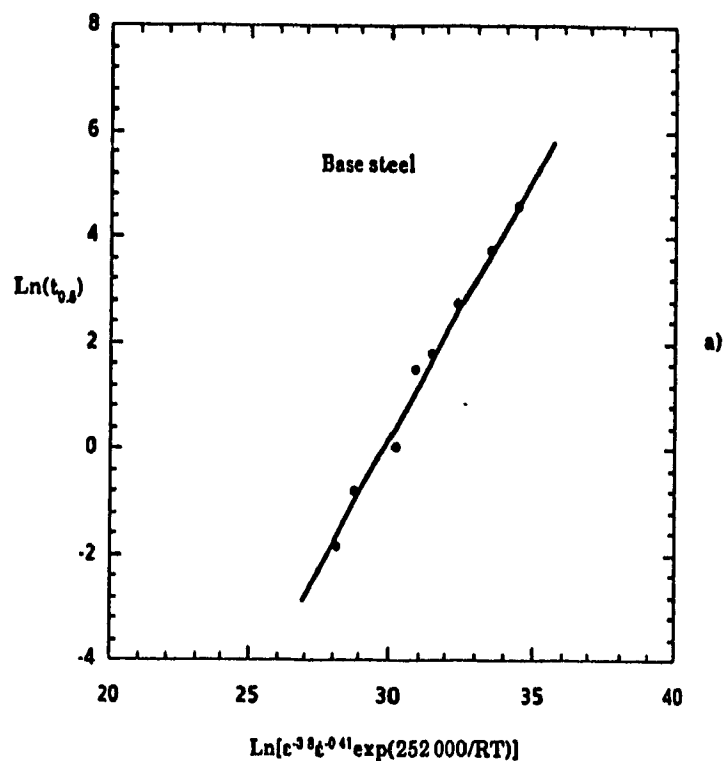


Figure 7.15 a) Comparison of the time for 50% softening and the deformation variables in the base steel.

b) Comparison of the time for 50% softening and the deformation variables in the Nb steel. The single point which is encircled is representative of strain-induced precipitation (contd.).

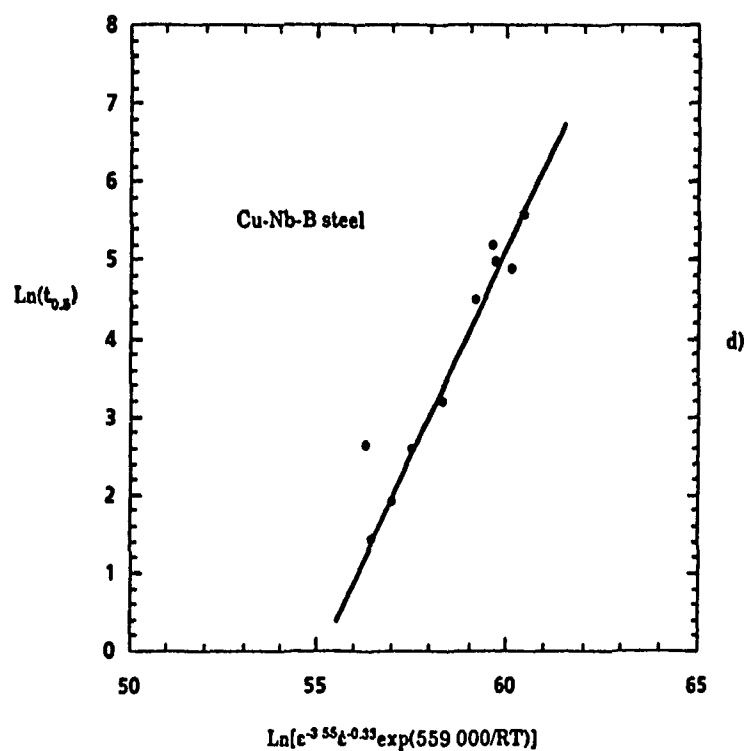
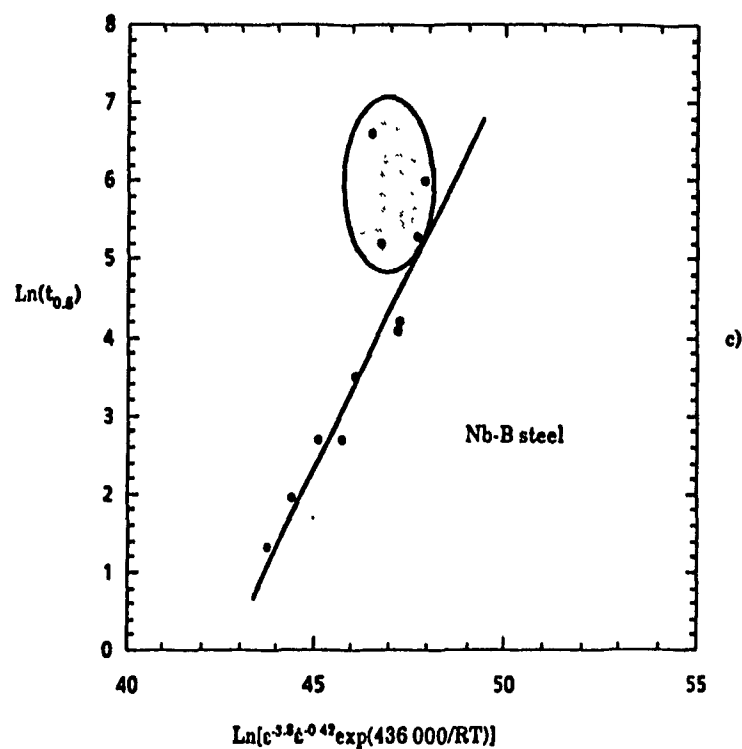


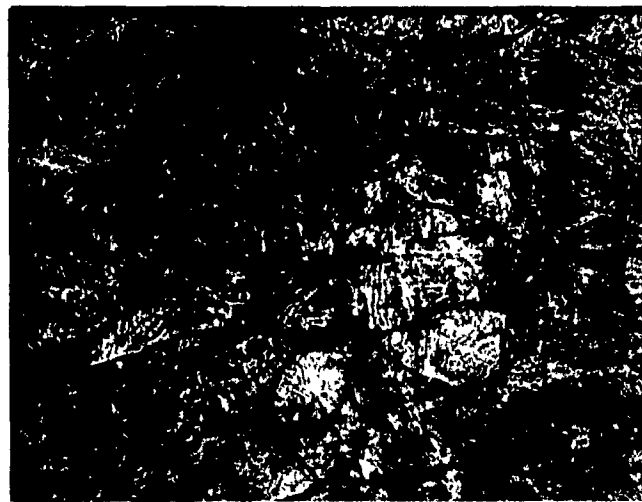
Figure 7.15 c) Comparison of the time for 50% softening and the deformation variables in the Nb-B steel. The encircled points correspond to conditions of strain-induced precipitation. d) Comparison of the time for 50% softening and the deformation variables in the Cu-Nb-B steel.

Figs. 7.15b and c). Thus, a second set of equations is required for the deformation conditions under which precipitation is favored. This necessitates more experimental data at temperatures lower than those employed in the present work. In plate rolling, the interpass time is about 10 seconds. This is similar to the incubation time for strain-induced precipitation, which takes place at the end of finishing, where the temperatures are low and the recrystallization kinetics are slow [161]. Thus the new equations would be useful for the control of plate mills. By contrast, in strip rolling, the interpass times are too short for this type of precipitation to occur. Thus, the present equations are valid, except when dynamic recrystallization is initiated. From the above, it is evident that, during the rolling of niobium steels, it is important to know when strain-induced precipitation begins and to include this information in the computer programs that deal with rolling schedule design and optimization. This would be very useful for the prediction of unusually high rolling loads.

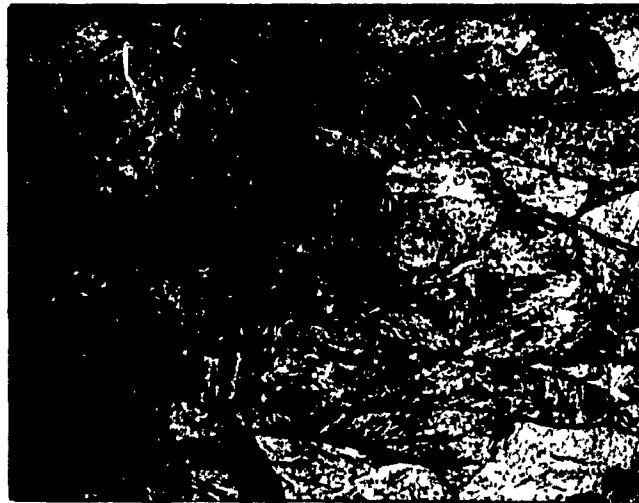
7.4. INFLUENCE OF DEFORMATION CONDITIONS ON AUSTENITE GRAIN SIZE

During the cam plastometer testing, the samples were quenched in water immediately after deformation. In all cases, the quenching time was less than one second. The prior austenite microstructures of Nb-B steel samples deformed to a strain of 0.4 at 800, 900 and 1100°C and quenched are presented in Fig. 7.16. The micrographs corresponding to the two lower temperatures show no signs of recrystallization; by contrast, the 1100°C sample is equiaxed and the deformed structure is no longer present. This is consistent with the complete recrystallization cycle predicted with the aid of Eqs. 7.11c and 7.6b after 0.5 seconds (\sim quenching time).

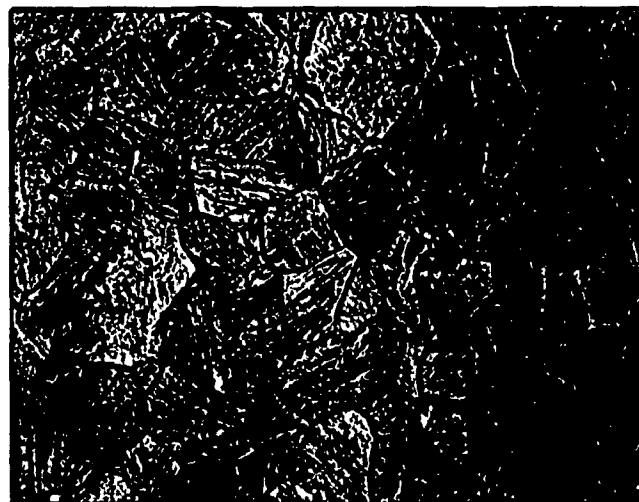
For the samples quenched after two hits, the mean austenite grain size was measured corresponding to different values of the fraction recrystallized (i.e., of fractional softening X_θ). This plot is displayed in Fig. 7.17 for X_θ between 0.25 and 0.99. An important feature of this figure is that, above 0.25, the average grain size \bar{d}_γ depends only weakly on the value of X_θ . This is true even though the grain size distribution is different at different stages of recrystallization (Figs. 7.18a and b). Similar results were reported recently by



DT = 800°C



DT = 900°C



DT = 1100°C

Figure 7.16 Optical microstructures of the Nb-B samples showing the prior austenite grains after a deformation of 0.4 at 10s^{-1} . The grains are deformed at the two lower temperatures and equiaxed at 1100°C .

Magnification 400X.

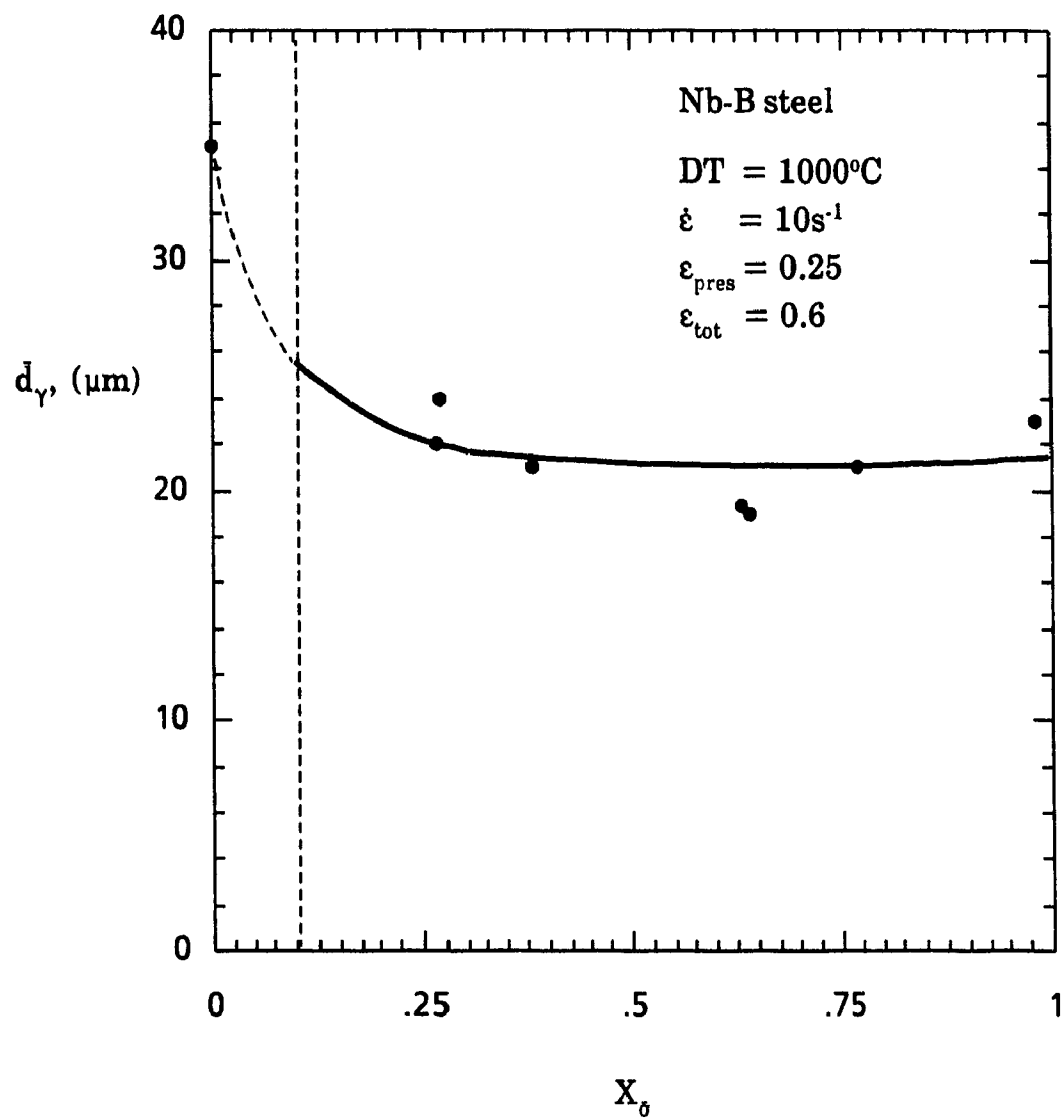


Figure 7.17 Evolution of the mean austenite grain size \bar{d}_γ of the partially recrystallized structure with the softening rate X_0 .

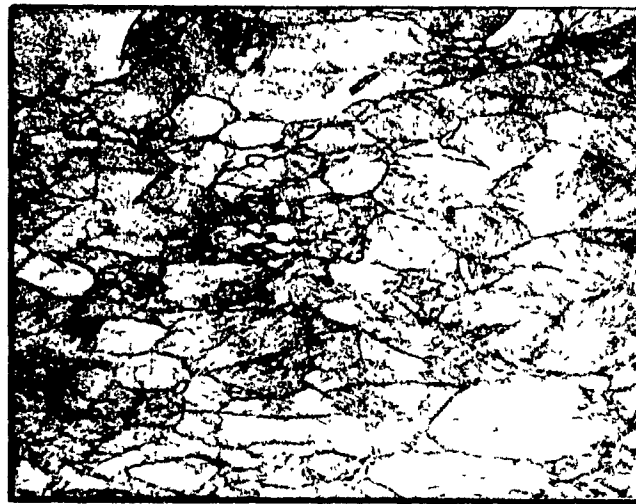
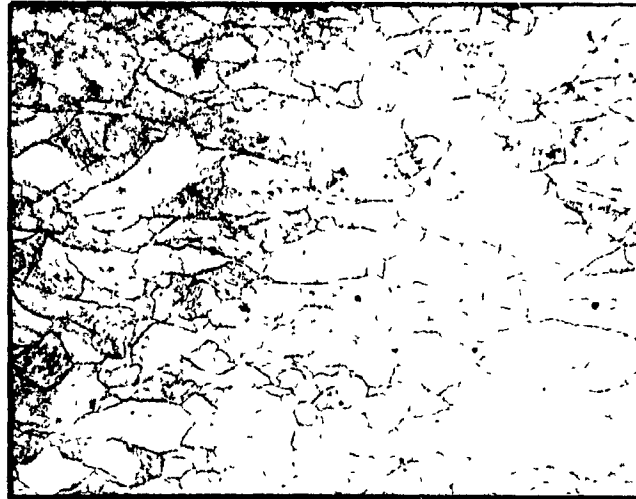
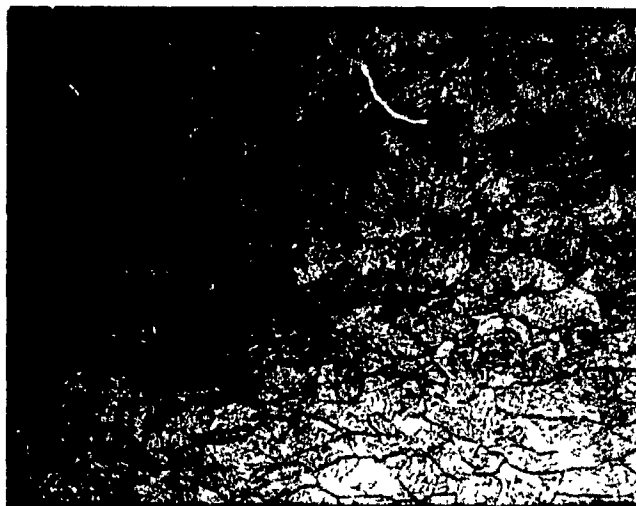
 $X_0 = 0.27$  $X_0 = 0.64$  $X_0 = 0.98$

Figure 7.18a Optical microstructures of the Nb-B steel showing the prior austenite grain structure after a double compression with a total deformation of 0.6 at 10s^{-1} . Magnification 250X.

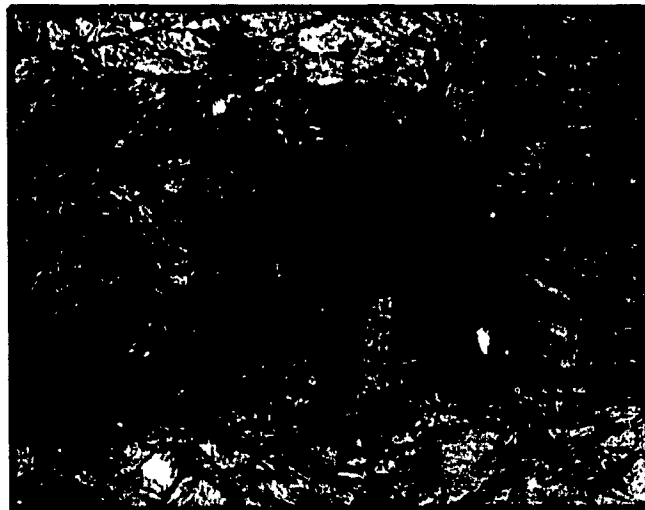
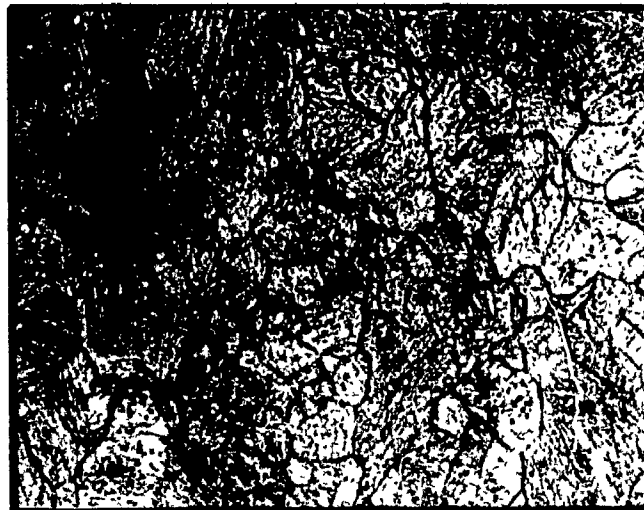
 $X_\delta = 0.27$  $X_\delta = 0.64$  $X_\delta = 0.98$

Figure 7.18b Optical microstructures of the Nb-B steel showing the prior austenite grain structure and grain size distribution after a double compression with a total deformation of 0.6 at 10s^{-1} . Magnification 400X.

Perdrix [161] at IRSID using torsion testing. He showed that the mean grain size of the partially recrystallized structure after two consecutive deformations is independent of the fractional softening when the latter is between 0.2 and 1.

The important consequence of the above observation is that separate populations of recrystallized and unrecrystallized grains need no longer to be followed during multipass deformation, as was done in the past by Sellars [17, 198], Roberts [167] and Sandberg and Sandström [180, 181]. Instead, the behavior of the partially recrystallized structure can be described by considering it *fictitiously* as fully recrystallized, with a uniform grain size d_γ but containing a residual strain $\Delta\epsilon$. This phenomenological description (which has no physical basis) is simpler and requires less calculation when the microstructural evolution of austenite is to be modelled. According to Sellars [179], the recrystallization kinetics of deformed partially recrystallized γ -structures only extend over narrow intervals of time. This makes it possible to use the above phenomenology which employs a single overall grain size for both the recrystallized and unrecrystallized structures. He added that such rapid, synchronized recrystallization takes place in steel but not in other metals such as aluminum, where the recrystallization kinetics of the two components of partially recrystallized deformed structures can differ by orders of magnitude.

By combining the measured average grain sizes of partially recrystallized structures with the recrystallization kinetics of annealed structures, Perdrix [161] was able to derive a relation between the residual strain $\Delta\epsilon$ and the recrystallized fraction as follows:

$$\lambda = \frac{\Delta\epsilon}{\epsilon_1} = D(1 - X_v) \quad (7.12)$$

Here X_v is the fraction recrystallized and D is a constant which takes the value 1 when X_v is below 0.1 and 0.5 when X_v is between 0.1 and 1 (see Fig. 7.19). Since X_v can be taken as X_θ , it can readily be verified from Eq. 7.12 that the unrecovered strain fraction $1 - \lambda$ leads to higher values than X_θ , a result presented above in Fig. 7.1b. The residual strain $\Delta\epsilon$ calculated in this way can be added to the pass strain giving an effective strain ϵ_{eff} which can be used in

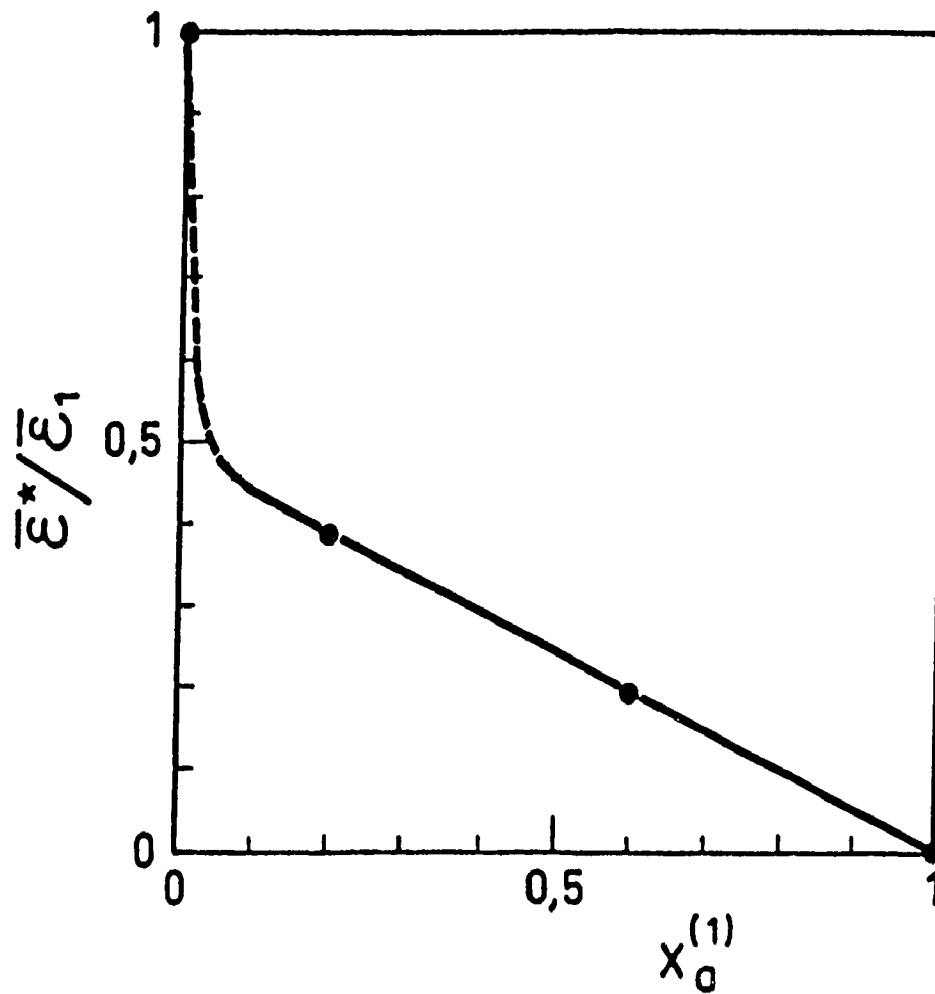


Figure 7.19 Influence of fractional softening on the residual strain ^[161].
 (ϵ^* is the residual strain, ϵ_1 the strain in the first pass and $X_a^{(1)}$ is the
 fractional softening between the first and second pass.)

empirical equations to predict the mean austenite grain size of partially recrystallized structures. Such equations have been derived by several authors for the prediction of recrystallized austenite grain size; these are shown in Table 7.3. The empirical nature of these equations requires systematic validation using measurements of the grain size in multipass deformation experiments.

Table 7.3 Empirical equations for the prediction of recrystallized austenite grain size.

Equation	Conditions	Reference
$d_{\text{rex}} = 0.9d_o^{0.67}\epsilon^{-0.67}$	Nb, $\epsilon < \epsilon_p$, $T > 950^\circ\text{C}$	[17]
$d_{\text{rex}} = 0.5d_o^{0.67}\epsilon^{-0.67}$	C-Mn, $\epsilon < \epsilon_p$	[17]
$d_{\text{rex}} = 4.3 + 195.7d_o^{0.15}\epsilon^{-0.57}[\exp(350\,000/RT)]^{-0.11}$	Ti-V, $17 \leq d_o \leq 40\mu\text{m}$	[182]
$d_{\text{rex}} = 600Z^{-0.16}d_o^{0.48}$	Low alloy steels	[172]
$d_{\text{rex}} = 75\epsilon^{-0.6}d_o^{0.39}\exp(-3189/T)$	C-Mn, Nb	[183]
$d_{\text{rex}} = 18.5\ln(T/973)d_o^{0.374}\epsilon^u\dot{\epsilon}^{-0.1}$ $u = -0.5d_o^{0.267}(973/T)^{3.93}$	C-Mn-Al	[161]
$d_{\text{rex}} = 472\exp(-11\,620/RT)\epsilon^{-0.7}d_o^{0.277}$	Nb	[161]

Z = Zener-Hollomon parameter

d_{rex} is in μm and T in K

7.5. EFFECT OF ALLOYING ELEMENTS ON RECRYSTALLIZATION KINETICS

The effect of alloying elements on the recrystallization kinetics is very important for both alloy design and the optimization of rolling schedules. In the past few years, notable advances have been made regarding the effect of these microalloying elements on different aspects of steel behavior. One

example is the effect of Nb on recrystallization kinetics which is presented in Figs. 7.20a and b for temperatures of 1000 and 900°C, respectively. It is clear that, for both conditions, the recrystallization kinetics are strongly retarded when niobium is added to the base steel. This behavior is in agreement with numerous observations in the literature; the retarding effect of niobium is due to solution effects at high temperatures (1000°C and above) and to precipitation at lower temperatures.

Figs. 7.20a and b also show the effect of boron in the presence of niobium on the recrystallization kinetics. It is apparent from these data that boron plays a significant role in delaying recrystallization. The increased retarding ability of boron when added to niobium was investigated recently [94, 185, 186] and shown to be due to the strain-induced segregation of boron. Furthermore, a synergism between B and Nb has frequently been reported, i.e., the simultaneous presence of Nb and B leads to the greater retardation of recrystallization than the simple sum of the retardations produced by each solute alone.

While the influence of many alloying elements has been investigated in the past decade, few data are available regarding the effect of copper on the high temperature flow behavior of steel. Copper is usually added to produce precipitation strengthening after aging or to enhance corrosion resistance. Its effect as a solute on austenite recrystallization was measured in this study. This is exemplified in Fig. 7.21, where the recrystallization kinetics of the Nb-B and Cu-Nb-B steels are compared at 950 and 1000°C. Because the initial grain sizes of the two steels were different after reheating, the dashed lines corresponding to the Cu-Nb-B steel have been corrected for grain size using a quadratic dependence of $t_{0.5}$ on d_{γ_0} . As is clear from the above figure, there is a measurable further retardation of recrystallization when Cu is added to a Nb steel. This expands further the no-recrystallization region during hot rolling, thereby conferring an additional benefit on the final mechanical properties of the hot rolled steel.

The only data existing in the literature concerning the effect of copper addition on recrystallization during hot working is in the paper recently published by Abe and coworkers in Japan [187]. Using several Fe-Cu alloys,

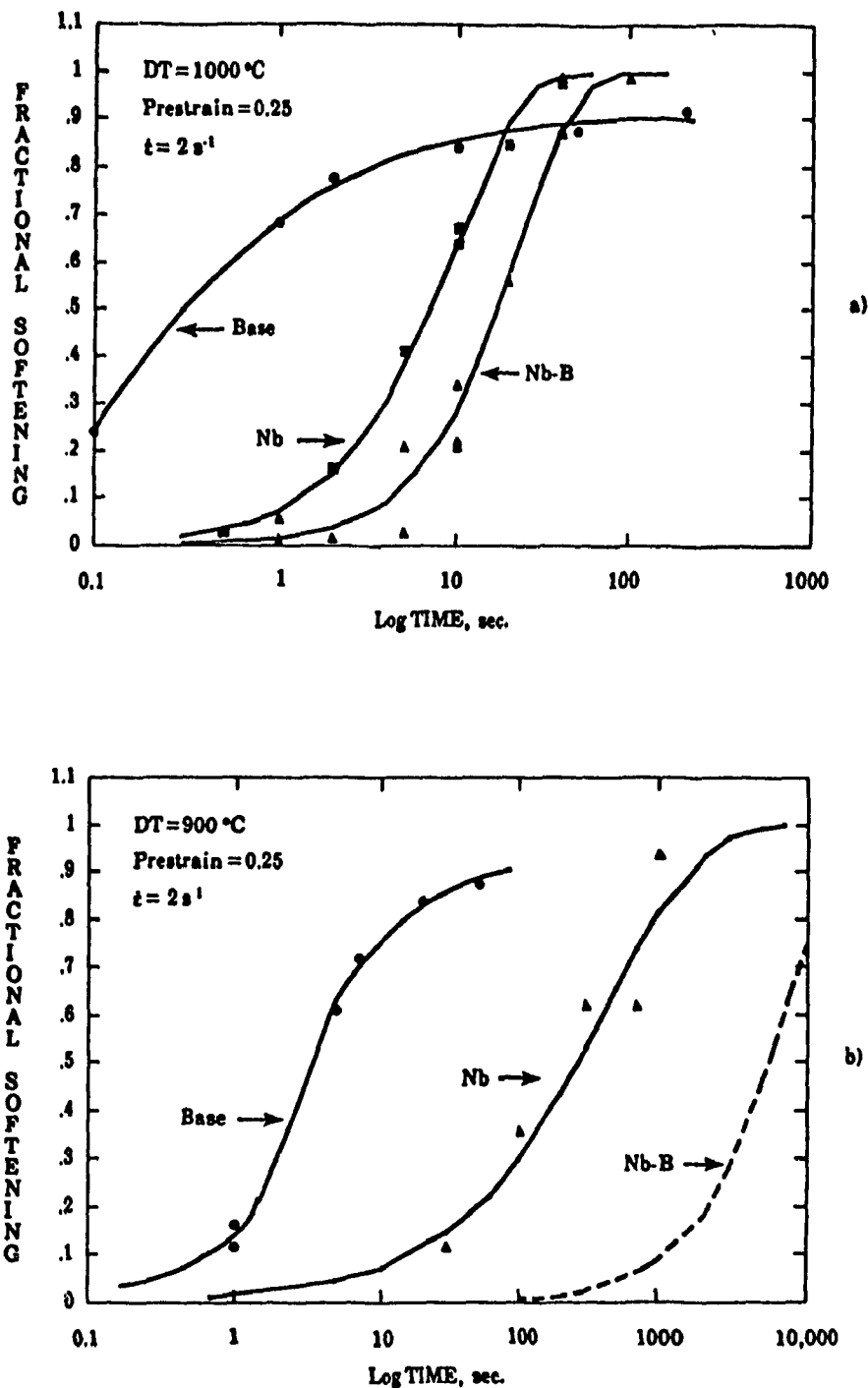


Figure 7.20 Effect of Nb and B addition on softening at
a) 1000°C
b) 900°C .

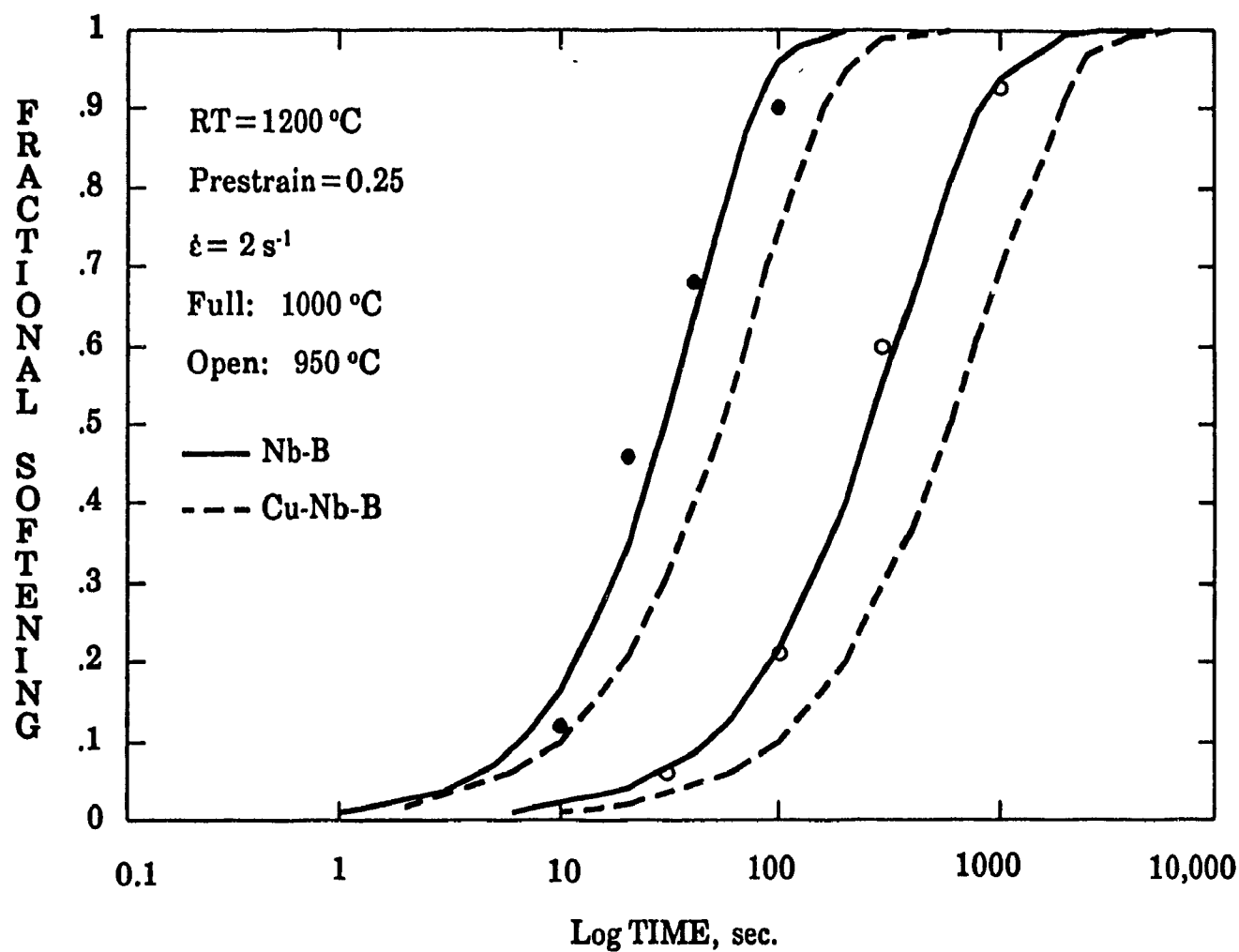


Figure 7.21 Effect of Cu addition on softening at 1000 and 900°C.

they found that an addition of 0.8% Cu led to a drastic reduction in the fractional softening, from 0.87 to 0.4, after a holding time of one second. They also showed that higher levels of copper addition are effective in delaying recrystallization to even longer holding times.

Several theories have been proposed regarding the retarding effect of alloying elements on static recrystallization after hot deformation [30, 81, 188, 189]. Mechanisms based on solute drag, electronic and modulus differences, and stacking fault energy effects have been considered. Regarding the delaying effect of copper on the recrystallization kinetics, Abe et al. [187] concluded that the solute drag effect was preponderant. As the size misfit of Cu in iron is less than that of Nb and Mo, they attributed the ability of Cu to retard recrystallization to the appreciable amount present. Their Cu addition of 1.2 wt% was greater than typical Mo additions of 0.2 wt% and Nb additions of 0.02 wt%. The slower kinetics of the Cu-Nb-B steel compared to the Nb-B steel observed in the present study (Fig. 7.21) can thus be explained in terms of the relatively large amount of copper (2 wt%) added, which is expected to expand still further the no-recrystallization region in austenite.

7.6. SUMMARY

The most important structural change that occurs during the interpass interval, i.e. static recrystallization, was described above. Appropriate relations were derived for the recrystallization kinetics and the mean austenite grain size was specified in terms of the thermomechanical conditions. Although most of the constitutive relations are empirical in nature, modelling of the microstructural evolution of steels after hot deformation would not be possible without a fundamental understanding of the physical metallurgy of such phenomena.

The constitutive equations between stress, strain, strain rate and temperature developed in Chapter 6 as well as the metallurgical aspects of the changes taking place after deformation described in the present chapter constitute the basic knowledge required for the construction of computer models of multipass hot rolling. Concrete applications of such concepts will be summarized in Chapter 8.

Chapter EIGHT

FOCUS OF THE STUDY - INDUSTRIAL APPLICATIONS

8.1. INTRODUCTION

The computer modelling of deformation processing has become an attractive subject for the research scientist and an efficient tool for manufacturing industry. For the former, it provides insights into the physical behavior of materials, and for the latter, it leads to the development and optimization of new schedules and thermomechanical processes. It also permits the scaling-up of laboratory results to industrial processes and makes possible the on-line control of hot forming operations.

With regard to the hot rolling of steels, such simulation is a synergistic product of the development of rolling theory, the accumulation of rolling experience, and progress in computer technology. The main objectives of computer modelling are not only to optimize the rolling process in terms of production rate, quality of the product and cost, but also to control the thermomechanical and microstructural evolution of the rolled material.

Several types of model have been developed recently in Europe, Japan and Australia [17, 74, 161, 167, 175, 190, 191]. These predict the roll force and power, the microstructural changes that take place during hot rolling, and the final mechanical properties. The predicted mechanical properties are a function of the microstructural evolution, which is in turn strongly dependent on the temperature changes (Fig. 8.1). The accurate calculation of temperature is therefore a critical matter since, in addition to the final

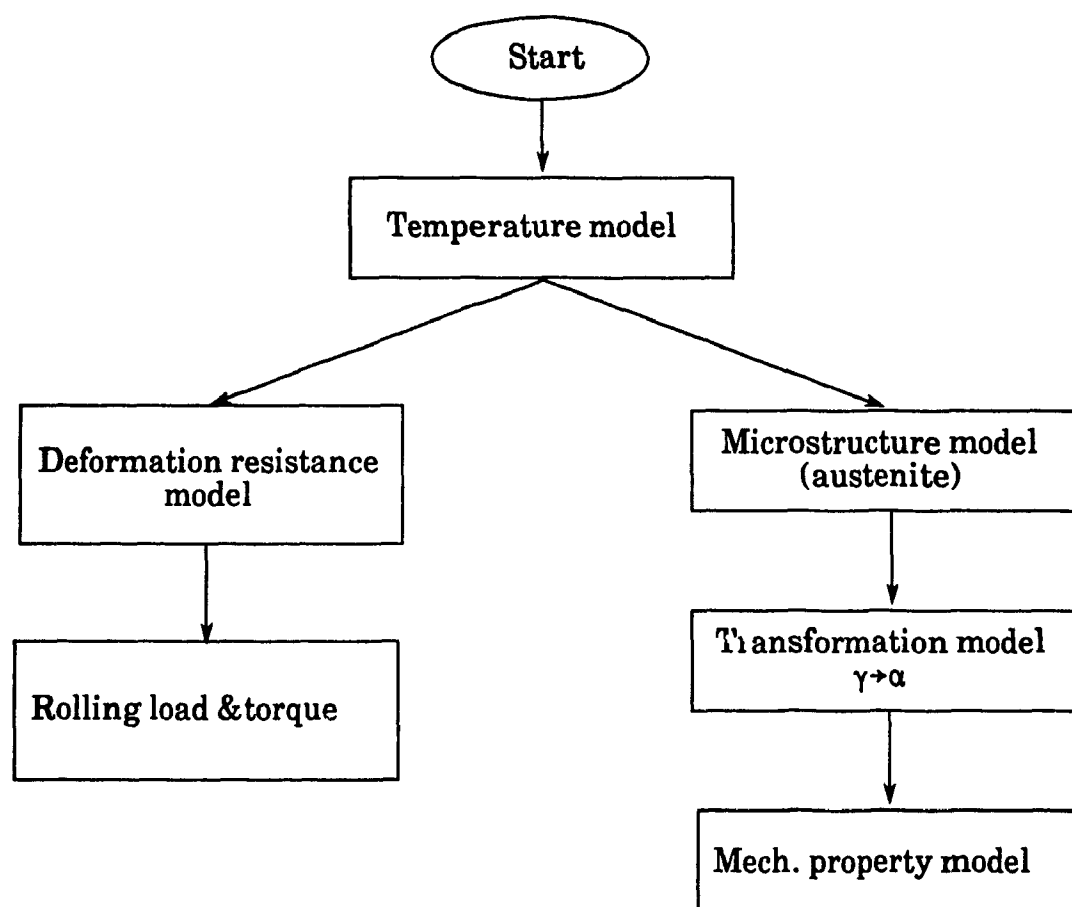


Figure 8.1 Schematic diagram illustrating the computer sub-models used in simulating hot rolling.

properties, the deformation resistance, which should not exceed a critical value corresponding to the limit of the mill, is also affected by this temperature.

The aim of this chapter is to use the mathematical and physical concepts outlined in the previous chapters to develop a computer model for the prediction of flow stress and microstructural evolution during hot rolling. The equations expressing the effect of softening between stands via static recrystallization proposed above are an important part of this model. Particular interest was paid to prediction of the temperature distribution through the thickness of the rolled plate or strip. The effects taken into account are radiation and convection from the surface when the material is between stands, and conduction to the rolls and the temperature increase due to mechanical work when the material is in the roll gap. As described in Chapter 5, an explicit finite difference method was used to calculate the temperature distribution through the thickness of the workpiece during processing. Some comparisons are made between the calculated and measured values of temperature and flow stress.

8.2. TEMPERATURE CHANGES DURING HOT ROLLING

8.2.1. Prediction of the Temperature Distribution

The hot strip mill at Stelco's Lake Erie works (LEW) is represented schematically in Fig. 8.2. The transfer bar leaving the reversing roughing mill enters the coilbox, a device which conserves energy and homogenizes the temperature by reducing the head-to-tail-end temperature difference. A crop shear is located downstream from the coilbox, followed by a descaler, which consists of four headers installed before the first stand of the mill. The bar is then reduced in thickness in five consecutive stands, crosses four banks of laminar sprays and finally arrives at the downcoiler. Details regarding this mill are provided in reference [61]. The time for each step in the process was calculated from the data supplied by Stelco regarding the dimensions of the mill and the rolling speeds.

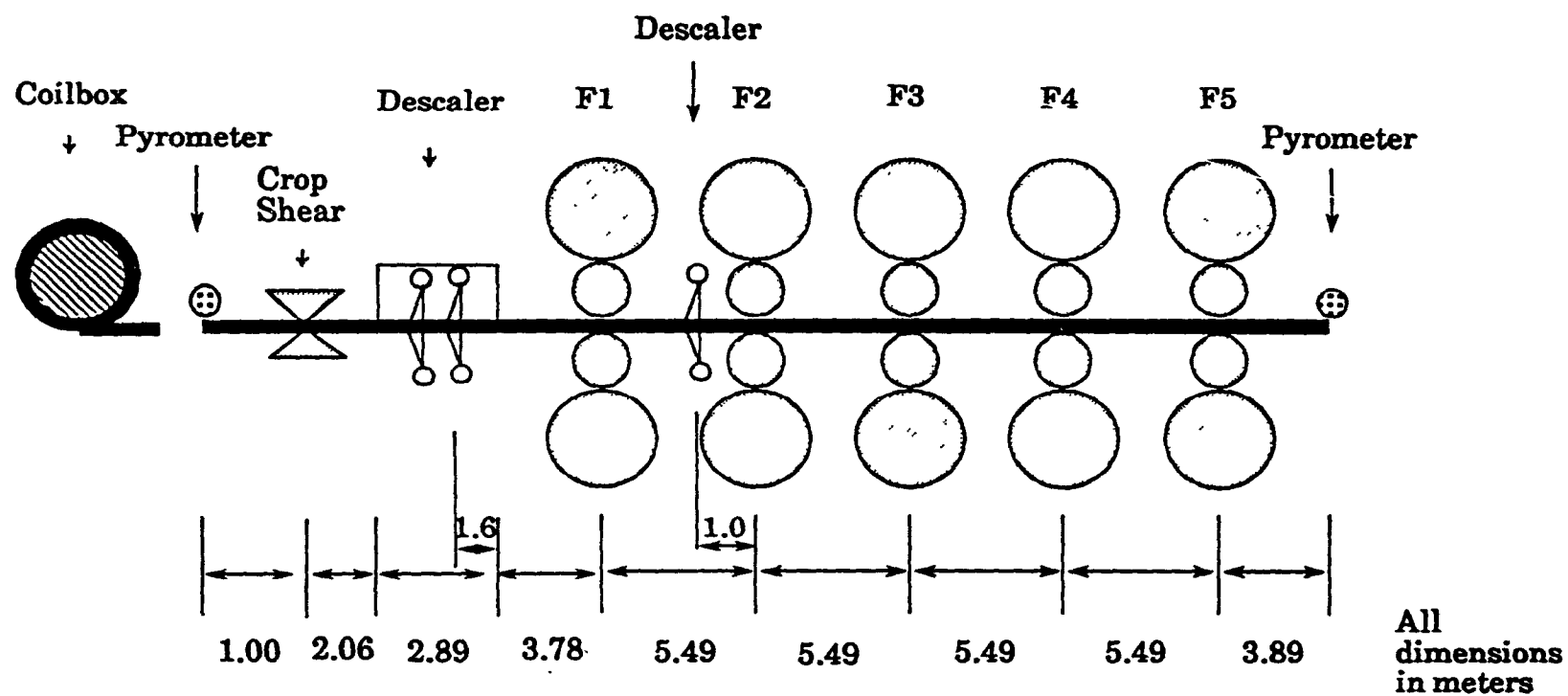


Figure 8.2 Schematic diagram of hot strip mill at Stelco, Lake Erie Works.

0 An example of the evolution of the through-thickness temperature distribution during processing, from the coilbox to the exit from the fifth stand, is given in Fig. 8.3. In this figure, the increase in center temperature due to plastic deformation is clearly evident, as is the chilling of the surface elements by contact with the rolls, as well as the reheating of the surface layers by conduction. It is of interest that for the specific schedule shown in Fig. 8.3, most of the heat loss between stands is due to radiation. The differences between the mean temperature values predicted by the present model and the ones calculated by the on-line process control model in use at Stelco LEW are due to several factors. The first involves the absence of information regarding the precise time taken for the transfer bar to pass through the descaler. The second is that the Stelco model uses several simplifications, particularly during deformation in the roll gap, where the contact is assumed to be perfect. Similar differences between the computed and measured surface temperatures were found recently by Devadas and Samarasekera [61] using a one-dimensional implicit finite difference method with 200 nodes through the half-thickness. A typical example of their computation for the Stelco hot strip mill is illustrated in Fig. 8.4, which is similar to Fig. 8.3 calculated by the present method.

An example of the evolution of the temperature distribution during plate rolling is illustrated in Fig. 8.5. The heat losses due to radiation are more important here because of the relatively low speed of the plate in comparison with that of the strip during hot rolling. The agreement between the predicted temperatures and those of the on-line process control model in use at Stelco LEW is again satisfactory.

For validation purposes, another comparison was made between the measured and computed center temperatures. This was performed by rolling the Cu-Nb-B steel in the CANMET pilot mill according to the nominal schedules shown in Table 4.3. Examples of the temperature predictions are shown in Figs. 8.6a, b and c for the three schedules. As can be noted from these figures, the temperature at the center is well simulated and the model is even sensitive to the difference in the rolling conditions during the last pass (compare Figs. 8.6a and b).

0

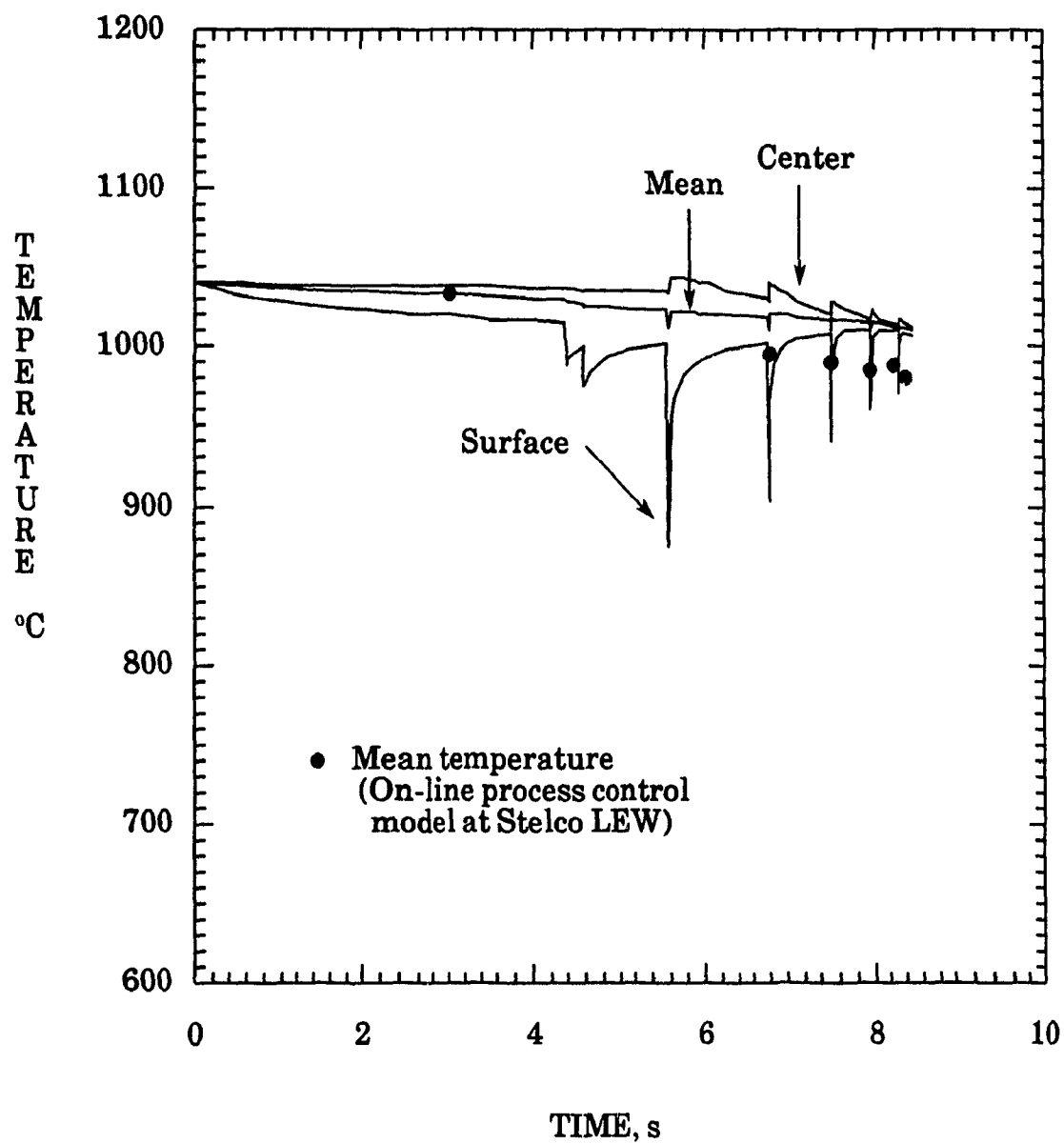


Figure 8.3 Evolution of temperature distribution during hot rolling of strip at Stelco.

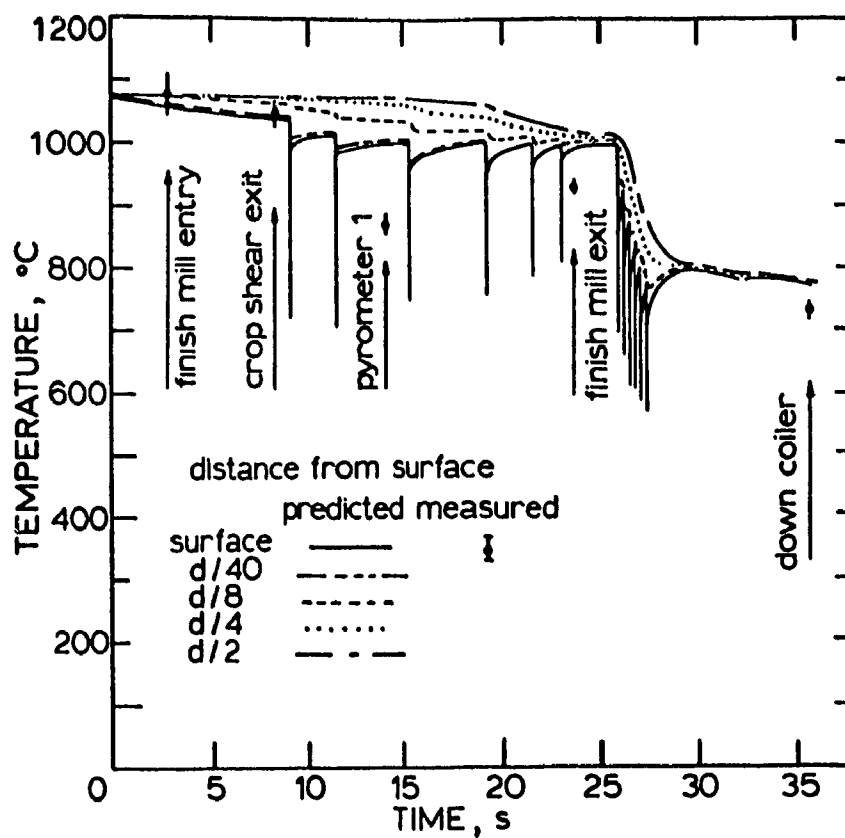


Figure 8.4 Comparison of measured and predicted surface temperatures for a strip ^[61].

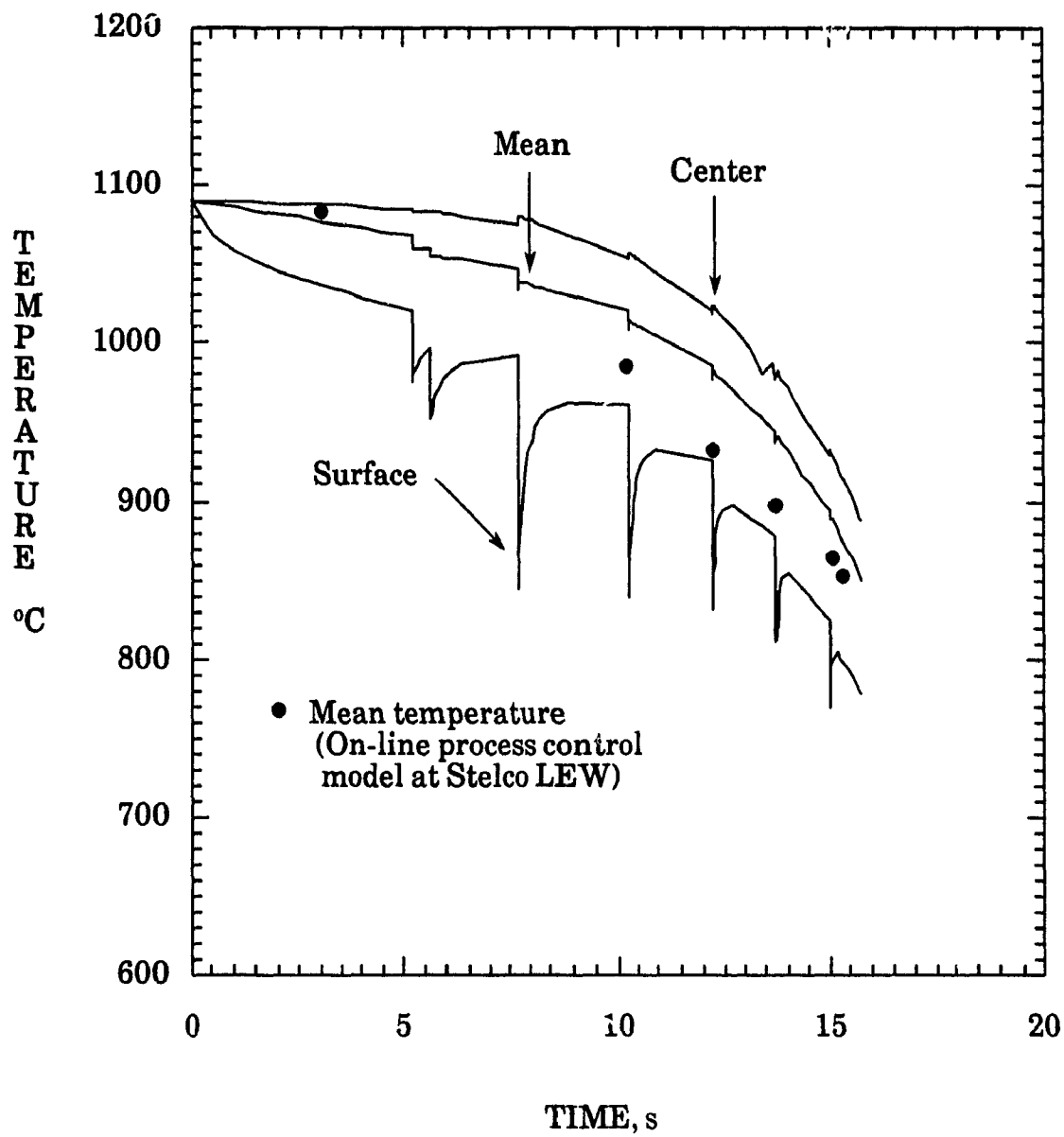


Figure 8.5 Evolution of temperature distribution during the hot rolling of thick strip.

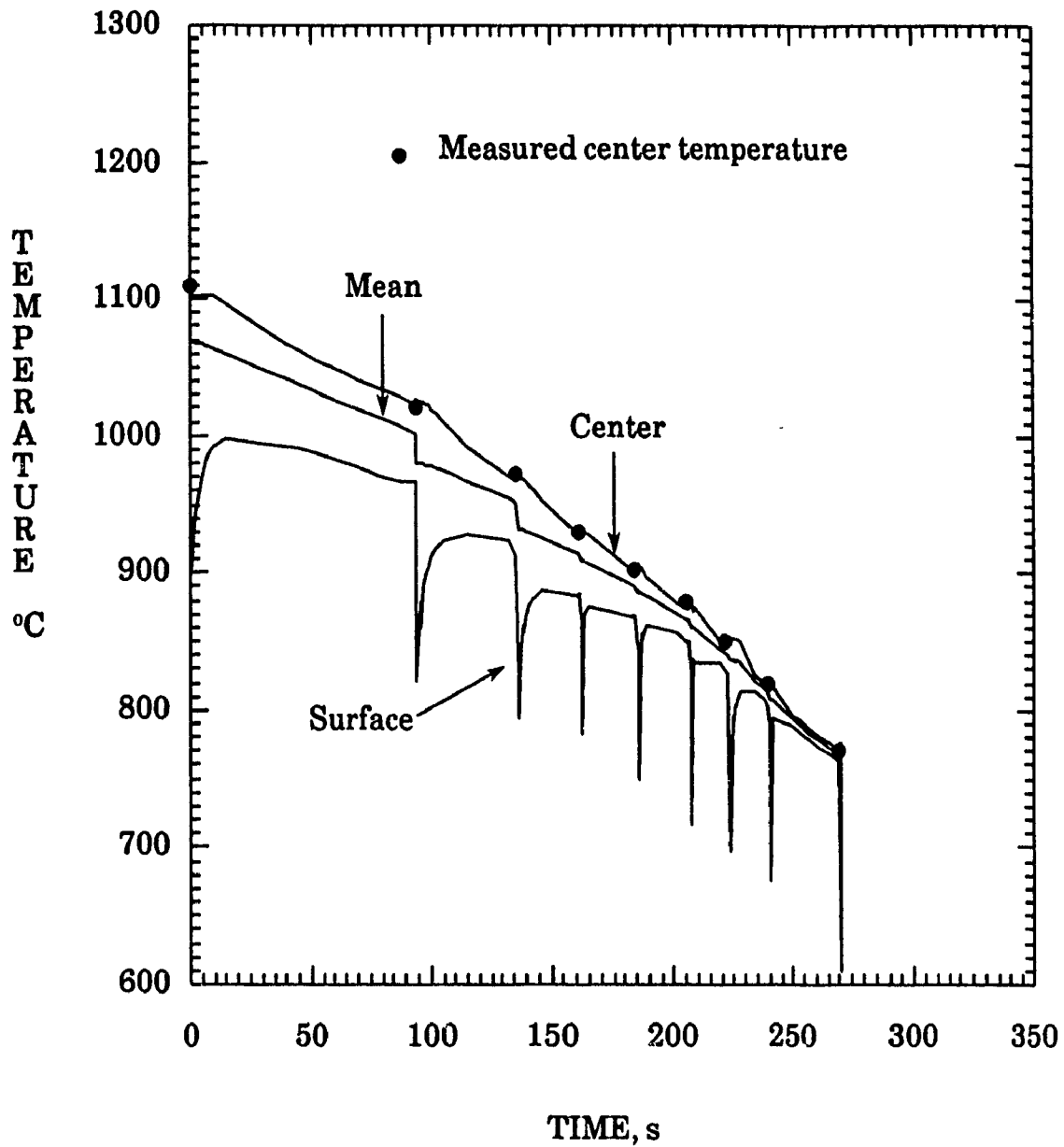


Figure 8.6a Evolution of temperature distribution during hot rolling of the experimental Cu-Nb-B steel on the pilot mill (Schedule D1).

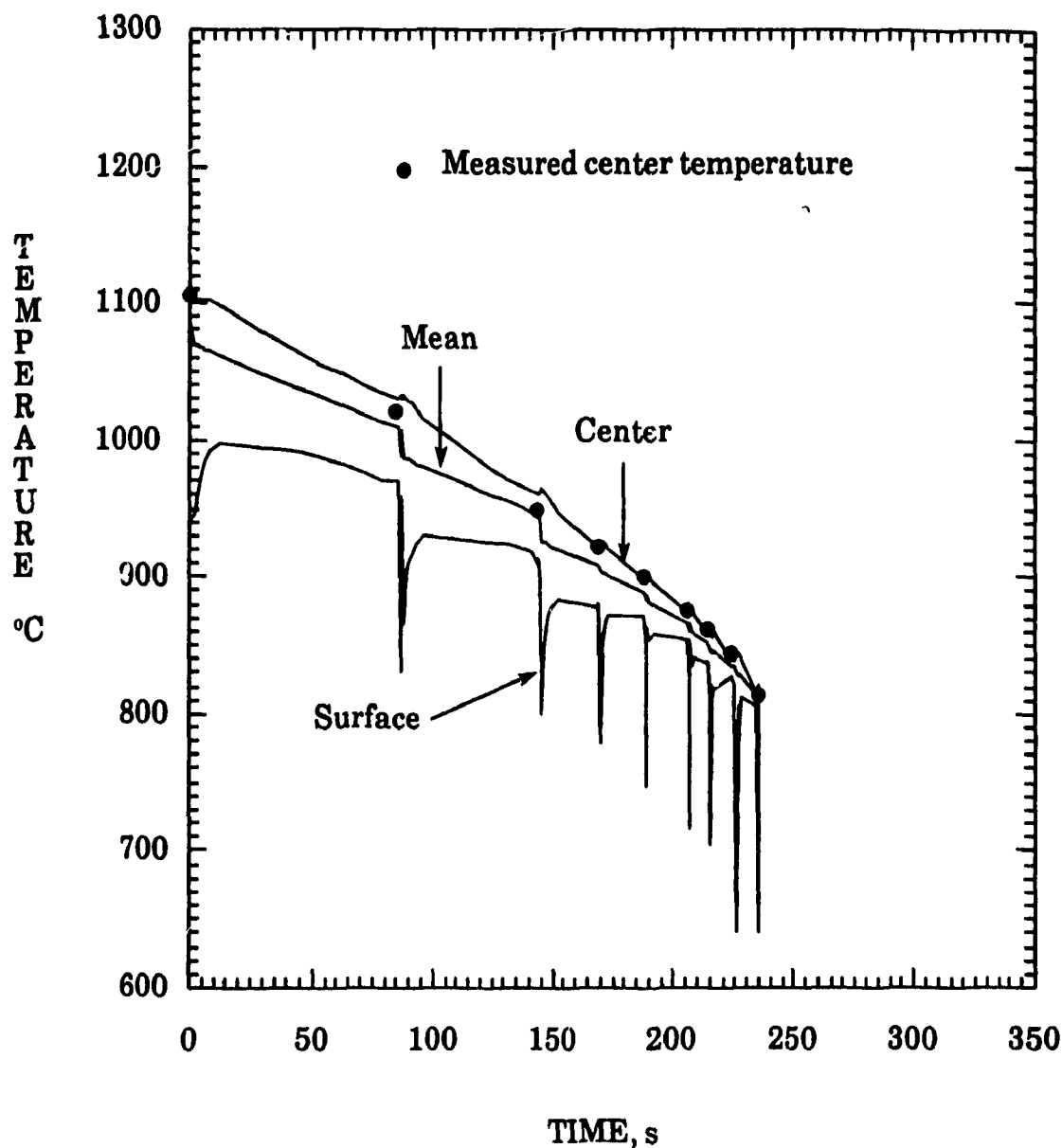


Figure 8.6b Evolution of temperature distribution during hot rolling of the experimental Cu-Nb-B steel on the pilot mill (Schedule D2).

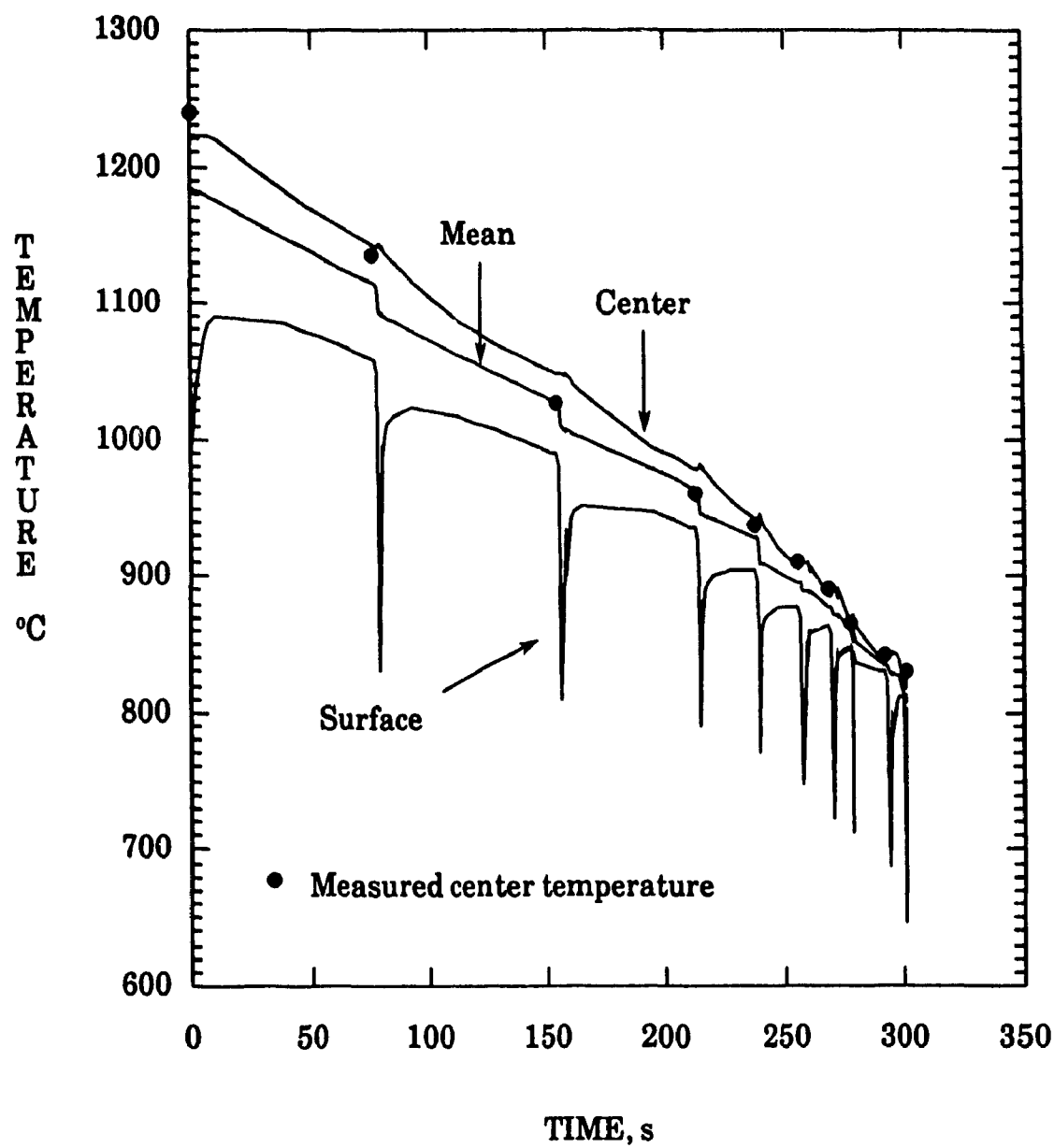


Figure 8.6c Evolution of temperature distribution during hot rolling of the experimental Cu-Nb-B steel on the pilot mill (Schedule C1).

While the temperatures are very well reproduced below 1000°C (corresponding to finishing), there is some disagreement at higher temperatures (roughing). The predicted values are higher than the measured ones. The reason for this is that, in the beginning of rolling, the width of the workpiece is as large as its thickness and the simplification concerning the neglect of heat conduction along the width is not justified in this case. A two-dimensional heat flow model would give better results for this stage of rolling. However, this matter is not critical because *i*) the disagreement at high temperatures is not of practical importance, and, *ii*) it can be compensated by modifying the heat transfer coefficient during contact of the bar with the rolls to keep the bulk temperature decreasing. This sort of calibration has no fundamental basis but provides a useful way in practice to replace a 2-D heat flow model by an equivalent but faster 1-D model suitable for the on-line prediction of temperature during roughing.

8.2.2. Heat Transfer Coefficients during Cooling Between the Stands

In the Stelco hot strip mill, the descale box consists of four headers installed before entry to the first stand of the finishing mill. Devadas and Samarasekera [61] measured the water flux and area of contact of the descale sprays to determine the heat transfer coefficient. Using an empirical relation for this coefficient, they determined it to be about $21 \text{ kWm}^{-2}\text{K}^{-1}$. This value corresponds to the peak of the curve in Fig. 3.1 given by Hollander and is used in this study.

For convection in air, a *static* value of $10 \text{ Wm}^{-2}\text{K}^{-1}$ was used. However, during strip rolling, the speeds are relatively high. Values of up to $105 \text{ W m}^{-2}\text{K}^{-1}$ were reported by Devadas [192]. In the present study, an attempt was made to calculate the *dynamic* heat transfer coefficient for convection to see the effect on the temperature distribution during air cooling, but insufficient data are available in the literature for comparison.

8.2.3. Temperature Drop during Contact with the Rolls

8.2.3.1. Heat Transfer Coefficient at the Interface

When the slab leaves the reheat furnace, a surface oxide layer is formed. The thickness of this layer depends on the stage of hot rolling and can vary from a few millimeters when the slab leaves the furnace, to a few microns during finishing [53]. Due to its low thermal conductivity, there is a large temperature gradient across the oxide layer and heat losses are considerably reduced when it is present. During deformation in the roll gap, heat transfer between the steel and roll is also affected by this layer. Assuming both the roll and the slab to be semi-infinite areas separated by a scale layer and having spatially uniform temperatures before contact, Pawelski [193] calculated the temperature gradient through the scale and derived the following expression for the heat transfer coefficient:

$$H_{CTC} = \frac{b_B \left[\frac{1}{z} e^{z^2} \operatorname{erf}(z) - \frac{1}{z} + \frac{2}{\pi} \right]}{2\sqrt{t_c}} \quad (8.1)$$

$$\text{where } z = \frac{2k_{scale}\sqrt{t_c}}{b_B s} \quad \text{and } b_B = \sqrt{k\rho C} \quad (8.2)$$

Here H_{CTC} is in $\text{Wm}^{-2}\text{K}^{-1}$, b_B is a parameter describing the heat penetration, z a dimensionless parameter, k_{scale} the thermal conductivity of the scale, and s the scale thickness.

Szalla et al. [194] also considered the thickness of the scale layer and used the following expression :

$$H_{CTC} = \frac{2k_{scale}}{\sqrt{\pi t_c}} \left[\frac{k\alpha^{-1/2} k_{Roll}\alpha_{Roll}^{-1/2}}{k\alpha^{-1/2} + k_{Roll}\alpha_{Roll}^{-1/2}} \right] \quad (8.3)$$

Using a layer thickness of 10 μm , which is typical of finish rolling [53, 56, 65], and $2.51 \text{ Wm}^{-2}\text{K}^{-1}$ for k_{scale} [53], some values of H_{CTC} were calculated as a function of contact time using the above equations. Table 8.1 compares these values with those reported by Murata et al. [65]. The values obtained from the two sets of equations vary by several orders of magnitude. This indicates that a general and valid expression for the heat transfer coefficient in the roll gap is difficult to derive. While Murata and coworkers give a value of $10.5 \text{ kWm}^{-2}\text{K}^{-1}$ for contact times from 1 to 3 seconds, Eq. 8.1 predicts zero thermal contact resistance. Furthermore, Eq. 8.3 gives values that decrease when the contact times increase and this seems to be unrealistic from a physical point of view, because the thermal resistance is expected to decrease as the rolling pressure is increased [195].

Harding [57] defined the rate of heat transfer per unit area between the transfer bar and the roll to be proportional to the difference in the respective surface temperatures. He found that a value of $1000 \text{ kWm}^{-2}\text{K}^{-1}$ for the constant of proportionality coincides closely with the assumption of zero contact resistance. In addition, the heat loss per unit area approached the theoretical dependence on the square root of the contact time when the constant of proportionality was increased to this level.

Table 8.1. Comparison of calculated values for H_{CTC} ($\text{kWm}^{-2}\text{K}^{-1}$).

Contact time, (s)	Eq. 8. 1	Eq. 8. 3	Murata et al. [65]
.0045	$2.49 \cdot 10^4$	279.5	-
.0060	$1.53 \cdot 10^5$	242.9	-
.0094	$1.36 \cdot 10^7$	193.4	-
.0145	$1.35 \cdot 10^{10}$	155.7	-
.0226	$9.78 \cdot 10^{14}$	124.7	-
1	∞	18.8	10.5
3	∞	10.8	10.5

8.2.3.2. Comparison of the Heat Balance Method with Hollander's Approach

During this study, the finite difference method was employed to predict the temperature distribution when the slab undergoes deformation in the roll gap. For this purpose, an appropriate value of the heat transfer coefficient must be used. As shown in the previous section, this is difficult to determine with accuracy. In addition to the difficulty of measuring the heat transfer coefficient in the roll gap, the values reported in the literature depend strongly on the conditions of measurement. For this reason, a second calculation was carried out using Hollander's approach, in which perfect contact between the workpiece and roll (Eq. 5.36) is assumed.

To estimate the sample thickness affected by contact with the roll (d_0 in Eq. 5.37), the finite difference calculation described above was repeated by refining the mesh. For this purpose, only the surface layer of thickness Δx , i.e. $1/6^{\text{th}}$ of the half thickness, was employed for the computation (Fig. 8.7). It was found that the thickness of the affected layer was reduced in half, regardless of the initial values of the temperatures. This is similar to the finding of Devadas and Samarasekera [61], who reported that only $1/10^{\text{th}}$ of the thickness of the rolled strip is significantly influenced by roll chilling. Also, the depth penetrated by the temperature gradient is independent of the initial surface temperature (Fig. 8.7).

Now that d_0 is known, Eq. 5.37 can be used to estimate the temperature drop at the surface during contact with the roll. To obtain correct values of ΔT , instead of using the value of the total heat loss given by Eq. 5.37, Hollander found that, after comparing his calculations and plant measurements, the actual value of Q was only 60% of the one calculated from Eq. 5.37. This means that, even though his approach was based on the assumption of perfect contact, he did not exclude the fact that a thermal resistance exists between the roll and workpiece.

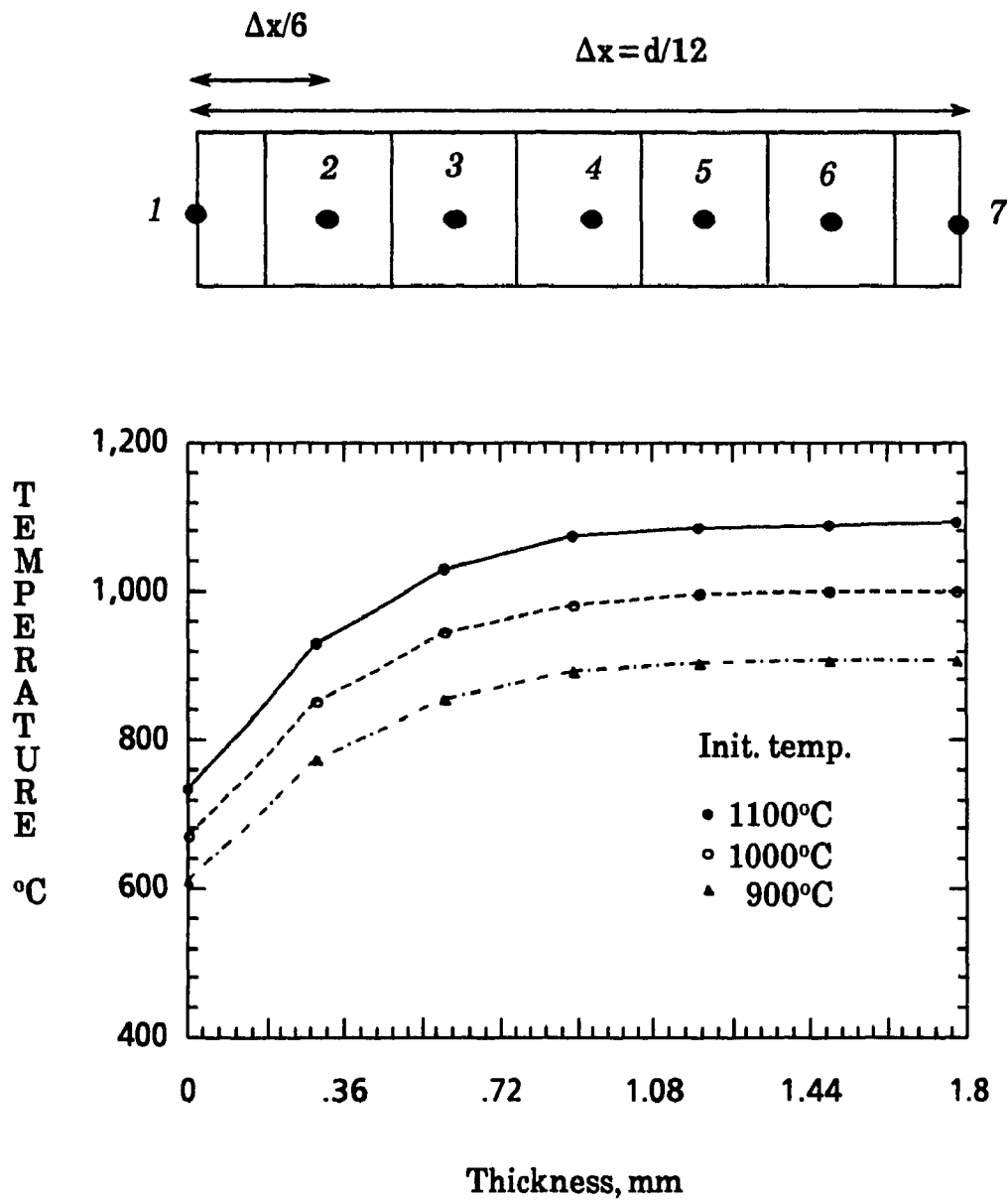


Figure 8.7 Temperature distribution in a surface element.

The surface temperatures of the rolled steel at the exit of each stand calculated by the two methods described above are compared in Table 8.2†. A value between 35 and 40 $\text{kWm}^{-2}\text{K}^{-1}$ for the heat transfer coefficient leads to temperature drops at the surface which compare very well with the ones determined from Eq. 5.37. However, some disagreement is observed when the contact times get very short. This is due to the fact that the perfect contact method includes the contact time in the calculation of the temperature drop at the surface, while the heat balance method uses a constant value of H_{CTC} . When the slight change in this coefficient from one stand to another (i.e. with contact time) is taken into account, better agreement is found. This finding is in agreement with that of Stevens et al. [64] as well as with the recent results of Devadas and Samarasekera [195] who have found that, during pilot mill rolling, the heat transfer coefficient varied with the contact time. The back calculated heat transfer coefficients from mill measurements by the latter authors are shown in Fig. 8.8 as a function of contact time and rerolling. On the figure, T-4, T-5 and T-11 represent trial numbers.

Table 8.2. Comparison of calculated surface temperatures.

Pass	Contact Time (s)	Temp.(°C) (H_{ctc} const.)	Temp.(°C) (H_{ctc} varying)	Temp.(°C) (Perf. contact)
1	0.023	959	959	961
2	0.015	923	920	922
3	0.009	875	869	872
4	0.006	821	811	815
5	0.005	769	698	703

† Because the time increment during the finite difference calculation varies from one stand (and interstand) to another, the surface temperatures at the exits shown in Table 8.2 are not taken after exactly the same times. However, after each stand, the time at which the surface temperature was taken was kept the same for both the heat balance and perfect contact methods.

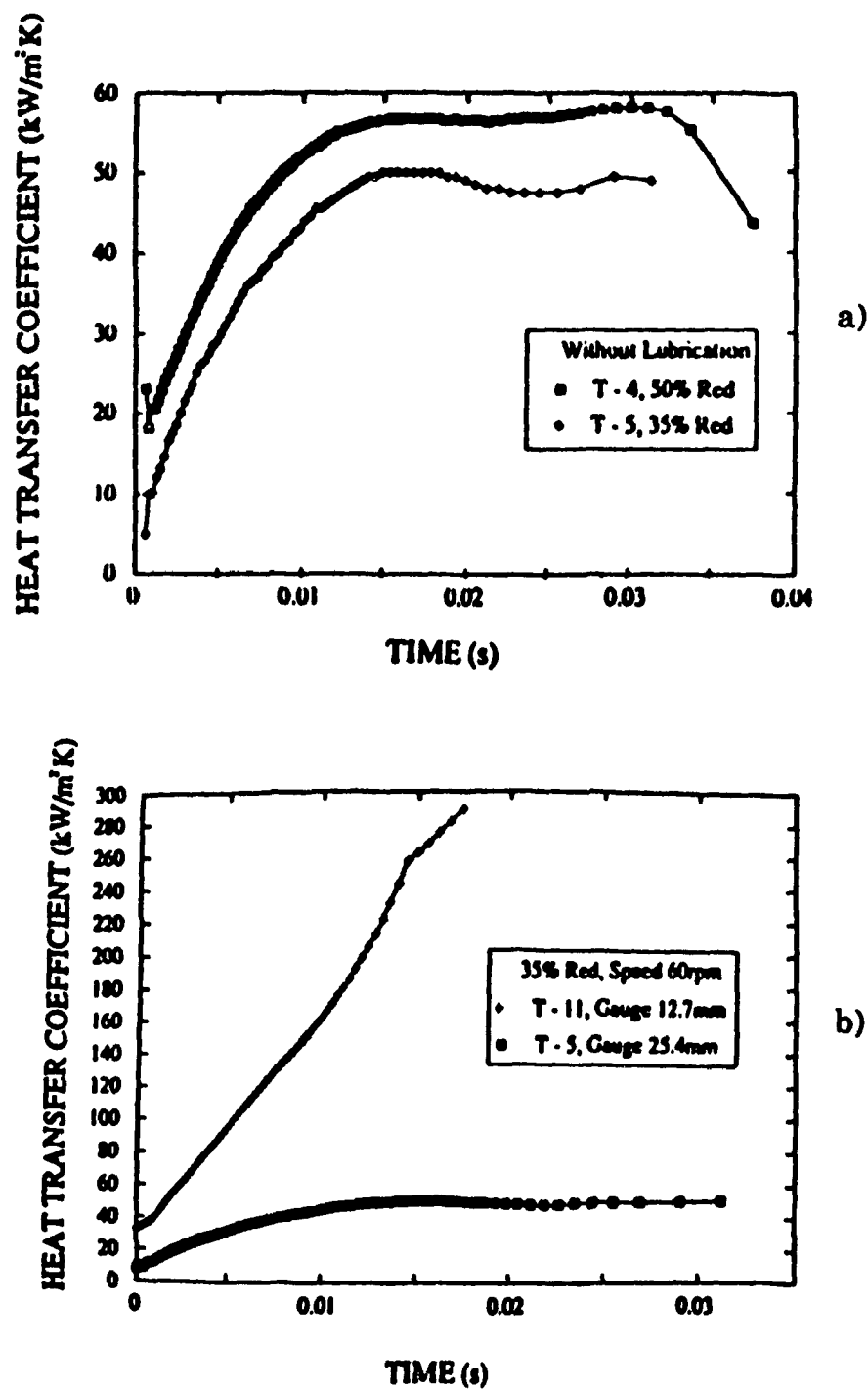


Figure 8.8 Effect of contact time on the roll gap heat transfer coefficient ^[195].

a) after 35 and 50% reductions

b) after rerolling.

8.2.4. Stability Validation

To check the validity of the present model in terms of accuracy and stability of the solution, a computer software package developed at McGill University and referred to as FASTP (Facility for the Analysis of Systems in Transport Phenomena) was used. This menu driven package is designed to analyze a variety of problems related to heat and mass transfer [196]. FASTP is based on an explicit finite difference algorithm and is able to generate results for one, two or three dimensions.

In order to use FASTP, the material properties must first be specified. For each stage of rolling, i.e. water cooling, cooling between the stands and contact of the slab with the rolls, the initial temperature distributions and the boundary conditions are given as inputs. Employing the time increments imposed by the stability criterion, the predictions of the present model turned out to be very close to those computed by FASTP, with differences of only about 0.5 °C in temperature.

8.3. FLOW STRESS AND MICROSTRUCTURAL EVOLUTION CALCULATIONS

8.3.1. Flow Chart

Fig. 8.9 shows an example of the application of the present constitutive equations for the flow stress and the recrystallization kinetics to the hot rolling of steel plate and strip. After prediction of the temperature distribution for each element of the thickness, the entire flow curve is calculated for the respective conditions of strain rate, mean temperature and initial structure, using the stress/strain relation described in Chapter 6. When softening is complete between stands, the mean flow stress is readily calculated by integration of the stress/strain curve. The recrystallized grain size under such conditions is determined from the pass strain. If the steel does not contain alloying elements that restrict grain growth after complete recrystallization, such as C-Mn steels, the grain size is calculated using grain growth kinetics [195]. When partial recrystallization occurs between stands, the problem becomes more complex. In such a case, the effective strain is employed

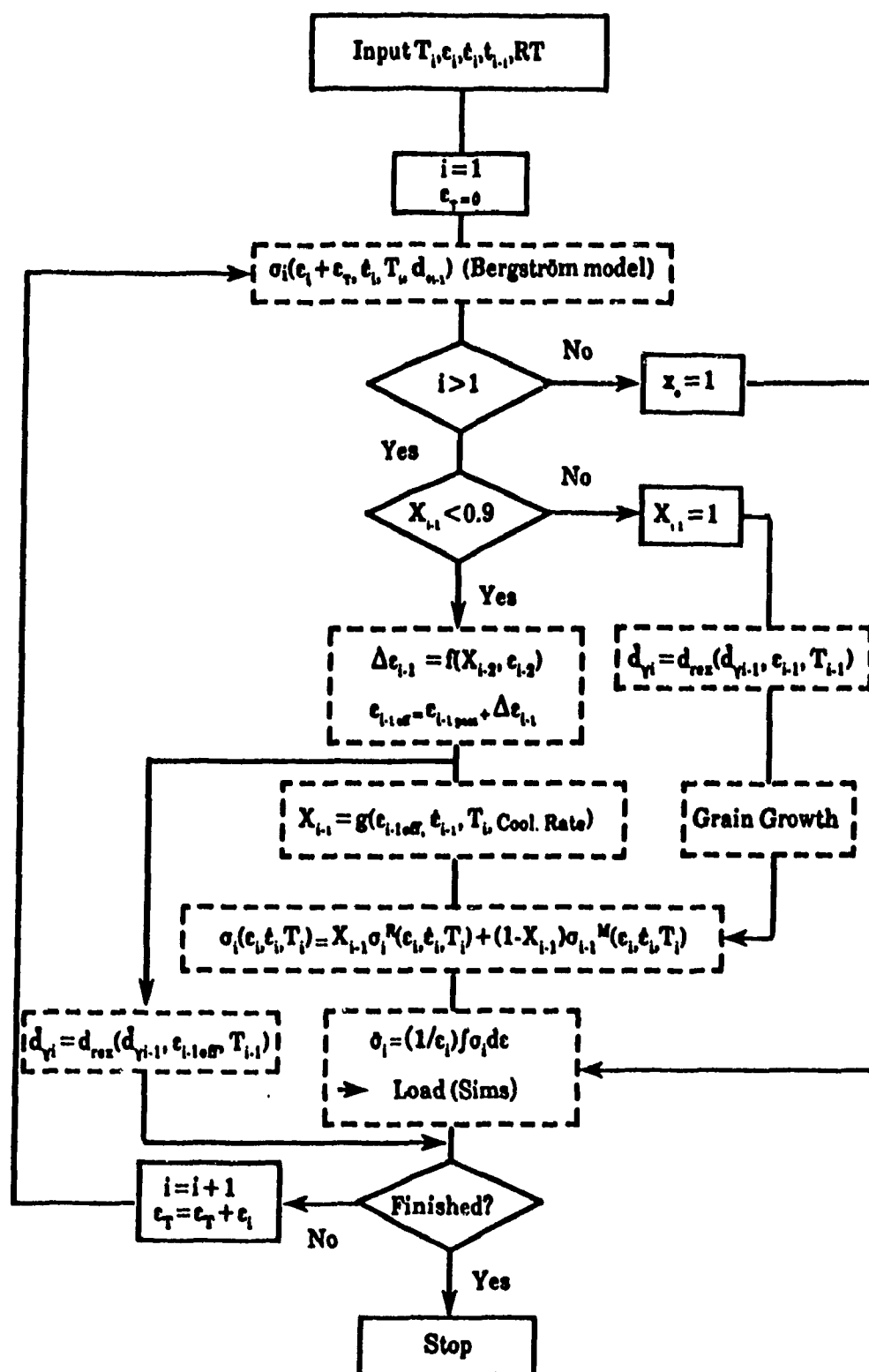


Figure 8.9 Simplified flow chart for rolling load and mean austenite grain size prediction during hot rolling.

instead of the pass strain by adding the latter to the residual strain, $\Delta\epsilon$, calculated by means of Eq. 7.12. The recrystallized fraction X under continuous cooling conditions is then determined using the following modified Avrami equation:

$$X = 1 - \exp \left[-0.693 \left(\frac{W}{W_{0.5}} \right)^{n_A} \right] \quad (8.4)$$

where W is the temperature compensated time corresponding to cooling during the time interval Δt_i :

$$W = \int_0^{\Delta t_i} \exp \left[\frac{-Q_r}{RT(t)} \right] dt \quad (8.5a)$$

and

$$W_{0.5} = t_{0.5} \exp \left[\frac{-Q_r}{RT(0)} \right] \quad (8.5b)$$

Here $t_{0.5}$ is the time for 50% recrystallization defined in section 7.3.4.1 and is evaluated using the effective strain ϵ_{eff}

During the hot rolling of steel, and in particular during the finishing of Nb steels, complete recrystallization is not possible between passes and the temperature decreases continuously while the strain rate increases rapidly. The flow stresses cannot instantaneously reach the stress levels given by the continuous curves (by the Bergström model, for instance) under the new conditions of temperature and strain rate. The short transient associated with such temperature and strain rate changes is due to the evolution of structure which tries but does not succeed to reach the state appropriate to the new conditions and is called "hysteresis" [161].

The change in temperature and strain rate from stand to stand is taken into account by correcting for the hysteresis using the simplest method via the following coefficient [132, 161]:

$$J = \frac{\sigma'(T', \dot{\epsilon}) - \sigma(T, \dot{\epsilon})}{\sigma'(T', \dot{\epsilon}) - \sigma_o(T, \dot{\epsilon})} \quad (8.6)$$

where $\sigma(T, \dot{\epsilon})$ is the flow stress at the old temperature T and strain rate $\dot{\epsilon}$ just before the change, and $\sigma(T', \dot{\epsilon})$ is the flow stress at the same strain as $\sigma(T, \dot{\epsilon})$ but evaluated at the new temperature T' and strain rate $\dot{\epsilon}'$. $\sigma_0(T', \dot{\epsilon})$ is the new flow stress at zero strain. The flow stress of the unrecrystallized material after the change in temperature and strain rate, $\sigma_i^M(\epsilon_i, \dot{\epsilon}_i, T_i)$, at pass i is evaluated as follows:

$$\sigma_i^M(\epsilon_i, \dot{\epsilon}_i, T_i) = J\sigma_i(\epsilon_i, \dot{\epsilon}_i, T_i) + (1 - J)\sigma_i(\epsilon_i + \epsilon_T, \dot{\epsilon}_i, T_i) \quad (8.7)$$

where ϵ_T is the total deformation prior to pass i . If partial recrystallization occurs, the mixture law is applied to the recrystallized and unrecrystallized materials and the stress/strain curve is reconstituted using the recrystallized fraction X_{i-1} :

$$\sigma_i(\epsilon_i, \dot{\epsilon}_i, T_i) = X_{i-1}\sigma_i^R(\epsilon_i, \dot{\epsilon}_i, T_i) + (1 - X_{i-1})\sigma_i^M(\epsilon_i, \dot{\epsilon}_i, T_i) \quad (8.8)$$

By integration of the stress/strain curve, the mean flow stress is calculated; this is finally coupled with the Sims [68] or other rolling theory to predict the rolling load.

For the specific case where incomplete cycles of recrystallization occur, the mean austenite grain size is calculated using the phenomenological approach discussed in section 7.4; i.e., the empirical equation for evaluating the *recrystallized* grain size is assumed to remain valid for the mixed structure provided the effective strain is employed instead of the pass strain.

Finally, for each pass and particularly during finishing, the peak strain for dynamic recrystallization is calculated and compared to the effective strain. If the latter is higher than ϵ_p , the effect of softening due to dynamic recrystallization on the flow stress is taken into account using the simple approach described in section 6.6.

8.3.2. Flow Stress Prediction during Hot Rolling

The procedure described above was used to predict the flow stresses during the experimental hot rolling of the Cu-Nb-B steel according to the nominal schedules given in Table 4.3. An example of the calculated stress/strain curves is displayed in Fig. 8.10. Because of the continuous decrease in temperature during rolling, it is difficult to determine from the above figure whether complete or only partial recrystallization occurs, particularly during roughing and the beginning of finishing. Details regarding the recrystallized fractions and residual strains are given in Table 8.3 for the three schedules. The residual strain $\Delta\epsilon$ is low at the beginning of rolling but increases with pass number to attain a value around 1 at the end of the schedule. Also, when the temperature is below 940°C, even though some partial recrystallization is predicted, the recrystallized fraction does not exceed 21%. While low recrystallized fractions are obtained after the third pass in the steels reheated to 1100°C (Tables 8.3a and b), partial recrystallization with X equal to 33% takes place after the third pass when the steel is reheated to 1250°C (Table 8.3c) because of the higher pass temperature. This leads to a more mixed structure, which may explain the lower impact properties obtained using this schedule (see section 8.5.3).

As was pointed out above, the residual strains are relatively high when little softening occurs between passes. Softening by dynamic recrystallization during deformation is unlikely to occur in the present Nb steels, even with cumulative strains above 1.0 ($\epsilon_i + \Delta\epsilon_i$ in Table 8.3), because the alloying elements delay dynamic recrystallization. However, in C-Mn steels, dynamic recrystallization is an alternative softening mechanism at low strip finishing temperatures. To ascertain whether such a softening mechanism may play a role during plate rolling, the schedule shown in Table 8.3b was applied to the base steel and the peak strain for dynamic recrystallization was calculated using Eq. 6.44 at each pass. Table 8.4 gives the effective (accumulated) strain ϵ_{eff} , the peak strain ϵ_p and the recrystallized fraction X for the temperatures, strain rates and interpass times used during the pilot mill rolling. Also included in this table are ϵ_{eff} , ϵ_p and X using a strain rate of 50s⁻¹ and average interpass times of 15 s between passes to simulate industrial conditions. It is apparent from this table that for both conditions of strain rate, the retained

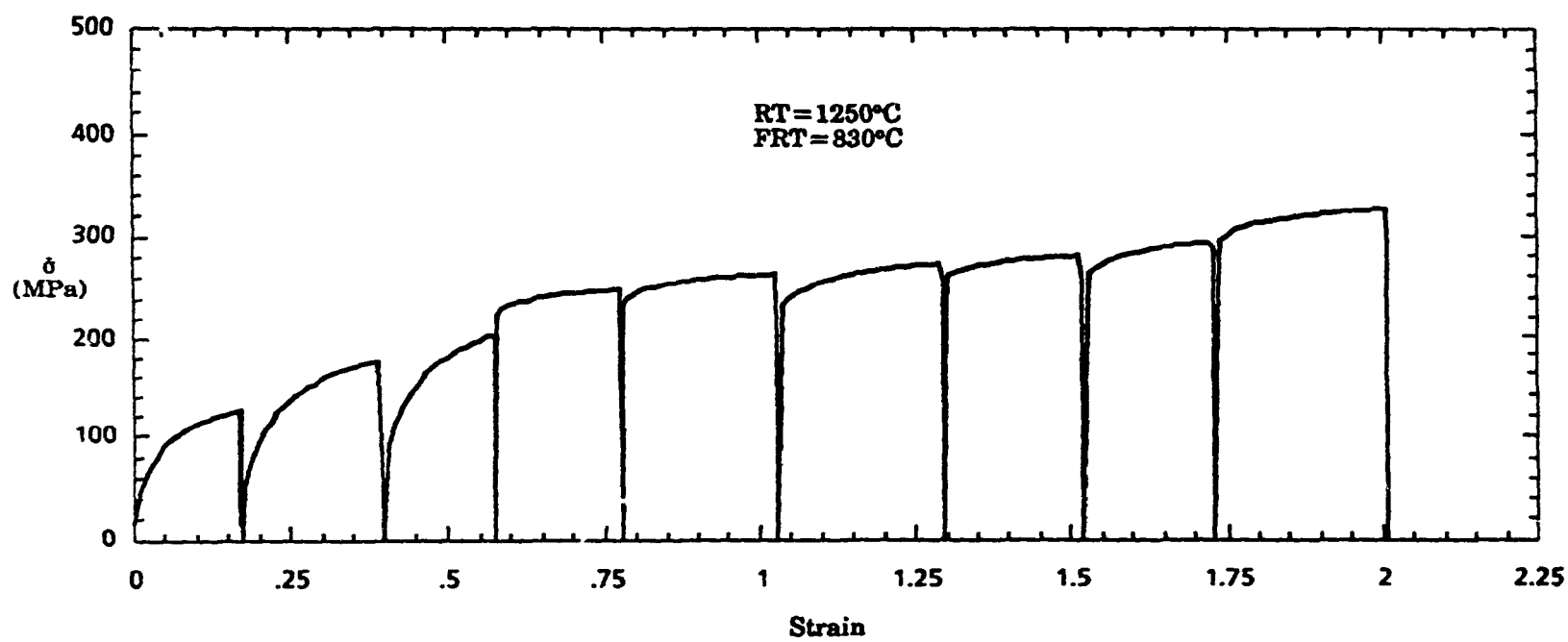


Figure 8.10 Stress/strain curves predicted by the present program for the hot rolling of the Cu-Nb-B steel.

Table 8.3a Evolution of the residual strain, recrystallized fraction and mean flow stress during hot rolling of the Cu-Nb-B steel
(RT = 1100°C, FRT = 750°C)

Pass #	\bar{T} (°C)	$\dot{\epsilon}$ (s ⁻¹)	ϵ_i	$\Delta\epsilon_i$	J	X	$\bar{\sigma}$ (MPa)
1	1086	3.28	0.19	-	-	-	99.7
2	990	3.90	0.23	0.00	0.00	1.00	133.5
3	940	3.75	0.17	0.02	0.13	0.77	154.0
4	910	4.40	0.21	0.18	0.10	0.08	218.6
5	887	5.30	0.25	0.26	0.08	0.21	236.5
6	865	6.08	0.27	0.37	0.07	0.17	251.6
7	836	6.38	0.23	0.61	0.09	0.07	283.2
8	810	6.57	0.20	0.84	0.06	0.04	308.6
9	762	8.44	0.28	1.03	0.15	0.02	340.0

Table 8.3b Evolution of the residual strain, recrystallized fraction and mean flow stress during hot rolling of the Cu-Nb-B steel
(RT = 1100°C, FRT = 830°C)

Pass #	\bar{T} (°C)	$\dot{\epsilon}$ (s ⁻¹)	ϵ_i	$\Delta\epsilon_i$	J	X	$\bar{\sigma}$ (MPa)
1	1086	3.13	0.17	-	-	-	98.5
2	1000	3.90	0.23	0.00	0.00	1.00	132.9
3	940	3.78	0.18	0.02	0.18	0.80	156.8
4	905	4.35	0.20	0.19	0.09	0.03	241.5
5	885	5.30	0.25	0.38	0.06	0.08	254.2
6	860	6.08	0.27	0.48	0.04	0.18	254.3
7	848	6.31	0.23	0.72	0.02	0.09	267.1
8	830	6.65	0.21	0.82	0.06	0.12	274.4
9	811	8.51	0.29	1.01	0.09	0.05	310.2

Table 8.3c Evolution of the residual strain, recrystallized fraction and mean flow stress during hot rolling of the Cu-Nb-B steel
(RT = 1250°C, FRT = 830°C)

Pass #	\dot{T} (°C)	$\dot{\epsilon}$ (s ⁻¹)	ϵ_i	$\Delta\epsilon_i$	J	X	$\bar{\sigma}$ (MPa)
1	1200	2.94	0.15	-	-	-	64.9
2	1100	3.07	0.14	0.00	0.00	1.00	86.3
3	1015	3.23	0.14	0.00	0.00	1.00	106.2
4	953	3.65	0.16	0.05	0.20	0.33	173.8
5	918	4.46	0.21	0.20	0.08	0.06	222.6
6	890	5.35	0.25	0.28	0.07	0.18	239.7
7	875	6.18	0.27	0.39	0.06	0.13	249.6
8	855	6.36	0.22	0.51	0.04	0.11	263.5
9	835	6.89	0.22	0.71	0.06	0.09	275.5
10	820	8.34	0.26	0.92	0.05	0.05	229.1

strains ($\epsilon_i + \Delta\epsilon_i$ in Table 8.3) are well below the predicted peak strains for dynamic recrystallization. Also, partial static recrystallization only occurs during the last few passes, leading to a slight accumulation of strain. This explains the mixed structures usually obtained after rolling C-Mn steels and the absence of pancaking during finishing.

While dynamic recrystallization does not occur during the plate (i.e. reversing) rolling of C-Mn steels, it can indeed be initiated in hot strip mills, particularly in Nb steels, and other grades containing alloying elements that retard static recrystallization. This is because, during strip rolling, the pass strains are higher than those shown in Table 8.4. Moreover, the times between passes are so short that static recrystallization is unable to take place; under these conditions, strains are accumulated. As a result, the retained strains can become high enough to exceed the peak strain for dynamic recrystallization.

Table 8.4 Comparison of the effective (accumulated) strain and peak strain for dynamic recrystallization during hot rolling of the base steel.

Pass #	ϵ_i	$\dot{\epsilon}$ (from Table 8.3b)			$\dot{\epsilon} = 50\text{s}^{-1}$		
		$\Delta\epsilon_i$	ϵ_p	X	$\Delta\epsilon_i$	ϵ_p	X
1	0.17	-	0.27	-	-	0.39	-
2	0.23	0.00	0.35	1.00	0.00	0.49	1.00
3	0.18	0.00	0.42	1.00	0.00	0.59	1.00
4	0.20	0.00	0.49	0.97	0.00	0.67	1.00
5	0.25	0.00	0.54	0.93	0.00	0.71	1.00
6	0.27	0.00	0.60	0.99	0.00	0.78	1.00
7	0.23	0.02	0.63	0.87	0.00	0.82	1.00
8	0.21	0.05	0.68	0.69	0.00	0.88	0.97
9	0.29	0.09	0.76	0.65	0.03	0.95	0.72

Figs. 8.11 and 8.12 compare the mean flow stresses calculated with the aid of the present model (full symbols) with the ones converted from the measured rolling loads using either the Sims [68] or the Ford and Alexander [197]† theory. It can be seen that the predictions of the model are in good agreement with the measurements. The slight differences between predicted and measured values are probably due to changes in the friction coefficient during rolling which are not taken into account in the present model. (Extensive work is needed to characterize this coefficient.) Comparison between the computed and measured mean stresses using the Sims and Ford and Alexander models is difficult because of the imperfections of these theories, which assume a uniform strain distribution in the roll gap. A finite element model, which can compute the strain and strain rate distributions during deformation in the roll gap, will lead to more accurate results and constitute a further interesting area of study.

† The CANMET program used to convert the measured rolling loads to mean flow stresses during off-line data processing is based on the Ford and Alexander approach

The calculated mean flow stresses using the pass strains instead of the effective strains are also included in Figs. 8.11a and b; i.e., the fraction recrystallized X was assumed equal to 1 after each pass for these simulation. The results demonstrate that the neglect of incomplete recrystallization between passes leads to the net underestimation of the loads, which can cause serious problems during rolling.

8.3.3. Evolution of the Mean Austenite Grain Size

Due to time limitations, the evolution of the austenite grain size during hot rolling was not studied systematically during the present work. This requires several trials followed by quenches after specified passes. Nevertheless, some mean austenite grain sizes were determined during the experimental rolling program. These were, unfortunately, difficult to assess because of pancaking during finishing. For this reason, the microstructure evolution that is described below is largely based on published models.

Fig. 8.13 shows the expected evolution of the mean austenite grain size d_γ after each pass during controlled rolling of the Cu-Nb-B steel. The empirical equation for the grain size as a function of initial structure, strain and temperature suggested by Roberts [182] was employed here (see Table 7.3), in conjunction with the phenomenological approach described in section 7.4. For the three schedules used, the mathematical model predicts grain coarsening after the first pass and grain refinement only after the fifth pass. Such grain coarsening is more pronounced when the 1250°C reheating temperature is used. Similar behavior was observed by Roberts in Ti-V steels where the starting grain sizes were similar to those in this work. According to the present model, grain coarsening took place after the first pass because the applied reductions were insufficient to engender grain refinement, even though the material was fully recrystallized. It is only when the effective strains are sufficiently high, i.e. after the fifth pass, that grain refinement occurs.

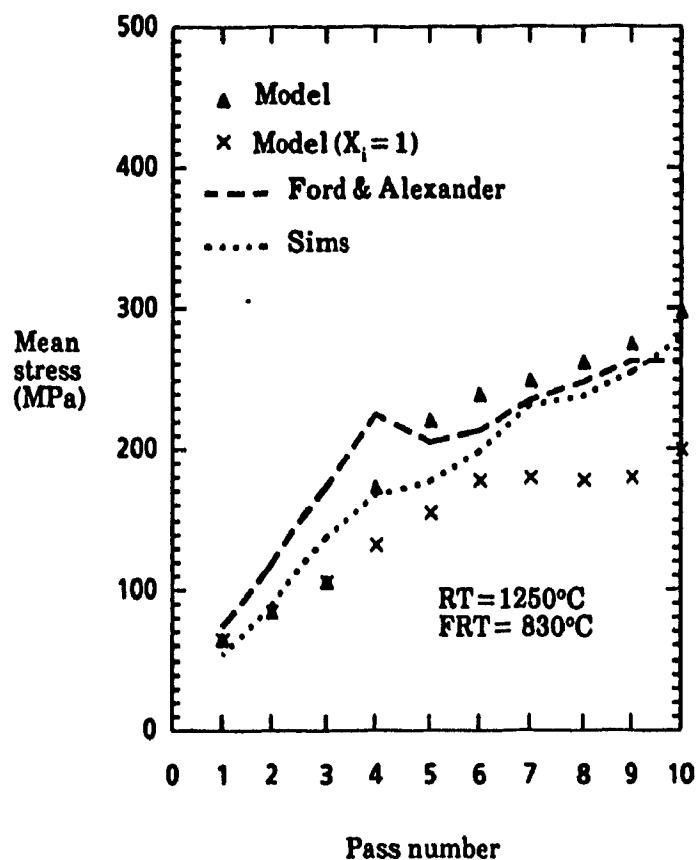
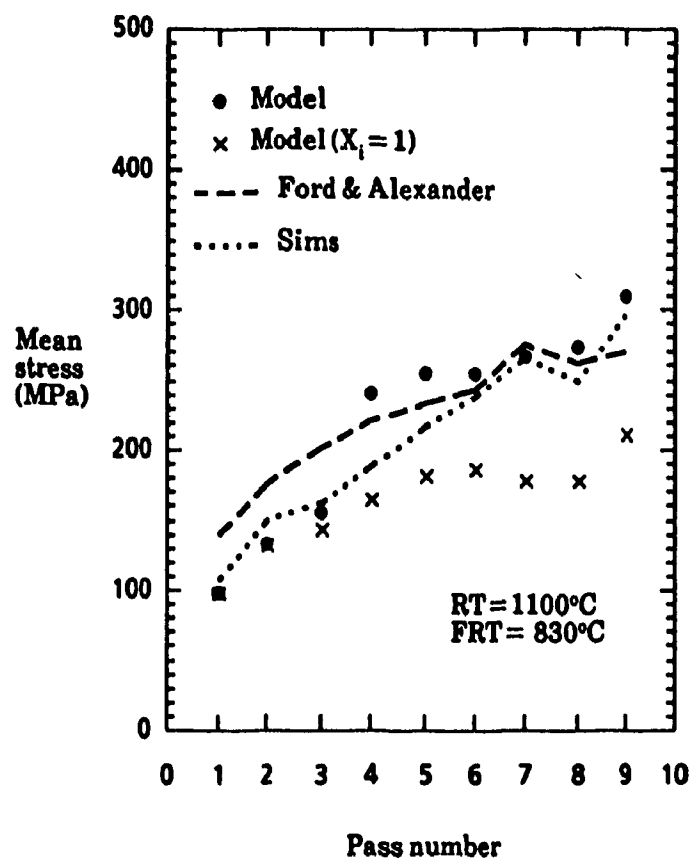


Figure 8.11 Comparison of calculated and measured mean stresses for rolling of the experimental Cu-Nb-B steel.

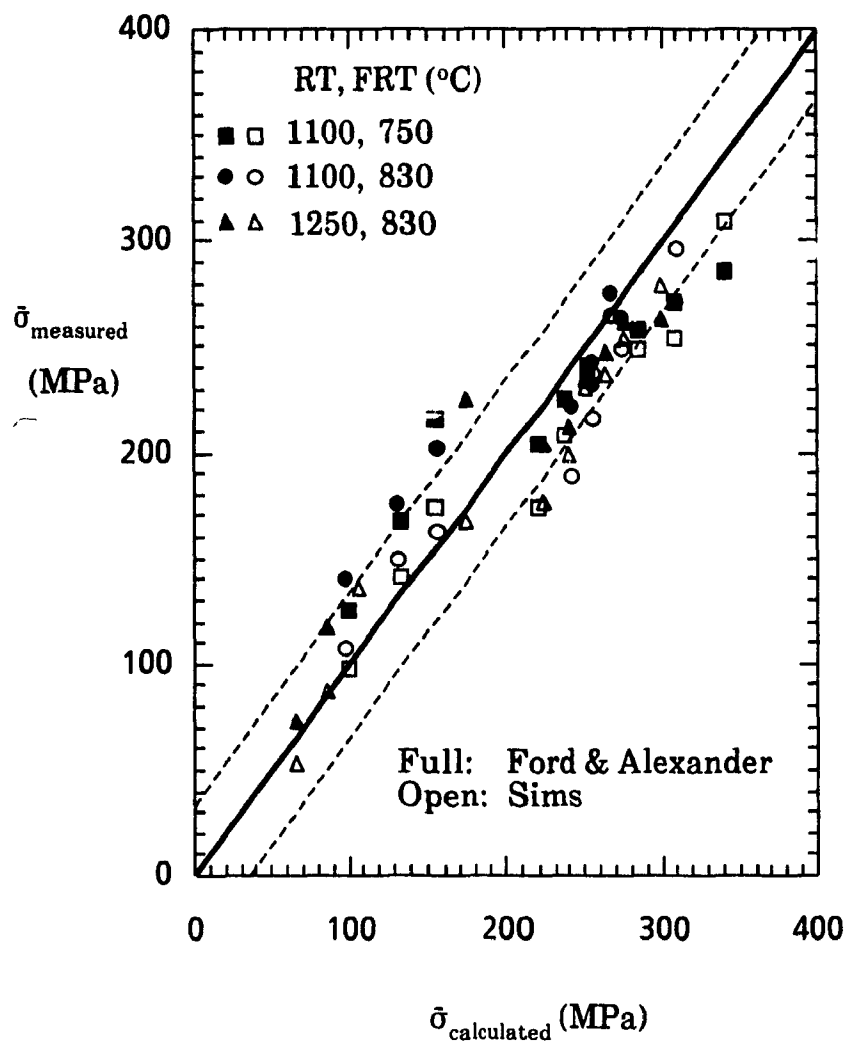


Figure 8.12 Comparison of calculated and measured mean stresses for rolling of the experimental Cu-Nb-B steel.

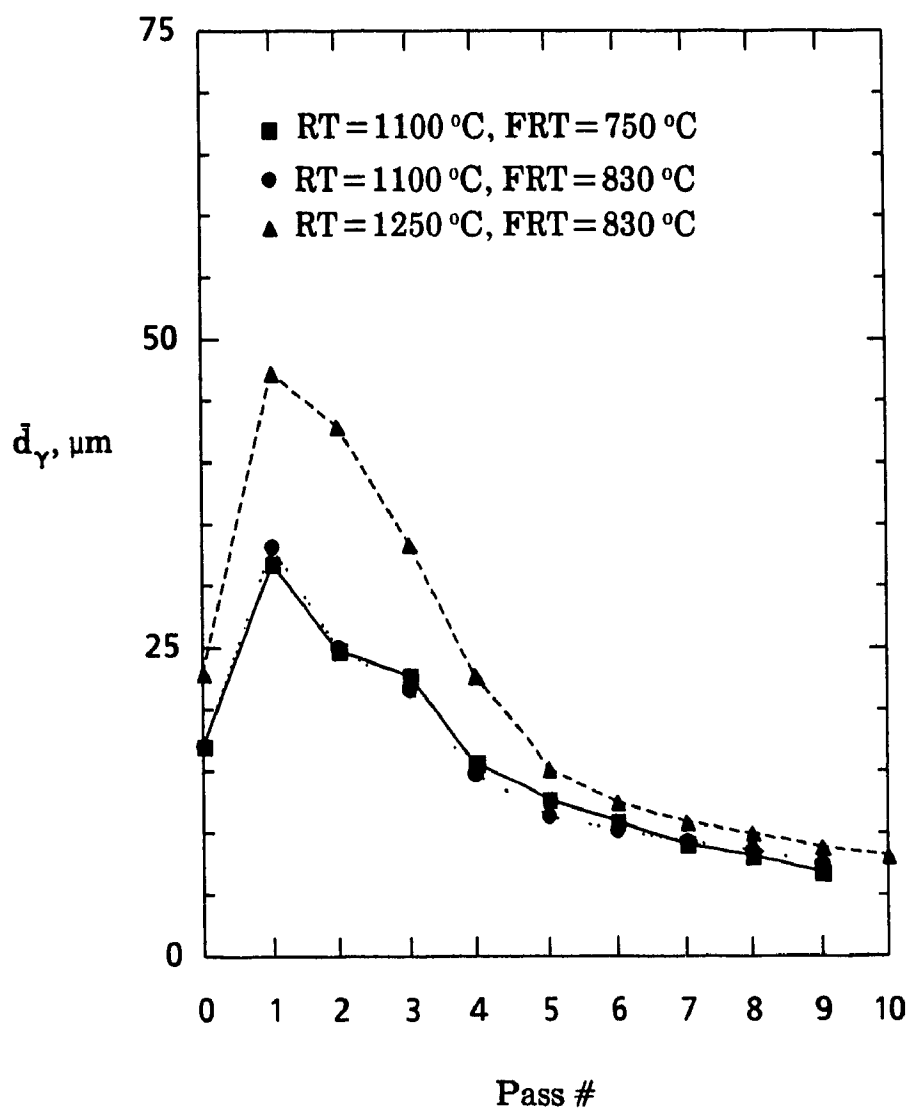


Figure 8.13 Predicted mean austenite grain sizes during the experimental rolling of the Cu-Nb-B steel.

For comparison purposes, the approach used to predict the mean austenite grain size was also applied to steels with large initial grain sizes such as C-Mn steels. The same rolling schedule with 10 passes was employed, with complete softening between passes to simulate the structural changes in C-Mn steels, where the recrystallization kinetics are relatively fast. Fig. 8.14 shows the grain size evolution using the equations for grain size prediction proposed by Roberts and by Sellars. It is of interest here that most of grain refinement occurs after the first two passes. The effect of subsequent passes on the grain size is much less important, the further refinement being small. This type of behavior was also observed by Sellars [17, 198, 199], who compared computed and measured grain sizes during the experimental plate rolling of a C-Mn steel. According to Sellars [200], knowledge of the behavior after two passes, in terms of the structural changes, is generally sufficient for the prediction of what happens after a large number of passes. The errors generated after the third pass are canceled in a such a way that the final structure is predicted with a certain degree of confidence.

8.4. EXTENSION OF THE TEMPERATURE, FLOW STRESS AND MICROSTRUCTURE EVOLUTION MODELS TO INDUSTRIAL PROCESSING

The temperature as well as the flow stress and microstructure evolution models can now be extrapolated to industrial situations, such as the hot rolling of strip and plate, with a certain degree of confidence. Although most of the validations were made using the pilot mill data for specific steels, care was exercised to reproduce the industrial thermomechanical variables, in particular the strain rate, and to derive appropriate constitutive equations. An extension of this model to other steel chemistries will constitute a step towards on-line automatic gauge control during hot rolling and the rational design and optimization of rolling schedules for the production of specific microstructures.

Finally, it should be emphasized that the principles used during the present work apply not only to steels, but could be extended to other metals, such as copper and aluminum, or even to other materials, provided appropriate

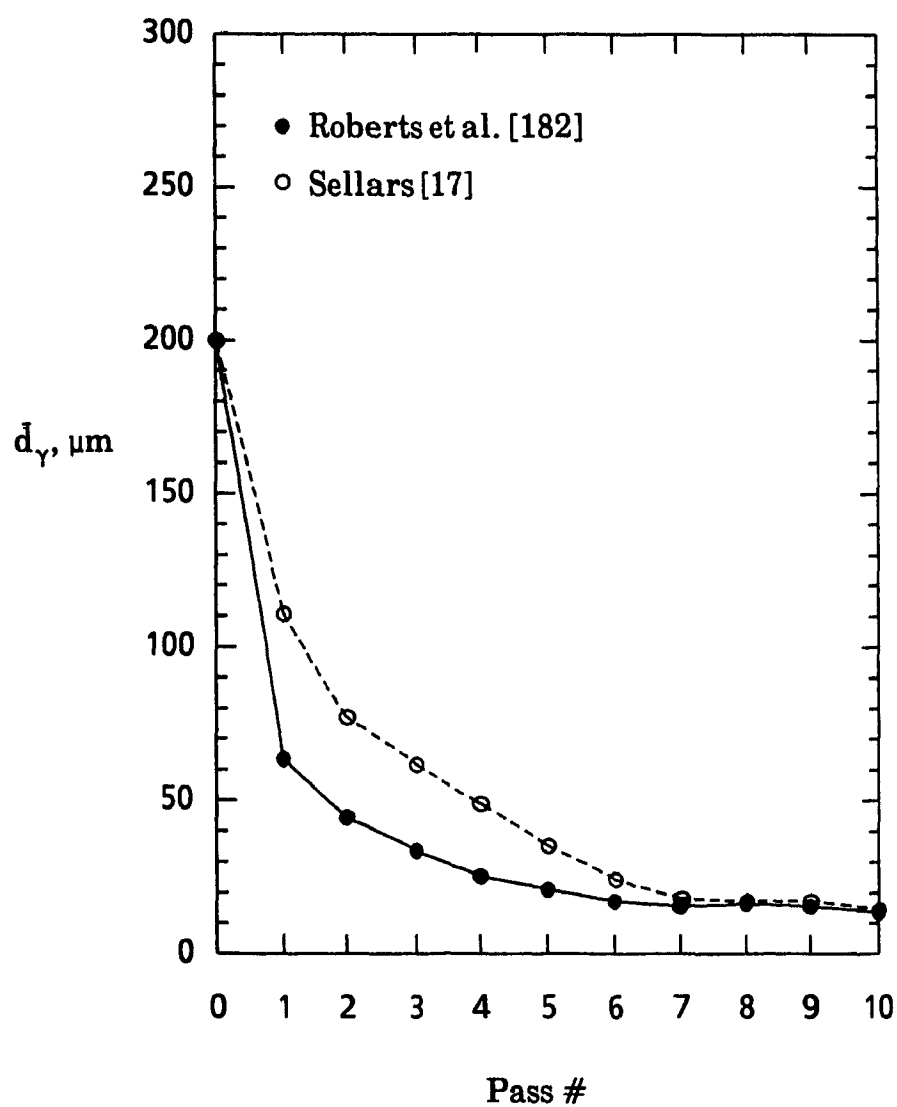


Figure 8.14 Predicted mean austenite grain sizes during the hypothetical rolling of a C-Mn steel with a large initial grain size.

laboratory simulations and plant trials are performed and used in conjunction with the mathematical model.

8.5. ROLLING TRIALS OF THE Cu-Nb-B STEEL

8.5.1. Introduction

The strength levels of commercial HSLA steels are generally between 485 and 550 MPa, with transition temperatures in the range 20 to 0°C, which make them unsuitable for low temperature applications. However, with judicious modification of the composition and appropriate thermomechanical control, the final microstructures and, in turn, the mechanical properties of these steels can be improved considerably.

8.5.2. Microstructures

The microstructures developed after rolling the present Cu-Nb-B steel are shown in Figs. 8.15 to 8.18 as a function of both the reheat and finish rolling temperatures. They all consist of acicular ferrite containing a lath structure. Some investigators call this bainite. However, this interpretation is often obscured by confusions in the nomenclature [201]. Other authors [79] call it low carbon bainite, which consists of fine high carbon martensite with a high dislocation density lying at the γ -boundaries, and "bainitic ferrite" (containing a lath structure). Previous electron microscopic studies on steels with similar compositions, reheated to 1250°C and finish rolled at 830°C [80] have shown that this structure consists of highly dislocated laths (Fig. 8.16) with elongated MA (martensite/austenite) observed between these laths.

From Fig. 8.15, a drastic difference can be observed between the steels reheated at 1250 and 1100°C. The steel reheated at the lower temperature exhibits a finer and more uniform structure than the one reheated at 1250°C. For the latter, the nonuniform structure is probably due to the marked grain coarsening after the first stand predicted by the microstructure model (Fig. 8.13). The effect of finish rolling temperature is shown in Fig. 8.17, where the microstructures of the samples reheated to 1100°C are compared. Decreasing



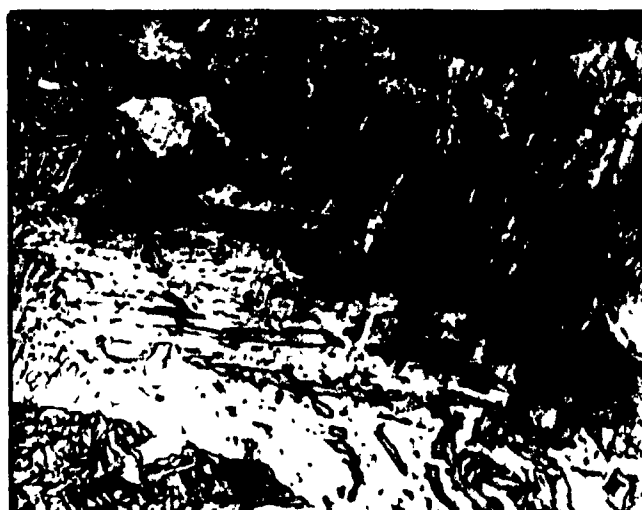
RT = 1100°C
FRT = 750°C

500X



RT = 1250°C
FRT = 830°C

500X



RT = 1250°C
FRT = 830°C

1000X

Figure 8.15 Optical microstructures obtained after rolling and quenching the Cu-Nb-B steel.

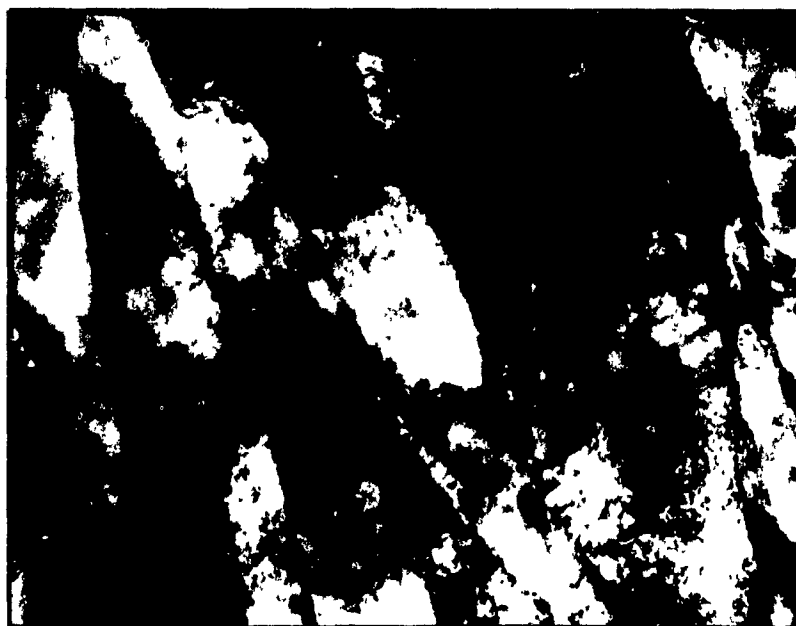


Figure 8.16 Transmission electron micrograph showing the high dislocation density lath structure (56,000X) ^[80].



RT = 1100°C
FRT = 750°C

1000X



RT = 1100°C
FRT = 830°C

1000X

Figure 8.17 Optical micrographs of the microstructures produced using two different finish rolling temperatures in the Cu-Nb-B steel.



Figure 8.18 Optical photograph showing the prior austenite grain boundaries after pancaking (RT=1250°C, FRT=830°C). Magnification 500X.

the FRT from 830 to 750°C increases slightly the volume fraction of fine grained ferrite present.

Finally, even after transformation, the prior austenite boundaries are preserved. These are apparent from Fig. 8.18, where the micrograph is taken along the normal to the plate surface. Each pancaked austenite grain contains packets of laths of different orientations, suggesting that nucleation during the $\gamma \rightarrow \alpha$ transformation also occurred on deformation bands in the interiors of the unrecrystallized γ -grains.

8.5.3. Mechanical Properties

The mechanical properties of the Cu-Nb-B steel rolled according to the three schedules used in the present study are listed in Table 8.5. Yield strengths between 560 and 718 MPa were obtained, with minimum total elongations of 21%. This excellent combination is mainly due to *i*) the relatively fine microstructure developed here, and *ii*) the synergistic effect of combined additions of copper, niobium and boron in delaying the $\gamma \rightarrow \alpha$ transformation, which results in a highly dislocated microstructure [80, 202], and therefore in high strength. According to Tamehiro et al. [79], the addition of niobium or titanium to a boron steel prevents the formation of iron boro-carbide ($\text{Fe}_{23}(\text{C},\text{B})_6$) precipitates, which normally act as nucleation sites for polygonal ferrite. The titanium addition protects the boron, which delays the $\gamma \rightarrow \alpha$ transformation. This retardation is made possible by the segregation of solute boron atoms at lattice defects such as the deformation bands resulting from rolling, as well as at the unrecrystallized austenite grain boundaries. Since solute niobium and titanium have stronger effects than boron in lowering the carbon diffusion rate, the precipitation of $\text{Fe}_{23}(\text{C},\text{B})_6$ is suppressed. Furthermore, in low carbon steels, the strain-induced precipitation of NbC or TiC limits the amount of carbon available for the precipitation of the iron boro-carbides.

A difference in strength of about 133 MPa is obtained between schedule C1 and D2, probably because of the greater amount of niobium in solution at 1250°C. The dissolved niobium leads to a higher driving force for the

Table 8.5 Mechanical properties of the Cu-Nb-B steel†.

Schedule	RT (°C)	FRT (°C)	YS (MPa)	UTS (MPa)	%El	%RA	TT (°C)
C1	1230	830	718	864	21	64	-85
D1	1100	750	560	726	27	71	< -100
D2	1100	830	585	745	26	68	-95

† Tensile and Charpy specimens were taken in the longitudinal direction.

precipitation of NbC in the transformed austenite, leading to more precipitation hardening.

On the other hand, when the FRT is increased from 750 to 830°C, the strength is only increased by about 25 MPa. This slight increase can be explained in terms of the slight increase in the volume fraction of acicular ferrite (versus fine-grained ferrite), which has a higher strength than equiaxed ferrite. Such behavior has also been observed by Nakasugi et al. [40] in bainitic steels containing 0.02% carbon and 10 ppm of boron.

The impact transition curves for full size V-notch Charpy specimens are shown in Fig. 8.19 and the transition temperatures are given in Table 8.5 as well. It is of interest that a transition temperature below -100°C is obtained for the steel reheated to 1100°C and finished at 750°C, without a large sacrifice of strength. Nakasugi et al. [40] found that, although the finish rolling temperature had no strong effect on strength, an optimum finishing temperature exists. This optimum was around 700°C, slightly above the bainite formation temperature, a result which was also reported by Cha'bout et al. [87].

When the steel is reheated to 1250°C, the impact properties (in terms of upper shelf energy and transition temperature) deteriorate. This is simply explained by the relatively coarse and mixed microstructure produced by rolling just below this temperature, as well as to additional Nb(C,N)

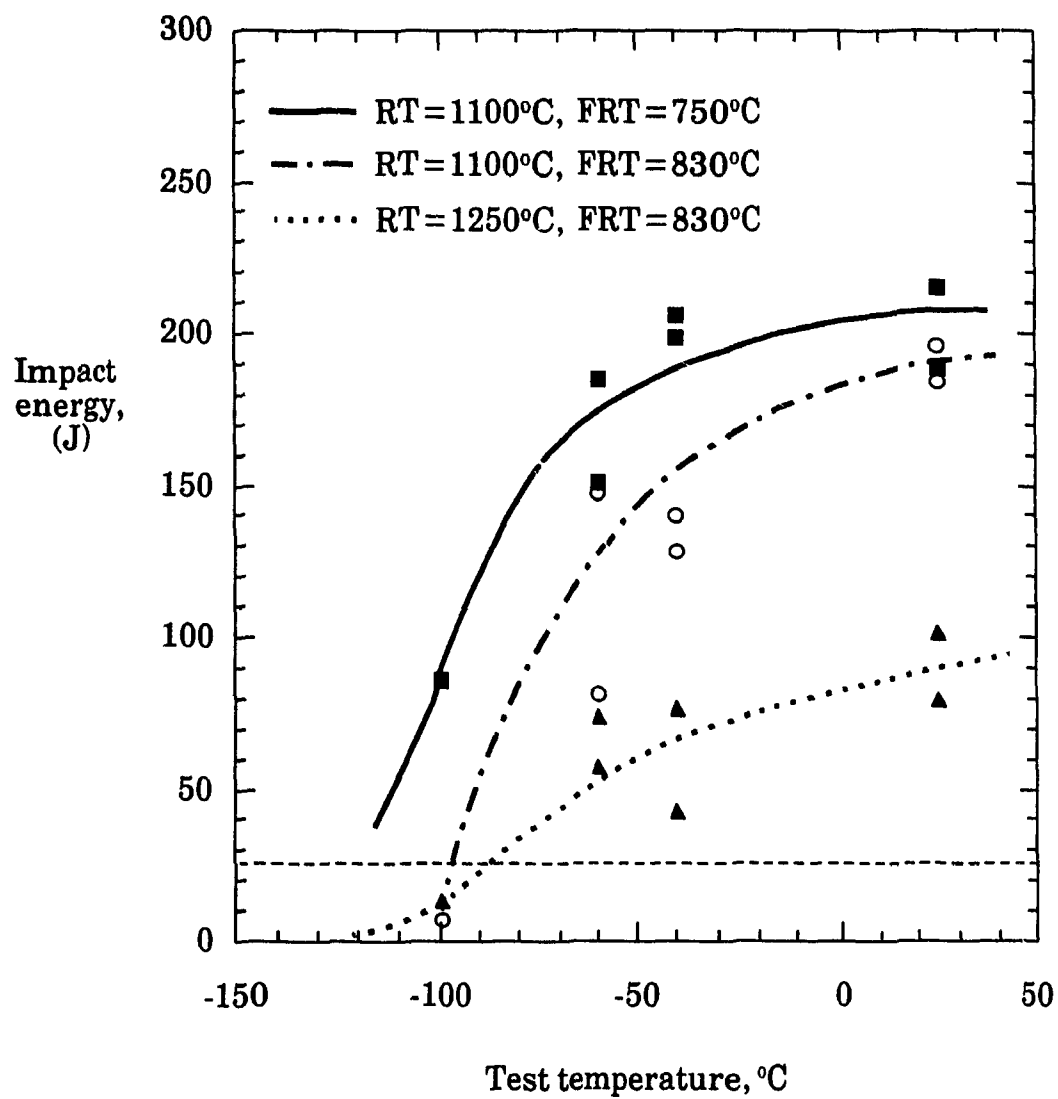


Figure 8.19 Charpy transition curves for the Cu-Nb-B steel.

precipitation in the transformed structure. The good impact properties obtained when the steel is reheated to 1100°C are due to *i*) the fine packet size of the transformed microstructure, and *ii*) the high crack propagation resistance associated with this microstructure, as measured by the energy absorbed after the maximum load (*see* Fig. 8.20). Pickering [37, 203] found that, although cleavage cracks form easily between the low angle boundary laths in bainitic steels, there is considerable resistance to crack propagation. These cracks are deflected by the high angle boundaries (packets), leading to a mixed mode of fracture. This explains the gradual decrease in the impact energy when the test temperature is decreased.

To summarize, the interesting mechanical properties achieved here are due to the type and fineness of the structures obtained. Reheating at a low temperature (around 1100°C) before controlled rolling avoids long delay times for cooling the slab, which can cause a decrease in productivity, and save energy and metal by reducing the scale losses. By selecting this economical thermomechanical treatment and judicious alloying, very high strength coupled with excellent toughness are obtained. These steels can be used in the construction of naval structures and offshore platforms, the manufacture of high pressure linepipe, as well as in energy transportation and other structural applications in low temperature arctic environments. It should be noted that the composition of such Cu-Nb-B steels can be modified as required for flexibility in terms of processing and microalloying requirements, so that a wide spectrum of steel mills with different capabilities could supply this product at competitive cost.

8.6. SUMMARY

This final chapter constitutes the bridge that links the fundamental concepts of physical metallurgy and mechanical engineering on the one hand, and the process of hot rolling in its industrial context on the other hand. In the light of what has been described, the preliminary results appear to be promising. However, a considerable amount of investigative work is still needed in the area of the computer modelling of the deformation processing of steels. Such models will rapidly become more mature because of the fruitful

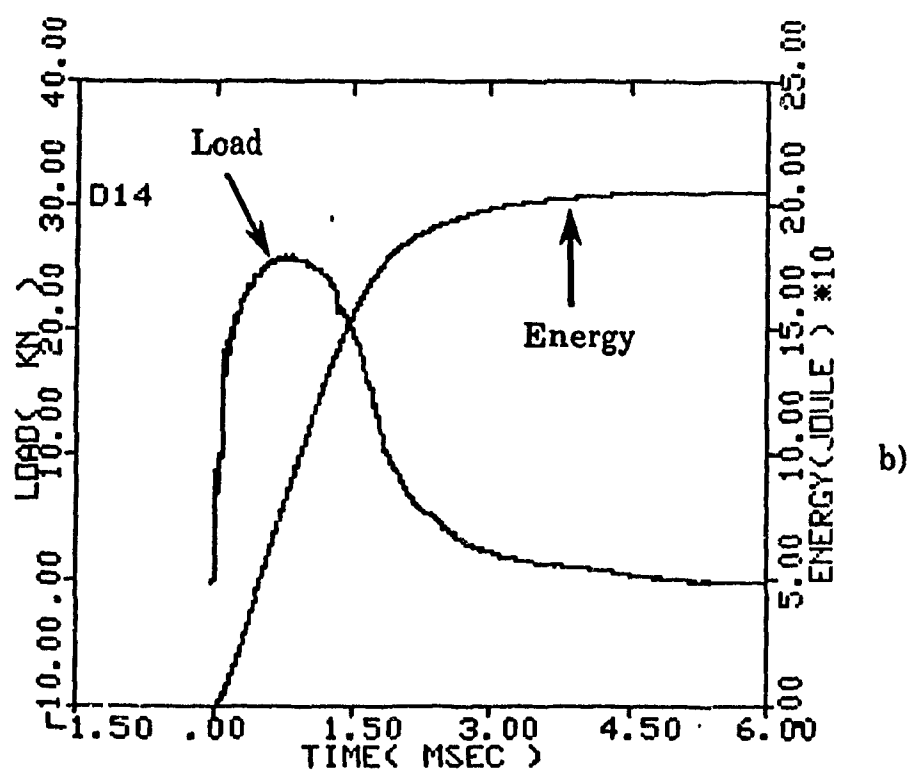
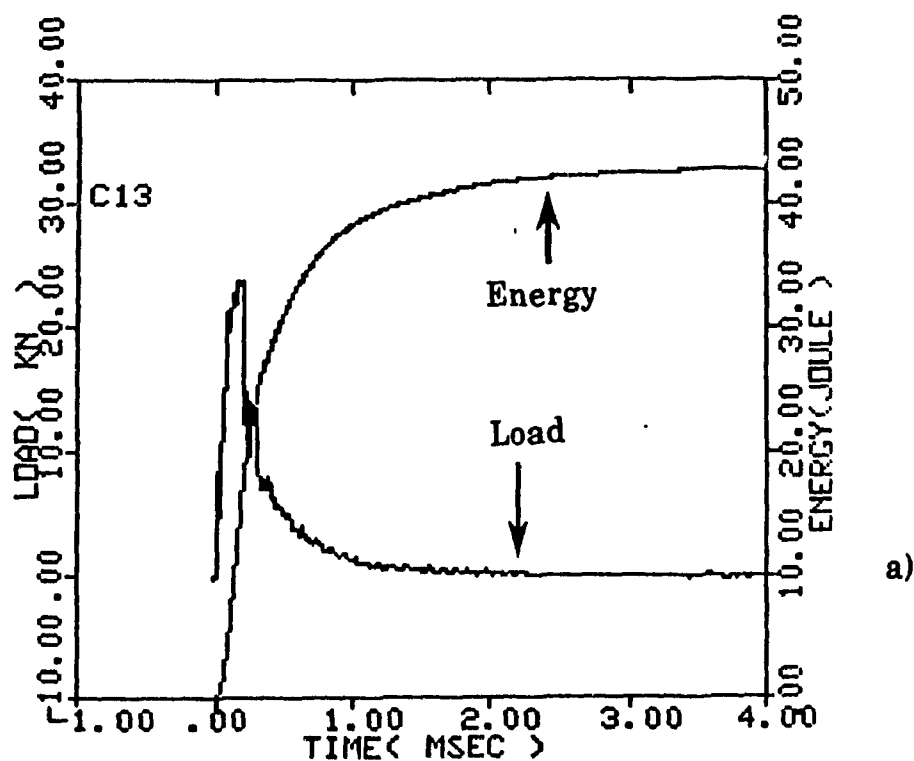


Figure 8.20 Load and energy-time curves obtained in the Charpy impact tests carried out at -40°C :

a) $\text{RT} = 1250^{\circ}\text{C}$, $\text{FRT} = 830^{\circ}\text{C}$

b) $\text{RT} = 1100^{\circ}\text{C}$, $\text{FRT} = 750^{\circ}\text{C}$.

interaction between the concepts contributed by different engineering disciplines.

Chapter NINE

CONCLUSIONS AND RECOMMENDATIONS

9.1. CONCLUSIONS

In the present investigation, single and double hit compression tests were performed over a wide range of temperatures and strain rates pertinent to hot rolling. The high temperature-high strain rate flow behavior as well as the microstructural changes taking place in the austenite were determined experimentally and modelled. Using a heat balance applied to hot rolling, the temperature distributions were also calculated in order to predict the flow stresses and microstructures more accurately. The main conclusions drawn from this work are the following:

-A- Continuous Deformation

- 1) The effect of adiabatic heating during deformation at high strain rates was determined using an incremental procedure. For the present materials, the corrected flow stresses differ from the uncorrected ones by up to 11 pct. at a strain of one.
- 2) The flow behavior of steels at high temperatures and strain rates can be completely described using a rate equation and a one-internal-variable evolution equation. In particular, the rate equation consists of a hyperbolic sine function which relates the strain rate, temperature and saturation stress. The apparent activation energies associated with this equation are close to that of self diffusion and range from 312 to 326 kJ/mole for the base, Nb and Nb-B steels. The high value of 382 kJ/mole determined for the Cu-Nb-B steel is probably due to the high level of

copper in solution. When a stress power law is employed in the rate equation, the apparent activation energies are strongly stress dependent. This is due to the dependence of the steady state structure on the saturation stress.

3) The Bergström model accurately describes the experimental stress/strain curves and is therefore suitable for modeling the flow behavior of steels undergoing dynamic recovery at high temperatures. This model has several advantages in that it permits saturation of the flow stress and the description of the entire curve with only two coefficients, which can also be given physical interpretations.

4) When dynamic recrystallization takes place, the simultaneous use of the Bergström model and the volume fraction that has recrystallized dynamically predicts the flow stress after the peak with accuracy.

-B- Recrystallization Kinetics

1) Different methods of defining the fractional softening were compared. The one based on the mean stress leads to values intermediate between the softening rates determined from the offset and back extrapolation yield stresses. The fractional softening defined by the mean flow stress method was corrected for adiabatic heating using a simple procedure. There is up to an 18 pct. difference between the isothermal and measured anisothermal restoration indices when the testing conditions are adiabatic.

2) When simulating static softening during the rolling of plain carbon and Nb-bearing HSLA steels, the test conditions must reproduce the industrial strain rates. At least one order of magnitude increase in softening rate occurs when the strain rate is increased by two orders of magnitude. The simple extrapolation of laboratory data determined at conventional strain rates to high speed mill conditions is therefore likely to be inaccurate. This is because the flow stress prior to holding, which constitutes the driving force for static recrystallization via the

dislocation density, does not vary linearly with strain rate at high rates of deformation.

3) When recrystallization is incomplete, particularly at low temperatures, the residual strain (retained work hardening) must be taken into account to predict the recrystallized fraction.

4) The addition of 2 wt% of copper to the Nb-B steel results in measurable retardation of the recrystallization kinetics. It extends the no-recrystallization region during hot rolling, thereby enabling the final mechanical properties to be improved.

-C- Temperature-Flow Stress-Microstructure Model

1) A mathematical model based on the explicit finite difference method was developed for the on-line prediction of temperature distributions during hot rolling. Preliminary validation of this model with the aid of both hot strip mill and pilot mill data appears promising. During contact between the workpiece and the rolls, the presence of thermal resistance at the interface was assumed. Values of the heat transfer coefficient between 35 and 40 kWm⁻²K⁻¹ lead to temperature drops near the surface close to those calculated by the Hollander (no thermal resistance) approach. During multi-stage hot rolling, the heat transfer coefficient at the interface between the workpiece and rolls is not constant but changes with the contact time.

2) On the basis of the heat flow model and the constitutive (i.e. rate and evolution) and kinetics of recrystallization equations, a computer model was developed for the prediction of rolling force and microstructural evolution. Simulations based on the above model show that softening by dynamic recrystallization does not occur in plain carbon steels under plate rolling conditions. However, when recrystallization is incomplete, effective strains above 1 are easily reached. This suggests that in hot strip rolling, where the interpass times are short and where both static recrystallization and strain-induced precipitation can be suppressed,

dynamic recrystallization becomes an alternative softening mechanism in solute containing grades such as Nb steel.

3) By appropriate control of the thermomechanical parameters, ultra high strength as-hot rolled steels with transition temperature below -100°C can be developed. The excellent impact properties obtained in the present Cu-Nb-B steel at the economical reheating temperature of 1100°C can be attributed to the fine packet size of the bainitic microstructure and the high crack propagation resistance. This makes the above steel a good candidate for low temperature use.

4) Reheating the Cu-Nb-B steel to 1250°C results in a deterioration of the impact properties in terms of the upper shelf energy and transition temperature. This is mainly due to the mixed microstructure produced by rolling just below this high reheating temperature. The relatively light reductions employed led to grain coarsening, which can be avoided by employing higher reductions at somewhat lower temperatures.

9.2. RECOMMENDATIONS FOR FUTURE WORK

1) Systematic laboratory experiments are needed to model the austenite grain size during the multi-stage hot rolling of plate and strip. This could be done by torsion simulation, where the deformed samples are quenched after selected passes.

2) Extensive studies are needed to characterize frictional effects in the roll gap and to determine the coefficient of friction at high temperatures as a function of the thermomechanical parameters. This information is required to improve the accuracy of rolling load calculations.

3) A finite element model which computes the strain and strain rate distribution during deformation in the roll gap is necessary to predict the flow stress and microstructure in multi-stage rolling more accurately. Linking of the present computer model with such a finite element model would enable the flow stress and microstructure in each element to be

computed as a function of the local temperatures, strains and strain rates. This will constitute a more efficient tool for the design and optimization of both rolling mills and schedules.

4) The effect of different steel chemistries should be entered into the computer model developed here. This could be obtained from mill data and would facilitate on-line application.

5) Computer models should be developed for predicting the kinetics of the $\gamma \rightarrow \alpha$ transformation under rolling conditions. When used in conjunction with the ones developed here, this would constitute a complete model, and lead to the more accurate prediction of the mechanical properties of the final product.

STATEMENT OF ORIGINALITY AND CONTRIBUTION TO KNOWLEDGE

The present work includes the following original contributions:

1) For the case where dynamic recovery is the sole mechanism of softening, the flow behavior of C-Mn and Nb-bearing HSLA steels was modelled in the high temperature and strain rate ranges 800 to 1200°C and 0.2 to 50 s⁻¹, respectively. The model is based on a rate equation, which consists of a hyperbolic sine function, and a one-internal-variable evolution equation; the latter is similar to the Bergstrom model employed at low temperatures. A phenomenological interpretation of evolution in mechanistic terms has also been proposed. When dynamic recrystallization takes place in addition to dynamic recovery, the simultaneous use of the above evolution equation and the volume fraction that has recrystallized dynamically makes it possible to predict the flow stress after the peak.

2) The effect of adiabatic heating was determined both during continuous and interrupted deformation. In the former case, an incremental procedure was used at each strain interval and in the latter, a simple method was employed to correct the fractional softening which is based on the mean stress technique. In both cases, it was shown that errors of 10 to 20 pct. can readily occur if this type of correction is not carried out.

3) Four methods of defining the fractional softening during interrupted compression testing, i.e. the offset, back extrapolation, unrecovered strain

fraction and mean stress methods, were compared for the first time using data determined at high temperatures and strain rates. It was shown that the fractional softening based on the mean stress is rapid and more accurate than the other methods. This is the definition of fractional softening that was used in the program designed for rolling load prediction, as it is not sensitive to the recovery effects occurring during hot rolling.

4) The effect of preloading strain rate on recrystallization kinetics at high temperatures was investigated systematically on a C-Mn and on Nb-bearing steels for the first time. It was shown in particular that there is at least a one order of magnitude increase in softening rate when the strain rate is increased by two orders of magnitude. This means that simple extrapolations of the laboratory data determined at conventional strain rates to high speed mill conditions are likely to be inaccurate.

5) A rapid heat flow model was developed based on the explicit finite difference method; it was designed for the on-line prediction of the temperature distribution during hot rolling. During contact of the workpiece with the rolls, two methods were employed to assess the temperature drop at the interface; the first is based on a heat balance and the second on Hollander's perfect contact approach. This comparison led to an estimate of the heat transfer coefficient during contact, and to the conclusion that this coefficient is time dependent. Moreover, a flow stress-microstructure model based on laboratory data was also developed and used in conjunction with the temperature model; this represents an important step towards the on-line prediction of rolling load.

6) The effect of the presence of 2 %wt copper in a Nb-bearing HSLA steel on the recrystallization kinetics was investigated under industrial conditions of strain rate and temperature. This addition was shown to extend the no-recrystallization temperature range. The flow stress and microstructural behaviors of this steel were characterized both with the aid of laboratory simulations and in pilot mill rolling. By controlling the thermomechanical parameters appropriately, ultra high strength as-hot rolled steels were developed, with transition temperatures below -100°C.

REFERENCES

1. H. J. McQueen and J. J. Jonas, "Plastic Deformation of Metals", ed. R. J. Arsenault, Academic Press, New York, (1975), p.393.
2. J. J. Jonas, *Acta Metall.*, 17, (1969), p.397.
3. W. Roberts and B. Ahlblom, *Acta Metall.*, 26, (1978), p.801.
4. M. J. Luton and C. M. Sellars, *Acta Metall.*, 17, (1969), p.1033.
5. C. M. Sellars and W. J. McG. Tegart, *Acta Metall.*, 14, (1966), p.1136.
6. C. Rossard, *Proc. 3rd Int. Conf. Strength Metals & Alloys, Vol.II*, (1973), p. 175.
7. S. Sakui, T. Sakai, K. Takeishi, *Trans. ISIJ*, 17, (1977), p.718.
8. J. P. Sah, G. J. Richardson and C. M. Sellars, *Journal of the Australian Institute of Metals*, 14, (1969), p.292.
9. G. Glover and C. M. Sellars, *Metall. Trans.*, 4, (1973), p.765.
10. W. J. McG. Tegart, "Ductility", ASM, Metals Park, Ohio, (1968), p.133.
11. R. A. Petković, M. J. Luton and J. J. Jonas, *Acta Metall.*, 27, (1979), p.1633.
12. R. W. Cahn, "Recovery and Recrystallization", *Physical Metallurgy*, ed. R.W. Cahn, Wiley, New York, (1965), p.925.
13. C.M. Sellars, *Phil. Trans. Roy. Soc. London A.*, 288, (1978), p.147.

References

14. G. Glover and C. M. Sellars, *Metall. Trans.*, **3**, (1972), p.2271.
15. R. A. P. Djaic and J. J. Jonas, *Metall. Trans.*, **4**, (1973), p.621.
16. D. R. Barraclough, Ph.D. Thesis, University of Sheffield, Sheffield, (1974).
17. C. M. Sellars, "Hot Rolling and Forming Processes", eds. C. M. Sellars and G. J. Davies, The Metals Society, London, (1980), p.3.
18. J. J. Jonas, C. M. Sellars and W. J. McG. Tegart, *Metall. Rev.*, **14**, (1969), p. 1.
19. R. A. P. Djaic and J. J. Jonas, *JISI*, **210**, (1972), p.256.
20. C. Ouchi, T. Sampei, T. Okita and I. Kozasu, "Hot Deformation of Austenite", ed. J. B. Ballance, AIME, New York, (1977), p.316.
21. J. J. Jonas, "High Strength Low Alloy Steels", eds. D. P. Dunne and T. Chandra, *Proc. Int. Conf.*, Wollongong, Australia, (1984), p.80.
22. A. LeBon and L. N. de Saint-Martin, "Microalloying 75", *Proc. Int. Symp. HSLA Steels*, Union Carbide Corporation, New York, (1977), p.90.
23. A. LeBon, J. Rofes-Vernis and C. Rossard, *Metal Sci.*, **9**, (1975), p.36.
24. A. T. Davenport, R. E. Miner and R. A. Kot, "Hot Deformation of Austenite", ed. J. B. Ballance, AIME, New York, (1977), p.186.
25. K. J. Irvine and T. N. Baker, *Metal Sci.*, **13**, (1979), p.228.
26. T. Gladman and D. Dulieu, *Metal Sci.*, **8**, (1974), p. 167.
27. I. Weiss and J. J. Jonas, *Metall. Trans.*, **10A**, (1979), p.831.

References

28. J. J. Jonas and I. Weiss, *Metal Sci.*, 13, (1979), p.238.
29. M. J. Luton, R. Dorvel and R. A. Petković, *Metall. Trans.*, 11A, (1980), p.411.
30. J. J. Jonas and M. G. Akben, *Metals Forum*, 4, (1981), p.92.
31. R. K. Amin and F. B. Pickering, "Thermomechanical Processing of Microalloyed Austenite", eds. A. J. DeArdo et al., AIME, Warrendale, Pa, USA, (1982), p.1.
32. J. P. Michel and J. J. Jonas, *Acta Metall.*, 29, (1981), p.513.
33. B. Bacroix, M. G. Akben and J. J. Jonas, "Thermomechanical Processing of Microalloyed Austenite", eds. A. J. deArdo et al., AIME, Warrendale, Pa, USA, (1982), p.293.
34. M. G. Akben, B. Bacroix and J. J. Jonas, *Acta Metall.*, 31, (1983), p.161.
35. T. Sakai, M. G. Akben and J. J. Jonas, "Thermomechanical Processing of Microalloyed Austenite", eds. A. J. deArdo et al., AIME, Warrendale, Pa, USA, (1982), p.237.
36. N. Shams, *Mat. Sci. Tech.*, 1, (1985), p.950.
37. F. B. Pickering, "Microalloying 75", *Proc. Int. Symp. HSLA Steels*, Union Carbide Corporation, New York, (1977), p.9.
38. W. Roberts, "HSLA Steels: Technology and Applications", *Proc. Int. Conf.*, Philadelphia, ASM, Metals Park, OH, (1984), p.33.
39. F. B. Pickering, *Metallurgical Achievements*, Pergamon Press, (1965), p.199.
40. H. Nakasugi, H. Matsuda and H. Tamehiro, *Proc. Int. Conf. Steel Rolling*, Vol. 2, ISIJ, Tokyo, (1980), p.1028.

References

41. G. J. Sojka, Ph.D. Thesis, Université Laval, Québec, (1981).
42. H. Wada, Y. Houbaert, J. Penning and J. Dilewijns, "Strengthening Effects of Copper in Structural Steels", C.I.M.N.F. -Cu30, Bruxelles, (1983), p.3.1.
43. A. Youle and B. Ralph, *Metal Sci.*, 6, (1972), p.149.
44. T. Tanaka, *Int. Metall. Rev.*, 4, (1981), p.185.
45. I. Kozasu, C. Ouchi, T. Sampei and T. Okita, "Microalloying 75", *Proc. Int. Symp. HSLA Steels*, Union Carbide Corporation, New York, (1977), p. 120.
46. J. P. Sah, G. J. Richardson and C. M. Sellars, *Metal Sci.*, 8, (1974), p.325.
47. T. Tanaka, "High Strength Low Alloy Steels", eds. D. P. Dunne and T. Chandra, *Proc. Int. Conf., Wollongong, Australia*, (1984), p.6.
48. T. Gladman, D. Dulieu and I. D. McIvor, "Microalloying 75", *Proc. Int. Symp. HSLA Steels*, Union Carbide Corporation, New York, (1977), p.32.
49. T. Tanaka, T. Funakoshi, M. Ueda, J. Tsuboi, T. Yasuda and C. Utahashi, "Microalloying 75", *Proc. Int. Symp. HSLA Steels*, Union Carbide Corporation, New York, (1977), p.399.
50. C. Ouchi, "High Strength Low Alloy Steels", eds. D. P. Dunne and T. Chandra, *Proc. Int. Conf., Wollongong, Australia*, (1984), p.17.
51. T. Tanaka, N. Tabata, T. Hatomura and C. Shiga, "Microalloying 75", *Proc. Int. Symp. HSLA Steels*, Union Carbide Corporation, New York, (1977), p. 107.
52. H. Höfgen, G. Zouhar, F. Birnstock and J. Bathelt, 4th Int. Steel

References

- Rolling Conf., eds. B. Fazan et al., IRSID/ATS, Deauville, France, Vol. 1, (1987), p. B.2.1.
53. F. Hollander, "Mathematical Models for Metallurgical Process Development", Iron and Steel Inst. Conf., London, (1969), p. 46.
54. D. Partington and L. Talbot, "Hot Working and Forming Processes", eds. C. M. Sellars and G. J. Davies, The Metals Society, London, (1980), p. 176.
55. V.B. Ginzburg, Iron and Steel Engineer, 62, (1985), p. 21.
56. L. A. Leduc, Ph.D. Thesis, University of Sheffield, Sheffield, (1980).
57. R. A. Harding, Ph.D. Thesis, University of Sheffield, Sheffield, (1976).
58. N. Lambert and M. Economulus, JISI, 208, (1970), p. 917.
59. A. Sigalla, JISI, 186, (1957), p. 90.
60. Y. Sekimoto, Trans. ISIJ, 10, (1970), p. 341.
61. C. Devadas and I.V. Samarasekera, Ironmaking and Steelmaking, 13, (1986), p. 311.
62. C. David, C. Bertrand, P. Montmitonnet, J. L. Chenot and P. Buessler, 4th Int. Steel Rolling Conf., eds. B. Fazan et al., IRSID/ATS, Deauville, France, Vol. 2, (1987), p. F.10.1.
63. F. Seredynski, JISI, 211, (1973), p. 197.
64. P. G. Stevens, K. P. Ivens and P. Harper, JISI, 209, (1971), p. 1.
65. K. Murata, H. Morise, M. Mitsutsuka, H. Haito, T. Komatsu and S. Shida, Trans. JISI, 24 (9), (1984), p. B309.

References

66. E. Orowan, *Proc. Inst. Mech. Eng.*, 150, (1943), p. 140.
67. D. R. Bland and H. Ford, *JISI*, 171, (1962), p.245.
68. R. B. Sims, *Proc. Inst. Mech. Eng.*, 168, (1954), p. 191.
69. A. Nadai, "Plasticity", McGraw-Hill, New York , (1931), p. 221.
70. J. M. Alexander, *Proc. Royal Soc. Lond. A*, 326, (1972), p. 535.
71. L. G. M. Sparling, *Metals Tech.*, 4, (1977), p. 301.
72. A. K. E. H. A. El-Kalay and L. G. M. Sparling, *JISI*, 206, (1968), p. 152.
73. S. Lička, L. Zela, E. Piontek, M. Kosar and T. Prnka, *Proc. Int. Conf. Steel Rolling*, Vol. 2, *ISIJ*, Tokyo, (1980), p. 840.
74. Y. Saito, T. Enami and T. Tanaka, *Trans. ISIJ*, 25, (1985), p. 1146.
75. J. H. Hollomon, *Trans. AIME*, 162, (1945), p. 268.
76. P. Ludwik, *Elem. der Tech. Mech.*, ed. Julius Springer, Berlin, (1909), p. 32.
77. H. W. Swift, *J. Mech. Phys. Sol.*, 1, (1952), p. 1.
78. E. Voce, *J. Inst. Metals*, 74, (1948), p. 537.
79. H. Tamehiro, M. Murata and R. Habu, *Trans. ISIJ*, 27, (1987), p. 120.
80. A. Laasraoui, M.Sc. Thesis, Université Laval, Québec, (1987).
81. M.G. Akben, Ph.D. Thesis, McGill University, Montreal, (1980).
82. M.J. Luton, Ph.D. Thesis, McGill University, Montreal, (1971).

References

83. A.T. English and W.A. Backofen, *Trans. TMS-AIME*, 230, (1964), p. 396
84. G.S. Ansell and J. Weertman, *Trans. TMS-AIME*, 215, (1959), p. 835.
85. R. Kopp, M. M. De Souza and C. M. Rogall, 4th Int. Steel Rolling Conf., eds. B. Fazan et al., IRSID/ATS, Deauville, France, Vol. 2, (1987), p. F.15.1.
86. D. L. Baragar, Internal Report, MTL 89/25 (TR), CANMET, Energy, Mines and Resources, (1989).
87. M. Chaboud, A. Coolen, M. Jeanneau and M. Lafrance, *Proc. Int. Conf. Steel Rolling*, Vol. 2, ISIJ, Tokyo, (1980), p. 980.
88. H. Nordberg and B. Aronsson, *JISI*, 206, (1968), p. 1263.
89. M. Lamberigts and T. Greday, C.R.M. Publication No. 38, March, (1974)
90. B. Aronsson, *Proc. of Conf. on Steel Strengthening Mechanisms*, Zurich, Climax Molybdenum Comp., (1969), p. 77.
91. J. Cordea, *Symp. on Low Alloy High Strength Steels*, Nurnberg, BRD, Metallurg. Companies, (1970), p. 61.
92. K. J. Irvine, F. B. Pickering and T. Gladman, *JISI*, 205, (1967), p. 161.
93. W. Liu, Ph.D. Thesis, McGill University, Montreal, (1987).
94. L.T. Mavropoulos, Ph.D. Thesis, McGill University, Montreal, (1986).
95. A. Macchione, M.Eng. Thesis, McGill University, Montreal, (1985).
96. A.S. Rodriguez, M.Eng. Thesis, McGill University, Montreal, (1984).

References

97. D. L. Baragar, "Cam Plastometer: Operational States and Plans for Upgrading", Division Report, MPR/PMRL 82-55 (TR), CANMET, Energy, Mines and Resources, (1982).
98. M. J. Stewart, "Cam Plastometer Operation Manual Including Theory and Design", Division Report MBR R 282, CANMET, Energy, Mines and Resources, (1974).
99. J.P.A. Immarigeon, Ph.D. Thesis, McGill University, Montreal, (1974).
100. R.A. Petković, Ph.D. Thesis, McGill University, Montreal, (1975).
101. G.A. Wilber, J. R. Bell, J. H. Bucher and W. J. Childs, Trans. AIME, 242, (1968), p. 2305.
102. T.L. Capeletti, L. A. Jackman and W. J. Childs, Metall. Trans., 3, (1972), p. 789.
103. S. Yamamoto, C. Ouchi and T. Osaka, "Thermomechanical Processing of Microalloyed Austenite", eds. A. J. deArdo et al., AIME, Warrendale, Pa, USA, (1982), p. 613.
104. H.L. Andrade, M.G. Akben and J.J. Jonas, Metall. Trans., 14A, (1983), p. 1967.
105. D.R Barraclough and C.M. Sellars, Metal Sci., 13, (1979), p. 257.
106. G. E. Ruddle, K. S. Milliken, G. Smelsky and A.F. Crawley, Can. Metall. Quart, 22, (1983), p. 271.
107. Metals Handbook, Vol. 8, ASM, (1973).
108. H. Abrams, Metallography, 4, (1971), p. 59.
109. A. Van Neste and M.R. Krishnadev, Metallography, 9, (1976), p. 63.

References

110. G. G. Bach, "Numerical Analysis for Computer Users", Department of Mechanical Engineering, McGill University, (1982).
111. F. B. Hildebrand, "Introduction to Numerical Analysis", McGraw Hill, New York, (1956).
112. Y. Bergström, Mater. Sci. Eng., 9, (1972), p. 101.
113. O. Kwon, Ph.D. Thesis, University of Pittsburgh, Pittsburgh, (1985).
114. H. L. Andrade, M. Eng. thesis, McGill University, Montreal, (1982).
115. R. A. Petković, M. J. Luton and J. J. Jonas, Can. Metall. Quart., 14, (1975), p. 137.
116. D. L. Baragar, J. Mech. Work. Tech., 14, (1987), p. 295.
117. S. L. Semiatin and J. J. Jonas, "Formability and Workability of Metals", ASM, Metals Park, Ohio, (1984), p. 109.
118. F. Mucciardi, "Process Engineering Metallurgy", Department of Metallurgical Engineering, McGill University, Montreal, (1985).
119. L. T. Mavropoulos and J. J. Jonas, Can. Metall. Quart., 27, (1988), p. 235.
120. D. S. Wright and T. Sheppard, Metals Tech., 6, (1979), p. 224.
121. P. Choquet, A. LeBon, C. Rossard, C. Perdrix and G. Joannes, THERMEC-88, ed. I. Tamura, Vol. 2, ISIJ, Tokyo, (1988), p. 729.
122. R. Colás and C. M. Sellars, "Strength of Metals and Alloys", ICSMA 7, eds. H. J. McQueen et al., Vol. 2, Pergamon Press, Oxford, (1986), p. 941.

References

123. C. Teodosiu, V. Nicolae, E. Soós and C. G. Radu, *Rev. Roum. Sci. Tech.-Mech. Appl.*, 24, (1979), p. 13.
124. S. K. Samanta, *Int. J. Mech. Sci.*, Pergamon Press, 10, (1968), p. 613.
125. K. P. Rao and S. M. Doraivelu, *J. Mech. Work. Tech.*, 6, (1982), p. 63.
126. P. L. Charpentier, B. C. Stone, S. C. Ernst and J. F. Thomas, Jr., *Metall. Trans.*, 17A, (1986), p. 2227.
127. A. S. Korhonen and H. J. Kleemola, *Metall. Trans.*, 9A, (1978), p. 979.
128. P. Dadras and J. F. Thomas, Jr., *Metall. Trans.*, 12A, (1981), p. 1867.
129. N. D. Ryan and H. J. McQueen, *Czech. J. Phys.*, B39, (1989), p.458.
130. H. J. McQueen and N. D. Ryan, "Strength of Metals and Alloys", ICSMA 8, eds. P. O. Keppunen et al., Pergamon Press, Vol. 1, (1989), p. 1323.
131. U. F. Kocks, *J. Eng. Mat. Tech. ASME*, 98, (1976), p. 76.
132. P. Choquet, B. de Lamberterie, C. Perdrix, and H. Biauxser, 4th Int. Steel Rolling Conf., eds. B. Fazan et al., IRSID/ATS, Deauville, France, Vol. 1, (1987), p. B.5.1.
133. W. Roberts, "Deformation, Processing and Structure", ed. G. Krauss, ASM, Metals Park, OH, (1984), p. 109.
134. J. L. Uvira and J. J. Jonas, *Trans. Met. Soc. AIME*, 242, (1968), p. 1619.
135. H. J. Frost and M. F. Ashby, "Deformation-Mechanism Maps", *The Plasticity and Creep of Metals and Ceramics*, Pergamon Press, Oxford, (1982).

References

136. H. Luthy, A. K. Miller and O. D. Sherby, *Acta Metall.*, 28, (1980), p. 169.
137. N. D. Ryan and H. J. McQueen, *J. Mech. Work. Tech.*, 12, (1986), p. 323.
138. U. F. Kocks, A. S. Argon and M. F. Ashby, "Thermodynamics and Kinetics of Slip", *Progress in Materials Science*, Vol. 19, Pergamon Press, Oxford, (1975).
139. J.-P. A. Immarigeon and J. J. Jonas, *Acta Metall.*, 22, (1974), p. 1235.
140. J.-P. A. Immarigeon, Private Communication, (1989).
141. G. Ferron and M. Mliha-Touati, *Acta Metall.*, 35, (1987), p. 1281.
142. A. R. Oludaisi, Ph.D. Thesis, Stanford University, Stanford, CA, (1988).
143. D. J. Dever, *J. Appl. Phys.*, 43, (1972), p. 3293.
144. J. J. Jonas and M. L. Luton, *Scripta. Metall.*, 5, (1971), p. 935.
145. A. Yoshie, H. Morikawa and Y. Onoe, *Trans. ISIJ*, 27, (1987), p. 425.
146. K. P. Rao, *J. Mech. Work. Tech.*, 13, (1986), p. 83.
147. M. Mliha-Touati, Doctorat ès Sciences Physiques, Université de Poitiers, France, (1985).
148. D. R. Diercks and W. F. Burke, "Elevated Temperature Properties of Austenitic Stainless Steels", ed. A. O. Schaefer, ASME, (1974), p. 19.
149. A. Cingara, L. St. Germain and H. J. McQueen, "Processing, Microstructure and Properties of HSLA Steels", ed. A. J. deArdo, AIME, Warrendale, PA, (1988), p. 91.
150. S. B. Brown, Ph.D. Thesis, Mass. Inst. Tech., Cambridge, MA, (1987).

References

151. S. B. Brown, K. H. Kim and L. Anand, Report of Research in Mechanics of Materials, Department of Mechanical Engineering, Mass. Inst. Tech., Cambridge, MA, (1987).
152. Y. Bergström, Mater. Sci. Eng., , (1969/70), p. 193.
153. Y. Bergström and B. Aronsson, Metall. Trans., 3, (1972), p. 1951.
154. Y. Estrin and H. Mecking, Acta Metall., 32, (1984), p. 57.
155. J. R. Klepaczko and C. Y. Chiem, J. Mech. Phys. Solids, 34, (1986), p. 29.
156. G. Ferron, E. L. Ouakdi, J. R. Klepaczko and M. Mliha-Touati, "Constitutive Relations and their Physical Basis", eds. S. I. Andersen et al., RISØ National Laboratory, Roskilde, Denmark, (1987), p. 311.
157. J. R. Klepaczko, "Constitutive Relations and their Physical Basis", eds. S. I. Andersen et al., RISØ National Laboratory, Roskilde, Denmark, (1987), p. 387.
158. J. E. Bailey and P. B. Hirsch, Phil. Mag., 5, (1960), p. 485.
159. T. Senuma and H. Yada, "Annealing Processes-Recovery, Recrystallization and Grain Growth", eds. N. Hansen et al., RISØ National Laboratory, Roskilde, Denmark, (1986), p. 547.
160. J. R. Klepaczko, Private Communication, (1989).
161. C. Perdrix, "Caractéristiques d'Écoulement Plastique du Métal dans les Conditions du T. A. B. à Chaud", IRSID, Recherche CECA N°. 7210-EA-311, (1987).
162. W. B. Morrison, Metall. Trans., 2A, (1971), p. 331.

References

163. E. W. Hart, *Acta Metall.*, 18, (1970), p. 599.
164. N. Christodoulou, Ph.D. Thesis, McGill University, Montreal, (1982).
165. N. Christodoulou and J. J. Jonas, *Acta Metall.*, 32, (1984), p. 1655.
166. E. W. Hart, C. Y. Li, H. Yamada and G. L. Wire, "Phenomenological Theory; A Guide to Constitutive Equations in Plasticity", ed. A. S. Argon, MIT Press, Cambridge, MA, (1975).
167. W. Roberts, "Strength of Metals and Alloys", ICSMA 7, eds. H. J. McQueen et al., Vol. 3, Pergamon Press, Oxford, (1986), p. 1859.
168. C. M. Sellars and J. A. Whiteman, *Metal. Sci.*, 13, (1979), p. 187.
169. M. J. Luton, R. A. Petković and J. J. Jonas, *Acta Metall.*, 28, (1979), p. 729.
170. A. Streißelberger, R. Kaspar and O. Pawelski, *Metall. Trans.*, 16A, (1985), p. 67.
171. E. A. Simielli, Ph.D. Thesis, McGill University, Montreal, (1990).
172. E. Ruibal, J. J. Urcola and M. Fuentes, *Z. Metallkde*, 76, (1985), p. 568.
173. T. Sakai, M. Ohashi and K. Chiba and J. J. Jonas, *Acta Metall.* 36, (1988), p. 1781.
174. T. Sakai, M. Ohashi and K. Chiba, "Annealing Processes-Recovery, Recrystallization and Grain Growth", eds. N. Hansen et al., RISØ National Laboratory, Roskilde, Denmark, (1986), p. 535.
175. P. Choquet, A. LeBon and C. Perdrix, "Strength of Metals and Alloys", ICSMA 7, eds. H. J. McQueen et al., Vol. 3, Pergamon Press, Oxford, (1986), p. 1025.

References

176. B. Migaud, "Hot Working and Forming Processes", eds. C. M. Sellars and G. J. Davies, The Metals Society, London, (1980), p. 67.
177. W. B. Morrison, JISI, 210, (1972), p. 618.
178. M. Avrami, J. Chem. Phys., 7, (1939), p. 1103.
179. C. M. Sellars, Private Communication, (1989).
180. A. Sandberg and R. Sandström, Mater. Sci. Tech, 2, (1986), p. 917.
181. A. Sandberg and R. Sandström, Mater. Sci. Tech, 2, (1986), p. 926.
182. W. Roberts, A. Sandberg, T. Siwecki and T. Werlefors, "HSLA Steels: Technology and Applications", Proc. Int. Conf., Philadelphia, ASM, (1984), p. 67
183. E. Anelli, M. Gherzi, A. Mascanzoni, M. Paolicchi, A. Aprile, F. Granato, G. Liguori and G. Rizzo, " HSLA Steels: Metallurgy and Applications", eds. J. M. Gray et al., The Chinese Society of Metals, ASM, (1986), p. 693.
184. E. Anelli, M. Gherzi, A. Mascanzoni and M. Paolicchi, Final Report ECSC Agreement, N° 7210-EA/410, (1984).
185. X. L. He, Y. Y. Chu and J. J. Jonas, Acta Metall, 37, 1989, p. 2905.
186. L. T. Mavropoulos and J. J. Jonas, Can Metall. Quart., 28, (1989), p. 159.
187. T. Abe, M. Kurihara and H. Tagawa, Trans. ISIJ, 27, (1987), p. 479.
188. S. Yamamoto, T. Sakiyama and C. Ouchi, Trans. ISIJ, 27, (1987), p. 447.
189. M. G. Akben, I. Weiss and J. J. Jonas, Acta Metall., 29, (1981), p. 111.

References

190. P. D. Hodgson, J. A. Szalla and P. J. Campbell, 4th Int. Steel Rolling Conf., eds. B. Fazan et al., IRSID/ATS, Deauville, France, Vol. 1, (1987), p. C.8.1.
191. C. McCulloch, A. Kumar, E. B. Hawbolt and I. V. Samarasekera, "Steel Product-Process Integration", ed. J. D. Boyd, CIM, Halifax, (1989), p. 216.
192. C. Devadas, Ph. D. Thesis, University of British Colombia, British Colombia, (1989).
193. O. Pawelski, Archiv für das Eisenhüttenwesen, cruppe C, Nr. 809, (1969), p. 821.
194. J. Szalla, P. Stone and G. Glover, 28th Mech. Work. Steel Process. Conf. Proc., ISS, Toronto, Vol. XXV, (1987), p. 87.
195. C. Devadas, I. V. Samarasekera and E. B. Hawbolt, "Steel Product-Process Integration", ed. J. D. Boyd, CIM, Halifax, (1989), p. 168.
196. M. J. Brown and F. Mucciardi, "Computer Software in Chemical and Extractive Metallurgy", eds. W. T. Thompson et al., CIM, Pergamon Press, New York, Vol. 11, (1988), p. 179.
197. H. Ford and J. M. Alexander, J. Inst. Metals, 92, (1963/64), p. 397.
198. C. M. Sellars, "Annealing Processes-Recovery, Recrystallization and Grain Growth", eds. N. Hansen et al., RISØ National Laboratory, Roskilde, Denmark, (1986), p. 167.
199. C. M. Sellars, AGARD -LS- 137, North Atlantic Treaty Organization, Neuilly-sur-Seine, (1984), p. 10-1

References

200. C. M. Sellars, "Thermomechanical Processing of Steel", Short course organized by Technexus Int. Corp. Tech. Transf. to the Steel Indus., Hamilton, Sept. 25-28, (1989).
201. B. L. Bramfitt and J. G. Speer, 31st Mech. Work. Steel Process. Conf. Proc, ISS, Chicago, (1989), in press.
202. L. R. Cutler, Ph. D. Thesis, Université Laval, Québec, (1984).
203. F. B. Pickering, "Transformation and Hardenability in Steels", Climax Molybdenum Comp. Symposium, Ann Arbor, (1967), p. 109.
204. T. Surek, M. J. Luton and J. J. Jonas, Phys. Stat. Sol., 57, (1973), p. 647.

APPENDIX A

Derivation of the Expression for
the Activation Free Energy

If $\dot{\epsilon}_0$ is assumed to be constant, and if we further assume that ΔG has the following form, as suggested by Kocks et al.[138]:

$$\frac{\Delta G}{\mu} = f\left(\frac{\sigma}{\mu}\right) \quad (A.1)$$

from the definitions of the activation entropy and volume, we have:

$$\Delta S = - \left. \frac{\partial \Delta G}{\partial T} \right|_{\sigma} = - \left. \frac{d\mu}{dT} f\left(\frac{\sigma}{\mu}\right) - \mu \frac{\partial f\left(\frac{\sigma}{\mu}\right)}{\partial T} \right|_{\sigma} = \left. \frac{d\mu}{dT} f\left(\frac{\sigma}{\mu}\right) - \mu \frac{df\left(\frac{\sigma}{\mu}\right)}{d\left(\frac{\sigma}{\mu}\right)} \cdot \frac{\partial\left(\frac{\sigma}{\mu}\right)}{\partial T} \right|_{\sigma} \quad (A.2)$$

$$V = - \left. \frac{\partial \Delta G}{\partial \tau} \right|_T = \frac{df\left(\frac{\sigma}{\mu}\right)}{d\left(\frac{\sigma}{\mu}\right)} \quad (A.3)$$

The activation free energy is also given by:

$$\Delta G = \Delta H - T\Delta S \quad (A.4)$$

Introducing Eqs. A.1, A.2 and A.3 into Eq. A.4 we have, after rearrangement:

$$\Delta G = \frac{\Delta H + V\sigma \frac{d\ln(\mu)}{d\ln(T)}}{1 - \frac{d\ln(\mu)}{d\ln(T)}} \quad (A.5)$$

The apparent activation enthalpy Q and volume V_{app} can be expressed in terms of ΔH and V by differentiating Eq. 6.15:

Appendix A

$$Q = -k_B \left. \frac{\partial \ln(\epsilon)}{\partial (1/T)} \right|_{\sigma} = k_B T \left. \frac{\partial \ln(\epsilon_o)}{\partial \ln(T)} \right|_{\sigma} + \Delta H \quad (\text{A.6})$$

$$V_{app} = \left. \frac{2k_B T}{\sigma} \frac{\partial \ln(\epsilon)}{\partial \ln(\sigma)} \right|_T = \left. \frac{2k_B T}{\sigma} \frac{\partial \ln(\epsilon_o)}{\partial \ln(\sigma)} \right|_T + V \quad (\text{A.7})$$

If ϵ_o is constant, Q is equal to ΔH and V_{app} is equal to V , according to the above two equations. In this case, ΔG is given by:

$$\Delta G = \frac{Q + V_{app} \sigma \frac{d \ln(\mu)}{d \ln(T)}}{1 - \frac{d \ln(\mu)}{d \ln(T)}} \quad (\text{A.8})$$

In the above equation, all the terms can be evaluated experimentally or are known.

If ϵ_o is assumed to be a function of σ/μ only, the following form suggested by Surek et al. [204] can be used:

$$\epsilon_o = k_{\epsilon} \left(\frac{\sigma}{\mu} \right)^{m_o} \quad (\text{A.9})$$

where k_{ϵ} and m_o are constants. In such a case, by expanding Q in terms of the independent parameters σ/μ and T , we again end-up with the above relation for ΔG (Eq. A.8). Thus, the two alternative conditions concerning ϵ_o , i.e., ϵ_o constant or a function of σ/μ only, yield the same expression for ΔG .

APPENDIX B Derivation of the Expression for the Dislocation Density During Deformation

Since work hardening and dynamic recovery proceed simultaneously during deformation, the change in dislocation density, ρ , can be expressed using the following differential equation:

$$d\rho = \frac{\partial \rho}{\partial \epsilon} d\epsilon + \frac{\partial \rho}{\partial t} dt \quad (\text{B.1})$$

The term $\partial \rho / \partial \epsilon$ is assumed to be constant [145] and set equal to K_1 . If the rate of dynamic recovery is taken to be of first order and expressed as:

$$\frac{\partial \rho}{\partial t} = -K_2 \rho \quad (\text{B.2})$$

where K_2 is constant at a given temperature and strain rate, then from Eq. B.1:

$$d\rho = K_1 d\epsilon - K_2 \rho dt \quad (\text{B.3})$$

or:

$$\frac{\partial \rho}{\partial \epsilon} = K_1 - \frac{K_2}{\dot{\epsilon}} \rho \quad \Rightarrow \quad \frac{\partial \rho}{\partial \epsilon} + \left(\frac{K_2}{\dot{\epsilon}} \right) \rho = K_1 \quad (\text{B.4})$$

Eq. B.4 is a first order differential equation which has the following solution:

$$\rho = \rho_0 e^{-K_3 \epsilon} + \frac{K_1}{K_3} (1 - e^{-K_3 \epsilon}) \quad (\text{B.5})$$

where ρ_0 is ρ at $\epsilon=0$ and $K_3 = K_2 / \dot{\epsilon}$. Eq. B.5 is similar to Eq. 6.22 derived by Bergström.

Appendix C

APPENDIX C Listings of the Programs Used for the Analysis of the Stress/Strain Curves and for Correction for Adiabatic Heating

```

1000 !
      *****
1010 !                               NONLINFIT
1020 !
1030 ! This program calculates the constants in the following equation:
1040 !                                $\sigma = [\sigma_{SS}^2 + (\sigma_0^2 - \sigma_{SS}^2) e^{-\Omega \epsilon}]^{0.5}$ 
1050 ! using a least square fit of the stress/strain data.
1060 ! It also plots the  $\sigma$ - $\epsilon$ ,  $\ln \sigma$ - $\ln \epsilon$ ,  $d\sigma/d\epsilon$ - $\sigma$  and  $d \ln \sigma / d \epsilon$ - $\sigma$  diagrams.
1070 !
1080 !
1090 !
      *****

1100
1110 OPEN #1: PRINTER
1120 DIM E(500), S(500), K(500), YF(500), WH(500), MSE(500), MSS(500)
1130 DIM EXPVAL(500), FITVAL(500), INTRCPT(500), XREG(500),
      YREG(500), CS1(500)
1140 DIM BE(500), RFCT(50), BNFCT(50), ANFCT(50), SGM2FCT(50),
      YFBEST(500)
1150 DIM RSLP(100), BETA(100), WHO(100), R1LOG(100), EN1(100),
      KEY1(100), EN2(100)
1160 DIM KEY2(100), R2LOG(100)
1170
1180 SET MODE "80"
1190
1200 !***** Information inputs *****
1210
1220 PRINT "INPUT NAME OF FILE"
1230 INPUT N$
1240 PRINT "DOES THE CURVE BEGIN AT ZERO STRAIN?(Y/N)"
1250 INPUT Z$
1260   IF Z$ = "N" THEN
1270     PRINT "INPUT THE STRAIN BY WHICH THE CURVE MUST
      BE TRANSLATED"
1280     INPUT ETRANS
1290   END IF
1300 PRINT "DO YOU WANT TO CORRECT FOR THE COMPLIANCE OF
      THE MACHINE?"
1310 INPUT ZCPL$
1320 PRINT "DO YOU WANT TO PRINT THE RESULTS?(Y/N)"
1330 INPUT ZPR$
1340
1350 !***** Reading data file *****

```

Appendix C

```

1360
1370 PRINT "LEVEL","T.STRAIN","T.STRESS"
1380 OPEN #2:NAME N$&"DAT",ORGANIZATION TEXT
1390 LET L0=11.9
1400 LET D0=7.9
1410 LET A0=PI*(D0)^2/4
1420 LET I=1
1430 DO WHILE MORE #2
1440 INPUT #2:AA$
1450 LET A$=AA$[17:22]
1460 LET B$=AA$[26:31]
1470 LET E(I)=VAL(A$)
1480 IF Z$="N" THEN LET E(I)=E(I)-ETTRANS
1490 LET S(I)=VAL(B$)
1500 IF ZCPL$="N" THEN 1660
1510
1520 !***** Correction for the compliance of the machine *****
1530
1540 LET L1=L0*EXP(-E(I))
1550 LET CS1(I)=2047*(L1-L0)/10
1560 LET BE(I)=-S(I)*2.2046*A0*2047*L0*4.4482/9.81/L1/25/1000
1570 LET LOAD=ABS(BE(I))*24.525/2047
1580 LET LOAD1=6.58960E-05*LOAD^2-.0164243*LOAD
1590 LET LOAD2=CS1(I)*10/2047
1600 LET LOAD3=L0+LOAD2-LOAD1
1610 LET E(I)=-LOG(LOAD3/L0)
1620 LET S(I)=1000*LOAD*LOAD3/A0/L0
1630 IF I>2 THEN
1640 IF S(I)-S(I-1)<-2 THEN GOTO 1680
1650 END IF
1660 PRINT I,E(I),S(I)
1670 LET I=I+1
1680 LOOP
1690 CLOSE #2
1700 LET IMAX=I-1
1710 PRINT TAB(1);"THE TOTAL STRAIN IS";TAB(22);E(IMAX)
1720 PRINT "INPUT THE STRAIN TO USE IN CALCULATION"
1730 INPUT EF
1740
1750 !***** Estimation of the saturation stress *****
1760 ! from the  $d\sigma/d\varepsilon$ - $\sigma$  diagram
1770
1780 FOR L=1 TO 5
1790 PRINT ""
1800 NEXT L
1810 PRINT "*****"
1820 PRINT " WAIT "
1830 PRINT "*****"
1840 FOR NMBMX=1 TO 100
1850 IF E(NMBMX)>=.01 THEN 1870
1860 NEXT NMBMX
1870 LET I01=NMBMX
1880
1890 FOR NMBTOT=1 TO 500

```


Appendix C

```

1900      IF E(NMBTOT) >= EF THEN 1920
1910      NEXT NMBTOT
1920      LET ITOT = NMBTOT
1930      /*****
1940      PRINT " "
1950      LET NRG = 4
1960      LET NH = INT(ITOT/NRG)
1970      LET NH1 = NH - 1
1980      LET I = 1
1990      LET COMPT = 0
2000      LET SE = 0
2010      LET SS = 0
2020      LET SES = 0
2030      LET SE2 = 0
2040      LET JMAX = I + NH1
2050      IF I + NH1 > ITOT THEN
2060          LET JMAX = ITOT
2070          LET COMPT = COMPT + 1
2080      END IF
2090
2100      FOR J = I TO JMAX
2110          LET SE = SE + E(J)
2120          LET SS = SS + S(J)
2130          LET SES = SES + E(J)*S(J)
2140          LET SE2 = SE2 + E(J)^2
2150      NEXT J
2160      IF I + NH1 > ITOT THEN
2170          LET MSE(I) = SE/(NH - COMPT)
2180          LET MSS(I) = SS/(NH - COMPT)
2190          LET WH(I) = (SES - (NH - COMPT)*MSE(I)*MSS(I))/(SE2 - (NH -
COMPT)*(MSE(I)^2))
2200          GOTO 2260
2210      END IF
2220
2230      LET MSE(I) = SE/NH
2240      LET MSS(I) = SS/NH
2250      LET WH(I) = (SES - NH*MSE(I)*MSS(I))/(SE2 - NH*(MSE(I)^2))
2260      LET INTRCPT(I) = MSS(I) - WH(I)*MSE(I)
2270
2280      LET IRI = I
2290      LET IRF = JMAX
2300      FOR LR = IRI TO IRF
2310          LET EXPVAL(LR) = S(LR)
2320          LET FITVAL(LR) = INTRCPT(I) + WH(I)*E(LR)
2330      NEXT LR
2340      GOSUB 7300
2350      PRINT I, ITOT, WH(I), MSS(I), R
2360
2370      IF I > ITOT - INT(NH/2) THEN 2400
2380      LET I = I + 1
2390      GOTO 2000
2400      LET IHMAX = I
2410
2420      /*****

```

Appendix C

```

2430 LET NB0=10
2440 LET RBEST=0
2450 FOR NB=NB0-5 TO NB0+20
2460   LET REGI=NB
2470   LET REGF=IHMAX
2480   FOR I=REGI TO IHMAX
2490     LET XREG(I)=MSS(I)
2500     LET YREG(I)=WH(I)
2510   NEXT I
2520   GOSUB 7130
2530   LET BETA(NB)=SLP
2540   LET WH0(NB)=INTERCEPT
2550
2560   LET IRI=REGI
2570   LET IRF=REGF
2580   FOR LR=IRI TO IRF
2590     LET EXPVAL(LR)=WH(LR)
2600     LET FITVAL(LR)=WH0(NB)+BETA(NB)*MSS(LR)
2610   NEXT LR
2620   GOSUB 7300
2630   LET RSLP(NB)=R
2640   IF (RSLP(NB)<>1 AND RBEST<RSLP(NB)) THEN
2650     LET RBEST=RSLP(NB)
2660     LET WHOBEST=WH0(NB)
2670     LET BETABEST=BETA(NB)
2680   END IF
2690 NEXT NB
2700 !*****
2710
2720 OPEN #5:SCREEN .35,1,0,1
2730 CLEAR
2740 SET WINDOW 0,300,0,3000
2750 SET MODE "HIRES"
2760 PLOT TEXT,AT 150,1500: "W.H. vs S"
2770 BOX LINES 0,300,0,3000
2780 FOR I=1 TO IHMAX
2790   PLOT POINTS:MSS(I),WH(I)
2800 NEXT I
2810 FOR X=0 TO S(ITOT)+100 STEP 1
2820   PLOT POINTS:X,WH0BEST+BETABEST*X
2830 NEXT X
2840 CLOSE #5
2850 OPEN #7: SCREEN 0,.34,0,.5
2860 SET WINDOW 0,.8,0,WH(2)/MSS(2)
2870 BOX LINES 0,.8,0,WH(2)/MSS(2)
2880 FOR I=1 TO IHMAX
2890   PLOT POINTS: MSE(I),WH(I)/MSS(I)
2900 NEXT I
2910 CLOSE #7
2920 OPEN #6:SCREEN 0,.3,.51,1
2930 PRINT "S(WH=0)","R "
2940 PRINT -WH0BEST/BETABEST,RBEST
2950
2960 PRINT #1:NB,-WH0BEST/BETABEST,RBEST

```

Appendix C

```

2970 PRINT ""
2980 PRINT "IS IT OK?"
2990 INPUT SL$
3000 IF SL$="Y" THEN
3010 LET SATS=-WHOBEST/BETABEST
3020 GOTO 3070
3030 END IF
3040 INPUT NB0
3050 CLOSE #6
3060 GOTO 2440
3070 CLOSE #6
3080 CLEAR
3090 OPEN #2: SCREEN 0,1,0,1
3100 SET MODE "80"
3110
3120 !*****
3130
3140 PRINT "THE ITERATION STARTS, THE TIME
IS: ";TAB(36);TIME$
3150
3160
3170 !*****
3180
3190 PRINT TAB(1);"THE STRAIN USED IN THE FITTING IS";
TAB(42); E(ITOT)
3200
3210 LET ISTART0=1
3220 LET SIGMA2=((1.68*9.81*1.E-4)^2)*1.E8
3230 PRINT ""
3240 FOR ISTART=1 TO IO1
3250 IF E(ISTART)<0 THEN
3260 LET ISTART0=ISTART+1
3270 GOTO 3920
3280 END IF
3290 PRINT ISTART0
3300 LET MM=ISTART
3310 LET NN=ITOT+1
3320 LET ISATM=2
3330 FOR ISAT=1 TO ISATM
3340 LET E(NN+ISAT)=2*E(ITOT)
3350 LET S(NN+ISAT)=SATS
3360 NEXT ISAT
3370
3380
3390 !***** The secant method is used for the iteration *****
3400
3410 FOR B=1 TO 20 STEP 1
3420 GOSUB 6850
3430 IF F>0 THEN 3450
3440 NEXT B
3450 LET B1=B
3460 LET B=B1
3470 GOSUB 6850
3480 LET F1=F

```

Appendix C

```

3490 LET B2=1.1*B1
3500 LET B=B2
3510 GOSUB 6850
3520 LET F2=F
3530 FOR N=1 TO 20
3540 LET BN=(B1*F2-B2*F1)/(F2-F1)
3550
3560 LET B=BN
3570 GOSUB 6850
3580 LET FN=F
3590 LET AN=A
3600 IF ABS(FN) < 1E-8 THEN GOTO 3660
3610 LET B1=B2
3620 LET B2=BN
3630 LET F1=F2
3640 LET F2=FN
3650 NEXT N
3660
3670 LET CN=SIGMA2-AN
3680 FOR IFIT=MM TO NN
3690 IF AN+CN*EXP(-BN*E(IFIT)) < 0 THEN 3920
3700 LET YF(IFIT)=(AN+CN*EXP(-BN*E(IFIT)))^.5
3710 NEXT IFIT
3720
3730 !***** Computing the correlation coefficients *****
3740
3750 LET IRI=MM
3760 LET IRF=NN
3770 FOR IR=IRI TO IRF
3780 LET EXPVAL(IR)=S(IR)
3790 LET FITVAL(IR)=YF(IR)
3800 NEXT IR
3810 GOSUB 7300
3820 LET RFCT(MM)=R
3830
3840 LET ANFCT(MM)=AN
3850 LET BNFCT(MM)=BN
3860 IF E(ITOT) > .4 THEN
3870 LET EEXTRPL=1.5*E(ITOT)
3880 GOTO 3910
3890 END IF
3900 LET EEXTRPL=2*E(ITOT)
3910 PRINT TAB(1);SIGMA2;TAB(10);AN*BN;TAB(20);BN;TAB(30);
E(ISTART);TAB(45);MM;TAB(50);NN;TAB(55);(AN+CN*EXP(-
BN*EEXTRPL))^.5;TAB(65);RFCT(MM)
3920 NEXT ISTART
3930
3940 PRINT "THE ITERATION IS FINISHED:";TAB(36);TIME$
3950 PRINT ""
3960
3970 !*****
3980
3990 LET RMAX=0
4000 FOR IMM=ISTARTO TO MM

```

Appendix C

```

4010     IF RMAX < RFCT(IMM) THEN
4020         LET RMAX = RFCT(IMM)
4030         LET STRNSTART = E(IMM)
4040         LET ANBEST = ANFCT(IMM)
4050         LET BNBEST = BNFCT(IMM)
4060     END IF
4070     NEXT IMM
4080     LET CNBEST = SIGMA2 - ANBEST
4090     PRINT
4100     IF CNBEST / (SATS ^ 2 - ANBEST) <= 0 THEN GOTO 4120
4110     LET SATE = (LOG(CNBEST / (SATS ^ 2 - ANBEST))) / BNBEST
4120     PRINT "DO YOU WANT THE FITTED DATA ?"
4130     INPUT Z$
4140     IF Z$ <> "Y" THEN GOTO 4220
4150     PRINT " "
4160     PRINT "LEVEL", "EPSLN.", "SIGMA.EXCT.", "SIGMA.FIT.", "ER.*
100/S. EXT"
4170     FOR I = 1 TO NN
4180         LET YFBEST(I) = (ANBEST + CNBEST * EXP(-
BNBEST * E(I))) ^ .5
4190         IF S(I) = 0 THEN GOTO 4210
4200         PRINT I, E(I), S(I), YFBEST(I), (S(I) - YFBEST(I)) * 100 / S(I)
4210     NEXT I
4220     PRINT
4230
4240     !*****
4250
4260     PRINT "-----"
4270     PRINT TAB(30); N$
4280     PRINT TAB(1); "E1"; TAB(18); "Ef"; TAB(30); "S02"; TAB(40); "Omega";
TAB(50); "α2(U)"; TAB(60); "R2"
4290     PRINT
TAB(1); STRNSTART; TAB(16); E(ITOT); TAB(27); SIGMA2; TAB(37);
BNBEST; TAB(47); BNBEST * ANBEST; TAB(57); RMAX
4300     PRINT "-----"
4310     PRINT ""
4320
4330     !*****
4340
4350     PRINT "-----"
4360     LET SECTRPL = (ANBEST + CNBEST * EXP(-
BNBEST * EEXTRPL)) ^ .5
4370     PRINT
TAB(1); "Exp.Strn"; TAB(15); "Exp.Strs"; TAB(40); "Sat.Strn"; TAB(55);
"Sat.Strs"
4380     PRINT ""
4390     PRINT
TAB(1); EEXTRPL; TAB(15); SECTRPL; TAB(40); SATE; TAB(55); SA
TS
4400     PRINT "-----"
4410     PRINT ""
4420
4430     !*****
4440

```

Appendix C

```

4450 PRINT "DO YOU WANT TO HAVE THE MEAN STRESS AT A
SPECIFIC STRAIN?"
4460 INPUT Z$
4470 IF Z$ <> "Y" THEN 4830
4480 PRINT TAB(1); "INPUT STRAIN, THIS MUST NOT BE HIGHER
THAN"; TAB(44); E(IMAX)
4490 INPUT STR
4500 FOR I=1 TO IMAX
4510     IF E(I) >= STR THEN 4520
4520 NEXT I
4530 LET ISTR=I
4540 LET AREA=0
4550 FOR I=2 TO ISTR
4560     LET AREA=AREA+(E(I)-E(I-1))*(S(I)+S(I-1))/2
4570 NEXT I
4580 LET MS=AREA/STR
4590 PRINT TAB(1); "THE MEAN STRESS IN (MPa) AT"; TAB(30); STR;
TAB(40); MS
4600
4610 LET STRF=STR
4620 LET H=STRF/10
4630 LET XS=0
4640 LET S4=0
4650 LET S2=0
4660 FOR K1=1 TO 5
4670     LET XS=XS+H
4680     LET S4=S4+(ANBEST+CNBEST*EXP(-BNBEST*XS))^.5
4690     LET XS=XS+H
4700     LET S2=S2+(ANBEST+CNBEST*EXP(-BNBEST*XS))^.5
4710 NEXT K1
4720 LET ISIM=(4*S4+2*S2-(ANBEST+CNBEST*EXP(-BNBEST*
STRF))^.5)*H/3
4730 LET MSF=ISIM/STRF
4740
4750 PRINT "THE FITTED MEAN STRESS IS: ", MSF
4760 PRINT "DO YOU WANT TO HAVE A FITTED MEAN STRESS AT
ANOTHER STRAIN?"
4770 INPUT Z$
4780 IF Z$ <> "Y" THEN 4830
4790 PRINT "INPUT STRAIN?"
4800 INPUT STR2
4810 LET STRF=STR2
4820 GOTO 4620
4830
4840 !***** Estimation of the exponent in Hollomon equation *****
4850
4860 LET NN0=MM+9
4870 LET R1LOGBEST=0
4880 FOR NN1=NN0-5 TO NN0+20
4890     LET REGI=MM
4900     LET REGF=NN1
4910
4920     FOR J=MM TO NN1
4930         LET XREG(J)=LOG(E(J))

```

Appendix C

```

4940      LET YREG(J)=LOG(S(J))
4950  NEXT J
4960      GOSUB 7130
4970      LET EN1(NN1)=SLP
4980      LET KEY1(NN1)=INTERCEPT
4990      LET IRI=REGI
5000      LET IRF=REGF
5010      FOR LR=IRI TO IRF
5020          LET EXPVAL(LR)=LOG(S(LR))
5030          LET
              FITVAL(LR)=KEY1(NN1)+EN1(NN1)*LOG(E(LR))
5040  NEXT LR
5050      GOSUB 7300
5060      LET R1LOG(NN1)=R
5070      IF R1LOGBEST<R1LOG(NN1) THEN
5080          LET R1LOGBEST=R1LOG(NN1)
5090          LET EN1BEST=EN1(NN1)
5100          LET KEY1BEST=KEY1(NN1)
5110          LET IBREAK1=NN1
5120      END IF
5130  NEXT NN1
5140
5150  PRINT
5160      LET R2LOGBEST=0
5170      FOR NN2=NN0 TO NN0+20
5180          LET REGI=NN2
5190          LET REGF=ITOT
5200
5210          FOR J=NN2 TO ITOT
5220              LET XREG(J)=LOG(E(J))
5230              LET YREG(J)=LOG(S(J))
5240          NEXT J
5250          GOSUB 7130
5260          LET EN2(NN2)=SLP
5270          LET KEY2(NN2)=INTERCEPT
5280          LET IRI=REGI
5290          LET IRF=REGF
5300          FOR LR=IRI TO IRF
5310              LET EXPVAL(LR)=LOG(S(LR))
5320              LET
                  FITVAL(LR)=KEY2(NN2)+EN2(NN2)*LOG(E(LR))
5330          NEXT LR
5340          GOSUB 7300
5350          LET R2LOG(NN2)=R
5360          IF R2LOGBEST<R2LOG(NN2) THEN
5370              LET R2LOGBEST=R2LOG(NN2)
5380              LET EN2BEST=EN2(NN2)
5390              LET KEY2BEST=KEY2(NN2)
5400              LET IBREAK2=NN2
5410          END IF
5420      NEXT NN2
5430      LET IBREAK=MIN(IBREAK1,IBREAK2)
5440
5450  PRINT "-----"

```

Appendix C

```

5460
5470 PRINT TAB(1);"n1";TAB(13);"R1";TAB(33);"n2";TAB(43);"R2"
5480 PRINT ""
5490 PRINT
      TAB(1);EN1BEST;TAB(10);R1LOGBEST;TAB(30);EN2BEST;TAB(4
      0);R2LOGBEST
5500 PRINT ""
5510 PRINT TAB(1);"USING HOLLOMON AT ";TAB(28);EEXTRPL;
      TAB(40);"THE EXTRAPOLATED STRESS IS:";TAB(67);
      EXP(KEY2BEST)*EEXTRPL^EN2BEST
5520 PRINT "-----"
5530 IF ZPR$="Y" THEN 5560
5540 GOTO 5770
5550
5560 !
      *****
5570
5580 PRINT #1: "-----"
5590 PRINT #1: TAB(30);N$
5600 PRINT #1: ""
5610 PRINT #1:
      TAB(5);"Ei";TAB(19);"Ef";TAB(30);"S02";TAB(40);"Omega";TAB(50
      );"a2(U)";TAB(60);"Cor. Coef"
5620 PRINT #1: ""
5630 PRINT #1: TAB(1);STRNSTART;TAB(15);E(ITOT);TAB(28);
      SIGMA2;
      TAB(38);BNBEST;TAB(48);BNBEST*ANBEST;TAB(58);RMAX
5640 PRINT #1: "-----"
5650 PRINT #1: "-----"
5660 PRINT #1:
      TAB(1);"Exp.Strn";TAB(15);"Exp.Strs";TAB(30);"Sat.Strs";TAB(45);"
      Sat.Strn"
5670 PRINT #1: ""
5680 PRINT #1:
      TAB(1);EEXTRPL;TAB(15);SEXTRPL;TAB(30);SATE;TAB(45);SA
      TS
5690 PRINT #1: "-----"
5700 PRINT #1: "-----"
5710 PRINT #1: "n1","R1","n2","R2"
5720 PRINT #1: EN1BEST,R1LOGBEST,EN2BEST,R2LOGBEST
5730 PRINT #1: "-----"
5740 PRINT #1: ""
5750
5760
5770
      !*****
5780
5790 PRINT "DO YOU WANT TO HAVE A LOG-LOG & WH.VS STRESS
      PLOTS?"
5800 INPUT Z$
5810 IF Z$ <> "Y" THEN 6820
5820
5830 !***** Log Stress vs Log Strain *****
5840

```


Appendix C

```

5850 OPEN #3: SCREEN 0,,5,,51,1
5860
5870 SET WINDOW LOG(E(MM)),LOG(E(ITOT)),LOG(S(MM))-.3,
    LOG(S(ITOT)) +.3
5880 SET MODE "HIRES"
5890 PLOT TEXT, AT 10*LOG(E(ITOT)),LOG(S(ITOT)/3): "Log(S) vs
    Log(E)"
5900 BOX LINES
    LOG(E(MM)),LOG(E(ITOT)),LOG(S(MM))-.3,LOG(S(ITOT)) +.3
5910
5920 FOR I=MM TO NN
5930     IF E(I) <=0 THEN GOTO 5950
5940     PLOT POINTS: LOG(E(I)),LOG(S(I))
5950 NEXT I
5960
5970 PLOT TEXT, AT (LOG(E(ITOT)))*4,LOG(S(ITOT)/2):
    USING$("###.###",EN1BEST)
5980 PLOT TEXT, AT (LOG(E(ITOT)))*2,LOG(S(ITOT)/1.5):
    USING$("###.###",EN2BEST)
5990     FOR X=LOG(E(MM)) TO LOG(E(IBREAK2)) STEP
        LOG(E(IBREAK2)/E(MM))/100
6000         PLOT POINTS :X,EN1BEST*X+KEY1BEST
6010     NEXT X
6020     FOR X=LOG(E(IBREAK1)) TO LOG(E(ITOT)) STEP
        LOG(E(ITOT)/E(IBREAK1))/100
6030         PLOT POINTS :X,EN2BEST*X+KEY2BEST
6040     NEXT X
6050
6060 !***** Stress vs Strain *****
6070
6080 OPEN #4: SCREEN 0,,5,0,,5
6090
6100 SET WINDOW -.005,1.25*E(IMAX),0,S(IMAX)+50
6110 PLOT TEXT, AT .74*E(IMAX),S(IMAX)/2:"S vs E"
6120 BOX LINES -.005,1.25*E(IMAX),0,S(IMAX)+50
6130
6140 FOR I=1 TO IMAX
6150     PLOT POINTS: E(I),S(I)
6160 NEXT I
6170
6180 FOR X=0 TO 1.25*E(IMAX) STEP .005
6190     PLOT POINTS:X,(ANBEST+CNBEST*EXP(-BNBEST*X))^.5
6200 NEXT X
6210
6220
6230 !***** Work Hardening vs Stress *****
6240
6250 OPEN #5: SCREEN .51,1,0,1
6260
6270 PRINT ""
6280 PRINT ""
6290 PRINT "DO YOU WANT"
6300 PRINT "W.H.VS STRS?"
6310 INPUT Z$

```

Appendix C

```

6320 IF Z$ = "Y" THEN CLEAR
6330 IF Z$ = "Y" THEN CLOSE #3
6340
6350 OPEN #6: SCREEN .51,1,.51,1
6360
6370 SET WINDOW 0,S(IMAX)+100,0,WH(1)+500
6380 PLOT TEXT,AT S(IMAX)*.6+50,WH(1)-400: "W.H. vs S"
6390 BOX LINES 0,S(IMAX)+100,0,WH(1)+500
6400
6410 FOR X=.000001 TO STRNSTART STEP .005
6420     IF ANBEST + CNBEST*EXP(-BNBEST*X) < 0 THEN GOTO
        6440
6430     PLOT POINTS : (ANBEST + CNBEST*EXP(-BNBEST*X))^.5,
        (-.5*CNBEST*BNBEST*EXP(-BNBEST*X))/(ANBEST +
        CNBEST*EXP(-BNBEST*X))^.5
6440 NEXT X
6450
6460 FOR X=STRNSTART TO E(IBREAK) STEP .005
6470     PLOT POINTS : (ANBEST + CNBEST*EXP(-BNBEST*X))^.5,
        (-.5*CNBEST*BNBEST*EXP(-BNBEST*X))/(ANBEST +
        CNBEST*EXP(-BNBEST*X))^.5
6480     PLOT POINTS : EXP(KEY1BEST)*X^EN1BEST,
        EXP(KEY1BEST)*X^(EN1BEST-1)
6490 NEXT X
6500
6510 FOR X = E(IBREAK) TO 2.25*E(ITOT) STEP .005
6520     PLOT POINTS : (ANBEST + CNBEST*EXP(-BNBEST*X))^.5,
        (-.5*CNBEST*BNBEST*EXP(-BNBEST*X))/(ANBEST +
        CNBEST*EXP(-BNBEST*X))^.5
6530     PLOT POINTS : EXP(KEY2BEST)*X^EN2BEST,
        EXP(KEY2BEST)*X^(EN2BEST-1)
6540 NEXT X
6550
6560 FOR I=1 TO IHMAX
6570     PLOT POINTS:MSS(I),WH(I)
6580 NEXT I
6590
6600 CLOSE #4
6610 CLOSE #5
6620
6630 !***** dln(Stress)/d(strain) vs Stress *****
6640
6650 OPEN #7: SCREEN .51,1,0,.5
6660
6670 SET WINDOW 0,300,-1,50
6680 PLOT TEXT,AT 200,40: "LOG(WH)/S vs S"
6690 BOX LINES 0,300,0,50
6700
6710 FOR X = 0 TO E(IMAX) STEP .001
6720     PLOT POINTS:(ANBEST+CNBEST*EXP(-BNBEST*X))^.5,
        (-.5*CNBEST*BNBEST*EXP(-BNBEST*X))/(ANBEST +
        CNBEST*EXP(-BNBEST*X))
6730 NEXT X
6740

```

Appendix C

```

6750  FOR I=1 TO IHMAX
6760    PLOT POINTS: MSS(I),WH(I)/MSS(I)
6770  NEXT I
6780
6790  PLOT LINES: 0,1;300,1
6800
6810  CLOSE #6
6820  CLOSE #7
6830
6840  STOP
6850  !*****
6860  LET S1=0
6870  LET S2=0
6880  LET S3=0
6890  LET S4=0
6900  LET S5=0
6910
6920
6930  FOR IT=MM TO NN+ISATM
6940    LET K(IT)=EXP(-B*E(IT))
6950    LET S1=S1+(1-K(IT))^2
6960    LET S2=S2+(1-K(IT))*(-SIGMA2*K(IT)+(S(IT)^2))
6970    LET S3=S3+(1-K(IT))*E(IT)*K(IT)
6980    LET S4=S4+E(IT)*K(IT)*(SIGMA2*K(IT)-(S(IT)^2)-
      SIGMA2*(1-
        K(IT)))
6990    LET S5=S5+E(IT)*SIGMA2*K(IT)*(-SIGMA2*K(IT)+(S(IT)^2))
7000
7010  NEXT IT
7020
7030
7040  IF (S4^2-4*S3*S5)<0 THEN
7050    LET A=S2/S1
7060    LET F=S3*A^2+S4*A+S5
7070    GOTO 7120
7080  END IF
7090  LET F=(((-S4+((S4)^2-4*S3*S5)^.5)/2/S3)-(S2/S1)
7100  LET A=S2/S1
7110
7120  RETURN
7130  !*****
7140  LET SX=0
7150  LET SY=0
7160  LET SXY=0
7170  LET SX2=0
7180  FOR IREG=REGI TO REGF
7190    LET SX=SX+XREG(IREG)
7200    LET SY=SY+YREG(IREG)
7210    LET SXY=SXY+XREG(IREG)*YREG(IREG)
7220    LET SX2=SX2+XREG(IREG)^2
7230  NEXT IREG
7240  LET NPT=REGF-REGI+1
7250  LET MSX=SX/NPT
7260  LET MSY=SY/NPT

```

Appendix C

7270 LET SLP=(SXY-NPT*MSX*MSY)/(SX2-NPT*MSX^2)
7280 LET INTERCEPT=MSY-SLP*MSX
7290 RETURN
7300 !*****
7310 LET SMOY=0
7320 FOR KR=IRI TO IRF
7330 LET SMOY=SMOY+EXPVAL(KR)
7340 NEXT KR
7350 LET SMOY=SMOY/(IRF-IRI+1)
7360 LET R1=0
7370 LET R2=0
7380 FOR KR=IRI TO IRF
7390 LET R1=R1+(EXPVAL(KR)-FITVAL(KR))^2
7400 LET R2=R2+(EXPVAL(KR)-SMOY)^2
7410 NEXT KR
7420 LET R=1-R1/R2
7430 RETURN
7440 !*****
7450 END

Appendix C

```

1000  !*****
1010  !                                     ADHECOR
1020  !
1030  ! This program corrects the stress/strain data for adiabatic heating.
1040  ! This correction is performed at each strain increment and the corrected
1050  ! stress/strain data are rewritten.
1060
1070  !*****
1080
1090  OPEN #1: PRINTER
1100  DIM E(500),S(500),SCOR1(500),F(500),H(500),AT(500),DT(500),
      INVTK(500),SR(500)
1110  DIM
      SG(500),OM(500),UA(500),SLOPST(500),XF(500),EXPVAL(500),
      FITVAL(500)
1120  DIM RST(500),AREA(500),DELTAT(500),DELTAS(500)
1130  LIBRARY "fnhlib"
1140  DECLARE DEF SINH
1150  SET MODE "80"
1160  PRINT "Input the file number"
1170  INPUT FN,N$
1180  PRINT "Input the strain rate"
1190  INPUT SRT
1200  PRINT "Input the austg. and def temperatures"
1210  INPUT ATP,DTP
1220  LET INVT=1/(DTP+273)
1230  PRINT "Do you want to use the mean str. or flow str.?(M/S)"
1240  INPUT Z$
1250  OPEN #2:NAME "PARAMCUB.TRU",ORGANIZATION TEXT
1260  LET I=0
1270  DO WHILE MORE #2
1280  LET I=I+1
1290  INPUT #2:AA$
1300  LET AF$=AA$[1:4]
1310  LET AH$=AA$[6:8]
1320  LET AAT$=AA$[11:17]
1330  LET ADT$=AA$[19:24]
1340  LET ASR$=AA$[27:29]
1350  LET ASG$=AA$[32:38]
1360  LET AOM$=AA$[40:49]
1370  LET AUA$=AA$[51:60]
1380  LET F(I)=VAL(AF$)
1390  LET H(I)=VAL(AH$)
1400  LET AT(I)=VAL(AAT$)
1410  LET DT(I)=VAL(ADT$)
1420  LET DT(I)=DT(I)+273
1430  LET INVTK(I)=1/DT(I)
1440  LET SR(I)=VAL(ASR$)
1450  LET SG(I)=VAL(ASG$)
1460  LET OM(I)=VAL(AOM$)
1470  LET UA(I)=VAL(AUA$)

```

Appendix C

```

1480 IF (F(I)=FN AND SR(I)=SRT AND AT(I)=ATP AND DT(I)=DTP)
    THEN
    PRINT "THE FILE EXISTS"
1490 PRINT I,AT(I),DT(I),SR(I)
1500 LOOP
1510 CLOSE #2
1520 LET IMAX=I
1530 DEF SIGMA(I,X)=(SG(I)*EXP(-OM(I)*X)+UA(I)/OM(I)*(1-EXP(-
    OM(I)*X)))^5
1540
1550 !*****
1560
1570 OPEN #3:SCREEN 0,.5,.5,1
1580 SET WINDOW 6.5E-4,9.9E-4,0,300
1590 SET MODE "HIRES"
1600 BOX LINES 6.5E-4,9.9E-4,0,300
1610 LET J=0
1620 FOR I=1 TO IMAX
1630     IF (AT(I)=ATP AND SR(I)=SRT) THEN LET J=J+1
1640 NEXT I
1650 LET JMAX=J
1660
1670 !*****
1680
1690 OPEN #4:NAME "A."&N$&".DAT",ORGANIZATION TEXT
1700 LET K=0
1710 DO WHILE MORE #4
1720 LET K=K+1
1730 INPUT #4:BB$
1740 LET A$=BB$(17:22)
1750 LET B$=BB$(26:31)
1760 LET E(K)=VAL(A$)
1770 LET S(K)=VAL(B$)
1780 LOOP
1790 CLOSE #4
1800 LET KMAX=K
1810
1820 LET RMAX=0
1830 LET RMIN=1
1840 FOR K=1 TO KMAX
1850     IF E(K)>=.05 THEN 1870
1860 NEXT K
1870 LET K05=K
1880
1890 FOR K=K05 TO KMAX
1900
1910     LET X=E(K)
1920
1930
1940     LET ST=0
1950     LET SS=0
1960     LET STS=0
1970     LET ST2=0
1980     FOR I=1 TO IMAX

```

Appendix C

```

1990      IF (AT(I)=ATP AND SR(I)=SRT) THEN
2000          IF (SG(I)*EXP(-OM(I)*X) + UA(I)/OM(I)*(1-EXP(-OM(I)*
              E(K05,,)) > 0 THEN 2040
2010
2020      GOTO 2710
2030      PRINT XSTART,I,X
2040      LET ST=ST+INVTK(I)
2050      LET ST2=ST2+INVTK(I)^2
2060
2070          IF Z$="M" THEN
2080              GOSUB 3320
2090              LET SS=SS+MSF
2100              LET STS=STS+INVTK(I)*MSF
2110              GOTO 2150
2120          END IF
2130          LET SS=SS+SIGMA(I,X)
2140          LET STS=STS+INVTK(I)*SIGMA(I,X)
2150      END IF
2160
2170      NEXT I
2180
2190      LET MST=ST/JMAX
2200      LET MSS=SS/JMAX
2210      LET SLPST=(STS-JMAX*MST*MSS)/(ST2-JMAX*MST^2)
2220      LET ITRCPTST=MSS-SLPST*MST
2230
2240      LET IRI=1
2250      LET IRF=JMAX
2260      FOR I=1 TO IMAX
2270          IF (AT(I)=ATP AND SR(I)=SRT) THEN
2280              IF Z$="M" THEN
2290                  GOSUB 3320
2300                  LET EXPVAL(I)=MSF
2310                  GOTO 2340
2320              END IF
2330              LET EXPVAL(I)=SIGMA(I,X)
2340              LET FITVAL(I)=ITRCPTST+SLPST*INVTK(I)
2350          END IF
2360      NEXT I
2370      GOSUB 3550
2380
2390      LET SLOPST(K)=SLPST
2400      LET XF(K)=X
2410      LET RST(K)=R
2420      IF RMAX<RST(K) THEN LET RMAX=RST(K)
2430      IF RMIN>RST(K) THEN LET RMIN=RST(K)
2440      FOR I=1 TO IMAX
2450          IF (AT(I)=ATP AND SR(I)=SRT) THEN
2460              IF Z$="M" THEN
2470                  GOSUB 3320
2480                  PLOT POINTS:INVTK(I),MSF
2490                  GOTO 2520
2500              END IF
2510              PLOT POINTS:INVTK(I),SIGMA(I,X)

```

Appendix C

```

2520     END IF
2530   NEXT I
2540   FOR T=800 TO 1200 STEP 2
2550     PLOT POINTS:1/(T+273),ITRCPTST+SLPST/(273+T)
2560   NEXT T
2570
2580   LET COEF1=SLOPST(K)
2590   LET RO=7.86
2600   LET CO=.11
2610   LET JO=4.18
2620   LET AREA(1)=0
2630   FOR IK=2 TO K
2640     LET AREA(IK)=AREA(IK-1)+(E(IK)-E(IK-1))*(S(IK)+S(IK-
                                     1))/2
2650   NEXT IK
2660
2670   LET DELTAT(K)=AREA(K)/JO/CO/RO
2680   LET DELTAS(K)=COEF1*(INVT-1/(DTP+273+DELTAT(K)))
2690   LET SCOR1(K)=S(K)+DELTAS(K)
2700   PRINT #1:X,DELTAT(K),DELTAS(K)
2710 NEXT K
2720
2730 CLOSE #3
2740
2750 OPEN #5: SCREEN .51,1,.5,1
2760 SET WINDOW 0,1.25*E(KMAX),0,1.25*S(KMAX)
2770 BOX LINES 0,1.25*E(KMAX),0,1.25*S(KMAX)
2780   FOR K=1 TO KMAX
2790     PLOT POINTS :E(K),S(K)
2800     PLOT POINTS :E(K),SCOR1(K)
2810   NEXT K
2820 CLOSE #5
2830
2840 OPEN #5: SCREEN 0,.5,0,.49
2850 SET WINDOW LOG(.01),LOG(.99),1.E5,1.E6
2860 BOX LINES LOG(.01),LOG(.99),1.E5,1.E6
2870   FOR K=K05 TO KMAX
2880     PLOT POINTS :LOG(XF(K)),SLOPST(K)
2890   NEXT K
2900 CLOSE #5
2910 OPEN #6: SCREEN .51,1,0,.49
2920 SET WINDOW E(K05),1.25*E(KMAX),1.E5,1.E6
2930 BOX LINES E(K05),1.25*E(KMAX),1.E5,1.E6
2940   FOR K=1 TO KMAX
2950     PLOT POINTS :XF(K),SLOPST(K)
2960   NEXT K
2970
2980 CLOSE #6
2990 PRINT #1:TAB(1);"FILE";TAB(15);"Aust. Temp.";TAB(35);"Def.
Temp.";TAB(48);"Strain Rate"
3000 PRINT #1:TAB(1);N$;TAB(17);ATP;TAB(38);DTP;TAB(50);SRT
3010 PRINT #1: " "
3020 PRINT #1:TAB(10);"Rmin IS: ";TAB(20);RMIN
3030 PRINT #1:TAB(10);"Rmax IS: ";TAB(20);RMAX

```


Appendix C

```

3040
3050 PRINT #1:""
3060
3070 PRINT
#1:TAB(1);"STRAIN";TAB(12);"TEMPER.";TAB(22);"DELTA
T";TAB(38);"DELTA S1";TAB(50);"DT/E";TAB(62);"DS/SE"
3080 PRINT " "
3090
3100 PRINT
#1:TAB(1);E(KMAX);TAB(12);DTP;TAB(21);DELTAT(KMAX);TAB
(37);SCOR1(KMAX)-S(KMAX);TAB(49);DELTAT(KMAX)/
E(KMAX);TAB(62);-(SCOR1(KMAX)-S(KMAX))/S(KMAX)/
E(KMAX)
3110
3120 PRINT #1:"-----"
3130 PRINT #1:" "
3140 PRINT #1:" "
3150 INPUT P$
3160 CLEAR
3170 PRINT "Do you want to write the stress-strain values?"
3180 INPUT W$
3190 IF W$="Y" THEN
3200 PRINT "Put disc in drive A and print C to start"
3210 INPUT D$
3220 OPEN #5:NAME "A:"&N$&".DAT",CREATE NEW
3230 FOR IW = 1 TO K05 - 1
3240 PRINT #5:TAB(1);IW;TAB(22);E(IW);TAB(34);S(IW)
3250 NEXT IW
3260 FOR IW = K05 TO KMAX
3270 PRINT #5:TAB(1);IW;TAB(22);E(IW);TAB(34);SCOR1(IW)
3280 NEXT IW
3290 CLOSE #5
3300 END IF
3310 STOP
3320 !*****
3330
3340 LET H$IM = X/10
3350
3360 LET X$ = 0
3370 LET S4 = 0
3380 LET S2 = 0
3390 FOR K1 = 1 TO 5
3400 LET X$ = X$ + H$IM
3410
3420 IF (SG(I)*EXP(-OM(I)*X$) + UA(I)/OM(I)*(1-EXP(-OM(I)*X$)))
< 0 THEN
3430 LET H$IM = H$IM + X$STEP/10
3440 GOTO 3360
3450 END IF
3460 LET S4 = S4 + SIGMA(I,X$)
3470 LET X$ = X$ + H$IM
3480 LET S2 = S2 + SIGMA(I,X$)
3490
3500 NEXT K1

```

Appendix C

```

3510 LET ISIM=(4*S4+2*S2-SIGMA(I,X))*HSIM/3
3520 LET MSF=ISIM/X
3530
3540 RETURN
3550 !*****
3560 LET SMOY=0
3570 FOR KR=1 TO IMAX
3580 IF (AT(KR)=ATP AND SR(KR)=SRT) THEN
3590 LET SMOY=SMOY+EXPVAL(KR)
3600 END IF
3610 NEXT KR
3620
3630 LET SMOY=SMOY/(IRF-IRI+1)
3640 LET R1=0
3650 LET R2=0
3660
3670 FOR KR=1 TO IMAX
3680 IF (AT(KR)=ATP AND SR(KR)=SRT) THEN
3690 LET R1=R1+(EXPVAL(KR)-FITVAL(KR))^2
3700 LET R2=R2+(EXPVAL(KR)-SMOY)^2
3710 END IF
3720 NEXT KR
3730
3740 LET R=1-R1/R2
3750 RETURN
3760 !*****
3770
3780 END

```